

© 2014

Michael James Berry

ALL RIGHTS RESERVED

THE EVOLUTION OF NEUTRAL GAS IN STAR-FORMING GALAXIES ACROSS COSMIC TIME

By

MICHAEL JAMES BERRY

A dissertation submitted to the
Graduate School—New Brunswick
Rutgers, The State University of New Jersey
in partial fulfillment of the requirements
for the degree of
Doctor of Philosophy
Graduate Program in Physics and Astronomy
written under the direction of
Dr. Rachel Somerville
and approved by

New Brunswick, New Jersey

May, 2014

ABSTRACT OF THE DISSERTATION

The Evolution of Neutral Gas in Star-Forming Galaxies Across Cosmic Time

By MICHAEL JAMES BERRY

Dissertation Director:

Dr. Rachel Somerville

We study the evolution of cold gas in distant galaxies by analyzing observations, semi-analytic models (SAMs), and simulations of star-forming galaxies (SFGs) and damped Ly α absorption systems (DLAs). First, we present individual and composite rest-frame ultraviolet (UV) spectra for 81 SFGs where we study the relations among Ly α emission, low and high ionization absorption strength, rest-ultraviolet continuum slope, redshift, and velocity offset. We find that galaxies with $R < 25.5$ and $W_{\text{Ly}\alpha} > 20\text{\AA}$ have bluer UV continua, weaker low-ionization interstellar absorption lines, weaker C IV absorption, and stronger Si II nebular emission than those with $W_{\text{Ly}\alpha} < 20\text{\AA}$. Next, we present our range of models which include “standard,” “extended,” and merger-based disks as well as a metallicity-dependent and pressure-based prescription for partitioning cold gas into atomic and molecular components. Using these models, we “observe” a catalog of mock DLAs, which we compare to observations. We find that extended disk models reproduce quite well the column density distribution of absorbers over the column density range $19 < \log N_{\text{HI}} < 22.5$, the observed line density of DLAs, HI gas density, the Δv distribution in the redshift range $2 < z < 3.5$, and the evolution of DLA metallicity with redshift. Using these models, we characterize the properties of DLA host galaxies and compare them to model SFGs “observed” in the SAMs.

We show that DLA host galaxies exhibit a broad range of galaxy properties spanning several decades in stellar mass, star formation rate, and luminosity and fall upon common galaxy scaling relations. Finally, we analyze the radial profiles and evolution of 15 galaxies in numerical simulations and compare them to predictions from the SAMs. Galaxies' cold gas and stellar components are moderately well-fit by exponential profiles, although both gas partitioning recipes predict more molecular gas and less star formation than is observed in the numerical simulations. Nonetheless, both types of simulations predict similar evolution in galaxy properties from $z = 2$ to $z = 0$.

Acknowledgments

First, I would like to thank Rachel Somerville, my advisor, for her incredibly high standards, confidence in my abilities, patience, huge amount of knowledge, and teaching me so much in general. I would also like to thank Eric Gawiser for teaching me to think critically, question my assumptions, and invent my own solutions in addition to being a good friend. I would like to thank Zeljko Ivezic for taking a chance on me and providing me with a fantastic opportunity to learn. I would also like to thank my committee members (Jack Hughes, Valerie Kiryukhin, and Ari Maller) for helpful comments that no doubt improved the quality of this work.

I would like to thank the Rutgers astronomy group for providing a stimulating, open, and friendly environment in which I have developed both personally and professionally. I have learned a great deal about how to think, the universe, and myself. I would also like to thank the astronomy graduate students (especially Brandon, Amitpal, Jean, Chelsea, and Curtis) for slogging through homework assignments together, burning the late night oil, and plenty of fun and interesting times.

Most of all, I would like to thank my family, Pat, Russell, and Sara, for always believing in me and providing an enormous amount of support. Finally, I would like to thank the countless other people who have made this work possible by positively influencing my life.

Portions of this work have appeared or will appear in publication elsewhere. Chapter 2 is published in Berry et al. (2012) and Chapter 4 is published in Berry et al. (2013). Chapters 5 and 6 will be submitted as Berry et al. (2014b) and Berry et al. (2014c). I would like to thank my coauthors (Rachel Somerville, Eric Gawiser, Lucia Guaita, Nelson Padilla, Ezequiel Treister, Gullirno A. Blanc, Robin Ciardullo, Harold Francke, Caryl Gronwall, Marcel Haas, Ari Maller, Gergo Popping, Scott C. Trager, Charlotte Christensen, and Alyson Brooks) in these works for helpful comments and discussions. These works have

been supported by NSF AST 08-07570 grant, NSF AST 08-07885 grant, NSF Career Grant 1055919, NSF Grant 1153335, and the Downsbrough fund.

Dedication

For Science

Table of Contents

Abstract	ii
Acknowledgments	iv
Dedication	vi
List of Tables	x
List of Figures	xi
1. Introduction	1
1.1. Galaxy Formation	1
1.2. Cold Gas	2
1.3. Star Formation	3
1.4. Star-Forming Galaxies at High-Redshift	6
1.5. Damped Ly α Absorption Systems	11
1.6. Semi-Analytic Models	14
1.7. The Contents of This Thesis	17
2. Stacked Rest-frame Ultraviolet Spectra of Lyα-emitting and Continuum- selected Galaxies at $2 < z < 3.5$	22
2.1. Introduction	22
2.2. Observations and Methodology	25
2.3. Individual Galaxy Properties	29
2.4. Stacking Procedure	33
2.5. Analysis of Composite Spectra	36

2.6. Discussion	50
2.7. Conclusions	65
3. Semi-Analytic Models	69
3.1. Semi-Analytic Models	69
4. Damped Lyα Absorption Systems in Semi-Analytic Models with Multi- phase Gas	81
4.1. Introduction	81
4.2. Results	88
4.3. Discussion	120
4.4. Conclusions	127
5. Relations among Damped Lyα Absorption Systems and Star-Forming Galaxies in Semi-Analytic Models at $z = 2$	129
5.1. Introduction	129
5.2. Galaxy Selection	133
5.3. Properties of Model and Observed Star-Forming Galaxies	139
5.4. Results	141
5.5. Discussion	166
5.6. Conclusions	173
6. Galaxy Structure in Numerical Simulations and Semi-Analytic Models	175
6.1. Introduction	175
6.2. Numerical Simulations	178
6.3. Results	181
6.4. Discussion	197
6.5. Conclusions	202
7. Conclusions	204

Bibliography	210
-------------------------------	-----

List of Tables

2.1. Subsample Criteria	34
2.2. Spectroscopic Properties of All-SFG Composite	38
2.3. Spectroscopic Properties of UV-bright non-LAE, UV-bright LAE, UV-bright SFG Composites	40
2.4. Si II* Emission in UV Bright SFG Composite	49
2.5. Spectroscopic Properties of $z \sim 2$ and $z \sim 3$ UV Bright Composites	62
3.1. Model Definitions	80
4.1. Halo mass vs. DLA cross-section ($M_h - \sigma_{DLA}$) Relation	105
4.2. DLA Metallicity vs. redshift Best-Fit Parameters	111
4.3. DLA Δv_{90} K-S Test	116
4.4. DLA Metallicity vs. Δv_{90} Best-Fit Parameters	120
5.1. Galaxy Properties	139
5.2. Average DLA Host Galaxy Properties	146
6.1. Average Galaxy Properties at $z = 0$	178

List of Figures

1.1. Relation between cold gas and star formation	5
1.2. LBG selection technique	8
1.3. LAE selection technique	10
1.4. Observation of 2 DLAs in QSO PSS0209	13
2.1. Individual LAE and non-LAE galaxy properties	31
2.2. Composite spectrum of 59 UV bright LAEs and non-LAEs	35
2.3. Composite spectra for UV faint LAEs, UV bright LAEs, and UV bright non-LAEs	37
2.4. Low- λ zoom-in composite spectra of LAEs and LBGs	42
2.5. High- λ zoom-in composite spectra of LAEs and LBGs	45
2.6. Spectroscopic incompleteness as a function of R band magnitude	52
2.7. Composite spectra based on UV spectral slope	56
2.8. Dependence of UV spectroscopic properties on Ly α equivalent width	57
2.9. Dependence of Ly α equivalent width on spectral slope and LIS absorption	60
2.10. Dependence of Ly α equivalent width and low ionization absorption on spectral slope	61
2.11. Composite spectra of UV bright LAEs and non-LAEs at $z = 2$ and $z = 3$	63
4.1. Cold gas radial profiles of galaxies in the SAMs	86
4.2. Galaxy distribution functions in the SAMs	90
4.3. Column density distribution function at $2 < z < 3.5$	93
4.4. Column density distribution function evolution with redshift	96
4.5. Comoving line density of DLAs	97
4.6. Cosmic density of HI contained in DLAs, Ω_{DLA}	100
4.7. DLA cross section versus halo mass	104

4.8. Distribution of DLA metallicities at $2 < z < 3.5$	107
4.9. DLA metallicity as a function of redshift	110
4.10. Distribution of DLA metallicities with a metallicity gradient	112
4.11. Distribution of DLA velocity widths, Δv	115
4.12. Distribution of DLA halo masses and Δv dependence on halo mass	118
4.13. DLA metallicities versus velocity widths	119
5.1. Relations among stellar mass, H band magnitude, halo mass, star formation rate, and B band magnitude	135
5.2. Redshift distribution for BMs/BXs, HST U225-/U275-band dropouts, and BzKs	137
5.3. Distribution of galaxy properties for BMs/BXs, HST U225-/U275-band dropouts, and BzKs	140
5.4. Distribution of galaxy properties for all galaxies and DLAs	143
5.5. Color-color diagrams for all galaxies and DLAs	148
5.6. Cumulative stellar mass and H band distributions for DLAs	149
5.7. Distribution of E(B-V) values for SFGs and DLAs	151
5.8. Distribution of impact parameters for DLAs	153
5.9. Distribution of average galaxy properties and those along the line of sight	155
5.10. Relations among DLA impact parameter, column density, and metallicity	157
5.11. DLA metallicity versus column density	159
5.12. DLA cross section and cold gas fraction versus stellar mass	161
5.13. Star formation rate and metallicity versus stellar mass	163
5.14. E(B-V) value versus stellar mass	165
6.1. Radial profiles of galaxies in the numerical simulations at $z = 2$	182
6.2. Radial profiles of galaxies in the numerical simulations at $z = 0$	183
6.3. Radial profiles of galaxy metallicities in the numerical simulations	186
6.4. Radial profiles of galaxy SFRs in the numerical simulations	188
6.5. Evolution of galaxy properties	190
6.6. Dependence of galaxy properties on stellar mass at $z = 2, 0$	192

6.7. Dependence of stellar disk size and gas fraction on stellar mass	194
6.8. Dependence of star formation rate and metallicity on stellar mass	196

Chapter 1

Introduction

1.1 Galaxy Formation

Galaxy formation is the process through which density fluctuations in the post-inflation universe became the galaxies observed today. First, quantum fluctuations were magnified by inflation, creating macroscopic density fluctuations. After inflation, baryonic matter and radiation were coupled so that acoustic oscillations were prevented from growing in amplitude, making it impossible for the first protogalaxies to collapse. The primordial universe continued to expand and cool until neutral hydrogen atoms formed, causing matter and radiation to decouple, allowing photons to travel freely. This decoupling occurred 380,000 years after the Big Bang and caused the Jeans mass, the threshold for which an overdensity will collapse, to drastically decrease, allowing the first dark matter overdensities to condense (Coles & Lucchin 2002). Dark matter consists of noninteracting particles that are unaffected by internal pressure due to heating, which resulted in them being the first to collapse and form gravitationally bound structures. The gas interior to these dark matter potentials radiatively cooled and collapsed, falling into the central regions of the galaxy. This gas held the same specific angular momentum as its dark matter halo. While collapsing, conservation of angular momentum dictates that it form a rotating disk. In these disks, smaller clouds of gas continued to cool and condense into the first stars, thereby creating the first protogalaxies.

After the first galaxies formed, cold gas continued to flow into them along streams and filaments, which fed further star formation. As stars near the end of their lifetimes, the cores of the most massive ones collapse in energetic explosions called supernovae. These supernovae in combination with stellar winds inject massive amounts of energy and momentum into the surrounding gas. Through repeated episodes of star formation, these

supernovae created cavities of hot gas, and if enough energy and momentum built up, they could launch galaxy-scale winds. These winds drove gas out of the galaxy in massive outflows, which could potentially shut off star formation. Understanding these processes of cold gas accretion, star formation, and feedback from supernovae at different epochs has been the subject of much observational and theoretical work, in addition to characterizing the types of galaxies in which they occur.

1.2 Cold Gas

Almost all visible matter in the Universe is made up of two basic components: stars and gas. Of the latter, gas largely divides into three phases: ionized gas, neutral gas, and molecular gas. After the Big Bang, the Universe was hot and dense enough for nucleosynthesis to occur. During this period, nuclear reactions occurred, leading to 25% of the mass of hydrogen being converted into helium along with trace amounts of heavier elements. As a result, 75% of the mass density of gas in the Universe is in the form of hydrogen. For this reason, we refer to ionized, atomic, and molecular gas as HII, HI, and H₂ respectively.

Hydrogen is neutral at a temperature of $T \sim 10^4$ K in typical conditions of the local interstellar medium (ISM). At this temperature, the pressure from surrounding hot, ionized gas forces it into clumps or clouds. These cold clouds of gas are difficult to observe as HI is only visible in absorption through one of the electronic transitions (e.g., Lyman series, Balmer series, etc.) or in emission through the 21 cm hyperfine structure transition. The most common electronic transition to view HI in absorption is the Ly α transition at $\lambda = 1216\text{\AA}$. However, this line occurs in the far ultraviolet (UV) where observations are limited to only a few space-based telescopes, making it difficult to observe in nearby galaxies.

The 21 cm hyperfine structure line is caused by the atomic transition between two hyperfine energy levels in the 1s ground state. Although this forbidden transition occurs with only a small probability of $2.9 \times 10^{-15} \text{ s}^{-1}$, large numbers of hydrogen atoms make this line observable in clouds of quiescent neutral gas. Locally, through the 21 cm spectral line, we can determine the mass, physical, and kinematic distribution of HI, allowing for detailed mapping of velocity structures. Through wide-field imaging surveys taken by interferometers

at radio wavelengths, maps of HI can be made of nearby galaxies.

Within these clouds of neutral gas, HI can cool and condense into H₂. Observing H₂ is even more challenging, as its transitions are not observable at the energies and typical conditions of molecular clouds. Its rotational transitions are forbidden and its vibration-rotation lines only are excited near hard, ionizing sources or in shock fronts. Observations of cold dense gas have revealed carbon monoxide, CO, to be a good tracer of H₂, as it is the next most common molecule and not easily destroyed by UV radiation. CO has several strong electric dipole moments whose frequencies occur at radio wavelengths that are easily excited by collisions in typical conditions of molecular clouds. Observations of these transitions yield information on the mass and distribution of CO, which can then be used to infer the amount of H₂ through an X_{CO} conversion factor. Similar to mapping HI, interferometers at radio wavelengths can generate maps of molecular gas in nearby galaxies.

1.3 Star Formation

In star forming regions, young massive stars emit strongly in the ultraviolet due to their high surface temperature. Hot young stars burn through their fuel at a much faster rate than their smaller redder counterparts and consequently have shorter lives by up to several orders of magnitude ($1M_{\odot}$, 10^{10} yrs; $5M_{\odot}$, 6.5×10^7 yrs Collins et al. 2003). The strength of the UV continua in galaxies is proportional to the number of high mass stars. Due to their short lives, the ongoing star formation rate can be determined by scaling the initial mass function, the mass distribution of stars, to the number of high mass stars then integrating over it. The instantaneous star formation rate is then calculated through dividing the total mass of stars formed in the high mass stars' lifetimes and dividing by the typical lifetime. In addition, hydrogen-ionizing photons, with a wavelength of $\lambda \lesssim 912\text{\AA}$ corresponding to $\gtrsim 13.6$ eV, ionize the surrounding ISM, which then produces strong hydrogen recombination lines. Assuming case B recombination, during these recombinations, a large number of Balmer H α photons ($\lambda = 6563\text{\AA}$) are produced. Thus, H α emission also tracks the ongoing star formation rate.

However for both UV and H α star formation rate measures, a correction must be applied

based on the amount of dust surrounding the star-forming regions. Dust preferentially absorbs bluer wavelengths, causing UV and optical emission to be quite sensitive to the amount of dust. To take this effect into account, dust corrections must be applied (e.g. Calzetti et al. 1994). As a result of this absorption, dust re-emits light in the infrared, causing the total infrared (IR) luminosity ($\lambda \sim 3 - 1100\mu\text{m}$) to track the star formation rate (e.g. Rieke et al. 2009).

Features in the radio and X-ray that are caused by short-lived objects are also good tracers of the star formation rate. Synchrotron emission from SN remnants and free-free emission in ionized gas at low radio frequencies ($\nu \sim 1.4$ GHz) have also been shown to be correlated with the star formation rate (Murphy et al. 2011). Moreover, emission in the soft X-ray (2-10 KeV) tracks high mass X-ray binaries, which have also been observed to correlate with previously mentioned tracers (Ranalli et al. 2003). By observing galaxies in these different parts of the spectrum, we can measure or infer the star formation rate.

Through mapping the distribution of cold gas and star formation rate in nearby spiral galaxies and starburst nuclei, Schmidt (1959) and Kennicutt (1989, 1998) observed a correlation between the star formation rate surface density (Σ_{SFR}) and the total gas surface density ($\Sigma_{\text{H}} = \Sigma_{\text{HI}} + \Sigma_{\text{H}_2}$). This relation, the classical “Kennicutt-Schmidt” (KS) relation, is frequently approximated as a power law, $\Sigma_{\text{SFR}} \propto \Sigma_{\text{H}}^N$, with $N \sim 1.4$, above a critical total gas surface density Σ_{crit} . Empirical studies have shown that $\Sigma_{\text{crit}} \simeq 3\text{--}10 \text{ M}_{\odot}\text{pc}^{-2}$ (Martin & Kennicutt 2001). Due to the apparent simplicity of this relation, the vast majority of cosmological simulations have relied on it as a recipe for describing how cool gas turns into stars. Figure 1.1 (Figure 15 from Bigiel et al. 2008a) shows the star formation rate surface density as a function of gas surface density in nearby spiral and starburst galaxies.

More recently using higher resolution maps of HI and H₂ in nearby galaxies, Wong & Blitz (2002) showed that Σ_{SFR} is more tightly correlated with the density of molecular hydrogen Σ_{H_2} (as traced by CO) than with the total gas density. These results were confirmed and expanded upon with the results from the THINGS survey (Walter et al. 2008) combined with CO maps from BIMA SONG and HERACLES (Helfer et al. 2003; Leroy et al. 2009). These studies showed that $\Sigma_{\text{SFR}} \propto \Sigma_{\text{H}_2}^N$ with N very close to unity, implying that star formation takes place in molecular gas with roughly constant efficiency (Bigiel et al.

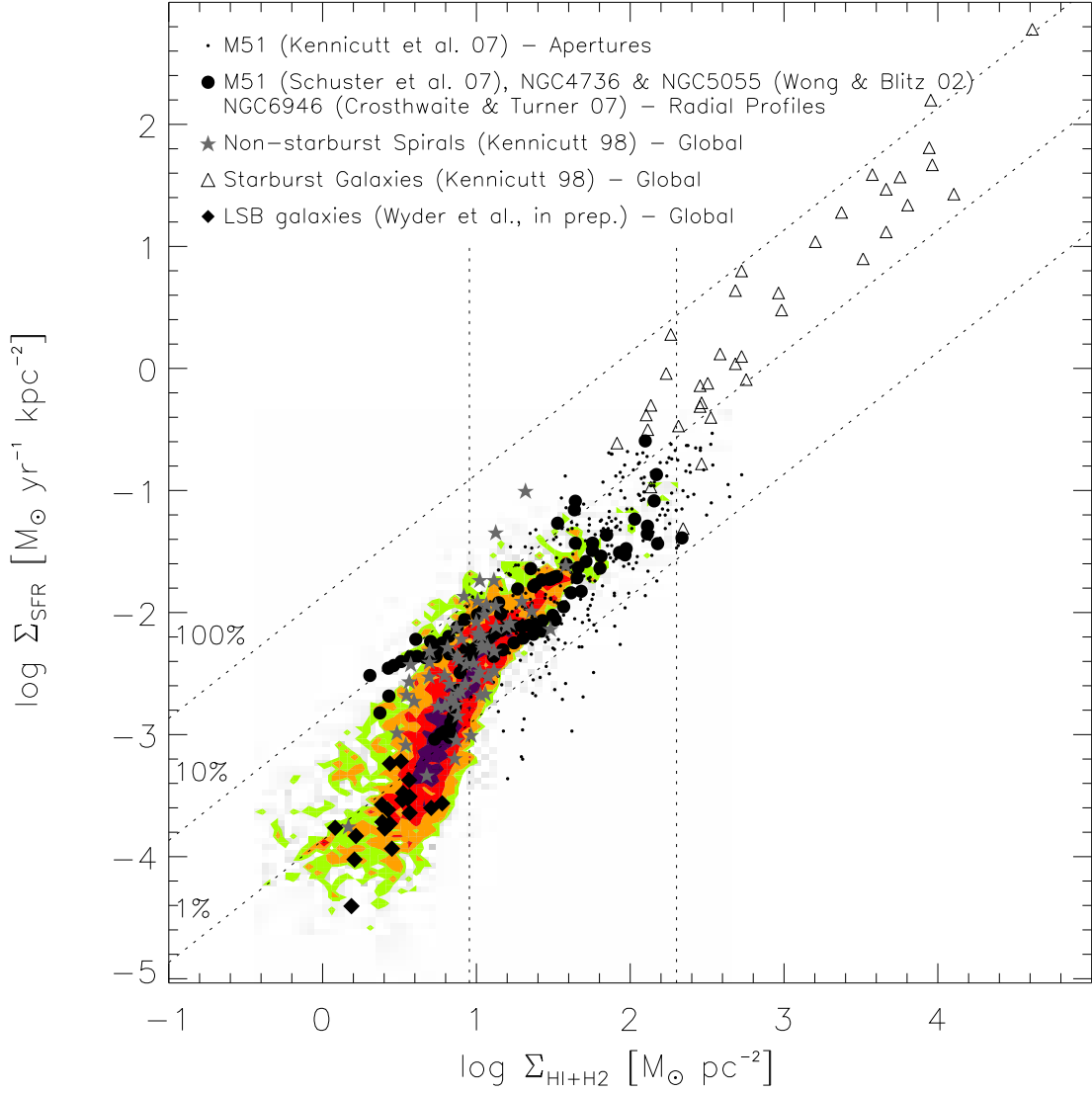


Figure 1.1 Star formation rate surface density Σ_{SFR} versus cold gas surface density $\Sigma_{\text{HI}+\text{H}_2}$ in nearby spirals and starburst galaxies. The diagonal dotted lines represent a constant star formation efficiency that will consume 1%, 10%, and 100% of the cold gas in 10^8 years. The vertical dotted line at $\Sigma_{\text{HI}+\text{H}_2} \sim 10 \text{ M}_{\odot} \text{ pc}^{-2}$ shows the surface density threshold above which HI is converted into H_2 . The vertical dotted line at $\Sigma_{\text{HI}+\text{H}_2} \sim 200 \text{ M}_{\odot} \text{ pc}^{-2}$ represents the transition to a superlinear star formation law, proposed to explain the high star formation rates seen in starburst galaxies. Above $\Sigma_{\text{HI}+\text{H}_2} \sim 10 \text{ M}_{\odot} \text{ pc}^{-2}$, the H_2 dominates the gas density, supporting the observed tighter correlation between SFR surface density and the surface density of H_2 (Figure 15 from Bigiel et al. 2008a).

2008a, 2011). These results underlined the importance of modeling the partitioning of gas into atomic and molecular phases in theoretical models of galaxy formation.

1.4 Star-Forming Galaxies at High-Redshift

Redshifting of light due to the expansion of the universe places the rest-frame ultraviolet in the observed optical at the epoch of peak cosmic star formation ($1 < z < 3$), thereby coinciding with the atmospheric transmission window (Madau et al. 1998). The bluest end located at 3200\AA corresponds to an emitted ultraviolet photon $\lambda_{\text{em}} = 1200\text{\AA}$ at a redshift of $z = 1.6$ as can be seen from Equation 1.1.

$$\lambda_{\text{obs}} = (\lambda_{\text{em}})(1 + z) \quad (1.1)$$

Thus, the large number of ground-based optical telescopes make extensive studies of UV-bright galaxies feasible. Star-forming galaxies exhibit strong rest-frame UV continua because the majority of the galaxy's luminosity emanates from young massive stars emitting strongly in the ultraviolet due to their high surface temperatures. Identifying star-forming galaxies based on their rest-frame UV features provides a convenient way to learn about the early stages of galaxy formation where galaxies were evolving rapidly.

1.4.1 Lyman Break Galaxies

Lyman break galaxies (LBGs) were the first significant statistical sample of high-redshift star-forming galaxies (Steidel et al. 1996b). At $z \sim 3$, they are selected to have a robust detection in optical filters yet an absence in ultraviolet ones (UV dropouts), meaning they have a much fainter observed U_n -band magnitude than G- or R-bands. As only galaxies with $R < 25.5$ are identified, this selection technique aims to search for star-forming galaxies with a strong rest-frame ultraviolet continuum. A Lyman break or Lyman limit occurs at a rest frame wavelength of 912\AA , the energy of a hydrogen ionizing photon. At $z \sim 3$ this break is redshifted to between the U_n - and G-band filters. This technique relies on the fact that light blueward of this wavelength is almost completely absorbed by neutral hydrogen surrounding the distant star-forming galaxy. Figure 1.2 shows an example of how LBGs

are selected with the U_n and G band filters placed around the Lyman break as is seen in the spectrum of the LBG. Observations of these galaxies have revealed them to be massive, highly star forming, with small amounts of dust, and driving galaxy-scale outflows of gas (Adelberger & Steidel 2000; Papovich et al. 2001; Shapley et al. 2001, 2005; Erb et al. 2006c; Reddy et al. 2006; Gawiser et al. 2006a; Pirzkal et al. 2007; Gawiser et al. 2007; Nilsson et al. 2007; Pentericci et al. 2007; Lai et al. 2008; Nilsson et al. 2009; Finkelstein et al. 2009; Guaita et al. 2010). Observations using similar techniques with different filter sets have revealed numerous other types of star-forming galaxies across a wide range of redshifts.

1.4.2 $\text{Ly}\alpha$ -Emitting Galaxies

A significant fraction of high-redshift LBGs exhibit $\text{Ly}\alpha$ emission (Shapley et al. 2001; Tapken et al. 2007; Pentericci et al. 2009; Kornei et al. 2010), leading to a focus on understanding the properties of this spectral feature as well as new surveys which sought to use it to identify high-redshift galaxies. Galaxies with a prominent $\text{Ly}\alpha$ emission line ($\lambda = 1216\text{\AA}$ or 10.2eV) can be selected by placing a narrowband filter at a wavelength targeting a certain redshift accompanied by encompassing broadband filters. Objects are selected as $\text{Ly}\alpha$ -emitting galaxies, LAEs, by having an excess narrowband flux density determined by fitting the average broadband flux to the narrowband, equivalent to assuming no $\text{Ly}\alpha$ emission. A generally accepted requirement for a galaxy to be classified as a LAE is having a $\text{Ly}\alpha$ equivalent width, a measure of the strength of a spectral feature, of $|\text{EW}_{\text{Ly}\alpha}| > 20\text{\AA}$, which typically corresponds to a $\text{Ly}\alpha$ emission line luminosity of $L_{\text{Ly}\alpha} > 10^{42} \text{ ergs s}^{-1}$ at $z \sim 2 - 3$ (e.g. Cowie & Hu 1998; Malhotra & Rhoads 2002; Ouchi et al. 2003, 2008; Finkelstein et al. 2008; Gronwall et al. 2007; Nilsson et al. 2007, 2009; Guaita et al. 2010). An example of this selection technique is shown in Figure 1.3. Most LAEs are found with $R > 25.5$, as this selection technique does not require detection in the continuum, allowing for the detection of fainter galaxies (e.g. Gawiser et al. 2006b; Nilsson et al. 2007; Gawiser et al. 2007; Lai et al. 2008; Ono et al. 2010; Finkelstein et al. 2008; Yuma et al. 2010; Pirzkal et al. 2007; Ono et al. 2010; Ouchi et al. 2010). In spite of their difference in luminosity, LAEs typically have similar colors to LBGs although there is significant variation in their

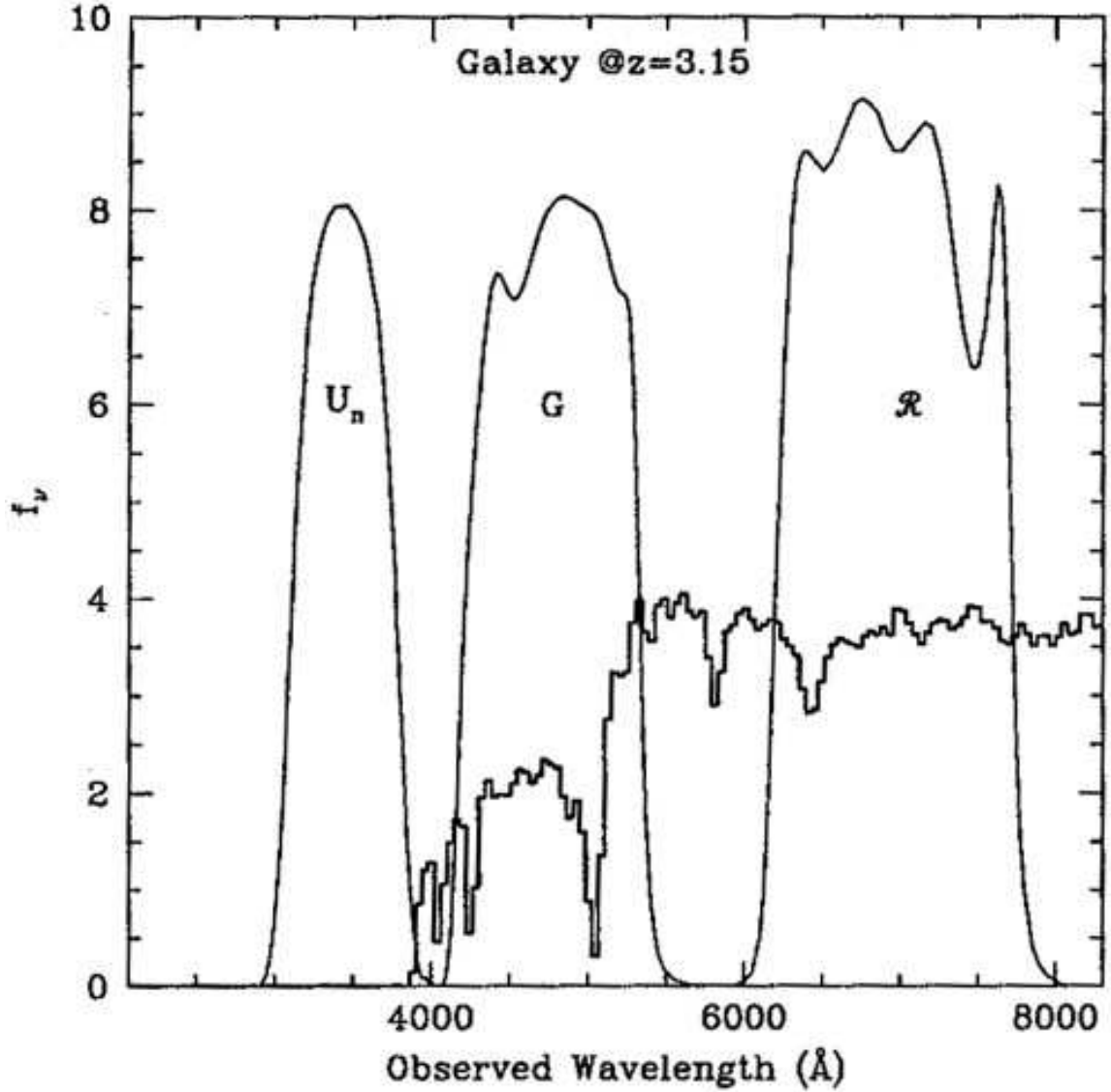


Figure 1.2 Spectrum of a Lyman break galaxy at $z = 3.15$ with the filter transmissions curves for the U_n , G , and R broadband filters overlaid. The Lyman break due to absorption from H I around the LBG can be seen at $\lambda \sim 3800 \text{\AA}$. LBGs are identified as having no flux in the U_n -band filter while robust detections in the G - and R -band filters. LBGs must be undergoing significant star formation and have little dust to be sufficiently bright in the UV to be detected (top panel of Figure 1 from Giavalisco 1998).

properties (Gronwall et al. 2007; Guaita et al. 2010). One advantage of this selection technique is that it allows us to probe star-forming galaxies at the faint end of the luminosity function where galaxies are less massive and the properties of galaxies in general are not well understood (Zheng et al. 2010; Cassata et al. 2011).

Partridge & Peebles (1967) first predicted that young star-forming galaxies could form enough massive stars to emit large quantities of hydrogen ionizing photons. They also predicted that this could amount to a Ly α emission of $> 5\%$ of the total luminosity of these galaxies, initiating the first searches for LAEs. Assuming case B, appropriate for star-forming regions, a Ly α photon will be emitted 67% of the time when a recombination occurs. In case B recombination, the interstellar medium is optically thick enough to cause Lyman line photons to be continually re-absorbed and re-emitted until they release a Balmer series photon and a Ly α photon (or a small probability of two continuum photons). Ly α photons will continue to be re-absorbed and re-emitted, called resonant scattering, until they are absorbed by a dust particle or escape the galaxy (Osterbrock & Mathews 1986).

The Ly α emission line is particularly interesting as its properties are strongly dependent on not only the star formation rate of the galaxy, but also the amount of dust reddening, the dust geometry, and the relative velocity structures of gas surrounding the galaxy. In the simplest scenario, Ly α photons originate in star-forming regions that are devoid of dust and undergoing one of their first starbursts. Since there is little or no dust to absorb Ly α photons, nearly every Ly α photon escapes the galaxy, and they will leave the galaxy with the relative velocity of the last hydrogen atom that re-emits them. However, most galaxies have at least trace amounts of dust, and hydrogen atoms re-emit the Ly α photon in a random direction. As hydrogen accounts for 75% of the baryonic mass of the universe and stars form in the most dense regions, Ly α photons must random walk their way out of a galaxy. This process results in much longer path lengths than continuum photons, making it more likely that a Ly α photon will collide with a dust grain and be absorbed. This causes Ly α photons to be much more sensitive to the effects of dust (Atek et al. 2008). Any significant amount of dust is expected to have a large impact on the Ly α flux by suppressing it. To further complicate this picture, most galaxies do not have a homogeneous ISM, but rather a dusty and clumpy one (Verhamme et al. 2006; Dijkstra et al. 2007).

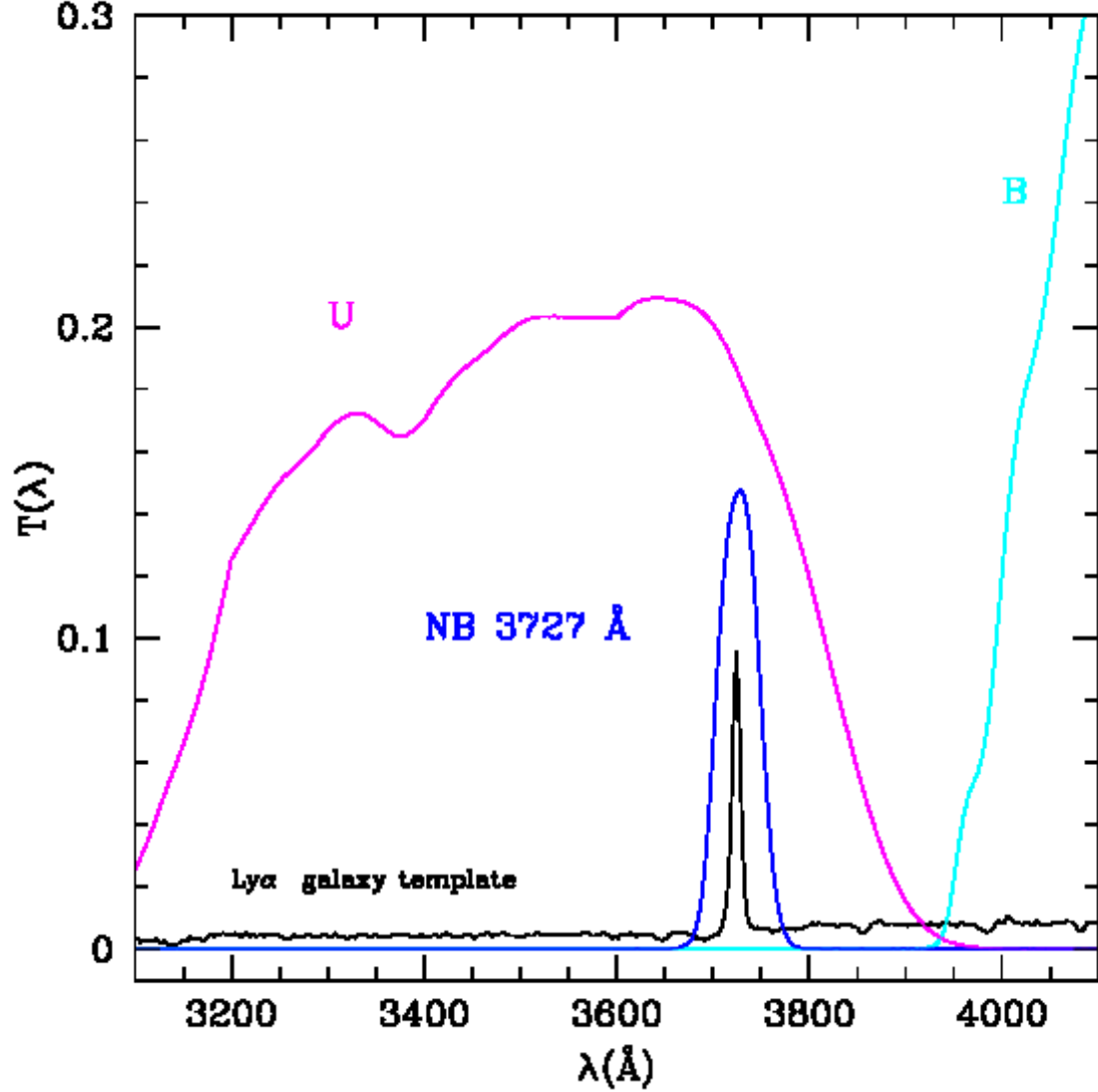


Figure 1.3 Spectrum of a template Ly α -emitting galaxy at $z = 2.07$ with the filter transmissions curves for the U, B, and NB3727Å filters overlaid. The LAE is identified as having narrowband excess flux relative to the continuum as predicted from the U band filter while also having a robust detection in the B band filter. Since these galaxies are selected based on a strong emission line relative to the continuum, they do not have to have significant continuum flux, permitting the identification of fainter galaxies than via the LBG selection method. (Figure 1 from Guaita et al. 2010).

1.5 Damped Ly α Absorption Systems

Although stars form out of molecular clouds, these clouds are embedded in cold neutral gas. Since neutral gas is more stable in the typical conditions of the ISM, it constitutes the bulk of the cold gas mass. In nearby galaxies, the HI surface density can be mapped through the hyperfine 21 cm line with radio telescopes, which places strong constraints on the density distributions of cold gas within galaxies as well as providing an accurate local benchmark on the total amount of cold gas in the local universe (e.g., Zwaan et al. 2005a; Martin et al. 2010). However, current radio telescopes are not yet powerful enough to be able to detect 21-cm emission in distant galaxies. Therefore in order to study HI at high redshift (e.g. $z \gtrsim 0.5$), we must observe HI through one of its electronic transitions (e.g., Lyman series, Balmer series, etc.).

As the bulk of HI is located in cool gas clouds, one must observe these transitions in absorption. Typically, HI is observed as one of the Lyman series lines in absorption, the most prominent of which being the Ly α transition (Wolfe et al. 1986, 1995; Storrie-Lombardi et al. 1996; Storrie-Lombardi & Wolfe 2000a; Péroux et al. 2003). At low HI column densities (defined as the number of atoms along the line of sight), corresponding to $10^{17} < N_{\text{HI}} < 10^{20.3} \text{ cm}^{-2}$, hydrogen is sufficiently dense to be optically thick yet is still mostly ionized. At higher column densities, $N_{\text{HI}} > 10^{20.3} \text{ cm}^{-2}$, the gas becomes predominantly neutral and self-shielding. This threshold is an estimate of what was originally believed the Milky Way disk would have if viewed face-on (Wolfe et al. 1994). Moreover, cold gas above this threshold is sufficiently dense to cause the Ly α transition to be damped, a signature absorption feature stemming from the characteristic damping wings of its Voigt profile.

In an electronic transition, due to the finite lifetime of the upper energy level and the uncertainty principle, the absorption profile of any transition is naturally broadened and follows a Lorentzian profile:

$$\phi(\nu) = \frac{\gamma}{\pi(\Delta\nu^2 + \gamma^2)} \quad (1.2)$$

where γ is determined from the lifetime of the upper energy level. Similarly, random motions in the gas cause Doppler broadening in the line profile, which can be described as:

$$\phi(\nu) = \exp[-(|\Delta\nu|/\Delta\nu_D)^2] \quad (1.3)$$

where $\Delta\nu = \nu - \nu_0$ and $\nu_D = \sqrt{2}\sigma_\nu\nu_0/c$ is an assumed Gaussian velocity distribution with dispersion σ_ν . The convolution of natural broadening and Doppler broadening results in a Voigt profile. Since the Doppler profile falls off as $\exp(-(\Delta\nu/\Delta\nu_D)^2)$ and the natural broadening profile falls off as $1/(\Delta\nu)^2$, the natural broadening profile will dominate for large $\Delta\nu$. At high column densities, these regions of the line profile become visible and are called the damping wings. Due to the large values of N_{HI} , Ly α is saturated at the center and has unit optical depth in the damping wings $\Delta\nu_{\tau=1} \approx [A_{21}f_{21}N_{\text{HI}}]^{1/2}$ when $N_{\text{HI}} > 10^{19}\text{cm}^{-2}$ and $\sigma_v < 70 \text{ km s}^{-1}$ where A_{21} and f_{21} are the Einstein spontaneous emission coefficient and oscillator strength for the Ly α transition, respectively (Wolfe et al. 2005). This characteristic feature gives damped Ly α absorption systems (DLAs) their name and allows us to identify clouds of neutral gas that are large reservoirs of cold gas.

Figure 1.4 shows the absorption profiles of two DLAs and several metal absorption lines in the spectrum of QSO PSS0209 + 0517 from Wolfe et al. (2005). The absorption lines with large widths and zero flux in the center have the characteristic damping wings of a Voigt profile. There are two DLAs at $\lambda 5913\text{\AA}$ ($z = 3.864$) and $\lambda 5674\text{\AA}$ ($z = 3.667$) as can be seen by their broad velocity widths and characteristic damping wings. Quasars are used as background illuminating sources to detect DLAs (Wolfe et al. 2005) where in the majority of systems, DLAs are at a sufficiently lower redshift than the background quasar, to make them independent of the specific properties of the quasar. Moreover, DLAs contain the majority of the neutral gas in the universe over a redshift range $1.6 < z < 5$ (Storrie-Lombardi & Wolfe 2000a; Wolfe & Prochaska 2000; Péroux et al. 2003; Prochaska et al. 2005; Noterdaeme et al. 2009). At lower redshifts ($z < 1.6$), observing DLAs is difficult due to the atmospheric cutoff at 3200\AA . Since the Ly α line falls in the atmospheric transmission window, it allows for efficient observations with large ground-based optical telescopes (Prochaska et al. 2005; Schneider et al. 2010, e.g., the Sloan Digital Sky Survey, SDSS; the Keck telescopes). As DLAs are easily observed in the spectra of quasars while containing most of the neutral hydrogen, they are perhaps the most valuable tool for studying the evolution of HI and the

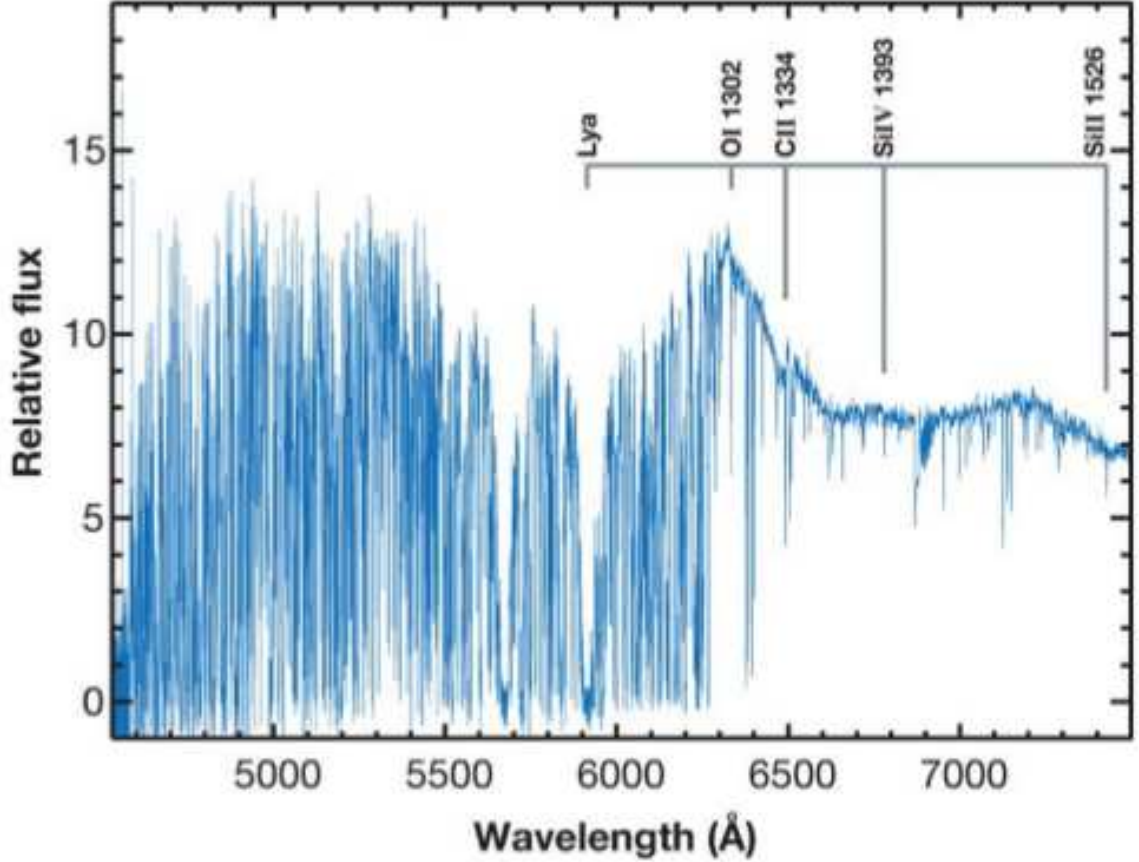


Figure 1.4 Keck/ESI spectrum of QSO PSS0209 + 0517 showing two DLAs and a series of metal absorption lines. Several key features of the DLA at $z = 3.864$ ($\lambda = 5913\text{\AA}$) are labelled in the figure. The second absorption trough at $\lambda = 5674\text{\AA}$ corresponds to a DLA at $z = 3.667$. Note that both damped $\text{Ly}\alpha$ lines are significantly stronger and wider than any of the $\text{Ly}\alpha$ forest or metal absorption lines (Figure 1 from Wolfe et al. 2005).

ISM in general at high redshift.

DLAs are of particular interest to galaxy formation as they allow us to study the gaseous components of galaxies across cosmic time, thereby complementing surveys that target galaxies in emission. At high redshift, the shape and normalization of the distribution of DLAs with different column densities determines the cosmological density of neutral gas in the universe as well as the fraction of neutral gas in different column density systems (Prochaska et al. 2003, 2005; Noterdaeme et al. 2009, 2012). The number density of DLAs at any redshift constrains the number of large reservoirs of cold gas, while the cosmological neutral gas density determines how much fuel there is for future star formation (Wolfe et al. 2005). We can use the metallicity of gas in DLAs to determine the amount of metals

produced in the Universe (Wolfe et al. 2005; Rafelski et al. 2012; Neeleman et al. 2013). The velocity widths of low ionization absorption lines yields information on the halo masses and kinematics of cold gas within DLAs (Prochaska & Wolfe 1997; Haehnelt et al. 1998; Pontzen et al. 2008; Fumagalli et al. 2011; Cen 2012). Using element ratios, the amount of metal production and depletion of various elements by dust can be measured, which allows for the amount of dust to be inferred. The star formation rates, impact parameters, and properties of host galaxy counterparts yield further information on which types of galaxies contain large amounts of cold gas. By tracking how each of these properties changes over cosmic time, we can study the effect of cold gas accretion, star formation, and outflows on the evolution of galaxies. Throughout this thesis, we discuss the relations among these processes by studying the evolution of these properties of DLAs in simulations.

1.6 Semi-Analytic Models

Semi-analytic models (SAMs) are an ideal laboratory to better understand the nature of the interstellar medium in distant star-forming galaxies and its connection to the evolution of star-forming galaxies. SAMs are based on a cold dark matter (CDM) framework for structure formation (Blumenthal et al. 1984) whereupon physical processes govern the evolution of galaxies. They produce a general picture of how density fluctuations in the primordial universe evolve into the observable galaxy population (Percival et al. 2002; Tegmark et al. 2004; Eisenstein et al. 2005). Rather than solving detailed equations of hydrodynamics and thermodynamics for individual particles or grid cells, SAMs use simple but physically motivated “recipes” to track bulk quantities such as the total mass in stars, hot gas, cold gas, metals, etc, in various “zones” (e.g., within a galaxy, within a dark matter halo, in a halo infall region, or in the intergalactic medium). In some cases, SAMs attempt to track these quantities in radial bins within a galactic disc (Kauffmann 1996; Avila-Reese et al. 2001; Dutton & van den Bosch 2009; Fu et al. 2010; Kauffmann et al. 2012). Although they cannot offer the detailed spatial and kinematic information provided by fully numerical hydrodynamical simulations, SAMs do have a number of advantages over these techniques. Numerical hydro simulations of galaxy formation still must rely heavily on “sub-grid” recipes for important processes such as star formation and stellar feedback. These are treated in a similar manner

in SAMs, but the effect of varying the details of these recipes and their parameters can be explored much more thoroughly because of their greater computational efficiency. SAMs can provide “mock catalogs” for very large numbers of galaxies, comparable to modern surveys, while this is still inaccessible for numerical hydro simulations. Finally, we still do not understand many of the details of the physics that shapes galaxy formation. It is easier to explore, albeit qualitatively, somewhat more schematic solutions in SAMs, which may point the way towards more physically rigorous investigations with numerical techniques.

SAMs have been used extensively to investigate and interpret observations of nearby and distant galaxies in emission. A recent generation of SAMs that incorporates feedback from accreting black holes has been shown to be successful at reproducing a broad range of observations. These include the stellar mass function and luminosity function, gas fraction vs. stellar mass relation, and relative fraction of early vs. late type galaxies as a function of stellar mass at $z = 0$, and the evolution of the global stellar mass density and star formation rate density with redshift from $z \sim 6$ to 0 (Bower et al. 2006; Croton et al. 2006; De Lucia & Blaizot 2007; Monaco et al. 2007; Somerville et al. 2008b; Hopkins et al. 2009a; Guo et al. 2010; Somerville et al. 2012). However, these models still fail to reproduce some important observations. For example, they predict that low mass galaxies form too early and are too quiescent at late times, reflecting star formation histories that apparently do not match observational constraints (Fontanot et al. 2009; Weinmann et al. 2012). Numerical hydrodynamical simulations with similar implementation of “sub-grid” recipes largely show the same successes and problems (Weinmann et al. 2012). It has been suggested (e.g., Fontanot et al. 2009; Krumholz & Dekel 2012) that inadequacies in our modeling of star formation and/or stellar feedback are likely culprits for these remaining difficulties in reproducing observations of low-mass galaxies.

Several SAM-based studies have modelled the partitioning of gas into atomic and molecular phases using various approaches, and studied the effect of using an H_2 -based star formation recipe. Obreschkow et al. (2009) partitioned gas into atomic and molecular components using the empirical pressure-based relation of Blitz & Rosolowsky (2006, hereafter BR) in post-processing on the Millennium semi-analytic models. Lagos et al. (2011) and Fu et al. (2010) implemented gas partitioning self-consistently into SAMs using two approaches: the

empirical pressure-based recipe of BR and the theoretically-motivated metallicity-dependent recipe of Krumholz et al. (2009b, hereafter KMT09). These models then implemented an H_2 -based star formation recipe based on their computed H_2 fractions. Using a similar approach, Somerville, Popping & Trager (in prep; SPT14) explored the partitioning of gas using the BR recipe, the KMT recipe, and an additional metallicity dependent recipe provided by Gnedin & Kravtsov (GK), along with an H_2 -based star formation recipe based on the Bigiel et al. (2008a) observational results. They concluded that the GK recipe was more successful and robust, particularly at low metallicities, than the KMT formulation (see also Krumholz & Gnedin 2011). Popping et al. (2013a, hereafter PST14) presented the predictions of these models for the gas content of galaxies in HI, H_2 , and CO from redshift six to zero for direct comparison with upcoming surveys of gas tracers in emission.

The SAM developed by SPT14 and used in this work does not predict the internal structure of galaxies in detail, so we assume that the density profiles of the gas and stellar discs are described by a smooth exponential function in both the vertical and radial dimensions. We rely on simplified approximations to estimate the scale length of the gas disc from the specific angular momentum (spin) of the host dark matter halo. This approach has been shown to reproduce the evolution of stellar disc sizes (as traced by their optical light) from $z \sim 2$ to 0 (Somerville et al. 2008b), and also reproduces the observed sizes of HI discs in the nearby universe, the observed sizes of CO discs in local and high redshift galaxies for the small sample currently available, and the spatial extent of the SFR density in nearby and high-redshift galaxies (PST14). However, we also consider models in which the gas is more extended than in our standard models, either because the gas that forms the disc or is accreted onto the disc has higher specific angular momentum than the dark matter halo (as some numerical simulations suggest; e.g., Robertson et al. 2004, 2006a; Agertz et al. 2011; Guedes et al. 2011), accreted gas from cold streams deposit their angular momentum to the inner parts of the halo (Kimm et al. 2011), or the gas is in a non-rotationally supported extended configuration such as tidal tails (Stewart et al. 2011, 2013) or an outflow (Cen 2012).

1.7 The Contents of This Thesis

Immense progress has been made in characterizing the properties and relations among distant galaxies, as well as simulating these complex physical processes. In spite of this, understanding these processes in detail and their effect on the evolution of galaxies and their surrounding environment remains an open challenge. We focus on the dominant physical processes that govern galaxy evolution and are associated with cold gas and star formation, namely the accretion of cold gas, the formation of stars, feedback from star formation and supernovae, and the ejection of gas from galaxies. Other processes including supermassive black hole growth, winds and feedback from active galactic nuclei (AGN), mass and environmental quenching, and merger events also significantly impact the evolution of galaxies, but are not the focus of this work.

At a redshift of $1.5 < z < 3$, the cosmic star formation rate was at a maximum (Madau et al. 1998), indicating that the aforementioned physical processes were strongly affecting the evolution of star-forming galaxies as well as the surrounding environment. Moreover, the large number of observational surveys targeting star-forming galaxies and DLAs at this epoch makes it a prime target for studying galaxy formation. Our method for understanding the impact and interconnectedness of these processes is a combined study of DLAs and star-forming galaxies where we focus on the neutral gas surrounding them during this pivotal period.

In **Chapter 2**, we seek to characterize the complex spatial and velocity structures, the covering fraction, and the nature of neutral and ionized gas in star-forming galaxies at this epoch. Galactic-scale outflows are not only important in understanding how feedback from star formation affects galaxy evolution, but also how they affect the metal enrichment, ionization state, and physical state of the IGM. First, we present the properties of individual and composite rest-UV spectra of 81 UV-bright star-forming galaxies at $2 < z < 3.5$ where 59 have $R < 25.5$. We then divide the data set into subsamples based on properties that we are able to measure for each individual galaxy: Ly α equivalent width, rest-frame UV colors, and redshift. Among our subsample of galaxies with $R < 25.5$, we show that the observed trends with Ly α emission are largely consistent with the mechanical energy

from star formation and supernovae powering galaxy-scale outflows of neutral and ionized gas. Evidence for these outflows is seen as strong blueshifted absorption in low- and high-ionization gas as well as redshifted H I Ly α emission relative to nebular features. We also show that these outflows are well described by neutral clouds and dust being embedded in ionized gas that cover a substantial fraction of the host galaxy. Finally, our sample of galaxies shows little evolution over the redshift interval and a diverse range of properties, indicating that while star formation and outflows are common amongst galaxies, they vary greatly in detail from galaxy to galaxy.

Since the gas in and around these galaxies is poorly understood and has proven to be quite challenging to “observe”, we then approach this topic from a different angle. We use semi-analytic models to observe model DLAs, thereby allowing us to study the nature of the cold neutral gas within and around these galaxies. In **Chapter 3**, we present the semi-analytic models we use to do this analysis. We also discuss the distinct properties of the models we make for studying the effects of partitioning cold gas and the size of our cold gas disk on galaxy properties. First, we present three recipes for partitioning cold gas into atomic and molecular components: a pressure-based recipe and two metallicity-based recipes with a fixed and varying UV radiation field. Second, we generate three sets of models for the size of cold gas disks in galaxies. We define a new parameter, $f_j = j_{\text{cg}}/j_{\text{DM}}$, which is equal to the specific angular momentum of the cold gas divided by the specific angular momentum of the dark matter. We set $f_j = 1$ for “standard” disks, $f_j = 2.5$ for “extended” disks, and $f_j = 1, 1.5$, or 2.5 depending on whether the galaxy underwent no mergers, only a minor merger, or a major merger in our merger models. In all of these models, cold gas is distributed following an exponential surface density profile with an exponential vertical density profile.

As semi-analytic models allow us to generate statistical samples of galaxies while also changing the physical processes within them, we create a lightcone for each combination of models described above, then generate catalogs of DLAs by “observing” them. In **Chapter 4**, we present the properties of these model DLAs, then compare them to observations in order to better understand the effects of changing these physical processes. We show

that models with “standard” gas disks fail to reproduce the observed column density distribution, the line density of DLAs, the distribution of velocity widths (Δv) as measured by low-ionization state metal systems, the cosmological neutral gas density (Ω_{HI}), and the metallicity distribution at $z < 3$, regardless of the gas partitioning. In contrast, our models with “extended” radial gas profiles with either a pressure-based gas partitioning or metallicity-based recipe with a varying UV radiation field reproduce quite well the column density distribution, line density of DLAs, Ω_{HI} , and Δv distribution at $z < 3$. However, all of the models investigated here underproduce DLAs and the HI gas density at $z > 3$, suggesting that DLAs at high redshift arise from a different physical phenomenon, such as outflows, clumps of cold gas, or filaments. If this is the case, the flatness in the number of DLAs and HI gas density over the redshift interval $0 < z < 5$ may be due to a cosmic coincidence where the majority of DLAs at $z > 3$ arise from intergalactic gas in filaments or streams while those at $z < 3$ arise predominantly in galactic discs. We also show that our favored models are in good agreement with the dependence of DLA metallicity on redshift and Δv , particularly when we include the effects of metallicity gradients. The success of our preferred models over previous ones in reproducing the evolution of neutral gas across time in addition to the properties of local galaxies suggests an improved understanding of the physical processes that govern H_2 formation and the size of cold gas disks.

After improving our description and understanding of these key physical processes, we shift our focus to studying the relations among the properties of galaxies that host large reservoirs of cold gas and those that are highly star forming, during the peak epoch of cosmic star formation. In **Chapter 5**, we study the properties of the galaxies that host DLAs; the differences between properties of DLAs as measured along the line of sight and the average for their host galaxies; and the relations among DLA host galaxies, star-forming galaxies, and the underlying galaxy population at a given stellar mass. This work is the first to use SAMs in a cosmological context to characterize the properties of DLA host galaxies, thereby yielding information on their luminosities, colors, masses, star formation rates, sizes, metallicities, and amount of dust. Through comparing the properties along the DLA line of sight to the average DLA host galaxy properties, we seek to understand how DLAs can be used to understand the distribution and composition of the interstellar

medium in and around high-redshift galaxies. Finally, we use our catalogs of DLAs and star-forming galaxies to study the relations between stellar mass and DLA cross section, cold gas fraction, star formation rate, metallicity, and dust reddening as traced by galaxy scaling relations. In this analysis, our models predict that galaxies with a wide range of physical properties host large cold gas reservoirs, which are not well characterized by any galaxy “type”. They range from low mass, gas-dominated galaxies that are too faint to see with current telescopes to massive star-forming galaxies that are likely powering galaxy-scale outflows. Due to the rarity of massive galaxies relative to lower mass ones, massive star-forming galaxies are more likely to host DLAs while the majority of DLAs originate in low mass galaxies.

Our focus then shifts to seeking to better understand the distribution and properties of cold gas within individual galaxies through the use of numerical simulations. We begin by examining the azimuthally-averaged stellar, cold gas (HI and H₂), metallicity, and star formation rate profiles of 15 individual galaxies in the GASOLINE numerical simulations (Wadsley et al. 2004) from $z = 2$ to 0. Then, we apply the assumptions of the semi-analytic models to these galaxies by fitting a double exponential to the bulge and disk components for the cold gas and stellar profiles. Using the pressure-based and metallicity-dependent cold gas partitioning as they are included in the semi-analytic models, we calculate the HI and H₂ profiles for each galaxy, which we use to calculate the star formation rate profiles as would be inferred from the semi-analytic models. Additionally, the numerical simulations allow us to track the evolution of individual galaxies and study how their properties change with redshift and stellar mass.

In **Chapter 6**, we show that in most galaxies in the numerical simulations, stellar and cold gas profiles are moderately well-fit by a double exponential, although smaller scale structure is missed. At $z = 0$, most cold gas disks are very flat and end at a given HI gas density that varies for each galaxy. The metallicity-dependent and pressure-based H₂ formation recipes produce similar H₂ density profiles; however in massive galaxies, both produce substantially more H₂ gas than is predicted by the numerical simulations. Using the H₂-based star formation recipe input in the semi-analytic models and observed in local galaxies (KS relation), we predict much lower star formation rates than are calculated in

the numerical simulations, indicating that in the numerical simulations either feedback is more efficient at disassociating H_2 or star formation is less efficient. Furthermore, most galaxy metallicity profiles are very flat at $z = 2$ where the interior regions of the disk enrich substantially with redshift. There is also a significant difference between star formation weighted metallicities and average gas phase ones as star-forming regions typically have higher average metallicities. As individual galaxies evolve from $z = 3$ to 0, their metallicities increase where more massive galaxies' metallicities increase at a faster rate and their stellar disks grow by $\gtrsim 2$ in size. Moreover, cold gas disks become flatter and low mass galaxies' cold gas disks become smaller relative to their stellar disks due to star formation in the outer regions of the disk and cold gas disks becoming more compact. Galaxies in the numerical simulations and semi-analytic models at $z = 0$ generally lie on the same r_s - M_s relation, f_g - M_s relation, $[Z]$ - M_s , and SFR- M_s relation as observations of local galaxies. At $z = 2$, both models predict similar r_s - M_s , SFR- M_s , and $[Z]$ - M_s relations, where they predict similar stellar disk sizes and metallicities as observations, but lower star formation rates.

Chapter 2

Stacked Rest-frame Ultraviolet Spectra of Ly α -emitting and Continuum-selected Galaxies at $2 < z < 3.5$

2.1 Introduction

Narrowband and broadband selection techniques around the Ly α emission line and Lyman limit respectively have made isolating Ly α emitters (LAEs) and UV-bright, continuum-selected galaxies quite effective at redshifts up to $z = 7$. Through stacking photometric samples and stellar population modeling, numerous groups have uncovered a wealth of information on these galaxies' properties including stellar masses, star formation rates, ages, amount of dust ($E(B - V)$), and star formation histories (e.g., Adelberger & Steidel 2000; Papovich et al. 2001; Shapley et al. 2001, 2005; Erb et al. 2006d; Reddy et al. 2006; Gawiser et al. 2006a; Pirzkal et al. 2007; Gawiser et al. 2007; Nilsson et al. 2007; Pentericci et al. 2007; Lai et al. 2008; Nilsson et al. 2009; Finkelstein et al. 2009; Guaita et al. 2010). As a result, there have been numerous follow-up rest-frame ultraviolet (UV) spectroscopic surveys (e.g., Shapley et al. 2003a; Erb et al. 2006d; Kornei et al. 2010; Talia et al. 2012; Jones et al. 2012). Rest-frame UV spectroscopy offers the ability to not only confirm redshifts, but also to study galactic-scale outflows, stellar photospheres and dust reddening through interstellar absorption line kinematics, the shape and strength of the Ly α emission line, P Cygni profiles from massive stars, and the UV spectral slope (Leitherer et al. 1995; Pettini et al. 2000; Shapley et al. 2003a).

In order to determine the impact of feedback from star formation on galaxy evolution, we have targeted the peak of cosmic star formation density occurring at a redshift of $1.5 < z < 3$ when galaxies and their surrounding gas were evolving rapidly. Understanding the relation between star-forming galaxies and the surrounding intergalactic medium (IGM) at these redshifts will give insight into this relation at higher redshifts where spectroscopy is much

more difficult. It is well known that outflows can occur in starburst galaxies in the local universe and, more recently, it has been shown that they are ubiquitous among high-redshift star-forming galaxies (Steidel et al. 1996a; Pettini et al. 2000, 2001; Shapley et al. 2003a; Martin 2005; Rupke et al. 2005; Tremonti et al. 2007; Weiner et al. 2009; Steidel et al. 2010). Analysis of these outflows has primarily been focused on modeling the complex spatial and velocity structures, the covering fraction, and the nature of neutral and ionized gas (e.g., Heckman et al. 1990; Lehnert & Heckman 1996; Martin 1999; Shapley et al. 2003a; Strickland et al. 2004; Schwartz et al. 2006; Grimes et al. 2009; Steidel et al. 2010). Galactic-scale outflows are not only important in understanding how feedback from star formation affects galaxy evolution, but also how they affect the metal enrichment, ionization state, and physical state of the IGM.

In order to understand the connection between LAEs and continuum-selected galaxies, it is important to understand the different classifications for each type of galaxy, namely the criteria by which they are selected. Continuum-selected galaxies are chosen via color cuts and apparent magnitude limits, while LAEs are selected via equivalent width and line flux cuts that are independent of their colors. As defined by Steidel et al. (1996c), Lyman break galaxies (LBGs) are continuum-selected galaxies at $z \sim 3$ and typically have an apparent magnitude limit of $R < 25.5$. Gawiser et al. (2006a) found LAEs at $z \sim 3$ with $L_{\text{Ly}\alpha} \geq 4 \times 10^{-17} \text{ ergs s}^{-1} \text{ cm}^{-2}$ to have a median apparent magnitude of $R = 27$. In spite of this luminosity difference, Gawiser et al. (2006a) find that $z = 3.1$ LAEs have similar rest-frame UV colors to LBGs, indicating that they are missed in continuum-selected surveys primarily due to their fainter continua. Similarly, (Shapley et al. 2003a, hereafter S03) find that 20 – 25 percent of their almost 1000 LBGs have strong enough Ly α emission lines ($W_0 > 20\text{\AA}$) to be classified as LAEs.

Given the faint nature of these galaxies ($R > 23$), previous analyses have focused on stacking large numbers of low signal-to-noise spectra. Similar to stacking photometric samples, this technique yields the average properties of a ‘typical’ galaxy. S03 applied this technique to almost 1000 LBGs at a redshift of $z \sim 3$ and found that they display a wide distribution of properties, with Ly α ranging from strong emission to absorption, varying UV continuum slopes, a range of velocity offsets between Ly α emission and interstellar

absorption, and different strengths of interstellar absorption lines. Through dividing their sample into quartiles of Ly α equivalent width, they found that the sample with strongest Ly α emission had bluer UV continua, weaker low-ionization absorption, smaller kinematic offsets, stronger nebular emission, and older stellar populations. With the exception of older stellar populations, these trends suggest that galaxies with stronger Ly α emission are less evolved, less rapidly forming stars, and likely less massive. Nonetheless, the presence of older stellar populations implies more evolution, indicating that galaxies with strong Ly α emission may be a heterogeneous population.

As the defining characteristic of LAEs, it is vital to understand the origin of the Ly α emission line, which is largely dependent on the effects of radiative transfer. Ly α photons are subject to resonant scattering and therefore have much longer pathlengths than continuum photons, making them more subject to extinction from dust. Thus, one explanation for LAEs' large Ly α equivalent widths is that they are young, chemically pristine galaxies undergoing one of their first major episodes of star formation. A second hypothesis suggests that they are older, more evolved galaxies where dust is segregated into clumps that are surrounded by a relatively dust-free intercloud medium (Neufeld 1991; Hansen & Oh 2006; Finkelstein et al. 2009). In this scenario, Ly α photons scatter off dust clumps while UV continuum photons penetrate them and are subject to extinction, thereby increasing the relative strength of the Ly α emission line. A lack of correlation between the spectral index of the UV continuum slope and Ly α equivalent width is interpreted as evidence for the decoupling of continuum and line extinction (S03) as would be expected if the neutral medium was inhomogeneous. For $2 < z < 4$ LAEs, Blanc et al. (2011) recently found $E(B-V)$ to correlate with Ly α escape fraction in such a way that Ly α photons are being extinguished by the same amount as UV continuum photons, leading them to suggest that among LAEs, the Ly α equivalent width is neither being enhanced due to a clumpy ISM nor being preferentially quenched by dust.

Through stellar population modeling, LAEs have been shown to encompass a broad range of physical properties. At an epoch of $2 < z < 4.5$, many groups find that they are characterized as young (< 100 Myr), relatively dust-free ($E(B-V) < 0.3$) galaxies with low stellar masses ($< 10^9 M_{\odot}$) and low star formation rates ($2-3 M_{\odot} \text{yr}^{-1}$) (Gawiser et al. 2006a;

Pirzkal et al. 2007; Gawiser et al. 2007; Nilsson et al. 2007). Furthermore, LAEs have very high specific star formation rates ($7 \times 10^{-9} \text{ yr}^{-1}$), defined as star formation rate per unit mass, as compared to LBGs ($3 \times 10^{-9} \text{ yr}^{-1}$) indicating they are building up stellar mass at a faster rate than continuum-selected galaxies. This picture is consistent with LAEs being chemically pristine and at the beginning of an evolutionary sequence. On the other hand, various authors have found LAEs to exhibit a broader range of properties with ages ranging up to $> 1 \text{ Gyr}$, stellar masses up to $10^{10} M_{\odot}$, and A_{1200} (defined as the absorption at 1200\AA) as high as 4.5 (Pentericci et al. (2007); Nilsson et al. (2009); Finkelstein et al. (2009)). These results indicate that some LAEs are older, dustier, more evolved galaxies similar to LBGs. Furthermore, Lai et al. (2008) and Guaita et al. (2010) found IRAC detected objects to exhibit properties similar to LBGs, motivating Lai et al. (2008) to suggest they may be a lower mass extension of LBGs.

In this chapter, our goal is to understand the relationship among $\text{Ly}\alpha$ emission, interstellar kinematics, multiphase gas, nebular emission, and spectral slope for a sample of $2 < z < 3.5$ UV-bright star-forming galaxies. We subdivide our sample in terms of their $\text{Ly}\alpha$ equivalent width, rest-UV colors, and redshift to examine the relationships among these properties. This chapter is organized as follows. In Section 2.2, we present the spectroscopic sample including details of the observations and data reduction. We discuss the spectroscopic properties of our individual spectra in Section 2.3. In Section 2.4 and 2.5, we describe the stacking technique and analyze the composite spectra as subdivided based on $\text{Ly}\alpha$ equivalent width. Selection effects and trends among the outflowing component and galaxy properties are presented in Section 2.6. Finally, in Section 2.7, we summarize our conclusions.

2.2 Observations and Methodology

The galaxies that will be presented and analyzed in the following sections include narrowband-excess objects and continuum-selected sources. The latter category includes U band drop-outs at $z \sim 3$ and galaxies with prominent $\text{Ly}\alpha$ decrements at $z \sim 2$ (LBGs and “BX” galaxies, based on Steidel et al. 1996c, 2004). The imaging data used to select our targets were collected using the MOSAIC II CCD camera on the CTIO Blanco 4 m telescope

(<http://www.astro.yale.edu/MUSYC/>). The narrowband data consisted of a series of exposures taken through 50Å wide full width at half-maximum (FWHM) filters at $\lambda 5007\text{\AA}$ and $\lambda 4990\text{\AA}$ for $z = 3.1$ LAEs and $\lambda 3727\text{\AA}$ for $z = 2.07$ LAEs. The details of these observations are presented in Gronwall et al. (2007) and Ciardullo et al. (2012) for LAEs at $z = 3.1$ and Guaita et al. (2010) at $z = 2.07$. Our LBG selection criteria is presented in Gawiser et al. (2006c), which covers a redshift interval of $2.6 < z < 3.5$, while our BX selection criteria is presented in Guaita et al. (2010) and spans $2 < z < 2.7$. Our spectroscopic candidates were chosen from these two photometric surveys. In this paper, we present spectra taken from two spectroscopic surveys using the FORS and VIMOS instruments on the Very Large Telescope (VLT). The first survey, using the FORS instrument, targeted primarily $z \sim 2$ LAEs and BXs, along with a few $z \sim 3$ LAEs and LBGs. The primary targets for observation using the VIMOS instrument were X-ray sources analyzed in Treister et al. (2009) with $z \sim 3$ LAE and LBG candidates used to fill the remaining slitlets.

2.2.1 FORS Spectroscopy

For our FORS spectroscopic sample, the primary targets were chosen by first prioritizing $z = 2.1$ LAE candidates, followed by BX candidates and finally $z \sim 3$ LAEs and LBGs were used to fill available slitlets. The targets covered six $7' \times 7'$ masks in the CDF-S, however one of these masks was unusable due to poor observing conditions and has been omitted from the dataset. Each of the five remaining slitmasks consisted of ~ 30 targets with $\sim 70\%$ expected to be at $z \sim 2$.

These data were obtained using the FORS2 spectrograph on UT1 with the B1200 grism, the e2V UV-sensitive CCD, an atmospheric dispersion corrector, and $1.''0$ slitlets. This configuration led to a dispersion of 0.86\AA per pixel corresponding to a nominal spectral resolution of 3.4\AA (FWHM) or $R \sim 1400$ over a spectral coverage of $3200 - 6000\text{\AA}$ for each slitlet. The small angular size of our targets caused the actual spectral resolution to be seeing limited in almost all cases, which varied from $0.''7$ to $1.''2$ leading to a minimum spectral resolution of 2.4\AA . The observations were taken in a series of four exposures with exposure times of $1800 - 2400$ seconds per mask. We also note that the throughput at $\lambda 3727\text{\AA}$ is ~ 2 times worse than that at $\lambda 5000\text{\AA}$.

The data were reduced using the standard FORS pipeline. This process included bias-subtraction, flat fielding of science data, sky subtraction, and wavelength calibration through arc lamp exposures. For 5 objects, we had difficulty wavelength calibrating the $\lambda 3200 - 4200\text{\AA}$ region. We found an optimal wavelength calibration by lowering the threshold for identifying arc lamp lines and adding two lines to the arc lamp file at 3612.87\AA (Cd I) and 3663.00\AA (Hg I). We removed three objects that had data in this region for which we were not able to correctly calibrate their wavelengths. The spectra were then divided into individual spectrograms whereby one dimensional spectra were extracted using IRAF's `apall` task. Finally, each one-dimensional spectrum was corrected for atmospheric extinction and flux calibrated using observations of spectrophotometric standards observed with a $1.''5$ long slit using the same B1200 grating. A one sigma error array was then extracted according to the FORS reduction pipeline.

2.2.2 VIMOS Spectroscopy

Targets observed with the VIMOS instrument were distributed across four slitmasks in the CDF-S, each with a field of view of $7' \times 8'$, covering an area of $15' \times 16'$. These observations typically targeted ~ 5 LAEs and ~ 40 LBGs per mask for a total of 23 LAEs and 164 LBGs. We used the VIMOS spectrograph with the MR grism and an OS-blue filter mounted at the Nasmyth focus B of UT3 to obtain these spectra. The pixel scale of the EEV 4k x 2k CCD was $0.''2 \text{ pixel}^{-1}$, which, in conjunction with the MR grism, led to a dispersion of 2.57\AA per pixel ($R \sim 400$) and a spectral coverage of $4300 - 6800\text{\AA}$ on each slitlet. The nominal spectral resolution in combination with the $1.''0$ slits is 12.5\AA (FWHM). For these observations, the seeing was required to be better than $1''$. Each mask was observed for three hours and eighteen minutes. The VIMOS data were reduced using the standard ESO VIMOS pipeline version 2.1.6. For more information on the observations and reduction, see Treister et al. (2009). One dimensional spectra were then extracted using IRAF's `apall` task.

The VIMOS spectra were not flux calibrated to a spectrophotometric standard. As a result, we empirically flux calibrated the individual spectra based upon the FORS spectra. This procedure consisted of fitting a powerlaw to the $\lambda > 1220\text{\AA}$ rest-frame continuum of

FORS and VIMOS spectra via a least-squares algorithm. The individual VIMOS galaxy spectral slopes were then adjusted by the difference between the median FORS and VIMOS spectral slopes ensuring the same relative spectral slope. The VIMOS spectra were then normalized individually by convolving their fluxes ($F_\lambda(\lambda)$) with the V-band transmission curve, then rescaled to match the observed V-band magnitude.

Due to the artificial flux calibration, we also extracted the one sigma error spectrum empirically. For each spectrum, a 515\AA wide top hat, corresponding to 200 pixels or 40 resolution elements, was shifted down the spectrum wherein, for each pixel, we recorded the median number of counts and relative root mean square deviation. Our error spectrum is conservative as we only masked the $\text{Ly}\alpha$ emission line and the $\lambda 5577$ skyline, but no other features. To check the accuracy of empirically extracting the error spectrum, we applied the same routine covering the same number of resolution elements to the FORS spectra. This process recovered an error spectrum comparable to the formal error spectrum produced by the FORS reduction pipeline.

2.2.3 Redshift Identification

Spectral identification and redshifts were assigned by interactively examining the observed spectra in both one and two dimensions. All redshifts were independently confirmed by two investigators. Because our spectra lack systemic redshifts from nebular emission lines, redshifts were determined from the $\text{Ly}\alpha$ emission line. There were four continuum-selected galaxies with interstellar absorption lines and no $\text{Ly}\alpha$ emission. For these objects, redshifts were determined from the observed wavelength of the Si II 1260\AA and C II 1334\AA absorption lines, as they are the strongest lines that are not affected by blending. We then calculate their expected $\text{Ly}\alpha$ emission line redshift by applying a median offset of $\text{Ly}\alpha$ emission and interstellar absorption ($\langle v \rangle = 650 \text{ km s}^{-1}$) found to be characteristic of $z \sim 3$ LBGs by S03. For stacking purposes, we use each object's $\text{Ly}\alpha$ emission line redshift to shift them into the rest-frame. We note that varying kinematic offsets between emission and absorption will artificially broaden the absorption lines.

For a large fraction of our LAEs, redshifts are determined solely from the $\text{Ly}\alpha$ emission line. There are many dangers involved in single line redshifts, which makes it very important

to correctly identify this line as high-redshift Ly α . Since we use an [O II] λ 3727 and an [O III] λ 5007 filter to select redshift $z=2.1$ and 3.1 LAEs, it is unlikely that local [O II] and [O III] emitting galaxies will survive the color cuts. However, intervening high-equivalent width [O II] λ 3727 emission line galaxies ($z = 0.34$) can be mistaken as $z=3.1$ LAEs. The [O II] doublet $\lambda\lambda$ 3726, 3729 is just resolved in our FORS $z = 3.1$ sample, which would identify the galaxy as a low-redshift [O II] emitting interloper. Unfortunately, the VIMOS spectral resolution is insufficient to resolve the two components of the doublet, making it difficult to distinguish [O II] from Ly α . Gawiser et al. (2006c) and Gronwall et al. (2007) do not find any interlopers among LAEs observed with the Inamori Magellan Areal Camera and Spectrograph (IMACS) covering a wavelength range 4000–10000Å that would show multiple emission lines. Nonetheless, as the transmission fraction of the IGM due to H I absorption is ~ 0.7 at $z = 3$ (Madau 1995), we can identify [O II] λ 3727 emitting galaxies from their lack of a Lyman decrement. We do not find any low-redshift emission line interlopers. Among the targets observed with the FORS spectra, we spectroscopically confirmed 13 of 36 $z = 2.1$ LAEs, 24 of 55 BXs, 23 of 25 $z = 3.1$ LAEs and 3 of 16 LBGs. Of the $z \sim 3$ VIMOS targets, we spectroscopically confirmed 17 of 23 LAEs and 40 of 132 LBGs.

2.3 Individual Galaxy Properties

In this section, we analyze the individual galaxy spectra included in the composites. For individual spectra, the faint nature of high-redshift SFGs limits us to studying trends based on only a few parameters that are measurable for each galaxy: Ly α equivalent width, redshift, rest-frame UV color, and rest-UV continuum luminosity. For certain galaxies with Ly α emission and interstellar absorption, we are also able to measure a relative velocity offset. Due to the complexities associated with selection effects, we do not attempt to study the relationship between rest-UV continuum luminosity and other galaxy properties. As a maximum apparent magnitude of $R<25.5$ is used for broadband-selected objects, the rest-UV luminosity threshold for $z \sim 2$ BX galaxies will be ~ 0.5 magnitudes brighter than for $z \sim 3$ LBGs. Additionally, we find that 5 BX galaxies, 3 $z = 2.1$ LAEs, and 4 LBGs, i.e., 22% of our $R<25.5$, Ly α emission line galaxies, show multiple-peaked Ly α emission. Similarly, Kulas et al. (2011) found that $\sim 30\%$ of their Ly α emission line galaxies at $2 < z < 3$

showed multi-peaked Ly α emission. We also note seeing evidence for fine-structure Si II* emission in the individual spectra of 7 BX galaxies and 3 LBGs.

In 8 of 17 BX galaxies and 15 of 28 LBGs, the only visible feature is Ly α emission. In 2 BXs and 2 LBGs, we observe multiple absorption lines and no Ly α emission, and in 3 of these 4 galaxies, Ly α appears as broad absorption. In these cases, interstellar absorption lines are used to measure the redshift. In the remaining 7 BXs and 11 LBGs, Ly α emission and interstellar absorption are present allowing a measurement of the relative velocity offset. For 77 of 81 galaxies, redshifts were measured from the Ly α emission line. This fraction differs significantly from S03, as nearly one third of their LBG spectroscopic sample had Ly α only in absorption. This difference is likely due to lower S/N in our spectra making absorption line-only redshifts difficult. The top left panel of Figure 2.1 shows the distribution of Ly α equivalent widths for our entire spectroscopic sample (black, solid line) and UV-bright LAEs (red, dot-dashed line). We discuss the impacts of the different Ly α equivalent width distribution in Section 2.6.2.

Among the narrowband-selected galaxies, in all except for one, the only visible spectroscopic feature is Ly α emission. This is likely due to the intrinsically faint nature of their continua. In the top right panel of Figure 2.1, photometric versus spectroscopic rest-frame equivalent width is plotted for $z \sim 3$ LAEs as black stars and $z \sim 2$ LAEs as red diamonds. We find that for $z \sim 3$ LAEs, photometric equivalent widths are systematically overestimated as the median photometric equivalent width is $W_{\text{phot},3} = 69.2\text{\AA}$ while the median spectroscopic equivalent width is $W_{\text{spec},3} = 36.6\text{\AA}$. However, for $z \sim 2$ LAEs, these two equivalent width measurements are consistent as $W_{\text{phot},2} = 27.3\text{\AA}$ and $W_{\text{spec},2} = 31.5\text{\AA}$. Photometric equivalent widths are calculated by using broadband filters (U+B at $z \sim 2$, and B+V at $z \sim 3$) to estimate the continuum flux density and a narrowband filter to estimate the amount of excess Ly α flux. For details on the photometric equivalent width calculations, see Gronwall et al. (2007); Guaita et al. (2010). For particularly faint objects, spectroscopic equivalent widths may be biased low as a result of fake continuum in individual spectra. Since we weight each object in the composites by signal divided by noise squared, these objects will have a minimal effect on the composite spectra of which all equivalent widths are measured spectroscopically. A more detailed analysis of photometric and spectroscopic

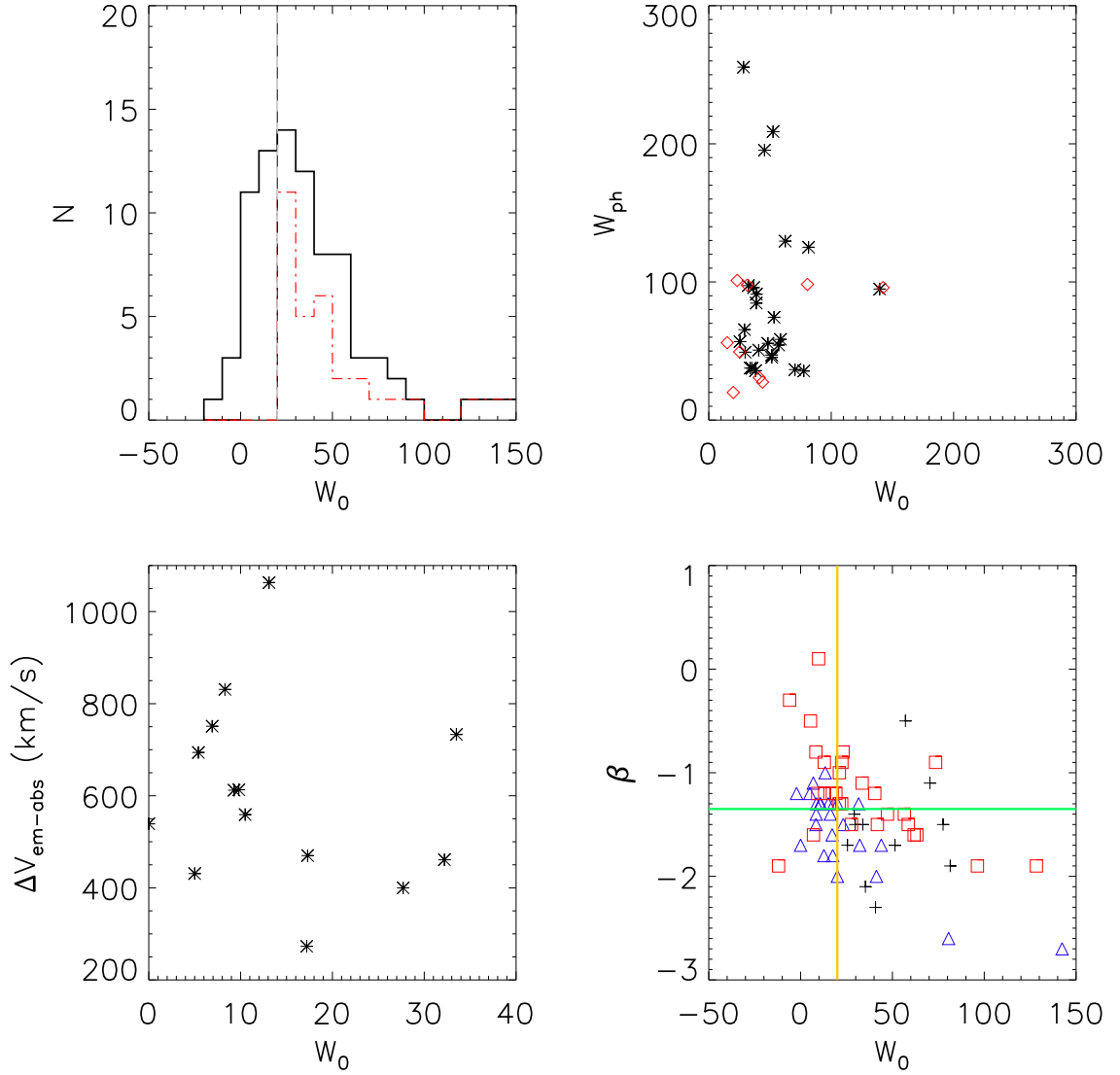


Figure 2.1 Top left: the rest-frame Ly α equivalent width (W_0) distribution for our spectroscopic sample (black solid line) and our UV-bright LAE subsample (red dot-dashed line). All reported equivalent widths are in \AA . Top right: W_{phot} v. W_0 for $z \sim 3$ LAEs (black stars) and $z \sim 2$ LAEs (red diamonds). Bottom left: $\Delta v_{\text{em-abs}}$ v. spectroscopic W_0 where errors in $\Delta v_{\text{em-abs}}$ are the range values found for different transitions. Bottom right: spectral slope index, β ($F_\lambda \propto \lambda^\beta$), as calculated from the photometric colors, v. W_0 for R > 25.5 galaxies (cyan crosses), $z \sim 3$ R < 25.5 galaxies (red squares), and $z \sim 2$ R < 25.5 galaxies (blue triangles). A typical error measurement is plotted in the upper right corner. LAEs from Guaita et al. (2011) (black X's) and Nilsson et al. (2009) (black crosses) are also plotted. The vertical line is the traditional cut for LAEs ($W_0 = 20 \text{\AA}$) and the horizontal line is the division between the blue and red spectral slope composites.

equivalent widths is necessary to fully understand the cause of this discrepancy.

In galaxy spectra with both Ly α emission and interstellar absorption, we measure the average relative velocity offset, $\Delta v_{\text{em-abs}}$. In the bottom left panel of Figure 2.1, the distribution of $\Delta v_{\text{em-abs}}$ as a function of Ly α equivalent width is plotted where the errors represent the range in velocity offsets measured from different transitions. The median velocity offset is $\Delta v_{\text{em-abs}} = 584 \text{ km s}^{-1}$, similar to S03 who found $\Delta v_{\text{em-abs}} = 650 \text{ km s}^{-1}$. In all of our galaxies, Ly α emission is at a higher redshift than interstellar absorption. This result is consistent with S03 who find that nearly all of their 323 LBGs show Ly α at a higher redshift than interstellar absorption. These velocity offsets indicate that most likely the emission is coming from the farside component of the outflow while interstellar absorption, Ly α absorption, and blueshifted Ly α emission are coming from the nearside component. Large-scale outflows are caused by feedback from star formation and supernovae, as first reported in $z \sim 3$ LBGs by Steidel et al. (1996a). In general, stellar systemic redshifts are measured from photospheric features from hot stars. In the rest-UV, photospheric features are too weak to be seen in individual spectra. Systemic redshifts can also be determined from rest-optical nebular emission lines, but these were not available. Therefore, in the rest of our analysis, we measure the relative velocity offset between Ly α emission and absorption. While velocity offset tends to decrease with increasing Ly α equivalent width, we do not find this trend to be very significant. Furthermore, none of the UV-bright SFGs with $W_{\text{Ly}\alpha} > 40 \text{ \AA}$ have visible interstellar absorption lines.

The spectral slope of the UV continuum is largely dependent on the star formation rate and amount of extinction. For UV-bright, star-forming galaxies, the unreddened UV continuum remains fairly constant for ages 10Myr to 1Gyr where the spectral slope index, β ($F_\lambda \propto \lambda^\beta$), ranges from -2.6 to -2.1 (Leitherer et al. 1999). Both narrowband- and continuum-selected galaxies at $2 < z < 3.5$ have typical ages within this range (Papovich et al. 2001; Shapley et al. 2001; Erb et al. 2006d; Gawiser et al. 2007; Kornei et al. 2010) indicating that large differences in UV spectral slope reflect varying amounts of dust extinction. For a large number of our galaxies, the individual spectra are of insufficient S/N to accurately measure a UV continuum slope. However, using broadband photometry, BVRI

for $z \sim 3$ and UBVRI for $z \sim 2$ SFGs, we calculate the UV spectral slope index after correcting for IGM extinction and Ly α equivalent width for each galaxy. The bottom right panel of Figure 2.1 shows the distribution of UV spectral slopes as a function of Ly α equivalent width for $R < 25.5$, $2 < z < 2.7$ galaxies (blue triangles), $R < 25.5$, $2.7 < z < 3.5$ galaxies (red squares), and $R > 25.5$ galaxies (cyan crosses) with a typical error measurement in the upper right corner. LAEs from Guaita et al. (2011) (black X's) and Nilsson et al. (2009) (black crosses) are also plotted. We find a median spectral slope of $\beta = -1.4$, then create a red ($\beta > -1.4$) and a blue ($\beta \leq -1.4$) spectral slope subsample. Galaxies with nondetections in the B, V, and/or R bands have been omitted from this plot. We find a large range in β values from $\beta = -2.7$ to $\beta = 0.1$, however, for galaxies with rest-frame $W_{\text{Ly}\alpha} > 20\text{\AA}$, β ranges from $\beta = -2.7$ to $\beta = -0.8$ indicating a relation between stronger Ly α emission and bluer spectral slopes. UV-bright SFGs with $W_{\text{Ly}\alpha} < 20\text{\AA}$ subset have a mean spectral slope of $\langle \beta \rangle = -1.22 \pm 0.47$ while UV-bright SFGs $W_{\text{Ly}\alpha} > 20\text{\AA}$ have a bluer mean spectral slope of $\langle \beta \rangle = -1.52 \pm 0.45$ where errors represent the standard deviation on the mean. Moreover, the red and blue spectral slope subsamples have median Ly α equivalent widths of $W_0 = 15.1\text{\AA}$ and $W_0 = 32.2\text{\AA}$ respectively. These trends display a relation between increasing Ly α equivalent width and bluer spectral slope, which has previously been observed in $z \sim 3$ LBGs (Shapley et al. 2003a; Steidel et al. 2010; Kornei et al. 2010).

Through dividing the sample into two redshift bins, $2.0 < z < 2.7$ and $2.7 < z < 3.5$, we find that galaxies at both redshifts show a similar relationship between Ly α equivalent width and spectral slope. Surprisingly, galaxies at $z \sim 2$ show bluer continuum slopes on average ($\langle \beta \rangle = -1.87 \pm 0.51$) than galaxies at $z \sim 3$ ($\langle \beta \rangle = -1.34 \pm 0.33$), which appears as a systematic offset independent of Ly α equivalent width and is further discussed in § 2.6.5. This trend is still observed when using the same observed photometry (BVRI) to determine rest-UV slopes at both redshifts.

2.4 Stacking Procedure

In generating the following composite spectra, we begin by identifying a subsample of galaxy spectra to be combined. We exclude LAEs whose spectra are plagued by poor sky subtraction or have minimal wavelength coverage. Of the 52 spectroscopically confirmed LAEs,

we include 26 observed with the FORS instrument and 10 with the VIMOS instrument. Additionally, SFGs lacking precise redshifts determined by either the $\text{Ly}\alpha$ emission line or several interstellar absorption lines are also excluded from the composite. These criteria yield 28 VIMOS LBGs and 17 FORS BXs out of 73 spectroscopically confirmed continuum-selected galaxies. The effects of omitting LBGs without detectable $\text{Ly}\alpha$ emission redshifts is discussed in section 2.6.1.

Table 2.1 Subsample Criteria

Type	Magnitude	$W_{\text{Ly}\alpha}$	N_{FORS}	N_{VIMOS}	N_{total}
UV-bright SFG	$R \leq 25.5$	all	29	30	59
UV-bright non-LAE	$R \leq 25.5$	$< 20\text{\AA}$	15	12	27
UV-bright LAE	$R \leq 25.5$	$\geq 20\text{\AA}$	14	18	32
UV-bright blue	$R \leq 25.5$	-	14	11	25
UV-bright red	$R \leq 25.5$	-	11	17	28
UV-faint LAE	$R > 25.5$	$\geq 20\text{\AA}$	14	8	22

We proceed to shift the extracted, one-dimensional, flux-calibrated spectra into the rest frame. The spectra are subsequently rebinned to a dispersion of 1\AA per pixel corresponding to roughly the FORS resolution. We then renormalize them to their $1250 - 1300\text{\AA}$ continuum. Outlying data points due to cosmic-ray events and sky subtraction residuals are systematically masked, totaling less than 0.2% of the data. Finally, using an optimal weighting routine where weights are defined as $1250 - 1300\text{\AA}$ continuum strength divided by noise squared, we co-add the individual spectra (Gawiser et al. 2006c). We note that a variety of UV spectral slopes in conjunction with the majority of the VIMOS spectra covering only $\lambda < 1600\text{\AA}$ causes the S/N to drop rapidly and the continuum level to become uncertain above this wavelength.

In order to understand the connection between UV-bright star-forming galaxies with and without strong $\text{Ly}\alpha$ emission, we divided our dataset into three subsamples: UV-bright non-LAE, UV-bright LAE, and UV-faint LAE. In Table 2.1 we present our selection criteria for and the number of galaxies in each composite. We also define a UV-bright SFG subsample with $R \leq 25.5$ which is composed of the UV-bright non-LAE and UV-bright LAE subsamples. The UV-bright non-LAE and UV-bright LAE subsets differ slightly in magnitude, $\langle R_{\text{UV-brightnon-LAE}} \rangle = 24.46$ and $\langle R_{\text{UV-brightLAE}} \rangle = 24.84$ with a scatter of

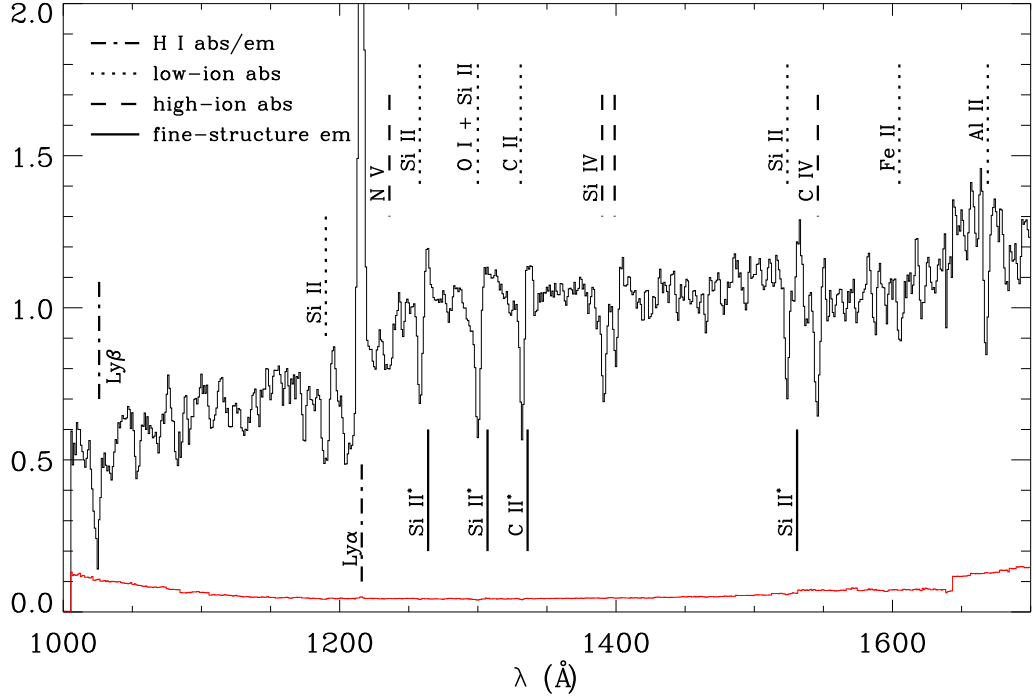


Figure 2.2 Composite continuum-normalized rest-frame UV spectrum of 59 SFGs ($R < 25.5$) with the composite one sigma error spectrum plotted in red. H I Ly α emission and low- and high-ionization interstellar absorption originating from the outflowing component are the most prominent features. Weaker features such as stellar emission from P Cygni profiles and fine-structure emission (Si II* and C II*) are also visible.

± 0.68 and ± 0.42 respectively, although this difference is not significant. This difference is in part due to the fact that larger Ly α line fluxes make spectroscopic identification easier. Selection effects based on luminosity and Ly α equivalent widths are discussed in detail in Section 2.6.1. The primary goal for these different spectroscopic subsamples is to understand the effects of increasing Ly α emission and decreasing magnitude on galaxy properties. We do note that our $R \leq 25.5$ LAE subsample contains galaxies with a broad range of properties including galaxies with strong interstellar absorption lines, Si II* fine-structure emission, and faint continua where the only feature seen is Ly α emission. We also subdivide our dataset into a red ($\beta > -1.4$) and blue ($\beta \leq -1.4$) spectral slope subsample based on their intrinsic rest-UV colors. We exclude 6 narrowband-selected galaxies with B, V, or R band magnitudes greater than 1 magnitude from these composites as their spectral slopes are not well constrained.

2.5 Analysis of Composite Spectra

The absorption and emission features observed in these spectra are produced in gas associated with galactic-scale outflows, H II regions, and the winds and photospheres of massive stars. Figure 2.2 shows the UV-bright SFG composite spectrum of 59 $R \leq 25.5$ SFGs. The most prominent features in the rest-UV composite spectra are blueshifted interstellar absorption and H I Ly α . These features trace large-scale outflows of interstellar medium, which have been modelled in detail for high-redshift LAEs and LBGs (Verhamme et al. 2008; Laursen et al. 2011). In individual galaxy spectra, due to low S/N, only redshifts can be determined from strong interstellar absorption. However, with higher S/N, composite spectra allow for more robust measurements of their equivalent widths as well as revealing fainter features such as nebular emission.

In Figure 2.3, the top panel displays our composite UV-bright non-LAE spectrum (27 UV-bright non-LAEs), the middle panel shows our UV-bright LAE composite spectrum (32 UV-bright LAEs) and the bottom panel shows our UV-faint LAE composite spectrum (22 LAEs). For our UV-faint LAE composite spectrum, limited spectral coverage in conjunction with all of these LAEs being at $z = 3.1$ causes our sample size to drop to 8 galaxies (35%) at $\lambda < 1340\text{\AA}$. In addition, we have masked the region around 1360\AA due to residuals from the $\lambda 5577\text{\AA}$ skyline. For this reason, we limit our analysis of the LAE composite to wavelengths blueward of 1340\AA .

Across the UV-bright LAE and UV-bright non-LAE composites, the most striking trends are the decrease in interstellar absorption and increase in Si II* nebular emission with increasing Ly α emission. In this section, we first focus our analysis on the Ly α emission and absorption line profile. We then discuss low- and high-ionization interstellar absorption line features. Finally, we proceed to discuss nebular features and fine-structure Si II* emission within the systemic component of the galaxies.

2.5.1 Lyman Alpha Emission and Absorption

Ly α photons originate from recombinations in H II regions around massive stars, yet a number of effects impact the strength, shape, and relative velocity of the emergent Ly α

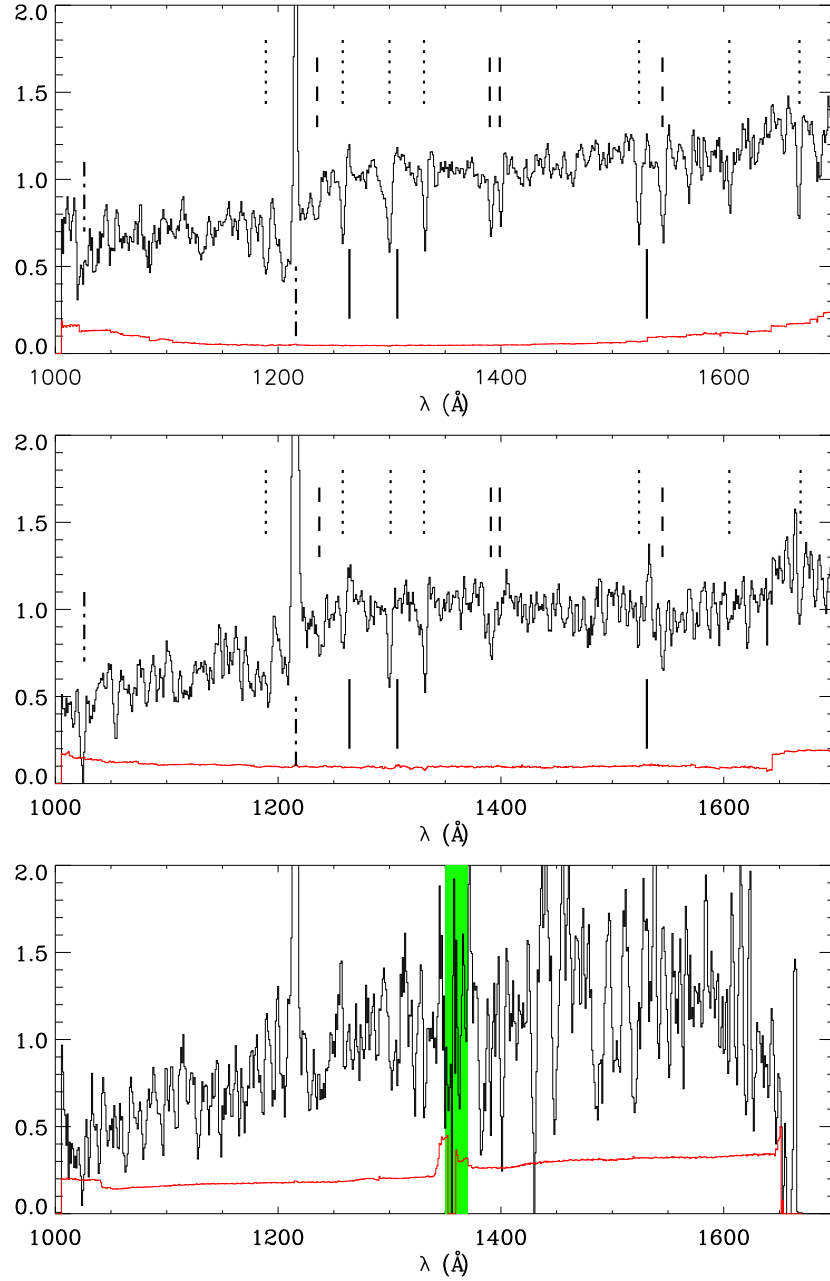


Figure 2.3 A series of continuum-normalized spectra for our three subsamples: top - UV-bright non-LAE, middle - UV-bright LAE, bottom - UV-faint LAE. The galaxies used to construct these spectra were shifted into the rest-frame using their Ly α emission line redshifts. The one-sigma composite error spectrum is plotted in red at the bottom of each composite. With increasing Ly α emission, interstellar absorption features become weaker, Si II* $\lambda\lambda$ 1265, 1309 emission becomes stronger, and the spectral slopes is bluer. The λ 5577 skyline has been masked in the UV-faint LAE composite (green) at 1360 \AA as all UV-faint LAEs lie at $z = 3.1$.

profile; including intrinsic star formation rate, amount of dust, dust geometry, covering fraction, and the kinematics of the outflowing gas. For a more in depth discussion on the shape of the Ly α profiles in this dataset, see Gawiser et al. (in prep.). Nonetheless, we are still equipped with the overall strength of Ly α emission and absorption as well as its relative velocity offset with respect to other spectroscopic features.

Table 2.2 All-SFG Spectroscopic Features

Ion	λ_{rest} (Å)	f	W_0 (Å)	σ (Å)	$\Delta v_{\text{em-abs}}$ (km s $^{-1}$)
Ly α_r	1215.67	-	19.1	1.5	-
Ly α_b	1215.67	-	-2.7	0.3	2400
Si II	1260.42	1.007	-1.3	0.15	520
O I	1302.17	0.0489	-2.1	0.2	760
Si II	1304.37	0.094	-2.1	0.2	540
C II	1334.53	0.128	-1.7	0.2	590
Si II	1526.71	0.130	-1.2	0.3	580
Fe II	1608.45	0.058	-0.7	0.3	590
Al II	1670.79	1.83	-1.2	0.4	560
N V	1238.82	0.157	-0.9	0.2	1320
N V	1242.80	0.0782	-0.9	0.2	1320
Si IV	1393.76	0.514	-1.5	0.2	550
Si IV	1402.77	0.255	-0.9	0.2	630
C IV	1548.20	0.191	-1.7	0.3	800
C IV	1550.78	0.0952	-1.7	0.3	800

Note. — Ly α_r and Ly α_b refer to the redshifted emission and blueshifted absorption of the Ly α profile. All values of Δv are relative to Ly α_r . Transition oscillator strengths as in Pettini et al. (2002). W_0 , σ , and Δv values listed for O I λ 1302 and Si II λ 1304 refer to the line profile for these two blended features assuming the rest wavelength is $\lambda = 1303.27\text{\AA}$. Similarly, the values for N V λ λ 1238.82, 1242.80 and C IV λ λ 1548.20, 1550.78 refer to the blended line profiles assuming a rest wavelength of $\lambda = 1240.81\text{\AA}$ and $\lambda = 1549.48\text{\AA}$ respectively.

For our UV-bright SFG composite (Fig. 2.2), we measure a rest-frame Ly α emission equivalent width of $W_0 = 19.1 \pm 1.5\text{\AA}$. We also note that there is evidence for weak blueshifted emission at a velocity offset of $\Delta v_{\text{em-abs}} \sim 5000 \text{ km s}^{-1}$ separated by Ly α absorption. Ly α photons are much more likely to escape from a galaxy if their relative velocities have been shifted off resonance with respect to the bulk component of the neutral material. We find it interesting that there is blueshifted emission at a very high velocity offset as the UV-bright SFG composite represents an average of all the UV-bright galaxies including several with strong Ly α absorption. For the main Ly α absorption, we measure

an equivalent width of $W_o = -2.7 \pm 0.3 \text{ \AA}$ at a velocity offset of $\Delta v_{\text{em-abs}} \sim 2400 \text{ km s}^{-1}$. Equivalent widths and velocity offsets for our UV-bright SFG composite spectra are presented in Table 2.2. Since the composite spectra include galaxies observed with the FORS and VIMOS instruments, we smooth all spectra by the VIMOS resolution ($v \sim 650 \text{ km s}^{-1}$), which we calculate to be 3.0 \AA under optimal observing conditions. We also set an upper bound of 3.1 \AA on our spectral resolution as the minimum FWHM value measured among the strong interstellar features. Assuming an effective spectral resolution of 3.0 \AA and subtracting the instrument FWHM from the observed FWHM in quadrature, we compute a deconvolved $\text{FWHM}(\text{Ly}\alpha) = 530 \pm 30 \text{ km s}^{-1}$ in the UV-bright SFG composite. While the UV-bright SFG composite represents the average strength of $\text{Ly}\alpha$ emission among our $R < 25.5$ SFGs, this is not representative of the entire population of SFGs due to selection effects. For instance, spectroscopic identification is easier using an emission line rather than an absorption line. As objects become fainter, the fraction of galaxies with $\text{Ly}\alpha$ in emission increases. We discuss the implications of this effect in Section 2.6.1. Additionally, the weight causes brighter galaxies to contribute more to the composite. These factors have opposing effects on the strength of the $\text{Ly}\alpha$ feature in Figure 2.2, so it will not necessarily be that of the average SFG. However, we do find the median $\text{Ly}\alpha$ equivalent width of the UV-bright SFG sample ($W_0 = 21.0 \text{ \AA}$) to be consistent with that of the UV-bright SFG composite. A wide distribution of $\text{Ly}\alpha$ equivalent widths and line profiles is seen in our individual spectra, which we discuss in Section 2.6.2. In Section 2.6.3, we discuss the relationships among the strength of the $\text{Ly}\alpha$ line and other galaxy properties.

In the UV-bright non-LAE composite (top panel of Fig. 2.3), we observe $\text{Ly}\alpha$ both in emission and blueshifted absorption with an average velocity offset of $\Delta v_{\text{em-abs}} \sim 2400 \text{ km s}^{-1}$. The blueshifted absorption extends from the $\text{Ly}\alpha$ emission line to $\Delta v_{\text{em-abs}} > 4500 \text{ km s}^{-1}$ with an equivalent width of $W_o = -4.9 \pm 0.9 \text{ \AA}$. For the emission component, we measure a $\text{Ly}\alpha$ emission line equivalent width of $W_o = 8.4 \pm 0.9 \text{ \AA}$, which we find to be comparable to the second highest $\text{Ly}\alpha$ equivalent width quartile of S03 ($W_o = 11.00 \pm 0.71 \text{ \AA}$). Our results for the UV-bright non-LAE and UV-bright LAE composites are presented in Table 2.3. The observed FWHM is right at our instrument resolution, so we set a 3σ upper limit of $\text{FWHM}(\text{Ly}\alpha) < 200 \text{ km s}^{-1}$.

Table 2.3 Spectroscopic Properties

	UV-bright non-LAE	UV-bright LAE	UV-bright SFG
N_{gal}	27	32	59
R	24.46	24.84	24.72
β_{phot}	-1.3	-1.5	-1.3
β_{spec}	-1.50	-2.25	-1.90
Δv_{em-abs}	640 ± 10	610 ± 60	630 ± 20
$FWHM_{LIS}$	340 ± 100	420 ± 90	430 ± 60
$W_{Ly\alpha_r}$	8.4 ± 0.9	50.0 ± 4.8	19.1 ± 1.5
$W_{Ly\alpha_b}$	-4.9 ± 0.9	1.2 ± 0.8	-2.7 ± 0.3
$W_{SiII,1193}$	-1.9 ± 0.3	-	2.0 ± 0.2
$W_{SiII,1260}$	-1.4 ± 0.25	-1.2 ± 0.2	-1.3 ± 0.15
$W_{OI+SiII,1303}$	-2.5 ± 0.3	-1.7 ± 0.3	-2.1 ± 0.2
$W_{CII,1334}$	-1.5 ± 0.25	-1.8 ± 0.3	-1.7 ± 0.2
$W_{SiII,1526}$	-1.8 ± 0.3	-0.5 ± 0.3	-1.2 ± 0.2
$W_{FeII,1608}$	-1.1 ± 0.4	-	-0.7 ± 0.3
$W_{AlIII,1670}$	-1.5 ± 0.45	-1.0 ± 0.5	-1.2 ± 0.3
$W_{NV,1240}$	-1.0 ± 0.35	-1.1 ± 0.4	-0.9 ± 0.2
$W_{SiIV,1393}$	-1.5 ± 0.3	-1.4 ± 0.35	-1.5 ± 0.2
$W_{SiIV,1402}$	-1.0 ± 0.3	-0.4 ± 0.35	-0.9 ± 0.2
$W_{CIV,1549}$	-2.2 ± 0.35	-1.1 ± 0.4	-1.7 ± 0.3
$W_{OIII,1664}$	-	0.8 ± 0.45	-

Note. — R and β_{phot} refer to the median values of the individual galaxies. β_{spec} refers to the spectral slope of the composite. The UV-bright LAE and UV-bright non-LAE subsets contain a similar fraction of galaxies observed with FORS and VIMOS. Δv_{em-abs} and $FWHM_{LIS}$ refer to the average values of the low-ionization lines.

The UV-bright LAE composite (middle panel of Fig. 2.3) has a complex Ly α profile, as it includes galaxies with redshifted absorption and multiple-peaked emission. For the main Ly α emission line component, we measure deconvolved $FWHM(Ly\alpha) = 410 \pm 100 \text{ km s}^{-1}$ and an equivalent width of $W_o = 50.0 \pm 4.8 \text{ \AA}$. The faint blueshifted emission at very high velocity offset in this composite is the origin of the same feature in the UV-bright SFG composite. We measure a velocity offset of $\Delta v_{em-abs} \sim 4600 \text{ km s}^{-1}$, which agrees with the maximum velocity offset of the Ly α absorption in the UV-bright non-LAE subsample. In the individual galaxy spectra contributing to the UV-bright LAE composite, we do not find any significant emission at this velocity offset, but we do note that the stacking procedure can reveal features too faint to be seen in individual spectra. The majority of Ly α photons will be absorbed at the relative velocity of the bulk of the outflowing neutral

medium. However, Ly α photons farther in velocity space from the line center are less likely to be re-absorbed. Steidel et al. (2010) find outflows around $z = 2.3$ SFGs to best be characterized by a powerlaw with larger velocities at larger radii. If the blueshifted emission at $\Delta v_{\text{em-abs}} \sim 4600 \text{ km s}^{-1}$ is real, it reveals extended emission of Ly α photons from a diffuse component of H I. Steidel et al. (2011) recently found extended Ly α emission in a sample of 92 continuum-selected galaxies at $z \sim 2.65$.

In our UV-faint LAE composite (bottom panel of Fig. 2.3), we see no strong evidence for blueshifted emission. We measure a Ly α equivalent width of $W_0 = 42.1 \pm 6.2 \text{ \AA}$ and a velocity FWHM of $\text{FWHM}(\text{Ly}\alpha) = 380 \pm 110 \text{ km s}^{-1}$, consistent with the UV-bright LAE composite.

2.5.2 Low-Ionization Absorption Lines

Blueshifted singly-ionized metal absorption lines probe the neutral component of outflowing interstellar material on the nearside of the galaxy. Among our composite spectra, there are a host of low-ionization interstellar absorption lines. Due to limited S/N, we restrict our analysis to the strongest low-ionization lines that we detect at high significance: Si II $\lambda 1260$, O I $\lambda 1302$ + Si II $\lambda 1304$, C II $\lambda 1334$, Si II $\lambda 1526$. All of these features have been well-studied in high-redshift LBGs (Pettini et al. 2000, 2002; Shapley et al. 2003a; Cabanac et al. 2008; Quider et al. 2009; Dessauges-Zavadsky et al. 2010; Talia et al. 2012; Jones et al. 2012) and nearby starburst galaxies (Heckman et al. 1998; Leitherer et al. 2011). We also find Fe II $\lambda 1608$ and Al II $\lambda 1670$ at low significance, but they are located in a region of the spectrum where we have fewer galaxies contributing to the composite and therefore lower S/N. For these reasons, we only record their equivalent widths. Table 2.3 reports measurements of equivalent widths and average velocity offsets of the interstellar lines. As we observe a distribution of velocity offsets among our individual galaxies, the FWHMs of all transitions other than Ly α will be artificially broadened to some extent. Due to the intrinsically faint nature of our UV-faint LAE galaxies' continua in combination with continuum normalization, we do not observe any significant interstellar features in the UV-faint LAE composite. As a result, we restrict our analysis to the UV-bright LAE and UV-bright non-LAE composites for the rest of the analysis.

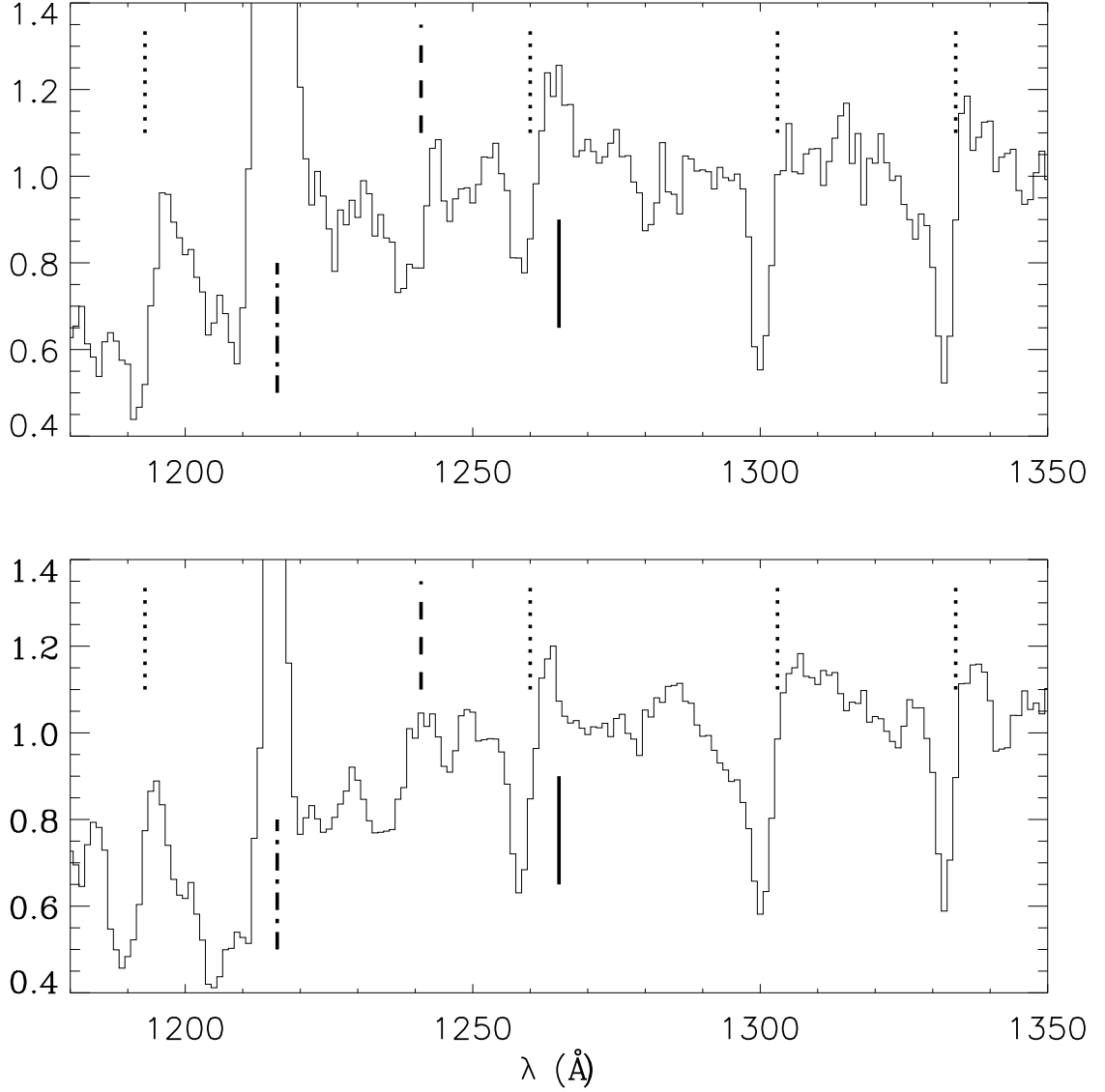


Figure 2.4 Zoomed-in regions of the UV-bright LAE (top panel) and UV-bright non-LAE (bottom panel) composite spectra shown in Figure 3. The adjusted scale allows for a more in depth look at the interstellar absorption line profiles as well as the nebular emission feature Si II* $\lambda\lambda$ 1265, 1309. Note the strength of the λ 1265 emission as compared to the lack of λ 1309 emission in both composites. The low-ionization transitions are all blueshifted with respect to Ly α and the N V $\lambda\lambda$ 1238, 1242 transition has a significantly higher velocity offset in the UV-bright non-LAE than LAE composite. The vertical lines indicate the Ly α rest-frame wavelengths with respect to Ly α emission for low-ionization absorption (dotted line), high-ionization absorption (dashed line), and Si II* emission (solid line).

The strong low-ionization interstellar lines are useful for measuring the kinematics of the neutral gas component within the outflow. Figure 2.4 and Figure 2.5 show zoomed in regions around the strong absorption lines for the UV-bright LAE composite (top panel) and UV-bright non-LAE composite (bottom panel). The vertical lines indicate the rest-frame wavelength of each transition with respect to Ly α emission. Relative to Ly α , we measure an average velocity offset of the low-ionization features of $\Delta v_{\text{em-abs}} = 640 \pm 10 \text{ km s}^{-1}$ and $\Delta v_{\text{em-abs}} = 610 \pm 60 \text{ km s}^{-1}$ for the UV-bright non-LAE and UV-bright LAE composites. Using the Si II $\lambda 1260$ and C II $\lambda 1334$ absorption lines, which are the least affected by blending, and assuming a spectral resolution of 3.0 \AA , we measure a deconvolved FWHM = $430 \pm 60 \text{ km s}^{-1}$ for the UV-bright SFG composite. We subsequently measure a FWHM in the UV-bright LAE and UV-bright non-LAE composites of FWHM = $420 \pm 80 \text{ km s}^{-1}$ and FWHM = $340 \pm 100 \text{ km s}^{-1}$ respectively. The different velocity offsets among individual galaxies in the UV-bright LAE and non-LAE composites is likely biasing the FWHM in the UV-bright SFG composite to larger values. Our results are consistent with S03, who stacked 811 LBGs at a spectral resolution of 2.6 \AA and found an average FWHM(LIS) = $450 \pm 150 \text{ km s}^{-1}$.

We measure the degree of saturation of the Si II transitions by comparing the equivalent widths of Si II $\lambda 1260$ and Si II $\lambda 1526$. On the linear part of the curve of growth, the ratio of $W_0(1260)/W_0(1526) > 5$, while we measure $W_0(1260)/W_0(1526) = 1.1 \pm 0.2$ in the UV-bright SFG composite, consistent with unity and the material being optically thick. This ratio is $W_0(1260)/W_0(1526) = 2.4 \pm 1.5$ in the UV-bright LAE composite, as the $\lambda 1526$ transition is marginally detected, making the uncertainty quite large. S03, Erb et al. (2006d), and Steidel et al. (2010) find the Si II transitions to be consistent with saturation in each of their composites, and S03 report a $W_0(1260)/W_0(1526) = 0.95$ in their all-LBG composite. Since the strong low-ionization transitions are all saturated, they are not useful for determining chemical abundances. Metal abundances can be derived from weaker features lying on the linear part of the curve of growth in conjunction with H I column densities (e.g., Pettini et al. 2000, 2002). We do not observe any of these features with high enough S/N and cannot measure H I column densities, so we focus our analysis on the strong transitions. We do note that Erb et al. (2006a) used the metallic absorption

lines near $\lambda 1370$ and $\lambda 1425$ to confirm their rest-frame optical metallicity measurements. We find these regions in our UV-bright SFG composite to be consistent with the low-mass composite of Erb et al. (2006a) which had a metallicity of $Z < 0.33Z_{\odot}$. Finkelstein et al. (2009) measured limits on the metallicities of two LAEs using rest-frame optical emission lines to be $Z < 0.17Z_{\odot}$ and $Z < 0.28Z_{\odot}$.

2.5.3 High-Ionization Absorption Lines

In addition to low-ionization absorption, we also detect several high-ionization interstellar absorption lines at high significance, namely N V $\lambda\lambda 1238, 1242$, Si IV $\lambda\lambda 1393, 1402$, and C IV $\lambda\lambda 1548, 1550$. These transitions trace gas at $T \geq 10^4$ K that has been ionized by feedback from supernovae, stellar winds, and collisional processes associated with the outflow. They are therefore useful for probing the ionized component and ionization state of the outflow. We analyze the most prominent high-ionization features first (Si IV and C IV), then interpret the N V line profile, which we detect at lower significance.

In the UV-bright non-LAE composite, for the $\lambda\lambda 1393, 1402$ Si IV transitions, we measure comparable velocity offsets of $\Delta v_{\text{em-abs}} \sim 560 \text{ km s}^{-1}$ and $\Delta v_{\text{em-abs}} \sim 590 \text{ km s}^{-1}$. In contrast, for the UV-bright LAE composite, we measure velocity offsets of $\Delta v_{\text{em-abs}} = 440 \text{ km s}^{-1}$ and $\Delta v_{\text{em-abs}} = 870 \text{ km s}^{-1}$ respectively. The UV-bright LAE composite shows strong absorption at $\lambda 1393$ while having marginally detected absorption at $\lambda 1402$ likely due to redshifted emission from a P Cygni component filling it in, and thereby biasing our velocity offset to a higher value. We also find the signature of a P Cygni profile in the UV-bright non-LAE composite, although at lower significance and it does not appear to have a significant effect on the velocity offset of the $\lambda 1402$ absorption. For a doublet ratio of 2:1, the Si IV $\lambda\lambda 1393, 1402$ transition is on the linear part of the curve of growth and therefore optically thin. In the UV-bright SFG composite, this ratio is 1.9:1, however, this ratio is 3.5:1 in the UV-bright LAE composite and 1.4:1 in the UV-bright non-LAE composite. The higher doublet ratio in the UV-bright LAE composite is again due to P Cygni emission filling in $\lambda 1402$ absorption. In the UV-bright non-LAE composite, continuum uncertainty due to broad stellar absorption makes measuring this ratio difficult and may bias this ratio towards 1:1. Thus, we conclude that the Si IV transition appears consistent with being

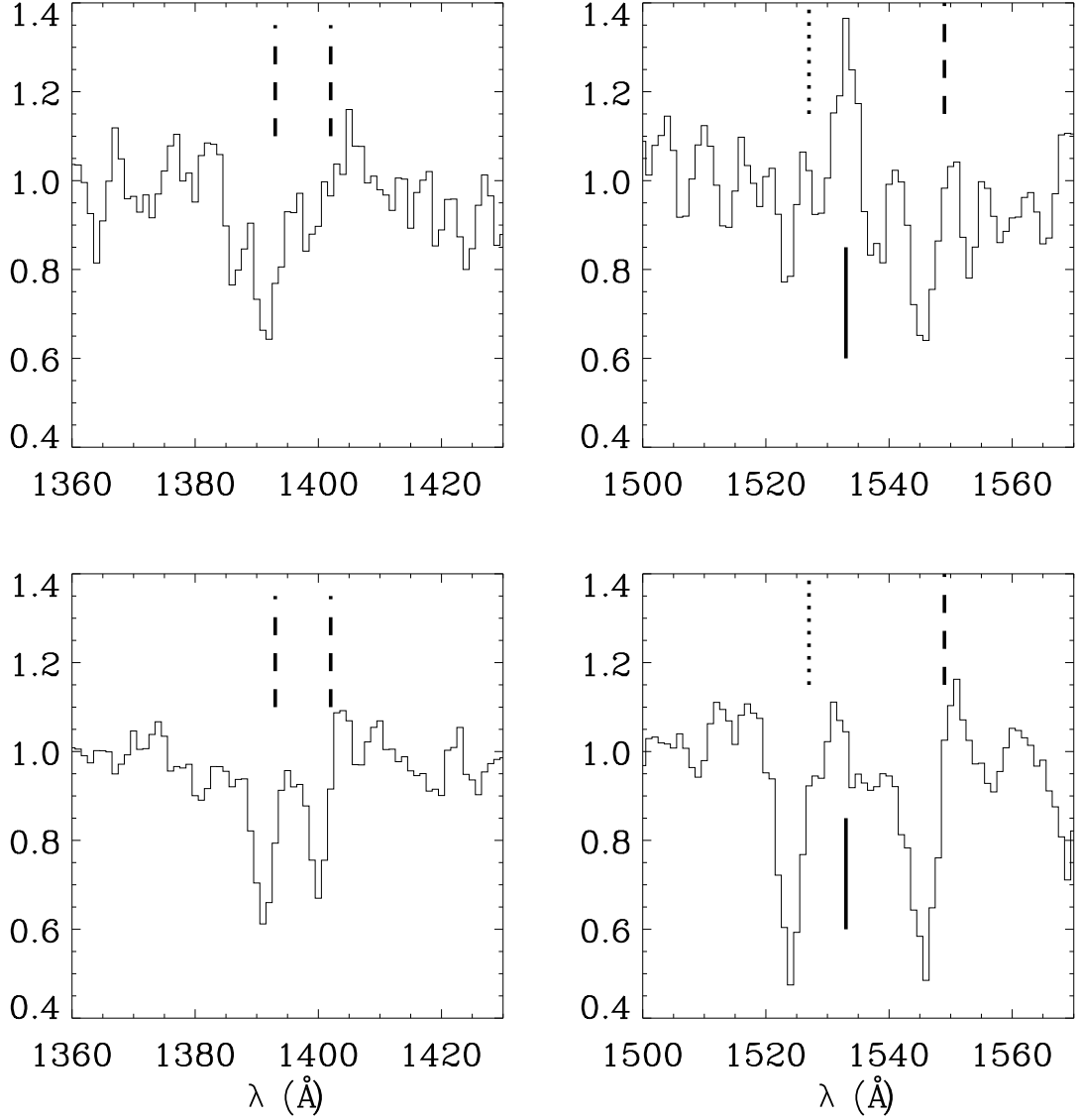


Figure 2.5 Analogous to Figure 4, except showing the Si IV $\lambda\lambda$ 1393, 1402, Si II λ 1526 and C IV $\lambda\lambda$ 1548, 1550 transitions for the UV-bright LAE composite (top row) and UV-bright non-LAE composite (bottom row). This view shows the lack of Si IV λ 1402 and Si II λ 1526 absorption as well as the strength of the Si II* λ 1533 emission in the UV-bright LAE composite. In the left panels, the Si IV redshifted emission is more apparent and the Si IV $\lambda\lambda$ 1393, 1402 absorption are seen at similar velocity offsets for each composite. In the right panels, the decrease in Si II* λ 1526 emission and increase in Si II λ 1526 and C IV $\lambda\lambda$ 1548, 1550 absorption with decreasing Ly α emission is clearer.

optically thin in all composites.

For the UV-bright SFG composite, we find the relative velocity offset of the Si IV λ 1393, 1402 transitions ($\Delta v_{\text{em-abs}} \sim 590 \text{ km s}^{-1}$) to be in good agreement with the average velocity shift of the low-ionization absorption lines ($\Delta v_{\text{em-abs}} = 550 \text{ km s}^{-1}$). Moreover, the average deconvolved FWHM of the Si IV doublet is $\text{FWHM}_{\text{SiIV}} = 420 \pm 110 \text{ km s}^{-1}$, also consistent with that of the low-ionization absorption lines $\text{FWHM}_{\text{LIS}} = 360 \pm 60 \text{ km s}^{-1}$.

In the UV-bright SFG composite, for C IV blended at $\lambda 1549.5$, assuming a doublet ratio of 1:1, we measure $\Delta v_{\text{em-abs}} = 800 \text{ km s}^{-1}$, significantly larger than the low-ionization lines. However, the velocity width of $\text{FWHM}_{\text{CIV}} = 450 \pm 60 \text{ km s}^{-1}$ is consistent with the low-ionization lines. There appears to be some broadening due to stellar winds along with redshifted emission characteristic of a P Cygni profile, which may be biasing the velocity offset to larger values. For both the UV-bright LAE and UV-bright non-LAE composites, we find comparable velocity offsets to the UV-bright SFG composite, which are in all cases larger than that of the Si IV $\lambda 1393$ transition and the low-ionization absorption lines.

In the UV-bright LAE composite, we see weak C IV absorption, yet in the UV-bright non-LAE composite, we find significantly stronger C IV absorption corresponding to an increase in absorption strength of $\sim 100\%$. S03 also report seeing more C IV absorption in their $W_{\text{Ly}\alpha} = 11\text{\AA}$ composite than their $W_{\text{Ly}\alpha} = 52\text{\AA}$ composite, although they only measure an increase in strength of $\sim 30\%$. The relatively weak C IV absorption seen in the UV-bright LAE composite is particularly interesting given that the strength of the Si IV $\lambda 1393$ absorption is comparable in both the UV-bright LAE and UV-bright non-LAE composites, and the velocity FWHMs of the high-ionization transitions are comparable across all composites. We further note from the relative strength of the interstellar C II $\lambda 1334$ absorption to C IV $\lambda 1549$ absorption that the outflowing component of carbon appears to have a higher covering fraction in a lower ionization state, as it is unlikely that the velocity FWHM of the neutral gas is higher than that of the ionized gas.

Significant N V absorption is visible in the UV-bright SFG composite with a large velocity FWHM ($\text{FWHM} \sim 1200 \text{ km s}^{-1}$) and velocity offset ($\Delta v_{\text{em-abs}} = 1150 \text{ km s}^{-1}$). The N V line profile shape is consistent with that of a P Cygni profile, indicating that there

is both a stellar and an interstellar component. The velocity offset of the N V absorption is significantly larger in the UV-bright non-LAE composite ($\Delta v_{\text{em-abs}} = 1300 \text{ km s}^{-1}$) than the UV-bright LAE composite ($\Delta v_{\text{em-abs}} = 600 \text{ km s}^{-1}$). In spite of this difference in velocity offset, the velocity width is consistent among all three composites (FWHM $\sim 1200 \text{ km s}^{-1}$). We interpret the larger velocity offset in the UV-bright non-LAE composite as evidence for a significant amount of interstellar N V absorption in the outflowing component. In this composite, both the N V velocity offset and velocity FWHM are significantly larger than that of the Si IV and C IV absorption.

2.5.4 Stellar Features

The radiation pressure from hot massive stars can generate winds of $2000\text{-}3000 \text{ km s}^{-1}$ (Groenewegen et al. 1989). These winds are seen spectroscopically as broad absorption in low density environments or P Cygni profiles, blueshifted absorption followed by redshifted emission, in higher density environments (Leitherer et al. 1995). In the far UV, the most prominent stellar features are N V $\lambda\lambda 1238, 1242$, Si IV $\lambda\lambda 1393, 1402$, C IV $\lambda\lambda 1548, 1550$, and He II $\lambda 1640$. There is no evidence for He II $\lambda 1640$ emission in any of the composites, however, the S/N in that region is much lower due to limited spectral coverage and an uncertain continuum level. For the Si IV and C IV transitions, a combination of strong interstellar and photospheric absorption contribute to the line profiles, which can be difficult to differentiate. In the UV-bright LAE composite, we find evidence for O III] $\lambda 1664$ nebular emission, which is not detected in the UV-bright non-LAE composite. Due to low S/N and an uncertain continuum level, we do not attempt any further analysis. This result is qualitatively consistent with S03 who reported significantly stronger O III] $\lambda 1664$ emission in their highest Ly α equivalent width quartile relative to their lower three Ly α equivalent width quartiles. A number of weak stellar features are also visible in the UV-bright SFG composite, the strongest being C III $\lambda 1176$ absorption at a velocity offset of $\Delta v_{\text{em-abs}} = 380 \text{ km s}^{-1}$, which further confirms that Ly α is typically redshifted from the systemic redshift of SFGs at these redshifts by $\sim 400 \text{ km s}^{-1}$ in excellent agreement with Steidel et al. (2010).

The stellar wind component of the Si IV transition is only significant for blue giant and supergiant stars. In the UV-bright SFG composite, we observe extended absorption

that ranges from zero velocity offset to $\Delta v_{\text{em-abs}} = 1600 \text{ km s}^{-1}$ as well as redshifted emission characteristic of a P Cygni profile, consistent with high velocity stellar winds from massive stars. We observe a similar profile in the UV-bright LAE composite except with redshifted emission filling in the Si IV $\lambda 1402$ absorption. Although the UV-bright non-LAE composite shows weak redshifted emission, there does not appear to be significant broad absorption. Given the strength of Si IV $\lambda 1393$, the most significant difference between these two composites is the much lower amount of Si IV $\lambda 1402$ interstellar absorption in the UV-bright LAE composite. The shape and strength of these line profiles indicates the presence of a population of young blue giant and supergiant stars.

The stellar wind contribution to the C IV profile is most dependent on the presence of main-sequence, giant and supergiant O stars. We observe strong C IV $\lambda\lambda 1548, 1550$ absorption in the UV-bright non-LAE composite, though it is difficult to disentangle the stellar wind component from the interstellar absorption component. We find evidence for weak extended absorption in the UV-bright SFG and UV-bright non-LAE composites, but not in the UV-bright LAE composite. We also find significant redshifted emission in the UV-bright non-LAE composite. A P Cygni profile indicates the presence of $M \geq 30 M_{\odot}$ stars (Leitherer et al. 1995; Pettini et al. 2000). This emission is also seen in the UV-bright SFG composite.

In both the UV-bright LAE and UV-bright SFG composites, there is significant blueshifted absorption and redshifted emission in the N V line profile, characteristic of a P Cygni profile. We interpret the low velocity offset ($\Delta v_{\text{em-abs}} = 600 \text{ km s}^{-1}$) and large velocity FWHM (FWHM $\sim 1200 \text{ km s}^{-1}$) of N V absorption in the UV-bright LAE composite as evidence for stellar emission and absorption dominating the N V profile (see Fig. 1 in Groenewegen et al. 1989). Given the shape of the N V line profile in the UV-bright SFG composite, we interpret this as evidence for a significant amount of high-ionization absorption in the outflow as well as emission and absorption due to stellar features at the systemic redshift.

2.5.5 Si II* Emission Lines

An advantage of composite spectra is the ability to reveal weak features that are typically undetected in individual spectra. Among these features, the most prominent are the Si II*

fine structure emission lines at $\lambda 1265$, $\lambda 1309$, and $\lambda 1533$. These transitions have also been observed in $z \sim 3$ LBGs by S03 and $z \sim 4$ LBGs by Jones et al. (2012).

Table 2.4 Si II* Emission in UV Bright SFG Composite

λ_{rest} (\AA)	A_{ul} (10^8 s^{-1})	W_0 (\AA)	Δv (km s^{-1})
1264.74	23.0	0.6 ± 0.2	280
1309.28	7.00	0.0 ± 0.2	-
1533.43	7.40	0.7 ± 0.3	140

Note. — Properties of Si II* Emission in the UV-bright SFG composite. Einstein A -coefficients from the NIST Atomic Spectra Database (http://physics.nist.gov/cgi-bin/AtData/main_asd). The Si II* $\lambda 1309$ feature is not seen, so we do not report a Δv .

The close proximity of these lines to strong absorption features (Si II $\lambda 1260$, O I + Si II $\lambda 1303$, and Si II $\lambda 1526$) may attenuate the blue edges, biasing the centroids to the red. Our results for Si II* emission in the UV-bright SFG composite are presented in Table 2.4. In the UV-bright non-LAE composite, we observe significant Si II* $\lambda 1265$ emission yet we do not see the $\lambda 1309$ and $\lambda 1533$ transitions. For the $\lambda 1265$ emission, we measure an equivalent width of $W_0 = 0.5 \pm 0.2 \text{\AA}$ at a velocity offset of $\Delta v_{\text{em-abs}} = 300 \text{ km s}^{-1}$. We find slightly stronger Si II* $\lambda 1265$ in the UV-bright LAE composite with an equivalent width of $W_0 = 0.7 \pm 0.2 \text{\AA}$ at a velocity offset of $\Delta v_{\text{em-abs}} = 120 \text{ km s}^{-1}$. In this composite, the Si II* $\lambda 1265$ emission is double-peaked, which is likely due to only individual galaxies having Si II* emission at different velocity offsets. We observe $\lambda 1533$ emission at a much higher significance in the UV-bright LAE composite than the UV-bright non-LAE composite with an equivalent width of $W_0 = 1.2 \pm 0.4 \text{\AA}$ compared to $W_0 < 0.3 \text{\AA}$ at velocity offsets of $\Delta v_{\text{em-abs}} = 30 \text{ km s}^{-1}$ and $\Delta v_{\text{em-abs}} = 380 \text{ km s}^{-1}$ respectively. We do not find any evidence for $\lambda 1309$ emission in any of the composite spectra. In contrast, both S03 and Jones et al. (2012) observe Si II* $\lambda 1309$ emission in their composite spectra.

Si II* emission likely stems from photoionized regions around massive stars in the systemic component of the galaxy where electron densities are $N_e = 10^2 - 10^3 \text{ cm}^{-3}$ with temperatures of $T = 10^4 \text{ K}$. In this environment, the Si II and Si III relative abundances are determined from radiative recombinations for which the recombination rates are comparable to the collisional excitation rates (Shull & van Steenberg 1982). S03 find, through modeling

the LBG nebular emission lines with the CLOUDY96 software package, that all models that simultaneously match their O, C, and $H\beta$ line ratios overpredict the Si II emission-line strengths by more than an order of magnitude. This result leads them to conclude that the Si II emission lines cannot originate from H II regions. As we do not observe these other transitions, we are unable to comment on the plausibility of Si II* fine structure emission stemming from H II regions.

A different explanation for Si II* emission is that these lines originate instead from the outflowing component. In this scenario, each UV photon absorbed at a resonance transition ($\lambda = 1260, 1304, 1526$) or a fine-structure transition must be re-emitted through either a resonance or a fine-structure transition. In the absence of dust, the sum of the resonance and fine-structure emission should equal the amount of absorption. Our UV-bright non-LAE composite has significantly stronger resonance absorption than fine-structure emission while our UV-bright LAE composite shows a much larger ratio of fine-structure emission to resonant absorption. In contrast, S03 observe the fine-structure emission lines to be an order of magnitude weaker than the resonance lines. The discrepancy between the emission and absorption components could be due to the presence of dust extinguishing Si II photons during resonant scattering. Furthermore, we observe the Si II* fine-structure lines to have narrow velocity widths, whereas we would expect the emission to come from the full range of outflow velocities and to therefore be as broad as the $Ly\alpha$ emission line. For these reasons, we find it unlikely that the Si II fine-structure lines originate from the outflowing component.

2.6 Discussion

Combining the spectra of both continuum- and narrowband-selected galaxies has allowed us to study the average properties of $2 < z < 3.5$ SFGs. Among these properties, we are able to examine trends based on $Ly\alpha$ equivalent width, rest-frame UV color corrected for IGM extinction, redshift, and R band luminosity for each individual galaxy. Due to the complexities associated with selection effects, we do not attempt to draw any inferences from different R band luminosities. We have divided our sample based upon $Ly\alpha$ equivalent width for galaxies with $R < 25.5$ and will first examine trends associated with different amounts

of Ly α emission. Due to the faint nature of our objects' continua, we parameterize their observed colors in terms of their photometrically measured rest-UV spectral slope after correcting for IGM extinction and Ly α equivalent width, then divide our sample in half based on this parameter. Additionally, our spectroscopic sample divides evenly into two redshift bins ($2 < z < 2.7$, $2.7 < z < 3.5$) allowing us to look for any trends across this redshift interval. This allows us to study trends in spectroscopic properties in relation to spectral slope and redshift.

2.6.1 Selection Effects

As our subsamples of galaxies are determined on the basis of different selection criteria, it is important to identify any photometric or spectroscopic biases that may affect our analysis of the underlying galaxy populations. For continuum-selected galaxies, one of the most influential effects is the dependence of color selection criteria on luminosity and redshift due to Ly α forest absorption. Another major bias stems from the prevalence of spectroscopic redshifts determined solely from Ly α emission in conjunction to a minimum Ly α flux necessary for Ly α emission to be seen. For galaxies without distinct absorption lines, this causes spectroscopic identification of Ly α to be flux dependent.

The selection process for our continuum-selected objects creates two major biases that affect our resultant galaxy population. First of all, our continuum-selected LBGs were chosen to have $V-R < 1.2$ thereby targeting objects within a redshift range of $2.6 < z < 3.5$. However, the V band is extinguished by the Ly α forest making it redshift dependent. At $z = 2.5$, the amount of IGM extinction in the V band is $\Delta V = 0.0$ mag, while at $z = 3.5$, $\Delta V = 0.5$ mag. For this reason, the range of intrinsic colors of the continuum-selected population is a function of redshift. Secondly, the colors of continuum-selected galaxies is also a function of R band magnitude. The combination of requiring our targets to have very faint U band magnitudes ($(U - V)_{AB} > 1.2$) and U band images having a finite depth will indirectly restrict the range of V-R color to bluer colors at fainter luminosities.

Spectroscopic success rate is not only dependent on apparent magnitude, but also on the fact that it is easier to measure a redshift from an emission line rather than an absorption line. Our spectroscopic incompleteness as a function of R band magnitude is plotted in Fig

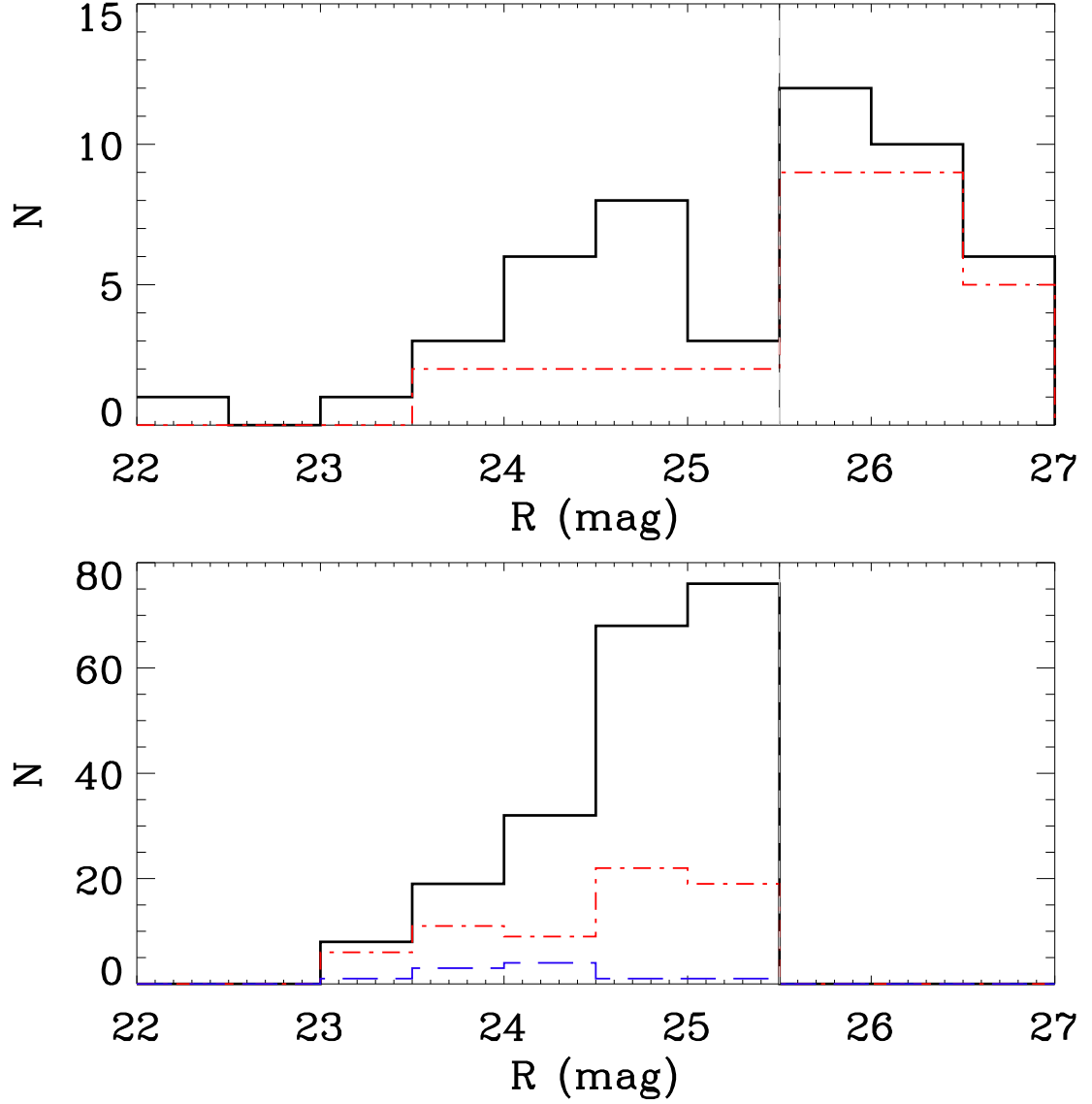


Figure 2.6 Spectroscopic incompleteness as a function of R band magnitude and spectral type is plotted for the entire catalog. Top panel - the black solid histogram indicates the total number of narrowband-selected objects targeted spectroscopically and the red dot dashed line shows the number that were spectroscopically confirmed. Bottom panel - the black solid histogram indicates the total number of broadband-selected objects targeted spectroscopically, the red dot dashed line shows the number that were spectroscopically confirmed, and the blue dashed line shows the number that were spectroscopically confirmed galaxies without $\text{Ly}\alpha$ in emission. Our spectroscopic confirmation rate is 33% for broadband-selected objects and 60% for narrowband-selected objects. The vertical dashed line represents the canonical $R \leq 25.5$ cut for broadband-selected galaxies.

2.6 for narrowband-selected objects (top panel) and broadband-selected objects (bottom panel). In each panel, the black line indicates the total number of objects observed spectroscopically and the red dot dashed line shows the number of spectroscopically confirmed galaxies. The blue dashed line shows the number of spectroscopically confirmed galaxies without Ly α emission. Our confirmation rates are 63% for narrowband-selected objects and 33% for broadband-selected objects. Only 5% of broadband-selected objects have redshifts determined solely from absorption lines. Due to the low S/N of our individual spectra, we found it difficult to robustly measure redshifts for galaxies without Ly α emission. Galaxies without Ly α emission line redshifts likely have Ly α equivalent widths below a certain threshold as a function of luminosity. We assume this to be consistent with no Ly α emission. Steidel et al. (2000) find that roughly half of their $z \sim 3$ spectroscopically-confirmed LBGs show Ly α in absorption. Assuming a similar distribution among our broadband-selected objects, this would imply a spectroscopic confirmation rate of 56%.

2.6.2 Individual Galaxy Ly α Profiles

Laursen et al. (2011) used cosmological hydrosimulations to examine the effect of the IGM on the Ly α line profile escaping high-redshift, star-forming galaxies. Their findings qualitatively agree on the shape and strength of the redshifted Ly α emission line, however, they predict more blueshifted emission than has typically been observed for high-redshift SFGs. At a redshift of $z = 3.5$, they find the effect of the IGM is insufficient to explain the lack of a blueshifted Ly α emission line. For our sample of 12 multiple-peaked Ly α emission line galaxies, we find a mean velocity offset of $\langle \Delta v_{\text{red-blue}} \rangle = 660 \pm 229 \text{ km s}^{-1}$. This measurement is in good agreement with Kulas et al. (2011) who found a mean velocity offset of $\langle \Delta v_{\text{red-blue}} \rangle = 741 \pm 39 \text{ km s}^{-1}$ (errors represent the standard deviation of the mean). However, we do find a larger range of velocity offsets than Kulas et al. (2011) from $\Delta v_{\text{red-blue}} = 330 \text{ km s}^{-1}$ to $\Delta v_{\text{red-blue}} = 1080 \text{ km s}^{-1}$. We note that this result is consistent with Steidel et al. (2010) who found a broad range of Ly α emission line velocity offsets ($\Delta v = +485 \pm 175 \text{ km s}^{-1}$) with respect to the systemic redshift. This distribution is also comparable to the observed velocity offset between Ly α emission and interstellar absorption seen in individual spectra (Fig. 2.1).

Among the spectroscopic sample, there is a broad distribution of Ly α line strengths and profile types, which fall into four categories: emission only, absorption only, both emission and absorption, and neither emission nor absorption. Out of the continuum-selected galaxies in our composites, we find 45% have Ly α emission lines strong enough to be classified as LAEs ($W_{\text{Ly}\alpha} > 20\text{\AA}$) while only 10% show Ly α only in absorption. This fraction of UV-bright LAEs is roughly a factor of two larger than the 20–25% that S03 report for their $z \sim 3$ LBGs. However, due to the poor S/N of our data, it was difficult to determine redshifts for LBGs without Ly α in emission and we remove any galaxies lacking precise redshifts. Removing all galaxies without Ly α emission, our fraction of LBGs that would be classified as LAEs rises to 50% and the fraction of LBG-LAEs from Steidel et al. (2000) increases to $\sim 40\%$. Excluding LBGs with Ly α in absorption, we report a median Ly α equivalent width of $W_{\text{Ly}\alpha} = 20.0\text{\AA}$. Similarly, two of our $R < 25.5$ narrowband-selected objects did not yield spectroscopic Ly α equivalent widths high enough to be classified as LAEs and were included in the UV-bright non-LAE stack. We find that 24% of our continuum-selected galaxies have both Ly α in emission and absorption. For these objects, we use their emission line equivalent widths in our analysis.

2.6.3 Composite Ly α Dependences

Through dividing our bright galaxies ($R < 25.5$) into a UV-bright non-LAE and a UV-bright LAE composite, we can look for trends based on Ly α equivalent width. The clearest trend across these two composites is stronger interstellar absorption with decreasing Ly α emission. The top panel of Figure 2.8 shows the highest Ly α equivalent width quartile of S03 (top, red; $W_{\text{Ly}\alpha} = 52.63\text{\AA}$) and the UV-bright LAE composite (bottom, black; $W_{\text{Ly}\alpha} = 50.0\text{\AA}$) while the bottom one shows the second highest Ly α equivalent width quartile of S03 (top, red; $W_{\text{Ly}\alpha} = 11.00\text{\AA}$) and the UV-bright non-LAE composite (bottom, black; $W_{\text{Ly}\alpha} = 8.4\text{\AA}$). Across these two pairs of composite spectra, there are many interesting differences including Si II* emission, low- and high-ionization absorption strength, UV spectral slope, and velocity offset. In both the UV-bright LAE and UV-bright non-LAE composites, we find stronger Si II* emission at $\lambda 1265$ and weaker Si II* emission at $\lambda 1309$ than the $W_{\text{Ly}\alpha} = 52.63\text{\AA}$ and $W_{\text{Ly}\alpha} = 11.00\text{\AA}$ composites of S03. Furthermore, for both our composite spectra and that

of S03, Si II* emission becomes stronger with increasing Ly α emission.

Due to poor S/N in the $\lambda > 1600\text{\AA}$ continuum, we only use the bluest low-ionization absorption lines ($\lambda 1260, \lambda 1303, \lambda 1334, \lambda 1527$) in determining the average low-ionization line equivalent widths. Figure 2.7 shows the dependences of various spectroscopic features on Ly α equivalent width. As can be seen in the top left panel of Figure 2.7, the average low-ionization equivalent width decreases from $W_{LIS} = -1.8\text{\AA}$ to $W_{LIS} = -1.25\text{\AA}$ for a change in Ly α equivalent width of $W_0 = 8.4\text{\AA}$ to $W_0 = 50.0\text{\AA}$. We find a similar trend in low-ionization absorption strength with respect to Ly α equivalent width as S03. Note that the average low-ionization equivalent widths for the four S03 quartiles are different from figure 9 of S03 as we do not include the Fe II $\lambda 1608$ and the Al II $\lambda 1670$ transitions in our measurement. For the same set of transitions, we find systematically stronger low-ionization absorption at a given Ly α equivalent width. In the UV-bright LAE composite, the Si II $\lambda 1526$ transition is only marginally detected, which differs from the highest Ly α equivalent width quartile in S03. The degree of saturation of Si II can be measured from the ratio of Si II $\lambda 1260$ to Si II $\lambda 1526$, which is optically thin for $W_0(1260)/W_0(1526) > 5$. The ratio of Si II absorption line equivalent widths is $W_0(1260)/W_0(1526) = 0.8 \pm 0.2$, consistent with unity in the UV-bright non-LAE composite while it is $W_0(1260)/W_0(1526) = 2.4 \pm 1.5$ in the UV-bright LAE composite. While this may indicate that Si II is not optically thick in the UV-bright LAE composite, the faint nature of both transitions makes this ratio uncertain. With increasing Ly α equivalent width, we observe an average decrease of $> 50\%$ in the strength of the Si II $\lambda \lambda 1260, 1526$ and O I + Si II $\lambda 1303$ absorption. However, we note that the strength of C II $\lambda 1334$ instead increases by 20% with larger Ly α equivalent width.

Robustly determining Si IV equivalent widths is challenging given the uncertainty in the continuum level, which is affected by broad stellar absorption as well as redshifted emission. In the top right panel of Figure 2.7, Si IV $\lambda \lambda 1393, 1402$ equivalent widths are plotted for this work (red diamonds) and S03 (black points). The UV-bright LAE Si IV $\lambda 1402$ equivalent width measurement is likely being filled in by redshifted emission, and the $\lambda 1393$ transition is the same strength as in the UV-bright non-LAE composite. For this reason, we find no significant change in Si IV equivalent widths and conclude that the transition is consistent with being optically thin, which for Si IV corresponds to a doublet ratio of

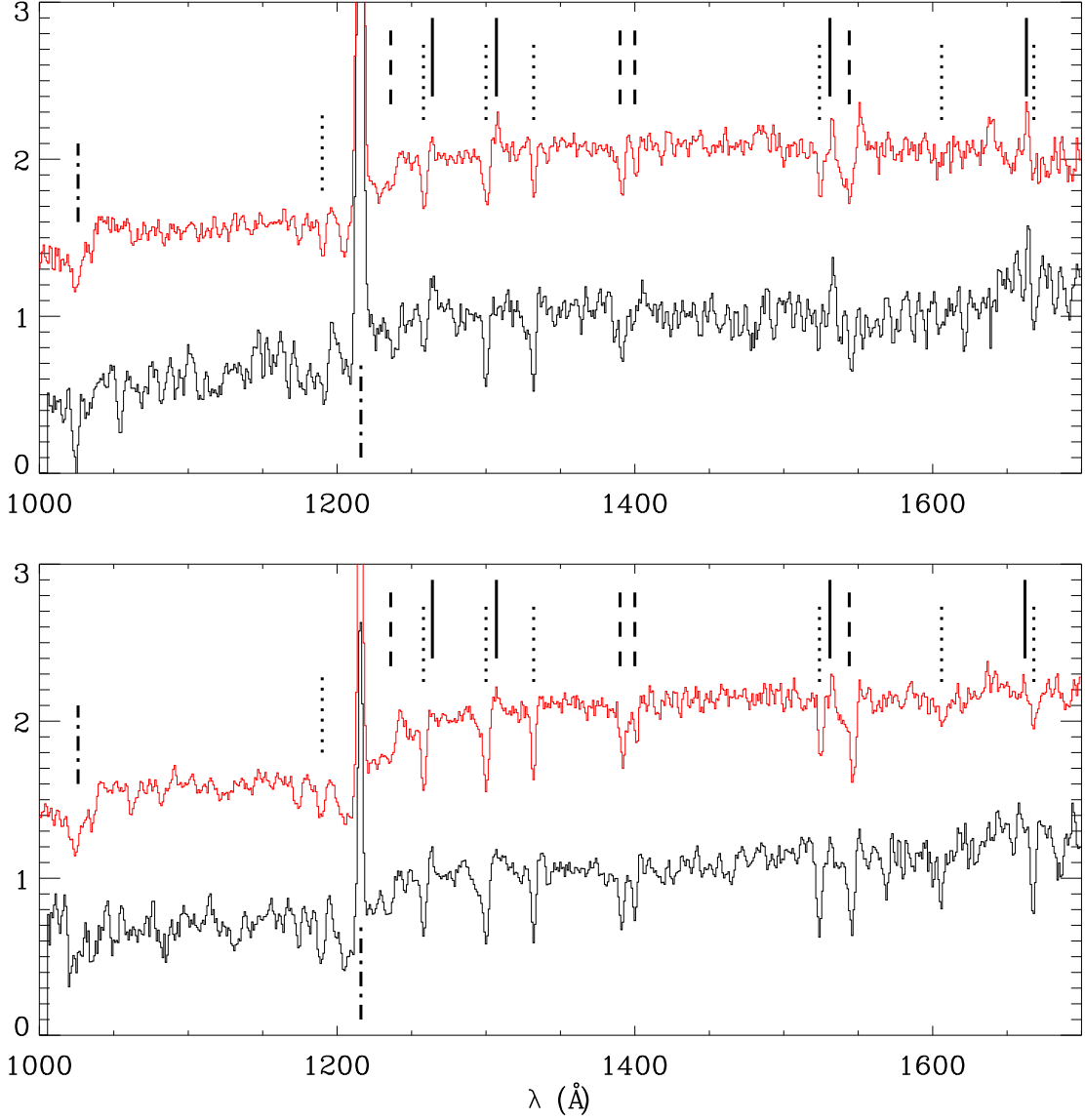


Figure 2.7 Top - the highest $\text{Ly}\alpha$ equivalent width quartile composite ($W_{\text{Ly}\alpha} = 52.63\text{\AA}$) from S03 in red and the UV-bright LAE composite ($W_{\text{Ly}\alpha} = 50.0\text{\AA}$) in black. Bottom - the second highest $\text{Ly}\alpha$ equivalent width quartile composite ($W_{\text{Ly}\alpha} = 11.00\text{\AA}$) from S03 in red and the UV-bright non-LAE composite ($W_{\text{Ly}\alpha} = 8.4\text{\AA}$) in black. Our composite spectra show similar trends in both interstellar absorption and Si II* emission as those of S03. In the top panel, S03 find stronger Si II* $\lambda 1309$ emission, weaker Si IV $\lambda 1402$ nebular emission, and a more prominent C IV $\lambda\lambda 1548, 1550$ profile. Note that the average low-ionization equivalent widths for the four S03 quartiles are different from figure 9 of S03 as we do not include the Fe II $\lambda 1608$ and the Al II $\lambda 1670$ transitions in our measurement.

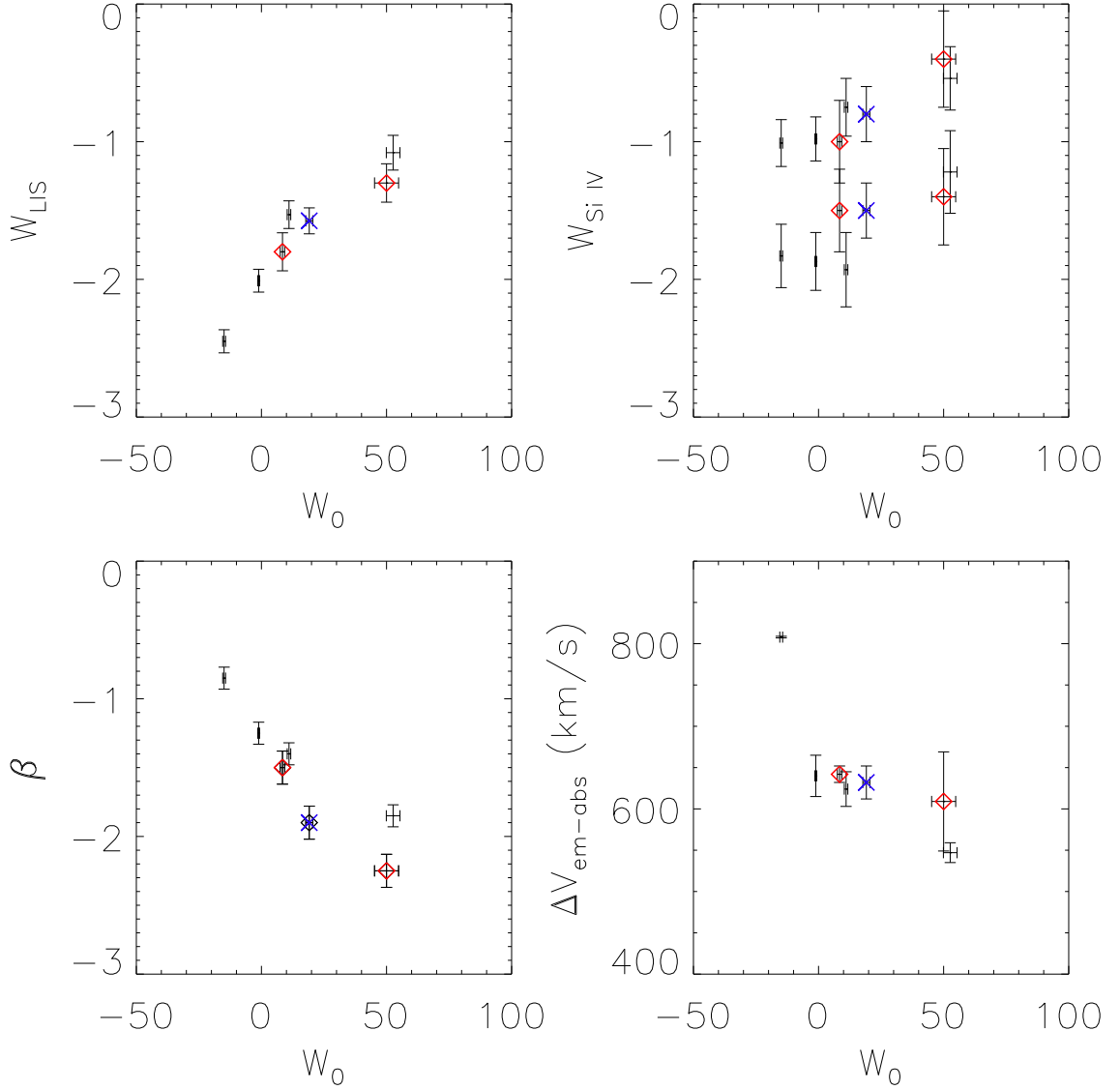


Figure 2.8 Dependences of UV spectroscopic properties on Ly α equivalent width for the UV-bright non-LAE and UV-bright LAE subsamples as red diamonds, the UV-bright SFG composite in blue and the four Ly α equivalent width quartiles from S03 in black. Top left - average low-ionization equivalent widths (Si II λ 1260, O I + Si II $\lambda\lambda$ 1302,1304, C II λ 1334, Si II λ 1526). Top right - Si IV equivalent widths. Bottom left - spectral slope, β , as measured from the composite spectra. The error bars for our β values reflect the error in spectral slope index and do not take into account the uncertainty in the artificial flux calibration of the VIMOS spectra. Bottom right - velocity offset $\Delta v_{\text{em-abs}}$. The errors in velocity offset represent the range of velocity offsets for different low-ionization lines. The trends in spectroscopic properties with increasing Ly α emission originally observed by S03 are confirmed for our smaller sample of SFGs spanning a larger range in redshift.

$W_{1393}/W_{1402} = 2$. Furthermore, we do observe a significantly smaller C IV absorption strength in the UV-bright LAE composite $W_{CIV} = -1.1 \pm 0.35$ than the UV-bright non-LAE composite $W_{CIV} = -2.2 \pm 0.4$, corresponding to a decrease of $\sim 100\%$. S03 reported finding 50% weaker high-ionization equivalent widths (Si IV and C IV) in their highest Ly α equivalent width quartile $W_{Ly\alpha} = 52.63$ with respect to their other three quartiles. However, they only find a decrease of $\sim 30\%$ in C IV equivalent widths. Due to the increase in C II equivalent width with increasing Ly α equivalent width, this may indicate that the neutral gas has a larger covering fraction than the ionized gas, which likely has a larger range of velocity offsets.

As can be seen in the lower left panel of Figure 2.8, for increasing Ly α equivalent width, the UV continuum slopes of the composite spectra become bluer. We do note that the spectral slopes of the VIMOS spectra were scaled so that their average spectral slope matched that of the FORS spectra. By fitting a power law to the 1250 – 1600Å region of the composite spectra, we find a UV spectral slope ($F_\lambda \propto \lambda^\beta$) of $\beta = -2.25$ and $\beta = -1.50$ for Ly α equivalent widths of $W_0 = 50.0\text{\AA}$ and $W_0 = 8.4\text{\AA}$. S03 also find a bluer continuum slope for galaxies with stronger Ly α emission. Similarly, we find a UV spectral slope of $\beta = -1.85$ and $\beta = -1.40$ for the highest and second highest Ly α equivalent width quartiles from S03 respectively. The bottom left panel of Figure 2.8 shows the relation between spectral slope index and Ly α equivalent width. Although we find the same trend of bluer continuum slopes with increasing Ly α equivalent width, we do find systematically bluer continuum slopes than S03, which may be impacted by the VIMOS flux calibration. Using photometrically determined β values, we find a mean spectral slope among individual galaxies of $\langle \beta \rangle = -1.52 \pm 0.45$ and $\langle \beta \rangle = -1.22 \pm 0.47$ for the UV-bright LAE and non-LAE composites.

Across the UV-bright non-LAE and UV-bright LAE composites, we measure the average velocity offset between low-ionization absorption and Ly α emission to remain constant from $\Delta v_{\text{em-abs}} = 640 \pm 10 \text{ km s}^{-1}$ to $\Delta v_{\text{em-abs}} = 610 \pm 60 \text{ km s}^{-1}$ with increasing Ly α equivalent width. As is shown in the bottom right panel of Figure 2.8, our measurements are plotted as red diamonds while those of S03 are in black. Our results are also consistent with S03, who found velocity offset to decrease monotonically with increasing Ly α equivalent width.

We do note finding consistently higher velocity offsets than S03 at each Ly α equivalent width. Steidel et al. (2010) found a median velocity offset of $\Delta v_{\text{em-abs}} = 609 \text{ km s}^{-1}$ with a scatter of 32 km s^{-1} for their sample of 89 $z \sim 2.3$ SFGs. With the exception of baryonic and dynamical mass, they report not finding any significant correlations between velocity offset and other galaxy parameters.

2.6.4 Intrinsic UV Color Dependences

The spectral slope of the far-UV continuum is determined by the star formation rate history and the amount of extinction. A continuously star-forming galaxy has an unreddened UV spectral energy distribution shape that remains fairly constant for ages 10Myr to 1Gyr whose spectral slope, β , ranges from -2.6 to -2.1 (Leitherer et al. 1999). UV-bright, $2 < z < 3.5$, star-forming galaxies typically have ages within this range (Papovich et al. 2001; Shapley et al. 2001; Erb et al. 2006d; Gawiser et al. 2007; Kornei et al. 2010) indicating that large differences in UV spectral slope reflect varying amounts of dust extinction. Due to uncertainties in the star formation histories and the form of the dust extinction law, we report trends based on the spectral slope index. Continuum spectral slopes are too difficult to measure in individual spectra, however, broadband photometry allows us to parameterize our data set based on spectral slopes as calculated from intrinsic UV colors.

Figure 2.9 displays two composite spectra composed of the red ($\beta > -1.4$) and blue ($\beta \leq -1.4$) half of our UV-bright galaxies. Through fitting a power law to the observed photometric colors, we find spectral slopes of $\langle \beta \rangle = -1.05 \pm 0.34$ and $\langle \beta \rangle = -1.73 \pm 0.34$ for the red and blue composites respectively where the errors represent the standard deviation. Since the spectral slopes of the VIMOS spectra were scaled so that their average spectral slope matched that of the FORS spectra, we use the photometric β values when examining the relationship among galaxy properties and spectral slope. Figure 2.10 shows the dependence of Ly α equivalent width on β (left panel) and the dependence of average low-ionization equivalent width on β (right panel) for this work (red diamonds) and S03 (black points). With bluer spectral slope, Ly α equivalent width increases from $W_0 = 11.0 \pm 1.1 \text{ \AA}$ to $W_0 = 27.0 \pm 1.8 \text{ \AA}$. Similarly, the average low-ionization absorption line strength decreases from $W_{\text{LIS}} = -1.83 \text{ \AA}$ to $W_{\text{LIS}} = -1.35 \text{ \AA}$. We note that similar to

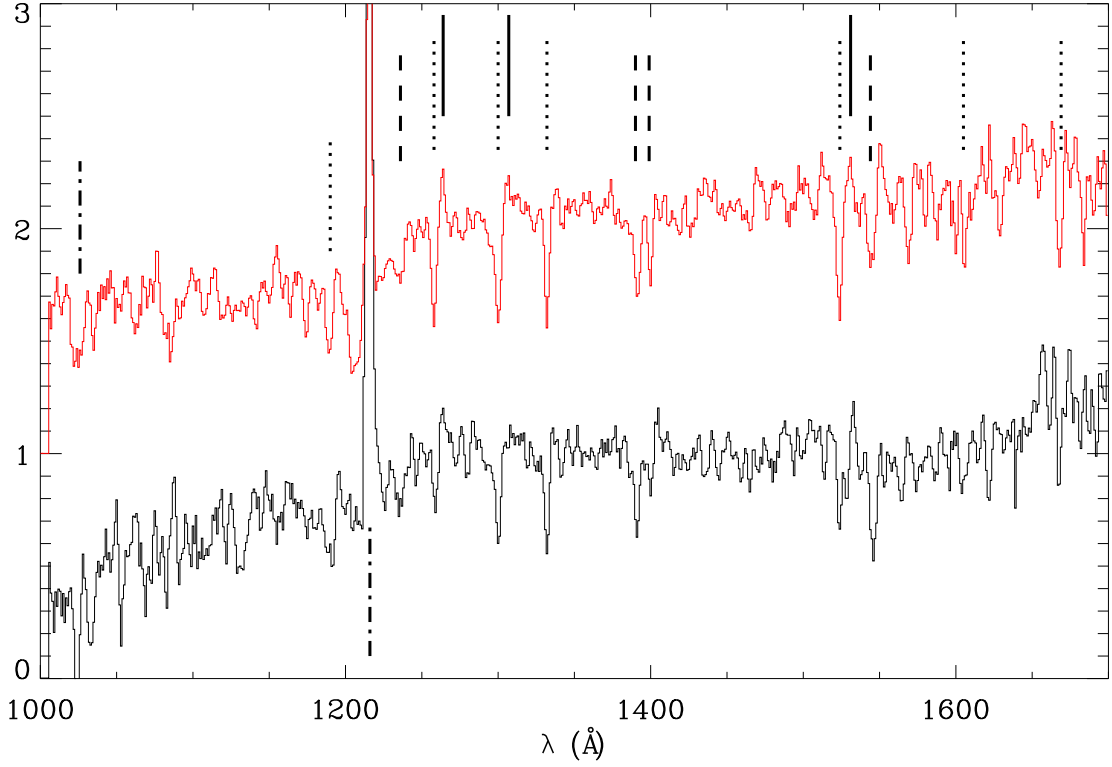


Figure 2.9 Composite spectra of SFGs divided into two subsamples based on intrinsic UV spectral slopes as calculated from photometric colors. Top - the red UV continuum slope composite ($\beta_{phot} > -1.4$). Bottom - the blue continuum slope composite ($\beta_{phot} \leq -1.4$). With bluer spectral slope, Ly α emission increases, low-ionization absorption become weaker and there is significantly stronger Si IV $\lambda 1402$ nebular emission.

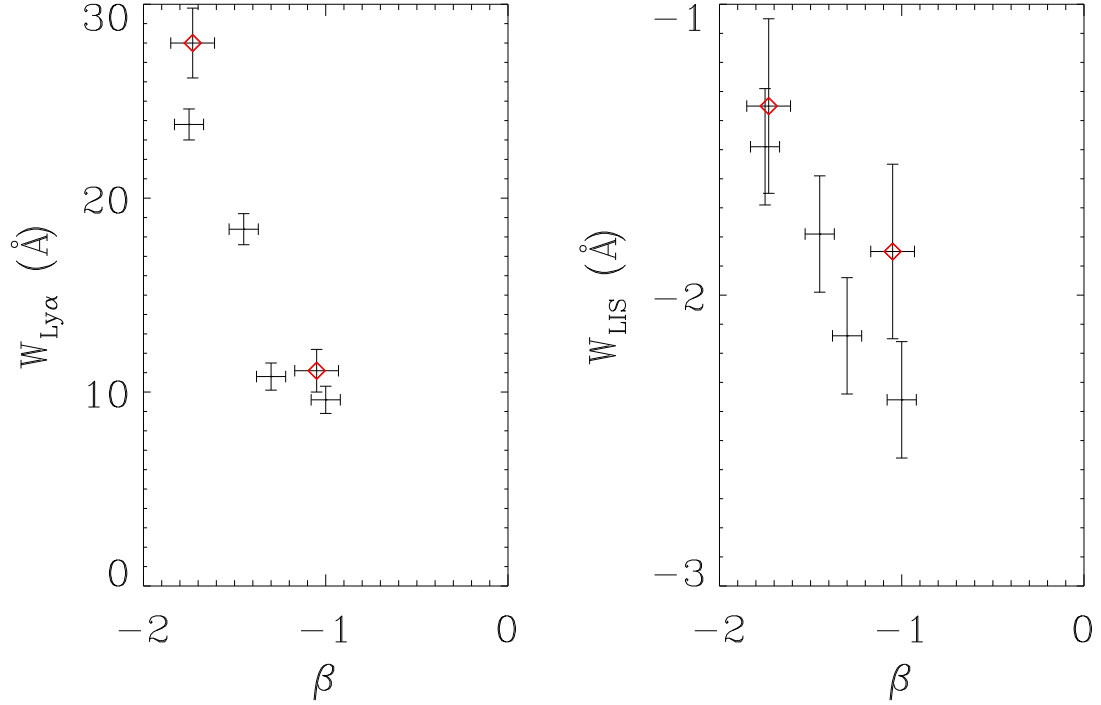


Figure 2.10 Left - the dependence of Ly α equivalent width on spectral slope, β , when the dataset is subdivided based on spectral slope for this work (red diamonds) and S03 (black points). Right - the dependence of low-ionization absorption on spectral slope. The trends in decreasing Ly α emission and increasing low-ionization absorption for bluer spectral slopes observed by S03 are confirmed.

the UV-bright LAE and non-LAE composites, while Si II absorption decreases significantly with bluer slopes, C II absorption does not. Additionally, the change in Ly α equivalent width is not sufficient to fully explain this decrease in low-ionization absorption strength, and therefore a correlation must exist between spectral slope and low-ionization absorption. In contrast to the UV-bright LAE composite, the ratio of Si II absorption line equivalent widths is $W_0(1260)/W_0(1526) = 1.0 \pm 0.5$ and $W_0(1260)/W_0(1526) = 0.8 \pm 0.2$ in the blue and red composites respectively, both consistent with unity. A ratio of unity indicates that Si II is optically thick, suggesting this is the case in both composites.

The Si IV $\lambda 1393$ and C IV $\lambda 1549$ high-ionization line strengths do not vary substantially with spectral slope. With bluer spectral slope, the Si IV $\lambda 1402$ absorption line strength decreases by $\sim 50\%$ due to P Cygni emission filling in the absorption. Moreover, relative to the red composite, the N V P Cygni profiles are more prominent. The N V $\lambda 1240$

Table 2.5 Spectroscopic Properties of $z \sim 2$ and $z \sim 3$ UV Bright Composites

	$z \sim 2$ non-LAE	$z \sim 3$ non-LAE	$z \sim 2$ LAE	$z \sim 3$ LAE	$z \sim 2$ SFG	$z \sim 3$ SFG
N_{gal}	16	11	12	20	28	31
R	24.55	24.36	24.69	24.94	24.62	24.85
β_{phot}	-1.3	-1.2	-1.7	-1.4	-1.4	-1.2
Δv_{em-abs}	640	740	600	590	630	660
$W_{Ly\alpha_r}$	8.2 ± 0.7	10.6 ± 1.4	29.5 ± 5.5	66.5 ± 6	12.3 ± 0.8	52.3 ± 3.5
$W_{Ly\alpha_b}$	-4.1 ± 0.5	-5.0 ± 1.5	1.8 ± 1.3	-	-3.9 ± 0.9	-
$W_{SiII,1193}$	-2.2 ± 0.4	-1.6 ± 0.6	-	-	-2.8 ± 0.4	-
$W_{SiII,1260}$	-1.3 ± 0.2	-2.0 ± 0.25	-1.2 ± 0.4	-	-1.3 ± 0.15	-1.2 ± 0.25
$W_{OI+SiII,1303}$	-2.6 ± 0.3	-2.0 ± 0.3	-2.2 ± 0.4	-0.8 ± 0.5	-2.3 ± 0.2	-1.1 ± 0.3
$W_{CII,1334}$	-1.5 ± 0.25	-1.6 ± 0.25	-2.3 ± 0.5	-	-1.7 ± 0.2	-1.3 ± 0.3
$W_{SiII,1526}$	-1.7 ± 0.4	-2.0 ± 0.4	-0.6 ± 0.5	-	-1.3 ± 0.25	-1.0 ± 0.3
$W_{NV,1240}$	-1.1 ± 0.5	-	-1.0 ± 0.3	-0.8 ± 0.4	-1.0 ± 0.25	-
$W_{SiIV,1393}$	-1.4 ± 0.35	-1.5 ± 0.45	-1.6 ± 0.5	-	-1.7 ± 0.25	-1.5 ± 0.35
$W_{SiIV,1402}$	-0.9 ± 0.35	-1.5 ± 0.45	-0.4 ± 0.5	-	-0.9 ± 0.25	-0.7 ± 0.35
$W_{CIV,1549}$	-2.1 ± 0.4	-3.4 ± 0.45	-1.5 ± 0.6	-0.9 ± 0.5	-1.8 ± 0.3	-2.0 ± 0.3

absorption equivalent width is $W_0 = 0.8 \pm 0.3$ with a large velocity offset, $\Delta v > 1200$ km s⁻¹. Nebular features originate from H II regions at the systemic redshift and indicate a larger presence of high mass O- and B-type stars. On the other hand, we do not find a C IV $\lambda 1549$ P Cygni profile in the blue spectral slope composite while we do observe one in the red one. Finally, there is no significant change in Si II* emission strength with spectral slope, in spite of a difference in Ly α equivalent width.

2.6.5 Redshift Evolution

There are roughly the same number of UV-bright LAEs and UV-bright non-LAE objects at $z \sim 2$ and $z \sim 3$, allowing us to divide our sample based on redshift and Ly α emission, generating four composite spectra. The low-redshift sample ($2 < z < 2.7$) is composed almost entirely of FORS objects while the high-redshift sample ($2.7 < z < 3.5$) is mostly VIMOS objects. In Figure 2.11, the top panel shows the two UV-bright LAE composites for $z \sim 2$ (red, upper) and $z \sim 3$ (black, lower). The bottom panel is the same as the top panel except for the UV-bright non-LAE composites. In this figure, the Ly α dependences discussed in Section 2.6.3 are also apparent. These trends are observed at both redshifts, as the two UV-bright LAE composites show significantly stronger low-ionization absorption. The S/N of the low-redshift composites degrades quickly blueward of Ly α due to poor atmospheric transmission and low throughput of the spectrograph below 3600Å. We present equivalent widths, velocity offsets and continuum spectral slopes for these composites as well as a $z \sim 3$ all-LBG and $z \sim 2$ all-BX composites in Table 2.5.

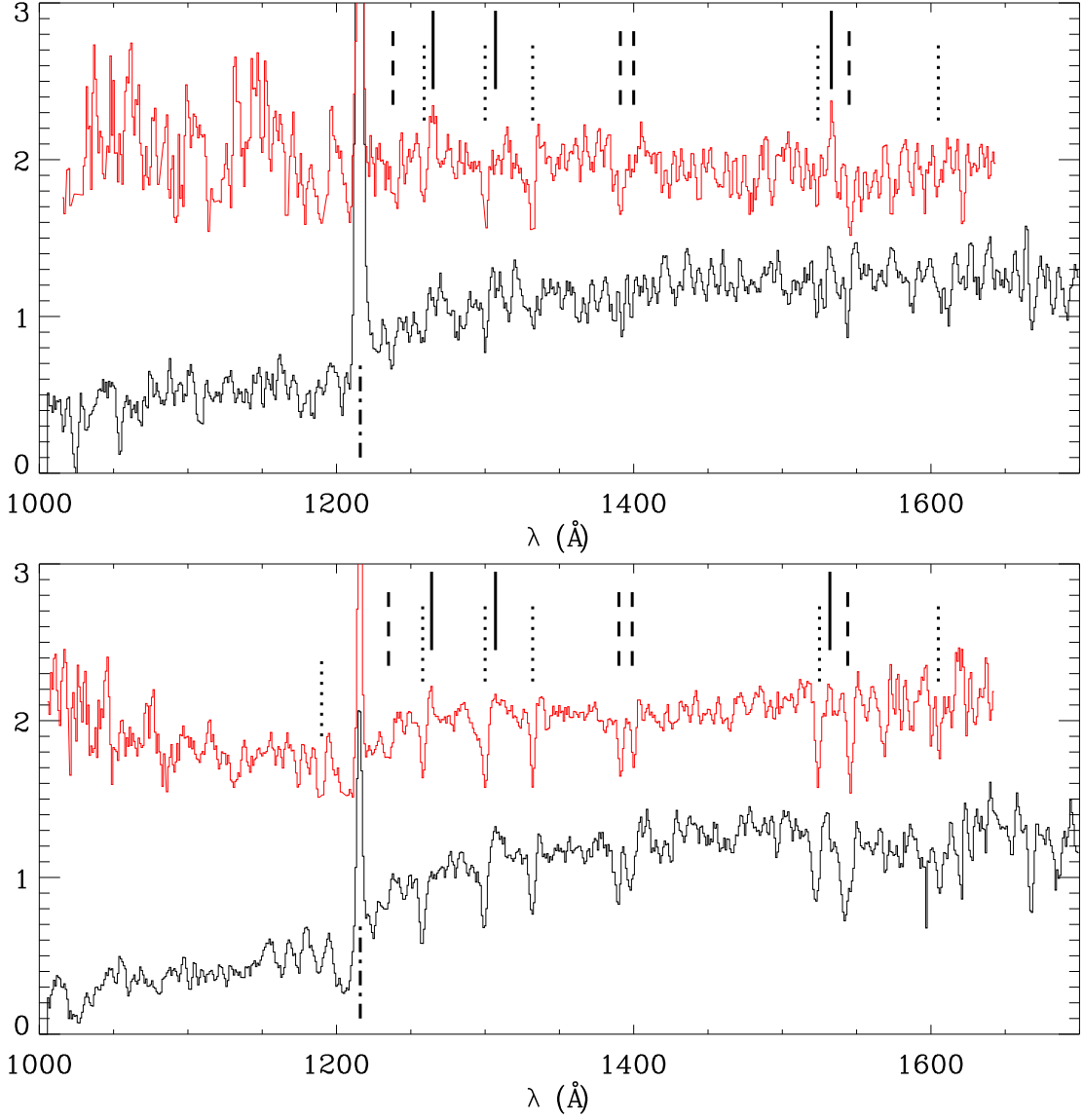


Figure 2.11 Composite spectra of UV-bright LAEs and UV-bright non-LAE objects for $2.0 < z < 2.7$ BXs in red and $2.7 < z < 3.5$ LBGs in black. Top - a composite of 13 BX-LAEs is plotted in red above a composite of 21 LBG-LAEs in black. For our sample of galaxies, few features are seen in the $z \sim 3$ composite, however we do see a decrease in Ly α emission with redshift. In spite of the low S/N of the BX-LAE composite, the relative strength of Si II* $\lambda\lambda$ 1265, 1533 emission to resonant Si II absorption is significantly higher than any other composite. Bottom - the BX-only composite composed of 15 BXs is plotted in red above the LBG-only composite consisting of 11 LBGs in black. These composite spectra are quite similar and show no significant evolution of spectroscopic properties across this redshift interval.

For UV-bright LAEs, there are several interesting trends with decreasing redshift, including weaker Ly α emission, stronger interstellar absorption, stronger Si II* emission, and bluer spectral slopes. The change in Ly α emission line strength is the clearest trend, as from $z \sim 3$ to $z \sim 2$, the Ly α equivalent width decreases from $W_0 = 66.5 \pm 6.0 \text{ \AA}$ to $W_0 = 29.5 \pm 5.5 \text{ \AA}$. We find interpreting this result difficult as there are a multitude of effects that contribute to the strength of the Ly α emission line. However, Nilsson et al. (2009) and Guaita et al. (2010) both find LAEs at $z \sim 2$ to appear more evolved than those at $z \sim 3$, although they do find comparable photometric Ly α equivalent widths. Aside from Ly α emission, very few features are seen in the $z \sim 3$ UV-bright LAE composite, which may be due to the faint continua of $z \sim 3$ UV-bright LAEs resulting in a low S/N. For this reason, it is difficult to determine if the differences between these two composites reflects an evolution in galaxy properties. In the $z \sim 2$ composite, the weak absorption strength of the Si II resonant lines are again apparent as the $\lambda 1260$ transition is faint and there is no $\lambda 1526$ absorption. In contrast, we do find evidence for Si II* fine-structure emission at $\lambda\lambda 1265, 1533$, but again we do not see Si II* $\lambda 1309$ emission. We also note that the relative strength of Si II* emission with respect to Si II resonant absorption is significantly higher in our low-redshift UV-bright LAE composite than either the high-redshift UV-bright LAE composite or the high-Ly α equivalent width quartile composite of S03, which was also composed of $z \sim 3$ galaxies.

In the UV-bright non-LAE composites, we find little evolution in galaxy properties from $z \sim 3$ to $z \sim 2$ with the exception of stronger high-ionization absorption at higher redshifts. The high-ionization interstellar absorption strengths are on average $\sim 50\%$ stronger in the high-redshift subsample. However, we note that the $z \sim 3$ subsample is dominated by VIMOS LBGs with a larger instrument FWHM. As can be seen in Table 2.5, we find comparable Ly α equivalent widths, low-ionization equivalent widths, and velocity offsets. Therefore, this discrepancy may not reflect an actual evolution in high-ionization strength. Furthermore, there is Si II* emission at $\lambda 1265$ of the $z \sim 2$ composite, although we find no other evidence for Si II* fine-structure emission at either redshift. Thus, the relative strength of Si II* emission for SFGs appears to be stronger at $z \sim 2$ than $z \sim 3$. As was previously seen in the UV-bright LAE and UV-bright non-LAE composites, Si II* emission

is stronger with stronger Ly α emission.

As discussed in § 2.3, the spectral slopes of individual galaxies were measured based on their photometric colors for which we found bluer spectral slopes at lower redshift. This trend is marginally significant among the UV-bright non-LAE and LAE subsets. We find bluer mean spectral slopes of $\beta_{LBG-only} = -0.97 \pm 0.58$ to $\beta_{BX-only} = -1.39 \pm 0.24$ for UV-bright non-LAE galaxies and $\beta_{LBG-LAE} = -1.34 \pm 0.33$ to $\beta_{BX-LAE} = -1.87 \pm 0.51$ for UV-bright LAE galaxies (errors represent the standard deviation of the mean). The errors due to photometric uncertainties are comparable to the standard deviation of the mean. We do not attempt to measure the spectral slope from the continuum of the composite spectra as all of our high-redshift subsamples are composed almost entirely of VIMOS objects whose individual spectra were scaled to match the FORS spectra. Bluer spectral slopes at lower redshifts would indicate that UV-bright non-LAE galaxies and UV-bright LAEs are becoming less evolved or less dusty with cosmic time. While this trend of bluer spectral slopes with decreasing redshift is both surprising and interesting, more observations will be necessary to understand if it is real. Finally at each redshift, we also find bluer spectral slopes with stronger Ly α emission indicating a connection between line and continuum extinction at both redshifts.

2.7 Conclusions

We have combined and analyzed the spectra of both narrowband- and continuum-selected star-forming galaxies across a redshift range of $2 < z < 3.5$. Through placing a canonical flux limit of $R < 25.5$, we are able to study the relationship among Ly α emission, intrinsic UV spectral slope, redshift, outflow kinematics, low- and high-ionization absorption, and nebular emission for a sample of galaxies spanning a similar luminosity range. Our results are summarized below.

- UV-bright SFGs have spectral slope indices, β , that span a large range from -2.7 to 0.1 while UV-bright LAEs ($W_{Ly\alpha} > 20\text{\AA}$) have bluer spectral slope indices with $-2.7 < \beta < -0.8$. Of the 59 $R < 25.5$ SFGs, 10 have Si II* emission and 12 have multiple-peaked Ly α emission.

- UV-bright LAEs with rest-frame $W_{\text{Ly}\alpha} > 20\text{\AA}$ have weaker low-ionization absorption, weaker C IV absorption, bluer spectral slopes, and stronger Si II* fine-structure emission than UV-bright non-LAE galaxies with rest-frame $W_{\text{Ly}\alpha} < 20\text{\AA}$. Among low- and high-ionization absorption strengths, individual elements also show different dependences on Ly α emission.
- SFGs with bluer spectral slopes have more prominent N V $\lambda\lambda$ 1238,1242 and Si IV λ 1402 P Cygni profiles, weaker low-ionization absorption, and stronger Ly α emission.
- From $2.7 < z < 3.5$ to $2.0 < z < 2.7$, SFGs exhibit bluer spectral slopes and stronger Si II* fine-structure emission. Additionally, those with rest-frame $W_{\text{Ly}\alpha} < 20\text{\AA}$ have comparable low- and high-ionization absorption strengths as well as similar Ly α emission strengths. In contrast, there is a significant decrease in Ly α emission strength in the subsample with rest-frame $W_{\text{Ly}\alpha} > 20\text{\AA}$, but we caution this may be due to selection effects.

The observed trends with Ly α emission are largely consistent with the physical picture put forth by S03 where the mechanical energy from star formation and supernovae in high-redshift UV-bright SFGs is powering galaxy-scale outflows of ionized and neutral gas. Evidence for these outflows is seen as strong blueshifted absorption as well as redshifted H I Ly α emission relative to nebular features at the systemic redshift. Amongst the individual galaxies, a wide range of velocity offsets between Ly α emission and interstellar absorption from $\Delta v_{\text{em-abs}} \sim 200 \text{ km s}^{-1}$ to $\Delta v_{\text{em-abs}} \sim 900 \text{ km s}^{-1}$ is observed. In spite of this range in velocity offsets, we do not find a significant change in $\Delta v_{\text{em-abs}}$ with respect to Ly α emission strength in the composite spectra. We note that our velocity offsets decrease slightly with Ly α emission and are also consistent with S03 who found velocity offset to decrease monotonically with increasing Ly α emission strength. The velocity offset of our UV-bright SFG composite of $\Delta v_{\text{em-abs}} = 630 \text{ km s}^{-1}$ is also remarkably similar to the average velocity offset of $\Delta v_{\text{em-abs}} = 609 \text{ km s}^{-1}$ from Steidel et al. (2010) for a sample of 89 continuum-selected galaxies at $z \sim 2.3$.

Within the outflowing component, the high-ionization features have similar kinematic properties to and span a similar velocity range as the low-ionization features. However, this

information says nothing about the physical distribution of the absorbing gas. Steidel et al. (2010) find significant absorption of both low- and high-ionization species displaying similar radial dependences at galactocentric radii spanning $3 - 125\text{kpc}$. This indicates that both ionized and neutral gas share not only the same velocity envelope, but also similar physical distributions.

Using the low-ionization absorption lines as a probe of the outflowing neutral gas, we find a direct correlation between $\text{Ly}\alpha$ emission strength and the average strength of low-ionization absorption. This trend is most clearly demonstrated by Si II ions. In the outflowing component, a difference in line strengths indicates a change in either the velocity dispersion, covering fraction, or both. While the Si IV transition is consistent with being optically thin in all composites, the Si II transition and the other low-ionization transitions are optically thick. We do note that among galaxies with rest-frame $W_{\text{Ly}\alpha} > 20\text{\AA}$, Si II absorption is significantly weaker and the $\lambda 1526$ transition in the UV-bright LAE composite is marginally detected leading to a Si II $\lambda 1260$ to $\lambda 1526$ ratio that is greater than one, which would be expected if Si II were not optically thick. While Steidel et al. (2010) found Si II to be unsaturated at $b \sim 63\text{kpc}$, those authors did find it to be saturated at $b \sim 3\text{kpc}$ and $b \sim 40\text{kpc}$. We also note that due to the low S/N, the ratio of these two line strengths is fairly uncertain. Given the similar kinematic properties of different Si ionization states, different ionization state dependences on $\text{Ly}\alpha$ emission, and similar physical distributions, we find it likely that the outflowing neutral gas is in the form of neutral clouds embedded in ionized gas as previously theorized by Steidel et al. (2010).

Similar to the results of S03, we find a significant correlation between bluer spectral slopes and weaker low-ionization absorption strength. SFGs with ages between 10Myr and 1Gyr and constant star-formation histories have similar UV spectral slopes, so the shape of the observed spectral slope is largely dependent on dust extinction. UV-bright SFGs and LAEs at $z \sim 2$ and $z \sim 3$ are well-characterized by these ages and star formation histories (Shapley et al. 2001; Lai et al. 2008; Nilsson et al. 2009; Guaita et al. 2010). Therefore, we interpret this result as evidence for the presence of dust in the outflowing component. In addition, these outflows must also cover a region sufficiently large to extinguish a significant amount of the UV continuum surface brightness. The increased prominence of nebular

features for bluer β values is not surprising as bluer spectral slopes indicate either a lower amount of extinction, the presence of hotter more massive stars, or both. Each of these effects would make stellar photospheric features more visible.

From a redshift of $2.7 < z < 3.5$ to $2.0 < z < 2.7$, the UV-bright non-LAE spectra look remarkably similar. They have comparable Ly α emission strengths, interstellar absorption strengths, and kinematics consistent with no significant evolution in SFGs with rest-frame $W_{\text{Ly}\alpha} < 20\text{\AA}$ or the nature of their outflows across this redshift interval. In contrast, for SFGs with $W_{\text{Ly}\alpha} > 20\text{\AA}$ we find significantly weaker Ly α emission in the lower redshift sample. If this trend is real, then it is consistent with UV-bright LAEs being more evolved at lower redshifts. Low- and high-ionization absorption also appear to be stronger in the low-redshift sample, although due to the faint continua of $z \sim 3$ UV-bright LAEs, this may not indicate an evolution in galaxy properties. For both subsets of SFGs, the lower-redshift composites have bluer spectral slopes, which is confirmed at marginal significance for the UV-bright LAE composite from the photometric spectral slopes of individual galaxies. As there are many systematic effects that can contribute to the spectral slope, additional investigation specifically a better constraint on their rest-UV spectral slopes would be needed to conclude that lower redshift continuum- and narrowband-selected galaxies are less evolved, as their bluer colors would imply.

Chapter 3

Semi-Analytic Models

3.1 Semi-Analytic Models

The semi-analytic models (SAMs) used in this work to compute the formation and evolution of galaxies within a Λ CDM cosmology were originally presented in Somerville & Primack (1999) and Somerville et al. (2001), with significant updates described in detail in Somerville et al. (2008b, hereafter S08), Somerville et al. (2012, hereafter S12), and most recently in Somerville, Popping, & Trager (2014, in prep., hereafter SPT14). The S12 SAM includes the following physically motivated properties: (1) the growth of dark matter structure in a hierarchical clustering framework as described by ‘merger trees’, (2) shock heating and radiative cooling of gas, (3) conversion of cold gas into stars via an empirical ‘Kennicutt-Schmidt’ relation, (4) evolution of stellar populations, (5) a combination of feedback and metal enrichment of the interstellar and intracluster medium from supernovae, (6) ‘quasar’ and ‘radio’ mode black hole growth and feedback from AGN, (7) starbursts and morphological transformation due to galaxy mergers. Here, we briefly summarize these ingredients — a more detailed description of the models is provided in S08, S12, and SPT14. Throughout this work, we assume a standard Λ CDM universe (Komatsu et al. 2011) and a Chabrier stellar initial mass function (IMF; Chabrier 2003).

The merging histories (or merger trees) of dark matter haloes are constructed based on the Extended Press-Schechter formalism using the method described in Somerville & Kolatt (1999), with improvements described in S08. These merger trees record the growth of dark matter haloes via merging and accretion, with each “branch” representing a merger of two or more haloes. We follow each branch back in time to a minimum dark matter progenitor mass M_{res} . We refer to M_{res} as the mass resolution of our simulation where we have adopted $M_{\text{res}} = 10^{9.5} M_{\odot}$ in all the models presented here. Our SAMs give nearly identical results

when run on the EPS merger trees or on merger trees extracted from dissipationless N-body simulations (Lu et al. 2013, Porter et al. in prep.).

Whenever dark matter haloes merge, the central galaxy of the largest progenitor becomes the new central galaxy, and all others become ‘satellites’. Satellite galaxies lose angular momentum due to dynamical friction as they orbit and may eventually merge with the central galaxy. To estimate this merger timescale we use a variant of the Chandrasekhar formula from Boylan-Kolchin et al. (2008). Tidal stripping and destruction of satellites are also included as described in S08. We have checked that the resulting mass function and radial distribution of satellites (sub-haloes) agrees with the results of high-resolution N-body simulations that explicitly follow sub-structure (Macciò et al. 2010).

Before reionization, each halo contains a mass of hot gas equal to the universal baryon fraction times the virial mass of the halo. After reionization, which we assume to be complete by $z = 11$ (Hinshaw et al. 2013), the photoionizing background suppresses the collapse of gas into low-mass haloes. We use the results of Gnedin (2000) and Gnedin et al. (2004) to model the fraction of baryons that can collapse as a function of halo mass after reionization.

When a dark matter halo collapses or experiences a merger that more than doubles the mass of the largest progenitor, the hot gas is shock-heated to the virial temperature of the new halo. This gas then cools and collapses based on a simple spherically symmetric model. Assuming that the density profile of the gas decreases monotonically with increasing radius, and the cooling rate is more rapid for dense gas, at any moment we can define the cooling radius as the radius within which all the gas will have had time to cool within a characteristic time t_{cool} . We assume that the gas starts out at the virial temperature, then compute the time required for gas to radiate away its energy

$$t_{cool} = \frac{\frac{3}{2}\mu m_p kT}{\rho_g(r)\Lambda(T, Z_h)} \quad (3.1)$$

where μm_p is the mean molecular mass, T is the virial temperature $T_{vir} = 35.9[V_{vir}/(\text{km s}^{-1})]^2 \text{K}$, $\rho_g(r)$ is the radial density profile of the gas, $\Lambda(T, Z_h)$ is the temperature and metallicity-dependent cooling function (Sutherland & Dopita 1993), and Z_h is the metallicity of the hot halo gas. Then, assuming that the initial density profile of the gas is a

singular isothermal sphere ($\rho_{gas} = M_{hot}/(4\pi r_{vir}r^2)$), writing the expression for the mass within r_{cool} , and differentiating, the cooling rate is given by

$$\frac{dm_{cool}}{dt} = \frac{1}{2}m_{hot}\frac{r_{cool}}{r_{vir}}\frac{1}{t_{cool}} \quad (3.2)$$

where m_{hot} is the mass of the hot halo gas, r_{vir} is the virial radius of the dark matter halo and r_{cool} is the cooling radius. In the models of S08, and also here, t_{cool} is assumed to be equal to the halo dynamical time, $t_{dyn} \propto r_{vir}/V_{vir}$, where V_{vir} is the virial velocity of the halo, following Springel et al. (2001) and Croton et al. (2006). If $r_{cool} > r_{vir}$, then the cooling time is shorter than the dynamical time. In this case, we assume that the cooling rate is given by the rate at which gas can fall into the halo, which is governed by the mass accretion history.

For simplicity, we assume that cold gas is accreted only by the central galaxy, even though realistically, satellite galaxies should receive some fraction of the new cold gas. All newly accreting gas collapses to form a rotationally supported disc, where a fixed fraction of the halo's original mass in the form of baryons is able to collapse into a disk. The scale radius is based on the initial angular momentum of the gas and the halo profile, assuming angular momentum is conserved and the self-gravity of the collapsing baryons causes contraction in the inner part of the halo (Blumenthal et al. 1986; Flores et al. 1993; Mo et al. 1998). Similarly, a fixed fraction of the halo's angular momentum is given to the disk, and specific angular momentum is conserved. We assume a thin disk with an exponential surface density profile $\Sigma(r) = \Sigma_0 \exp(-r/r_d)$, where r_d and Σ_0 are the disk scale length and central surface density and are related to the disk mass by $m_d = 2\pi\Sigma_0 r_d^2$. Then, the angular momentum of the disk is

$$J_d = 2\pi \int V_c \Sigma(r) r^2 dr \quad (3.3)$$

Since the initial dark matter density profile is a singular isothermal sphere and we neglect the self-gravity of the disk, the rotation velocity $V_c(r)$ is constant and equal to V_{vir} , and the angular momentum of the disk reduces to

$$J_d = 4\pi\Sigma_0 V_c r_d^3 = 2m_d r_d V_{vir} \quad (3.4)$$

The spin parameter, a dimensionless measure of the relative angular momentum of the halo, is defined as $\lambda \equiv J_h |E_h|^{1/2} G^{-1} M_{vir}^{-5/2}$ (Peebles 1969), where E_h is the total energy of the halo, and we can use this to write

$$r_d = \frac{\lambda G M_{vir}^{3/2}}{2 V_{vir} |E_h|^{1/2}} \frac{J_d/m_d}{J_H/m_{vir}} \quad (3.5)$$

where $j_{\text{gas}} = J_d/m_d$ and $j_{\text{DM}} = J_h/m_{vir}$ are the cold gas specific angular momentum and dark matter specific angular momentum, and define $f_j \equiv j_{\text{gas}}/j_{\text{DM}}$. Accordingly, the infall limited cooling regime ($r_{cool} > r_{vir}$) is associated with cold flows, in which gas streams into the halo along dense filaments, without ever getting heated (Birnboim & Dekel 2003; Dekel & Birnboim 2006; Kereš et al. 2005). Somerville et al. (2008a) showed that this approach reproduces the observed size versus stellar mass relation for discs from $z \sim 0$ to 2 when $f_j = 1$.

In these models, star formation occurs in two modes, a “normal” mode in isolated discs, and a merger-driven “starburst” mode. Star formation in the “normal” mode is modelled as described in Section 3.1.2. The efficiency and timescale of the merger driven burst mode is a function of the merger mass ratio and the gas fractions of the progenitors, and is based on the results of hydrodynamic simulations of binary galaxy mergers (Robertson et al. 2006b; Hopkins et al. 2009b).

Some of the energy from supernovae and massive stars is assumed to be deposited in the ISM, resulting in the driving of a large-scale outflow of cold gas from the galaxy. The mass outflow rate is parameterized as a function of the galaxy circular velocity times the star formation rate, as motivated by the “energy driven” wind scenario.

Some fraction of this ejected gas escapes from the potential of the dark matter halo, while some is deposited in the hot gas reservoir within the halo, where it becomes eligible to cool again. The fraction of gas that is ejected from the disc but retained in the halo versus ejected from the disc and halo is a function of the halo circular velocity (see S08 for details), such that low-mass haloes lose a larger fraction of their gas. The gas that is ejected from

the halo is kept in a larger “reservoir”, along with the gas that has been prevented from falling in due to the photoionizing background. This gas is allowed to “re-accrete” onto the halo as described in S08.

Each generation of stars also produces heavy elements, and chemical enrichment is modelled in a simple manner using the instantaneous recycling approximation. For each parcel of new stars dm_* , we also create a mass of metals $dM_Z = y dm_*$, which we assume to be instantaneously mixed with the cold gas in the disc. The yield y is assumed to be constant and is treated as a free parameter. When gas is removed from the disc by supernova driven winds as described above, a corresponding proportion of metals is also removed and deposited either in the hot gas or outside the halo, following the same proportions as the ejected gas.

Mergers are assumed to remove angular momentum from the disc stars and to build up a spheroid. The efficiency of disc destruction and spheroid growth is a function of progenitor gas fraction and merger mass ratio, and is parameterized based on hydrodynamic simulations of disc-disc mergers (Hopkins et al. 2009b). These simulations indicate that more “major” (closer to equal mass ratio) and more gas-poor mergers are more efficient at removing angular momentum, destroying discs, and building spheroids. Note that the treatment of spheroid formation in mergers used here has been updated relative to S08 as described in Hopkins et al. (2009c). The updated model produces good agreement with the observed fraction of disc vs. spheroid dominated galaxies as a function of stellar mass (Hopkins et al. 2009c, Porter et al. in prep).

In addition, mergers drive gas into galactic nuclei, fueling black hole growth. Every galaxy is born with a small “seed” black hole (typically $\sim 100 M_\odot$ in our standard models). Following a merger, any pre-existing black holes are assumed to merge fairly quickly, and the resulting hole grows at its Eddington rate until the energy being deposited into the ISM in the central region of the galaxy is sufficient to significantly offset and eventually halt accretion via a pressure-driven outflow. This results in self-regulated accretion that leaves behind black holes that obey the observed correlation between BH mass and spheroid mass or velocity dispersion (Di Matteo et al. 2005; Robertson et al. 2006a; Somerville et al. 2008c).

There is a second mode of black hole growth, termed “radio mode”, that is thought to be associated with powerful jets observed at radio frequencies. In contrast to the merger-triggered mode of BH growth described above (sometimes called “bright mode” or “quasar mode”), in which the BH accretion is fueled by cold gas in the nucleus, here, hot halo gas is assumed to be accreted according to the Bondi-Hoyle approximation (Bondi 1952). This leads to accretion rates that are typically only about $\sim 10^{-3}$ times the Eddington rate, so that most of the BH’s mass is acquired during episodes of “bright mode” accretion. However, the radio jets are assumed to couple very efficiently with the hot halo gas, and to provide a heating term that can partially or completely offset cooling during the “hot flow” mode (we assume that the jets cannot couple efficiently to the cold, dense gas in the infall-limited or cold flow regime).

3.1.1 Multiphase Gas Partitioning

Throughout this chapter we refer rather loosely to “cold” gas, which is gas that according to our simple cooling model has been able to cool below 10^4 K via radiative atomic cooling. Most previous cosmological simulations have considered all of this “cold” gas to be eligible to form stars. Here, we partition it into components that we label atomic, molecular, and ionized, and only allow the “molecular” component to participate in star formation. As we do not explicitly track the temperature or density of the “cold” gas in our models, this is obviously still extremely schematic. However, when we refer to “cold” gas, we are referring to gas that is in one of these three states and is dynamically associated with the galactic disc (rather than in an extended hot halo, an outflow, etc).

At each timestep, we compute the scale radius of the cold gas disc using the angular momentum based approach described above, and assume that the *total* (HI + H₂) cold gas distribution is described by an exponential with scale radius r_{gas} . We do not attempt to track the scale radius of the stellar disc separately but make the simple assumption that $r_{\text{gas}} = \chi_{\text{gas}} r_{\text{star}}$, with $\chi_{\text{gas}} = 1.7$ fixed to match stellar scale lengths at $z = 0$. Bigiel & Blitz (2012) showed that this is a fairly good representation, on average, for the discs of nearby spirals. We then divide the gas disc into radial annuli and compute the fraction of molecular gas, $f_{\text{H}_2}(r) \equiv \Sigma_{\text{H}_2}(r)/[\Sigma_{\text{H}_2}(r) + \Sigma_{\text{HI}}(r)]$, in each annulus, as described below.

Ionized Gas

Most (if not all) previous semi-analytic models have neglected the ionized gas associated with galaxies, which may be ionized either by an external background or by the radiation field from stars within the galaxy. Here we include a simple analytic estimate of the ionized gas fraction motivated by the model presented in Gnedin (2012). We assume that some fraction of the total cold gas in the galaxy, $f_{\text{ion,int}}$, is ionized by the galaxy's own stars. In addition, a slab of gas on each side of the disc is ionized by the external background radiation field. Gas is assumed to be ionized if it lies below a critical threshold surface density Σ_{HII} . Throughout this paper we assume $f_{\text{ion,int}} = 0.2$ (as in the Milky Way) and $\Sigma_{\text{HII}} = 0.4, \text{ M}_{\odot}\text{pc}^{-2}$ (Gnedin 2012). Applying this model within our SAM gives remarkably good agreement with the ionized fractions as a function of circular velocity shown in Fig. 2 of Gnedin (2012), obtained from hydrodynamic simulations with time dependent and spatially variable 3D radiative transfer of ionizing radiation from local sources and the cosmic background.

Molecular Gas: Pressure Based Partitioning

We consider two approaches for computing the molecular gas fractions in galaxies. The first is based on the empirical pressure-based recipe presented by Blitz & Rosolowsky (2006, BR) who found that the molecular fraction $R_{\text{mol}} \equiv \Sigma_{\text{H}_2}/\Sigma_{\text{H}_i}$ is correlated with the disc hydrostatic mid-plane pressure P :

$$R_{\text{mol}} = \left(\frac{P}{P_0} \right)^{\alpha_{\text{BR}}} \quad (3.6)$$

where P_0 and α_{BR} are free parameters that are obtained from a fit to the observational data. We adopted $\log P_0/k_B = 4.23 \text{ cm}^3 \text{ K}$ and $\alpha_{\text{BR}} = 0.8$ from Leroy et al. (2008).

We estimate the hydrostatic pressure as a function of the distance from the center of the disc r as (Elmegreen 1989, 1993; Fu et al. 2010):

$$P(r) = \frac{\pi}{2} G \Sigma_{\text{gas}}(r) [\Sigma_{\text{gas}}(r) + f_{\sigma}(r) \Sigma_{*}(r)] \quad (3.7)$$

where G is the gravitational constant, Σ_{gas} is the cold gas surface density, Σ_* is the stellar surface density, and f_σ is the ratio of the vertical velocity dispersions of the gas and stars:

$$f_\sigma(r) = \frac{\sigma_{\text{gas}}}{\sigma_*} \quad (3.8)$$

Following Fu et al. (2010), we adopt $f_\sigma(r) = 0.1\sqrt{\Sigma_{*,0}/\Sigma_*}$, where $\Sigma_{*,0} \equiv m_*/(2\pi r_*^2)$, based on empirical scalings for nearby disc galaxies.

Molecular Gas: Metallicity Based Partitioning

Gnedin & Kravtsov (2011) performed high-resolution “zoom-in” cosmological simulations with the Adaptive Refinement Tree (ART) code of Kravtsov & et al. (1999), including gravity, hydrodynamics, non-equilibrium chemistry, and simplified radiative transfer. These simulations are able to follow the formation of molecular hydrogen through primordial channels and on dust grains, as well as dissociation of molecular hydrogen and self- and dust- shielding. These simulations also include an empirical H_2 -based star formation recipe.

Blitz & Rosolowsky (2004, 2006) showed that, empirically, the fraction of molecular to molecular plus atomic gas, $f_{\text{H}_2} = M_{\text{H}_2}/(M_{\text{HI}} + M_{\text{H}_2})$, in nearby spirals is tightly correlated with the disc midplane pressure. Ostriker et al. (2010) proposed a theoretical explanation for this relationship, arguing that the thermal pressure in the diffuse interstellar medium (ISM), which is proportional to the UV heating rate and therefore to the SFR, adjusts until it balances the midplane hydrostatic pressure set by the vertical gravitational field. Other recent theoretical work has argued that, as H_2 forms most efficiently on dust grains, the metallicity of the gas, along with its surface density, should be an important factor in determining f_{H_2} (Krumholz et al. 2008, 2009a; Gnedin & Kravtsov 2010). Using high resolution numerical simulations of isolated galaxies with detailed chemistry and an H_2 -based star formation recipe, Robertson & Kravtsov (2008) showed that f_{H_2} depended on metallicity, gas surface density, and the UV background radiation. Gnedin & Kravtsov (2010, 2011) characterized this dependence in detail with high resolution numerical cosmological simulations with detailed chemistry. The impact on the structural properties of disc galaxies of

using an H_2 -based star formation recipe rather than a traditional KS recipe has recently been explored with high resolution “zoom-in” cosmological simulations (Christensen et al. 2012b).

Gnedin & Kravtsov (2011) presented a fitting function based on their simulations, which effectively parameterizes the fraction of molecular hydrogen as a function of the dust-to-gas ratio relative to the Milky Way, D_{MW} , the UV ionizing background relative to the Milky Way U_{MW} , and the neutral gas surface density $\Sigma_{\text{HI}+\text{H}_2}$. Following Gnedin & Kravtsov (2010), we take the dust-to-gas ratio to be equal to the metallicity of the cold gas in solar units, $D_{\text{MW}} = Z/Z_{\odot}$. The ionizing background is defined as the ratio of the interstellar FUV flux at 1000\AA , J_{1000} , relative to the Milky Way, $J_{\text{MW}} = 10^6 \text{ photons cm}^{-2} \text{ s}^{-1} \text{ sr}^{-1} \text{ eV}^{-1}$ (Draine 1978; Mathis et al. 1983), $U_{\text{MW}} = J_{1000}/J_{\text{MW}}$. In this work, we create two sets of models: one where the ionizing background is fixed to the Milky Way value ($U_{\text{MW}} = 1$) (Murray & Rahman 2010; Robitaille & Whitney 2010), and one where it is equal to the star formation rate $U_{\text{MW}} = \text{SFR } \text{M}_{\odot}^{-1} \text{ yr}$.

The fitting functions from Gnedin & Kravtsov (2010) are intended to characterize the formation of H_2 on dust grains, which is the dominant mechanism once the gas is enriched to more than a few tenths of Solar metallicity. However, other channels for H_2 formation in primordial gas must be responsible for producing the molecular hydrogen out of which the first stars formed. Studies with numerical hydrodynamic simulations containing detailed chemical networks and analytic calculations have shown that H_2 can form through primordial channels in dark matter haloes once they grow above a critical mass of $M_{\text{III}} \sim 10^5 \text{ M}_{\odot}$ (e.g. Nakamura & Umemura 2001; Glover 2013). This gas can then form “Pop III” stars which pollute their surroundings and enrich the ISM to $Z_{\text{III}} \sim 10^{-3} Z_{\odot}$ (Schneider et al. 2002; Greif et al. 2010; Wise et al. 2012). Since these processes are thought to have taken place in haloes that are much smaller than our resolution limit, we represent them in a simple manner. By setting a “floor” to the molecular hydrogen fraction in our haloes, $f_{\text{H}_2, \text{floor}}$, we “pre-enrich” the initial hot gas in haloes, and the gas that is accreted onto haloes due to cosmological infall, to a metallicity of $Z_{\text{pre-enrich}}$. We adopt typical values of $f_{\text{H}_2, \text{floor}} = 10^{-4}$ and $Z_{\text{pre-enrich}} \sim 10^{-3} Z_{\odot}$, based on the numerical simulation results mentioned above (Haiman et al. 1996; Bromm & Larson 2004). Moreover, the results are

not sensitive to reasonable changes in these values (see SPT14).

3.1.2 Star Formation

The “classical” Kennicutt-Schmidt (KS) recipe (Kennicutt 1998) assumes that the surface density of star formation in a galaxy is a function of the *total* surface density of the cold neutral gas (atomic and molecular), above some threshold surface density Σ_{crit} . This approach has been used to model star formation in most previous SAMs and numerical hydrodynamical simulations. Here, we instead use a star formation recipe based on the H_2 content of the galaxy, motivated by recent observational results.

Bigiel et al. (2008b) found, based on observations of spiral galaxies from the THINGS survey, that the star formation timescale in molecular gas is approximately constant, i.e.

$$\Sigma_{\text{SFR}} = A_{\text{SF}} \Sigma_{\text{H}_2}^{N_{\text{SF}}} \quad (3.9)$$

with $N_{\text{SF}} \simeq 1$.

Observations of higher density environments, such as starbursts and high redshift galaxies, suggest that above a critical H_2 surface density, the star formation timescale becomes a function of Σ_{H_2} such that the star formation law steepens. Recent work in which a variable conversion factor between CO and H_2 is accounted for suggests that $N_{\text{SF}} \simeq 2$ for high Σ_{H_2} (Narayanan et al. 2012b). This steepening is also expected on theoretical grounds (Krumholz et al. 2009c; Ostriker & Shetty 2011). Therefore, in SPT14 we also considered an H_2 -based star formation recipe of the form

$$\Sigma_{\text{SFR}} = A_{\text{SF}} \left(\Sigma_{\text{H}_2} / (10 \text{M}_{\odot} \text{pc}^{-2}) \left(1 + \frac{\Sigma_{\text{H}_2}}{\Sigma_{\text{H}_2, \text{crit}}} \right)^{N_{\text{SF}}} \right) \quad (3.10)$$

In SPT14, we found that the “two-slope” star formation recipe produces better agreement with observations of star formation rates and stellar masses in high redshift galaxies, so we adopt it in all of the models presented in this work. We additionally adopt $A_{\text{SF}} = 6.0 \times 10^{-3} \text{M}_{\odot} \text{yr}^{-1} \text{kpc}^{-2}$, $\Sigma_{\text{H}_2, \text{crit}} = 70 \text{M}_{\odot} \text{pc}^{-2}$, and $N_{\text{SF}} = 1.0$, based on the observational results of Bigiel & Blitz (2012).

3.1.3 Model Variants

We consider nine main variants of our models: three recipes for gas partitioning (the pressure-based BR recipe and the metallicity-based GK recipe with a fixed/variable UV radiation field), and three choices for the specific angular momentum of the gas relative to the dark matter halo, parameterized by f_j . We consider fixed values of $f_j = 1$ and $f_j = 2.5$, and also a set of models in which f_j is set based on the merger history of the galaxy. The $f_j = 2.5$ models result in stellar and gaseous disks with higher specific angular momentum than their dark matter halos, and are motivated by numerical simulations that suggest this situation may arise due to stellar driven winds and/or cold flows (see Section 4.1 for a more detailed discussion and references). In the merger models, we compute the disc properties and star formation rates using the $f_j = 1$ models, then place the gas in a more extended distribution based on the halo’s merger history, as we discuss further below. These model variants are denoted GKfj1, GKj1, BRj1, GKfj25, GKj25, BRj25, GKfjm, GKjm, and BRjm and are summarized in Table 3.1. While we only model azimuthally symmetric extended cold gas discs, we consider them as a proxy for other processes that may cause the gas to be more extended.

Although we use the same H_2 -based star formation recipe in all of our models, both the choice of f_j and the gas partitioning recipe can affect the star formation efficiency. A larger value of f_j leads to larger discs and lower gas densities overall, less efficient formation of H_2 and less efficient star formation. Similarly, the different gas partitioning recipes lead to different H_2 fractions as a function of mass and redshift (see PST14) and therefore again to higher or lower star formation efficiency, since only H_2 can form stars in our models. Increasing the disk sizes causes the $f_j = 2.5$ models to overpredict the sizes of disks as measured by their SFR half-light radii by a factor of 1.5 to 2 both locally and at $z = 2$ relative to the results of Leroy et al. (2008) and Tacconi et al. (2013).

Our merger-based models are very crude and are used to investigate the impact of mergers on the angular momentum of the gas discs. In these merger models, we begin with the BRj1 and GKj1 models respectively. In post-processing, we boost the f_j value to 1.5 or 2.5 after the galaxy has had a minor or major merger, respectively. These models reflect the

Table 3.1 Model Definitions

Model	f_{H_2}	U_{MW}	$f_j = j_{\text{gas}}/j_{\text{DM}}$
GKfj1	GK	1	1.0
GKj1	GK	$\propto \text{SFR}$	1.0
BRj1	BR	-	1.0
GKfj25	GK	1	2.5
GKj25	GK	$\propto \text{SFR}$	2.5
BRj25	BR	-	2.5
GKfjm*	GK	1	1.0, 1.5, 2.5
GKjm*	GK	$\propto \text{SFR}$	1.0, 1.5, 2.5
BRjm*	BR	-	1.0, 1.5, 2.5

* $f_j = 1.0, 1.5, 2.5$ depending on if the galaxy has undergone no mergers, only minor mergers, or at least one major merger respectively.

idea that some of the orbital angular momentum of the merging galaxy may be transferred to internal (spin) angular momentum following a merger. This effect has been observed in numerical simulations (e.g. Robertson et al. 2006a; Robertson & Kravtsov 2008; Sharma et al. 2012), which suggest that major mergers have a larger effect on the specific angular momentum distribution. Our f_j values in these models contain a small, but arbitrary offset, comparable to their results. One important inconsistency in the merger models is that by increasing the cold gas angular momentum, we decrease the cold gas density, which in turn will decrease the star formation rate. Since f_j is increased after running the semi-analytic model, the stellar masses and star formation rates reflect those of the $f_j = 1$ models and are artificially high. We discuss the implications of these effects in section 4.2.1. For these reasons, we treat the ‘merger’ models more as toy models that provide some information on the different effects of the distribution of cold gas on DLA properties; however, we focus the majority of our analysis on the four other models.

The semi-analytic models contain a number of free parameters. These are kept fixed to the same values used in SPT14, which were found to reproduce fundamental galaxy properties at $z = 0$ in their baseline models. We note that SPT14 and PST14 only consider models corresponding to our $f_j = 1$ models.

Chapter 4

Damped Ly α Absorption Systems in Semi-Analytic Models with Multiphase Gas

4.1 Introduction

Observations of DLAs provide important constraints on the gas content of galaxies at high redshift, and indirectly constrain how gas is converted into stars, and how gas and metals are cycled into and out of galaxies in inflows and outflows. These, in turn, provide key constraints on some of the most uncertain aspects of our models of galaxy formation.

There has been a significant amount of observational activity and progress in this area in recent years. Large surveys such as the Sloan Digital Sky Survey (SDSS Schneider et al. 2010) and BOSS (Eisenstein et al. 2011) have provided extensive target samples of optically detected quasars, yielding greatly improved statistics for samples of high redshift absorbers ($1.5 \lesssim z \lesssim 4.5$). These improved statistics have greatly tightened the constraints on the shape of the column density distribution function, comoving line density of DLAs, and the evolution of the cosmological neutral gas density (e.g., Noterdaeme et al. 2012). Font-Ribera et al. (2012) employed a cross-correlation analysis of DLAs from the BOSS survey with the Ly α forest and were able to obtain constraints on the DLA cross-section as a function of halo mass. Rafelski et al. (2012) have published metallicities for a large number of DLAs in the redshift interval $2 < z < 4$, providing constraints on the build-up of heavy elements in the cold gas phase of galaxies across cosmic time. In addition, the UV-sensitive Cosmic Origins Spectrograph (COS) on the Hubble Space Telescope (HST) is now enabling studies of DLAs at lower redshift $z \lesssim 1$, which may be more easily connected with populations detected in emission and with the present day galaxy population (Meiring et al. 2011; Battisti et al. 2012). Recent studies with COS have also yielded a wealth of information on ionized gas within low-redshift haloes (e.g. Tumlinson et al. 2011).

Two different pictures for the origin and nature of DLAs have been debated in the literature. Based on the observed kinematics of low-ionization metal systems in DLAs, Wolfe et al. (1986) and Prochaska & Wolfe (1997, hereafter PW97) presented a picture in which thick, extended disc galaxies give rise to DLAs, yet explaining how a sufficient number of large disc galaxies could have formed by $z \sim 3$ remains a challenge. In contrast, in the context of the hierarchical picture arising in a Cold Dark Matter (CDM) cosmogony, many DLAs would be expected to be associated with smaller, lower mass systems (e.g., Haehnelt et al. 1998). However, reproducing the distribution of DLA kinematics has remained a significant challenge for hierarchical models (Maller et al. 2001; Razoumov et al. 2008; Pontzen et al. 2008). These two scenarios have very different implications for galaxy evolution — the former requires large disc galaxies to be in place by $z \sim 3$, and the latter has implications for the expected star formation rates, stellar masses, and kinematics of DLAs and their counterparts.

A number of previous theoretical studies have made specific predictions for the properties of DLAs in the framework of the CDM paradigm (e.g., Kauffmann & Charlot 1994; Kauffmann 1996; Gardner et al. 1997; Haehnelt et al. 1998; Maller et al. 2001, 2003; Nagamine et al. 2004b,a, 2007; Pontzen et al. 2008; Fumagalli et al. 2011; Altay et al. 2011; Cen 2012; van de Voort et al. 2012; Kulkarni et al. 2013; Altay et al. 2013). Early numerical hydrodynamic simulations typically neglected feedback from stellar and supernova-driven winds, or contained weak forms of stellar feedback. These simulations had moderate success in reproducing the column density distribution, cosmological neutral gas density, and line density of DLAs at high redshift ($1 \lesssim z \lesssim 4$), although they had difficulty reproducing the turnover in the column density distribution at $\log N_{\text{HI}} \sim 22 \text{ atoms cm}^{-2}$ (Nagamine et al. 2004a). These simulations were not able to discriminate between different phases of gas, and it was speculated that the turnover could be due to the HI-H₂ transition. However, recent observational results from the BOSS survey (Font-Ribera et al. 2012) have shown that while these high column density systems are rare, they do exist, relaxing some of this tension, although the origin of the turnover still remains something of a puzzle (Erkal et al. 2012). Many of these simulations had relatively small volumes and modeled the DLA column density distribution by characterizing the relationship between DLA cross-section

and dark matter (DM) halo mass, then convolving this relationship with a DM halo mass function from larger volume dissipationless simulations.

More recent simulations found that the inclusion of more effective stellar feedback and winds had a significant effect on the predicted DM halo mass to DLA cross section relationship. For example, Nagamine et al. (2007) found that in simulations with strong winds, galaxies in low mass haloes ejected much of their gas, resulting in a lower DLA cross section, thus shifting the DLA population into higher mass host haloes. Qualitatively similar results have been found by Pontzen et al. (2008), Fumagalli et al. (2011), and Cen (2012), although the detailed slope, normalization, and redshift dependence of the predicted halo mass to DLA cross section relationship are different in these different simulations. Recently, Cen (2012) particularly emphasized the importance of outflows for reproducing the observed properties of DLAs including their kinematics.

CDM-based models have also had difficulty reproducing the observed metallicities of DLAs (Somerville et al. 2001; Maller et al. 2001; Nagamine et al. 2004b, 2005; Pontzen et al. 2008; Fumagalli et al. 2011). They have consistently predicted higher average metallicities, and none have reproduced the tail to very low metallicity, although again, simulations with strong stellar feedback and winds have been more successful. Cen (2012) find that a significant number of $z \gtrsim 3$ DLAs originate in intergalactic gas. A combination of these intergalactic DLAs and the ejection of metals by galactic winds lowers the average metallicities, bringing them into better agreement with observations.

Meanwhile, recent observational and theoretical work has greatly advanced our understanding of the physics that regulates star formation on galactic scales. The vast majority of previous cosmological simulations relied on the classical “Kennicutt-Schmidt” (KS) relation as a recipe for describing how cool gas turns into stars. The KS relation, based on observations of nearby spiral galaxies and starburst nuclei, says that the star formation rate surface density (Σ_{SFR}) is proportional to the total gas surface density ($\Sigma_H = \Sigma_{HI} + \Sigma_{H_2}$) (Schmidt 1959; Kennicutt 1989, 1998). The KS relation is frequently approximated as a power law, $\Sigma_{SFR} \propto \Sigma_H^N$, with $N \sim 1.4$, above a critical total gas surface density Σ_{crit} . Empirical studies have shown that $\Sigma_{crit} \simeq 3\text{--}10 \text{ M}_\odot\text{pc}^{-2}$ (Martin & Kennicutt 2001).

However, Wong & Blitz (2002) showed that Σ_{SFR} is more tightly correlated with the

density of *molecular* hydrogen Σ_{H_2} (as traced by CO) than with the total gas density. These results were confirmed and expanded upon with the results from the THINGS survey (Walter et al. 2008) combined with CO maps from BIMA SONG and HERACLES (Helfer et al. 2003; Leroy et al. 2009). These studies showed that $\Sigma_{SFR} \propto \Sigma_{H_2}^N$ with N very close to unity, implying that star formation takes place in molecular gas with roughly constant efficiency (Bigiel et al. 2008a, 2011). These results underlined the importance of modeling the partitioning of gas into atomic and molecular phases in theoretical models of galaxy formation.

In this chapter, we make use of the SAMs developed in SPT14 and PST14 and described in Chapter 3 to explore for the first time the predictions for the properties of DLAs in semi-analytic models with partitioning of gas into different phases and an H_2 -based star formation recipe. We investigate the impact of the gas partitioning, star formation recipe, and assumptions about the structure of the cold gaseous disc on the main observable properties of DLAs and confront our predictions with the latest observations. The chapter is organized as follows. In 4.1.1, we also describe how we compile mock catalogs of DLAs. In section 4.2, we present our predictions for key DLA observables, including the DLA column density distribution as a function of redshift, DLA cross-section as a function of halo mass and redshift, comoving density of DLAs and cosmological neutral gas density as a function of redshift, distribution of DLA velocity widths, DLA metallicity distribution, and DLA metallicity as a function of velocity width and redshift. We discuss the implications of our results in section 4.3, and summarize and conclude in section 4.4. Throughout this chapter, we adopt the following values for the cosmological parameters: $\Omega_m = 0.28$, $\Omega_\Lambda = 0.72$, $H_0 = 70.0$, $\sigma_8 = 0.81$, and $n_s = 0.96$. Our adopted baryon fraction is 0.1658. These values are consistent with the seven-year *Wilkinson Microwave Anisotropy Probe* (WMAP) results (Komatsu et al. 2011). All quoted metallicities are relative to solar.

4.1.1 Selecting H I absorption systems

We obtain a catalog of host haloes by extracting haloes along lightcones from the Bolshoi simulations (Klypin et al. 2011; Behroozi et al. 2010). These lightcones cover a 1 by 1 deg² area on the sky over a redshift range $0 < z < 5$ and contain galaxies with dark matter

halo masses from $10^{9.5}$ to $\sim 10^{14.5} M_\odot$. However, the Bolshoi simulation begins to become incomplete at or below $V_{vir} \simeq 50 \text{ km s}^{-1}$, $M_h \simeq 10^{10} M_\odot$; see Klypin et al. (2011) for more details. These haloes are then populated with galaxies as described above.

The molecular and atomic hydrogen gas is distributed in a disc with an exponential radial and vertical profile. The vertical scale height is proportional to the radial scale length, $z_g = \chi_z r_g$, where $\chi_z = 0.4$ is a constant, in agreement with observations of moderate redshift galaxies (Bruce et al. 2012). We explore different values of χ_z , although reasonable values of χ_z (i.e. not razor-thin discs) have a minimal effect on our results.

The central gas density is then defined as $n_0 = M_{cg}/(4\pi\mu m_H r_g^2 z_g)$, where M_{cg} is the atomic and molecular gas, m_H is the mass of the hydrogen atom, and μ is the mean molecular weight of the gas. The atomic gas density as a function of radius along and height above the plane is given by

$$n_{HI}(r, z) = n_0 \left(1 - f_{H_2}(r)\right) \exp\left(-\frac{r}{r_g}\right) \exp\left(-\frac{|z|}{z_g}\right) \quad (4.1)$$

In Figure 4.1 we show gas profiles for three galaxies with cold gas masses of $\log M_{cold}/M_\odot = 8, 9, 10$ and metallicities $\log Z/Z_\odot = -2.5, -1.5, -0.5$ at $2 < z < 3$ for the $f_j = 1$ and 2.5 models in the SAMs (as seen face-on). Each row shows the difference in cold gas partitioning for our three models and three fiducial galaxies. Star formation is much more efficient in low mass halos in the BR and GK models than the GKf models due to the high cold gas density threshold for H_2 formation in the latter. However once a significant amount of metals have been produced, the star formation efficiency converges in all three models as can be seen in galaxies with high masses and metallicities. For reference, a neutral hydrogen column density of $N_{HI} = 2 \times 10^{20} \text{ cm}^{-2}$ corresponds to a gas surface density of $\Sigma_{HI} = 10 M_\odot \text{ pc}^{-2}$. Figure 4.1 demonstrates the impact on the gas distribution of the different assumptions for gas partitioning, star formation, and gas angular momentum.

The models provide the radial distance from the central galaxy for each satellite galaxy, and we assign a random azimuth and polar angle ϕ and θ for each satellite's position with respect to the central. With the positions determined for every galaxy in each lightcone,

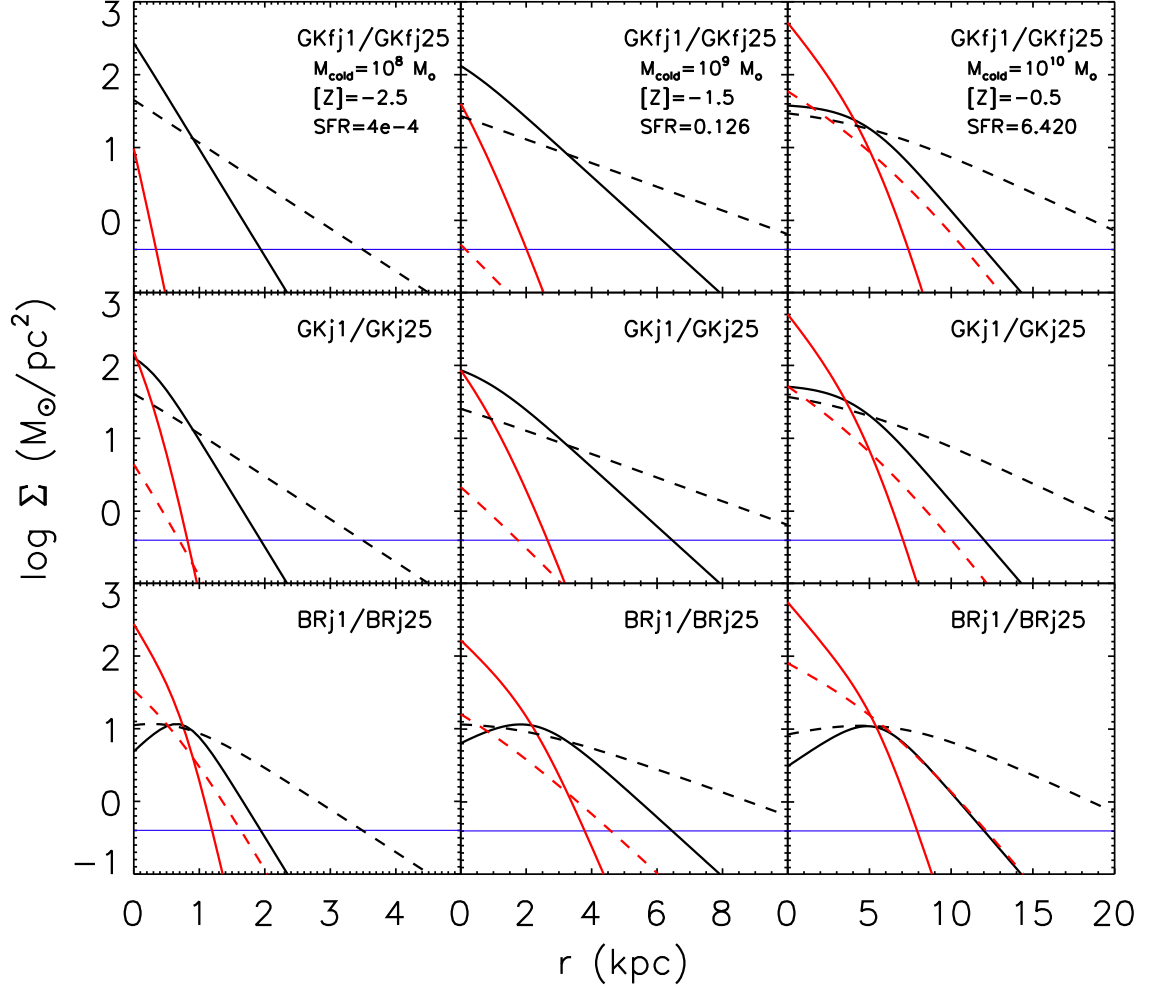


Figure 4.1 Cold gas radial profiles for three typical galaxies in the $f_j = 1$ (solid line) and $f_j = 2.5$ (dashed line) models with redshifts $2 < z < 3$. The H I gas (black), H₂ (red), and H II (blue) surface densities are shown. Cold gas mass and metallicity increase from left to right from $\log Z = -2.5$ to -0.5 and $\log M_{\text{cold}}/M_{\odot} = 8$ to 10 . The top row shows the GKf models, the middle row the GK models, and the bottom row the BR models. Since stars form based on the density of H₂ (red), this illustrates that the $f_j = 1$ models are more efficient at forming stars than the $f_j = 2.5$ models. Moreover, star formation is much more efficient in low mass halos in the BR and GK models than the GKf models (note the lack of any H₂ in the lowest mass galaxy in the GKfj25 model). However, the star formation efficiency becomes similar in all three models at high masses and metallicities.

we generate 20,000 random sightlines and integrate the three-dimensional gas density distribution along the sightline. Each galaxy is given a random orientation angle with respect to the sightline. All sightlines as well as the properties of all haloes with observed column densities above a threshold of $N_{\text{HI}} > 10^{19}$ atoms cm^{-2} are then saved as our catalog of absorption systems.

We then generate low-ionization line profiles by assuming the gas is distributed in small clouds within the disc, using a similar approach to that of Maller et al. (2001). The relevant parameters are: σ_{int} , the internal velocity dispersion of each cloud; N_c , the number of clouds; and σ_{cc} , their isotropic random motions. Following PW97, we take $\sigma_{\text{int}} = 4.3$ km s^{-1} . PW97 derived this value from Voigt profile fits to their observations with $N_c = 5$ being the minimum acceptable number of components. Increasing the number of clouds to as high as 60 did not improve the goodness of fit for a disc model since the model discs are relatively thin. Following Maller et al. (2001), we assume the gas discs are cold and set $\sigma_{\text{cc}} = 10$ km s^{-1} . We combine these internal velocities with the rotational velocity of the disc as well as the relative orbital velocity of the satellite galaxy with respect to the central (when applicable). For each sightline, we treat the gas density distribution as a continuous probability distribution for the positions of the clouds (Maller et al. 2001). We then generate low ionization line profiles by randomly distributing 20 clouds with the same optical depth along the line of sight. Finally, we ‘measure’ the velocity width, Δv_{90} , by taking the difference between the pixel containing 5% and 95% of the total optical depth.

In generating the low-ionization line profiles, we make a number of simplifying assumptions. Satellite galaxies are assumed to be on circular orbits. Gas discs are assumed to have a simple radial profile in addition to being axisymmetric. The gas distribution is independent of galaxy environment or Hubble type. We do not account for distortion in gas discs due to the gravitational effects of other galaxies or effects due to previous merger events, except very crudely in the merger (“m”) models as described above.

4.2 Results

In this section, we compare the predictions for our suite of models with a set of observations of DLAs. To calibrate our models, in Section 4.2.1 we present the $z = 0$ stellar, HI, and H₂ mass functions for our models along with observations from local galaxies. In Section 4.2.2 - 4.2.4, we present column density distribution functions, the comoving line density of DLAs, the cosmological neutral gas density in DLAs (Ω_{DLA}), and DLA cross sections and halo masses as a function of redshift for all of our models and high-redshift DLAs. The DLA metallicity distribution, the cosmic evolution of DLA metallicities, the effects of metallicity gradients, and DLA kinematics are presented in sections 4.2.5 and 4.2.6. In Sections 4.2.5 and 4.2.6, we only consider the $f_j = 1$ and 2.5 models as the merger-based models have very similar metallicities to the $f_j = 1$ models. Additionally, we feel that our merger-based models are too crude to meaningfully attempt to predict the kinematics. We focus the majority of our analysis on the GKj25 and BRj25 models, since the $f_j = 1$ models fail to reproduce the column density distribution, the number of DLAs, and the mass of HI in DLAs (although the $f_j = 1$ models are actually the closest to the ‘fiducial’ model presented in previous SAMs, e.g. S08 and S12). The GKfj25 model produces a large number of low mass “pristine” halos, which experience no star formation and so contain gas close to the pre-enriched metallicity, which we believe to be unphysical. Note that in this chapter, we focus on the observational properties of the DLAs themselves. In the next chapter, we present the optical properties of the DLA host galaxies in our models.

4.2.1 Local Stellar and Cold Gas Mass Functions

The usual approach used in semi-analytic models is to calibrate the models using a subset of observations of $z \sim 0$ galaxies. The galaxy stellar mass function and cold gas fractions, or mass functions of cold gas, are commonly used quantities for this calibration procedure. A more extensive comparison with observations for the GKfj1, GKj1, and BRj1 models is presented in SPT14 and PST14. In addition, the BRj1 model produces extremely similar predictions to the models presented in S08 and S12. Here we examine the impact of varying

the H_2 formation recipe and the distribution of cold gas (f_j) on several fundamental calibration quantities: the local galaxy stellar mass function (GSMF), H I mass function (HIMF), and H_2 mass function (H2MF).

Figure 4.2 shows the $z = 0$ GSMFs, HIMFs, and H2MFs for all of our models. We do not show the GKfjm, GKjm, and BRjm mass functions as they are the same as the GKfj1, GKj1, and BRj1 models respectively, since the gas is redistributed only in post-processing. As can be seen in the top row, the predicted $z = 0$ stellar mass function is extremely similar for the $f_j = 1$ models, and is in reasonable agreement with observations of the local GSMF. The $f_j = 2.5$ models tend to produce too few galaxies with large stellar masses, with the largest discrepancy around the knee of the GSMF. Of the $f_j = 2.5$ models, the BRj25 model is in the best agreement with the observed GSMF. In the models with extended gas distributions, the lower gas densities cause star formation to be less efficient. In the GK models, H_2 formation is more efficient in gas with higher metallicity, but more H_2 is photo-dissociated if the UV background is high. In the GK model with a fixed UV background, star formation becomes very inefficient in low mass, low-metallicity halos. In the GK model with a varying UV background, the UV radiation field intensity is also lower in these low-mass halos, which goes in the opposite direction, leading to a larger net fraction of H_2 and therefore less suppression of star formation relative to the GKf model.

We also find that the GK and BR extended disk ($f_j = 2.5$) models produce reasonable agreement with the observed GSMF and galaxy star formation rate function for galaxies selected via their stellar emission at $z \sim 2$. We show these results along with a more detailed comparison of our model predictions with the optical properties of DLA host galaxies in the next chapter.

The middle row of Figure 4.2 shows the HIMFs for the models along with local 21-cm observations from the HIPASS and ALFALFA surveys (Zwaan et al. 2005a; Martin et al. 2010), which highlights the power of using cold gas observations to discriminate between models. None of our models matches the observed H I mass function well in detail. The BRj1 and GKj1 models provide the best match to the observations, but produce slightly too few systems with intermediate H I masses ($10^8 \text{ M}_\odot \lesssim M_{\text{HI}} \lesssim 10^{10} \text{ M}_\odot$). The GKfj1 model overproduces the number of systems with $M_{\text{HI}} \lesssim 10^{9.5} \text{ M}_\odot$. The BRj25 and GKj25 models

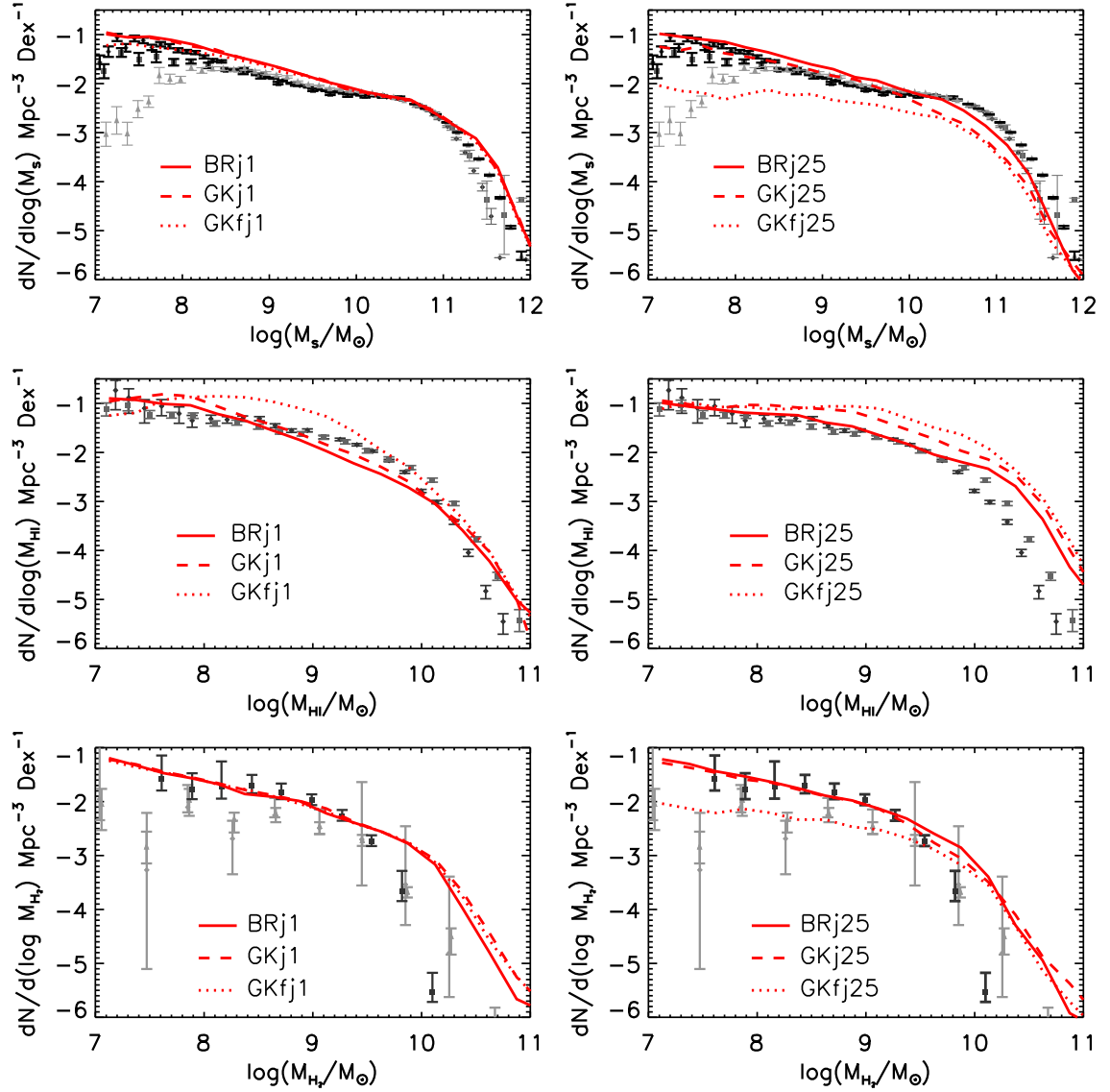


Figure 4.2 Top left - galaxy stellar mass functions (GSMFs) for all galaxies in the GKfj1 (dotted lines), GKj1 (dashed lines) and BRj1 (solid lines) models at $z = 0$. The local GSMFs are overplotted, with Baldry et al. (2008, 2012) in bold above and Panter et al. (2007) and Li & White (2009) in bold below $\log M_*/M_\odot = 10.65$ to emphasize where each is more reliable. Middle left - same as top left except for the HI mass functions at $z = 0$, with the local HIMF from Zwaan et al. (2005a, gray) and Martin et al. (2010, black) overplotted. Bottom left - same as top left except for the H₂ mass functions (H2MFs) at $z = 0$, with the local H2MFs for a constant and variable X_{CO} factor from Keres et al. (2003, gray) and Obreschkow et al. (2009, black) overplotted. Right column - similar to left column except for the GKfj25 (dotted lines), GKj25 (dashed lines) and BRj25 (solid lines) models. The middle panels highlight how the HI gas content of galaxies can help to constrain galaxy formation models.

are more successful at reproducing the slope of the observed HIMF at low masses, but significantly overpredict the number of systems with high HI masses. The GKfj25 model produces too many galaxies at all HI masses. In general, the model HIMFs show that galaxies in the fixed-UV GK models have more HI than in the varying-UV and BR models, for the reasons discussed above. Similarly, galaxies with more extended gas distributions have more HI and shallower slopes for their HIMFs than the traditional disc models.

The bottom row of Figure 4.2 shows the $z \sim 0$ H2MFs for the models along with the inferred H2MF from the FCRAO Extragalactic CO survey (Keres et al. 2003) assuming a constant $X_{CO} = 2 \times 10^{20}$ factor and using a variable X_{CO} factor as computed by Obreschkow et al. (2009). The H2MFs for the $f_j = 1$ models are almost identical to each other and are in good agreement with both observational estimates at low M_{H_2} , but overproduce the number of high- M_{H_2} systems. The predictions of the BRj25 and GKj25 models are very similar to the $f_j = 1$ models, but have a slightly better fit at high- H_2 mass. the GKfj25 model produces substantially fewer systems with low M_{H_2} , leading to a flatter H2MF low-mass end slope. For all four models, the high mass end of the H2MFs are in better agreement with the observational estimates of Keres et al. (2003), which assumed a constant conversion factor between CO and $H_2(X_{CO})$. However, the estimates obtained by Obreschkow et al. (2009) with a variable X_{CO} are likely to be more accurate. In Keres et al. (2003), the highest mass bin contains a number of CO luminous starburst galaxies. PST14 provide a more detailed comparison between the observed CO luminosity function and the $f_j = 1$ models.

In addition, PST14 show a comparison of the radial sizes of galaxies in the $f_j = 1$ models with observations, finding good agreement for the HI radii and SFR half-light radii from $z = 0$ to 2. The $f_j = 2.5$ models produce SFR half-light radii that are still consistent with observations at $z = 0$, but are about a factor of two larger than the $f_j = 1$ model disks at $z = 2$, in apparent conflict with observations. However, it is unknown to what extent the observed $z \sim 2$ star forming galaxies may be biased towards compact objects, due to selection. PST14 also show the ratio of HI mass to stellar mass, ratio of H_2 mass to stellar mass, and ratio of HI to H_2 mass, as a function of galaxy stellar mass and surface density, showing good agreement with observations for $z = 0$ disk-dominated galaxies in the $f_j = 1$ models. We have carried out this comparison for the $f_j = 2.5$ models as well, and find that

relative to the $f_j = 1$ models they tend to produce slightly higher gas fractions overall, and slightly less H_2 relative to H I . However, the results are still within the uncertainty on the observational values.

4.2.2 Column Density Distribution

The H I column density distribution function, $f(N_{\text{HI}}, X)$, is one of the best constrained observational quantities for H I absorption systems. It is defined as the number of absorbers with column densities in the range $[N_{\text{HI}}, N_{\text{HI}} + dN_{\text{HI}}]$ per comoving absorption length $[X, X + dX]$

$$f_{\text{HI}}(N_{\text{HI}}, X) dN_{\text{HI}} dX = n_{\text{DLA}}(N_{\text{HI}}, X) \quad (4.2)$$

where $dX = \frac{H_0}{H(z)}(1+z)^2 dz$. Absorption systems with a constant comoving density and proper size have a constant density per unit X along the sight-line. Observations indicate only mild evolution in the column density distribution function with redshift (e.g. Prochaska & Wolfe 2009).

The top panel of Figure 4.3 shows the predicted column density distribution function at $2 < z < 3.5$ for the $f_j = 1$ models in the range $10^{19} < N_{\text{HI}} < 10^{22.5} \text{ cm}^{-2}$ compared with the SDSS DR9 results from Noterdaeme et al. (2012) and observations of sub-DLAs ($10^{19} < N_{\text{HI}}$) from Zafar et al. (2013). We can see that all models do moderately well at reproducing the number of high column density systems, but greatly underproduce the lower column density systems. This result has been shown before by Maller et al. (2001), and may indicate that the gas discs in the $f_j = 1$ models are too compact. An alternative is that there are a large number of DLAs that are hosted in haloes below our resolution limit or that do not arise from gas in galactic discs, although neither of these effects seems to be very likely to make a large contribution, based on recent results from numerical simulations (e.g. Fumagalli et al. 2011; Cen 2012). In addition, we find this scenario to be unlikely as they would have small velocity widths, inconsistent with observations.

Historically, no DLAs were known with column densities $\log N_{\text{HI}} > 10^{22} \text{ cm}^{-2}$, and simulations had difficulty reproducing this very sharp cutoff (e.g. Nagamine et al. 2004a;

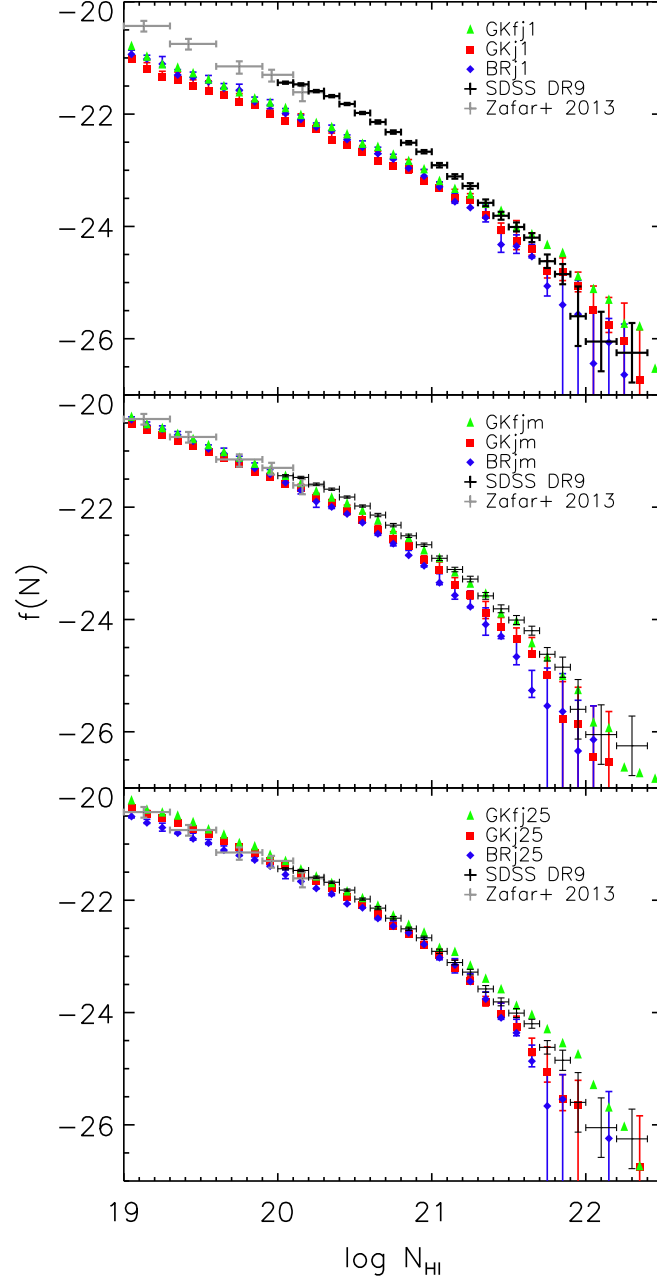


Figure 4.3 Top panel - column density distribution function for HI absorption systems in the $f_j = 1$ models (GKfj1: green triangles; GKj1: red squares; BRj1: blue diamonds) in the redshift range $2 < z < 3.5$. Middle panel - same as top except for the $f_j = 2.5$ models. Bottom panel - same as top except for the merger models (GKfj25: green triangles; GKj25: red squares; BRj25: blue diamonds). The model errors represent the maximum field-to-field variation for four subfields of $0.5 \times 0.5 \text{ deg}^{-2}$. The fixed- and varying-UV GK models have similar errors. The SDSS DR9 results from Noterdaeme et al. (2012) are overplotted in black and the sub-DLA results from Zafar et al. (2013) in gray. The $f_j = 1$ models have a shallower slope in $f(N_{\text{HI}})$, causing them to produce too few low- N_{HI} systems, which is most apparent at $\log N_{\text{HI}} < 21$. The $f_j = 2.5$ models provide the closest fit and are a good match to the data.

Pontzen et al. 2008). Recently, larger volume surveys such as SDSS DR9 have revealed that although rare, these high HI column density systems do exist. We note that, in the paradigm in which metallicity is a fundamental parameter controlling the HI-H₂ transition, it is more likely to produce high HI column density systems at high redshift as the threshold density for forming H₂ becomes higher for lower metallicity gas (e.g. Schaye 2004; Erkal et al. 2012). In our models, this is reflected in the larger numbers of high column density systems predicted in the metallicity-dependent GK models. We include HII gas, but find it makes no significant difference to the predicted column density distribution.

Motivated by the discrepancies in the number of low column density systems in the models with $f_j = 1$, we explore a simple model with a more extended distribution of cold gas with $f_j = 2.5$. The bottom panel in Figure 4.3 shows the column density distribution for the GKfj25, GKj25, and BRj25 models. These ‘extended gas’ models do significantly better than the $f_j = 1$ models at matching the observed column density distribution function, reproducing the general shape of the column density distribution over a wide range of column densities. The BRj25 model is not as successful at reproducing the number of DLAs at all column densities especially at high- N_{HI} specifically at $\log N_{\text{HI}} \gtrsim 21.6$, although uncertainties due to cosmic variance are larger in this regime. Again, all models produce DLAs with $\log N_{\text{HI}} \gtrsim 22 \text{ cm}^{-2}$, although they are rarer in the BRj25 model than the GK models, due to the differing amount of gas and the density threshold for the HI-H₂ transition, discussed further below. The success of the $f_j = 2.5$ models suggests that either the gas that forms discs has higher specific angular momentum than the dark matter halo material, or DLAs arise from gas in an alternate extended distribution such as an outflow or tidal tails, although we have not specifically modeled these configurations here. The picture of DLAs arising from extended gas is supported by numerical simulations, which have shown that stellar driven winds can preferentially remove low-angular momentum material, leading to a higher average specific angular momentum (e.g. Brooks et al. 2011). In addition, the gas specific angular momentum can also be boosted by cold flows and mergers (Robertson et al. 2006a; Agertz et al. 2011; Stewart et al. 2013).

To explore the possible boosting of specific angular momentum by mergers, we also consider a simple merger-based model in which f_j is increased following major and minor

mergers, as described in Section 3.1.3. The resulting column density distribution for the GKfjm, GKjm, and BRjm models is shown in the middle panel of Figure 4.3. Interestingly, these simple models do fairly well at reproducing the column density distribution over the whole range shown, much better than the $f_j = 1$ models, although they slightly underproduce the number of DLAs at all N_{HI} . As they contain the same amount of HI as the $f_j = 1$ models, their success suggests that the cold gas may be in an extended distribution in a subset of galaxies due to the conditions of their formation.

At the low- N_{HI} end of the column density distribution, sub-DLAs ($19 < \log N_{\text{HI}} < 20.3$) in the $f_j = 2.5$ models are in agreement with the results of Zafar et al. (2013), although our results become more uncertain at $\log N_{\text{HI}} \lesssim 19.5$. Low column density systems are more likely to have been produced in outflows and filaments of cold gas. Furthermore, the distribution of gas in exponential discs likely does not extend smoothly down to arbitrarily low- N_{HI} , and haloes below our mass resolution ($\log M_h / M_\odot < 9.5$) may also make a significant contribution to sub-DLAs. Therefore, we restrict the rest of our analysis to systems selected as DLAs ($\log N_{\text{HI}} > 20.3 \text{ atoms cm}^{-2}$) as the majority are likely produced in cold dense gas that is closely associated with galaxies.

Figure 4.4 shows the column density distribution function at $2 < z < 2.5$, $2.5 < z < 3.5$, and $3.5 < z < 4.5$ for the GKj25 and BRj25 models with the SDSS DR5 observations at the same redshifts overplotted (Prochaska & Wolfe 2009). The models at $2 < z < 3.5$ are consistent with observations, although at $3.5 < z < 4.5$, both produce fewer DLAs than are observed. The shape of the column density distribution functions become flatter at higher redshifts in both models, consistent with observations. However, in the models this flattening results in a reduced number of low- N_{HI} systems in the highest redshift bin, which is in conflict with observations. All of our models fail to reproduce the observed number of DLAs at $z \gtrsim 3$ (see section 4.2.3), and we see this here reflected in the column density distribution.

We also show the column density distribution function of the BRj25 and GKj25 models where gas is left unpartitioned, BRj25-up and GKj25-up respectively. In these models, the total cold neutral gas density, regardless of whether it is in HI or H₂, is used to compute the column density, as in most previous models. These models allow us to study the effect

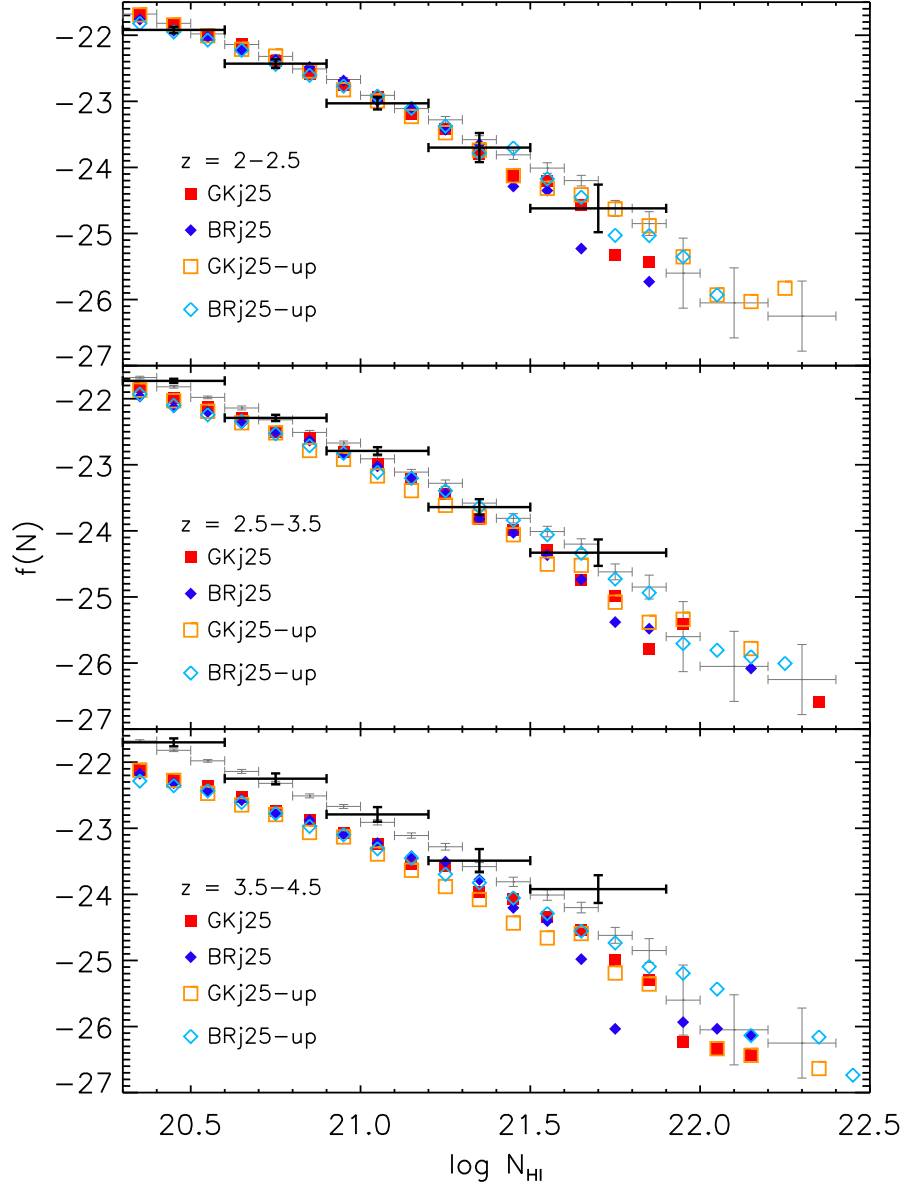


Figure 4.4 Similar to Figure 4.3 except the column density distribution function is plotted for DLAs at redshifts $2 < z < 2.5$ (top), $2.5 < z < 3.5$ (middle), and $3.5 < z < 4.5$ (bottom) in the GKj25 (red squares) and BRj25 (blue diamonds) models. Open points show the total cold neutral gas column density including H_2 . Observations from SDSS DR5 (Prochaska & Wolfe 2009) at the same redshifts are overplotted (black), along with the SDSS DR9 results at $2 < z < 3.5$ (gray) for reference. Both the models and observations show a flattening of the column density distribution at higher redshifts. Each model shows a decline in the number of low- N_{HI} DLAs with redshift yet a comparable number of high- N_{HI} DLAs. At $3.5 < z < 4.5$, observations produce this flattening with more high- N_{HI} DLAs. Additionally, the unpartitioned models indicate that the HI-H_2 transition becomes important at $\log N_{\text{HI}} \sim 21.7$, in qualitative agreement with the observations.

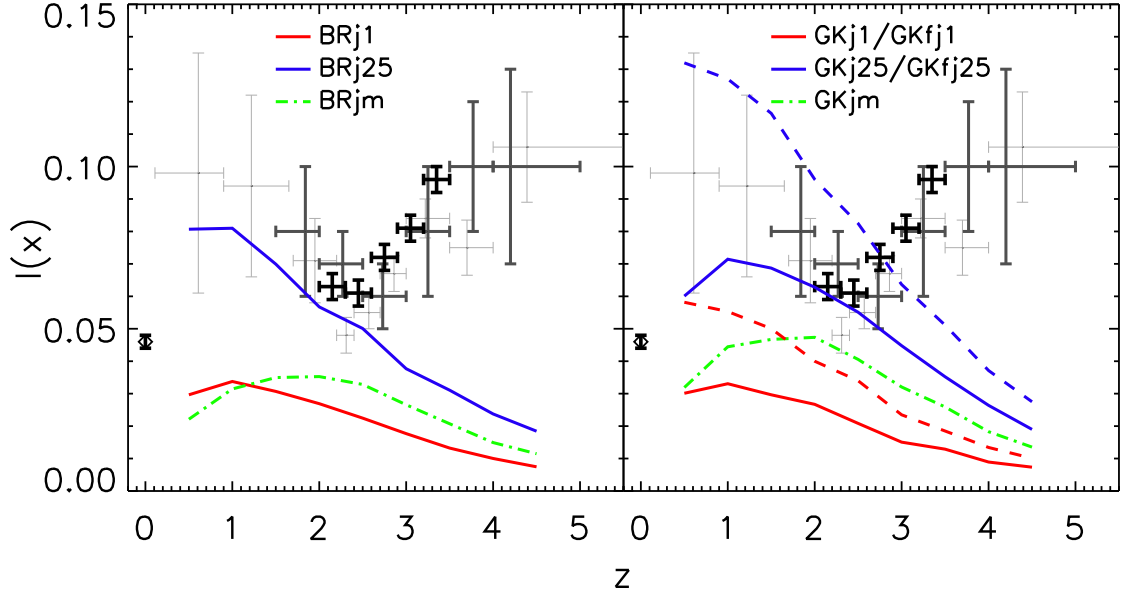


Figure 4.5 Left panel - the comoving line density of DLAs as a function of redshift for the BRj1 (red), BRj25 (blue), and BRjm (green dot-dashed) models. Right panel - same as the left except for the GKj1, GKjm, and GKj25 models with the GKfj1 and GKfj25 models (dashed) overplotted. Observations of Mg II absorbers (Rao et al. 2006) and high-redshift DLAs from Prochaska & Wolfe (2009) are overplotted in light gray while those from Zafar et al. (2013) are shown in dark gray. Observations of local galaxies (Zwaan et al. 2005b) and high-redshift DLAs (Noterdaeme et al. 2012) are overplotted in black. All models fail at $z > 3$, and the $f_j = 1$ models produce too few DLAs at all redshifts. The BRj25 and GKj25 models are in the best agreement with the observations at $z \lesssim 2.5$, and the merger models are only a modest improvement over the $f_j = 1$ models.

of multiphase partitioning on the column density distribution function. We can see by comparing the partitioned and unpartitioned models that the HI-H₂ transition does lead to a slightly steeper drop in the number of high column density systems. This transition can be seen in Figure 4.4 at $\log N_{\text{HI}} \sim 21.7$, qualitatively consistent with observations. The small number of high- N_{HI} systems causes there to be significant scatter at high column densities. Both models produce more DLAs with very high column densities at higher redshifts, while these very high- N_{HI} DLAs are only seen in the unpartitioned models at $z \sim 2$, suggesting that the HI-H₂ transition may occur at lower density at high redshift.

4.2.3 Comoving line density and $\Omega_g(z)$

The column density distribution function gives the number of DLAs per unit absorption path length for a given column density. The zeroth moment of this distribution is the line density of DLAs, which measures the number of DLAs per comoving absorption distance:

$$l_{\text{DLA}}(X)dX = \int_{N_{20.3}}^{\infty} f_{\text{HI}}(N, X)dN dX \quad (4.3)$$

Figure 4.5 shows the comoving line density of DLAs as a function of redshift for the BR models (left) and fixed- and varying-UV GK models (right). Observational estimates of the line density of high redshift DLAs from Prochaska & Wolfe (2009) and Noterdaeme et al. (2012), and that inferred from Mg II absorbers from Rao et al. (2006) are also overplotted. As compared to the $f_j = 1$ models, the larger HI masses in the BRj25 and GKj25 models, discussed in Section 4.2.1, are also reflected in the larger number of DLAs at all redshifts, in much better agreement with observations at $z \lesssim 2.5$. The compact gas distributions of galaxies in the $f_j = 1$ models cannot reproduce the observed number of DLAs at any redshift. Additionally, the merger-based models are only a modest improvement over the $f_j = 1$ models. Relative to the other models, the GKfj25 model gives rise to significantly more DLAs at all redshifts. As we will see later, a large number of DLAs in the GKfj25 model are hosted in low mass dark matter haloes. These systems have low metallicity, and in the GKf models, they are inefficient at converting gas into H₂ and subsequently into stars, so they have large HI masses. Therefore a large number are selected as DLAs, boosting the

line density. The BRj25 and GKj25 models produce the best agreement with the data at $z < 3$.

At $z > 3$, all of our models produce far too few DLAs, and show the opposite trend as observations (the number density of DLAs decreases, rather than increases, with increasing redshift). The reasons for this fairly dramatic discrepancy are unclear. Two possible explanations are that an increasing number of DLAs are associated with gas in filaments or outflows at higher redshifts, or that the distribution of gas in galactic discs evolves over cosmic time. Note that the gas would have to be *more extended* at higher redshifts to alleviate this discrepancy.

Fumagalli et al. (2011) and Cen (2012) found that large amounts of DLA column density gas arise in filaments extending up to the virial radius at $z = 4$. This fraction of DLA column density gas in filamentary structures is significant at $z \gtrsim 3$ and decreases monotonically with cosmic time, in keeping with the discrepancy between our models and observations. Moreover, the majority of missing DLAs in our models are at low- N_{HI} , as would be expected for intergalactic DLAs. If intergalactic DLAs, produced for example in filaments of cold gas, make up a significant fraction of the DLA population, then many DLAs will not be included in our models. Alternatively, if a significant number of high-redshift DLAs are associated with haloes of mass $\log (M_h / M_\odot) < 10$, then the discrepancy might be a resolution effect since our simulations are incomplete below this mass. Since DLA metallicities at these redshifts are very low, and the formation of H_2 in this regime is not well-understood, the amount of neutral hydrogen gas in a given halo and the number of DLAs may be affected.

Using the column density distribution function and the comoving line density of DLAs, we can calculate the total neutral hydrogen gas mass density in DLAs using:

$$\Omega_{\text{DLA}} = \frac{m_H H_0}{c \rho_{c,0}} \frac{\sum N(\text{HI})}{\Delta X} \quad (4.4)$$

where m_H is the mass of the hydrogen atom, H_0 is the Hubble constant, $\rho_{c,0}$ is the critical density at $z = 0$, and the sum is calculated for systems with $\log N(\text{HI}) > 20.3$ across a total absorption pathlength of ΔX . Figure 4.6 shows the total cold gas density ($\Omega_{\text{HI}+\text{H}_2}(z)$), neutral hydrogen density in all galaxies ($\Omega_{\text{HI}}(z)$), and the neutral hydrogen density inferred

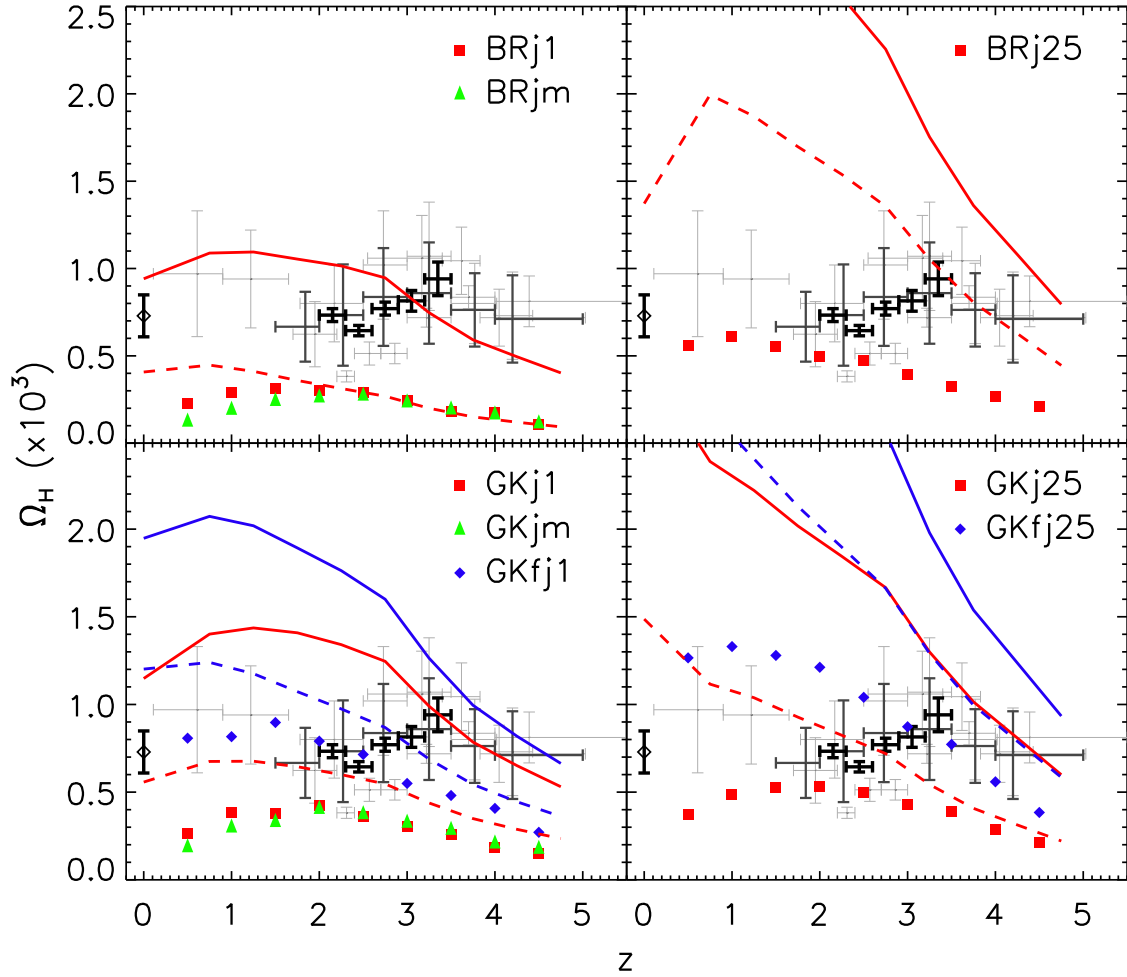


Figure 4.6 The cosmic density of HI contained in DLAs (Ω_{DLA}) as a function of redshift (solid shapes) and the amount of HI in all galaxies (Ω_{HI} ; dashed line) along with the total amount of cold neutral gas in all galaxies $\Omega_{\text{HI}+\text{H}_2}$ (solid line). Observations of DLAs and Mg II absorbers (Zwaan et al. 2005a; Péroux et al. 2005; Rao et al. 2006; Prochaska & Wolfe 2009; Noterdaeme et al. 2009; Guimarães et al. 2009) are overplotted in light gray. The dark gray observations of DLAs and sub-DLAs are from Zafar et al. (2013). Both the SDSS DR9 observations of high-redshift DLAs (Noterdaeme et al. 2012) and observations of local galaxies (Braun 2012) are shown in black. Upper left panel - BRj1 (red squares) and BRjm (green triangles) models. Upper right panel - BRj25 model. Lower left panel - GKfj1 (blue diamonds), GKj1 (red squares), and GKjm (green triangles) models. Lower right panel - GKfj25 (blue diamonds) and GKj25 (red squares) models. The BRj25, GKj25, and GKfj1 models are in reasonable agreement with observations at $z \lesssim 2.5$ while the GKj1, BRj1, and merger-based models underproduce Ω_{DLA} at all redshifts. The GKfj25 model is the only model that is remotely close to the data at $z \gtrsim 2.5$, but it predicts Ω_{DLA} somewhat higher than observational measurements at lower redshift, and the column density distribution is in conflict with observations.

from systems selected as DLAs (Ω_{DLA}) in the BRj1 and BRjm (top left) models; BRj25 (top right) model; GKfj1, GKj1, and GKjm (bottom left) models; and GKfj25 and GKj25 (bottom right) models. Observational estimates of $\Omega_{\text{DLA}}(z)$ from DLAs and Mg II absorbers are overplotted for reference (Péroux et al. 2005; Rao et al. 2006; Noterdaeme et al. 2009; Prochaska & Wolfe 2009; Guimarães et al. 2009; Braun 2012; Noterdaeme et al. 2012). As can be seen in Figure 4.6, the $f_j = 1$ and merger-based models underproduce the amount of $\Omega_{\text{DLA}}(z)$. The GKfj1, GKj25 and BRj25 models produce the best fit to the $\Omega_{\text{DLA}}(z)$ distribution. The GKfj1 model produces too few DLAs and too many high- N_{HI} DLAs (see Figure 4.3), causing it to be a coincidence that it reproduces the observed amount of Ω_{DLA} . On the other hand, the GKfj25 model produces too much HI while the BRj1, GKj1, and merger-based models produce too little HI at these redshifts. This is consistent with the conclusions drawn from their respective column density distribution functions and comoving line densities. As already anticipated from Figure 4.5, all of our models contain less HI in DLAs than is observed at $z \gtrsim 3$. Only the GKfj25 model is marginally consistent with the observations at these redshifts.

Note that the different models make different predictions for the total amount of cold gas in galaxies, as well as for the amount of HI in galaxies and the fraction of HI in systems that would have been selected as DLAs. The GKfj25 model predicts the largest amount of cold gas overall, as well as the highest values of $\Omega_{\text{HI}}(z)$ and $\Omega_{\text{DLA}}(z)$. This is because in this model, a lot of gas has low metallicity and is at low surface density, leading to inefficient H_2 formation and star formation in many systems. It is interesting to note that while the total cold gas density and Ω_{HI} tend to rise with decreasing redshift in all models, the fraction of gas in systems that are selected as DLAs decreases, leading to a flatter dependence of Ω_{DLA} on redshift, in better agreement with observations. Overall, the $f_j = 2.5$ models predict a lower fraction of HI to be contained in DLAs than the $f_j = 1$ models. As high- N_{HI} systems make the largest contribution to Ω_{DLA} and the $f_j = 1$ models have relatively more high- N_{HI} DLAs due to a flatter column density distribution function, we expect a larger fraction of the total cold gas to come from the central regions of galaxies. Although there are more DLAs in the GKjm and BRjm models, the reduced number of high- N_{HI} systems is evident as $\Omega_{\text{DLA}}(z)$ for the GKjm model is comparable to the GKj1 and BRj1 models at all redshifts.

An overproduction of high- N_{HI} DLAs in the BRj1 model causes the inferred amount of HI in DLAs at $z \sim 4$ to be slightly *larger* than the total amount in all galaxies. In spite of a significant decrease in the number density of DLAs at $z > 3$ in all models, the $\Omega_{\text{DLA}}(z)$ distribution remains relatively flat. This result is in agreement with the flattening of the column density distribution as was discussed in section 4.2.2.

Returning to the discrepancy between our model predictions and observations at $z \gtrsim 3$, it is first interesting to note that in the BRj1 model, even the *total* cold gas density at $z \gtrsim 3$ is lower than the observational estimates of Ω_{HI} from DLAs. Indeed, this model is quite similar to the model presented in S08, and this discrepancy has already been pointed out in that work (see their Figure 14). It can also be seen from the results presented in S08 that the predicted $\Omega_{\text{HI}+\text{H}_2}$ at high redshift is quite sensitive to the assumed cosmological parameters, in particular the power spectrum normalization σ_8 . This suggests that part of the problem may be due to too-efficient star formation and/or overly efficient ejection of gas by strong stellar winds at these epochs in these models.

At redshifts $z < 2$, all of the models predict a relatively flat dependence of Ω_{DLA} on redshift, in qualitative agreement with observations, although the normalization is too low in the BRj1/BRjm models and a bit high in the GKfj25 model. This is the case even in models (BRj25, GKj25) with much more rapidly rising total gas density and Ω_{HI} . The large amount of HI in galaxies that would not be selected as DLAs in the BRj25 and GKj25 models arises from HI in lower column density systems in low mass haloes ($\log M_h / M_\odot < 10$), which have low gas surface densities and small DLA cross sections.

Taken together, our model results suggest that the rather flat dependence of Ω_{DLA} on cosmic time from $4.5 \gtrsim z \gtrsim 1$ derived from observations of DLAs could be a cosmic coincidence: at $z \gtrsim 3$, Ω_{DLA} may be ‘contaminated’ by cold gas that is not closely associated with galaxies, while at lower redshifts ($z \lesssim 3$), Ω_{DLA} may significantly underestimate the total atomic gas content of all galaxies. These results show the danger in assuming that $\Omega_{\text{DLA}} = \Omega_{\text{cold}}$ or even Ω_{HI} .

4.2.4 DLA Halo Masses and Cross-sections

The DLA cross section represents the area in kpc^2 for which a galaxy's gas surface density (corrected for inclination) would be high enough for it to be selected as a DLA. It is straightforward to compute this quantity in our models, as using our assumed density profile we can easily compute the projected area within which the column density is greater than $\log N_{\text{HI}} > 20.3$, which is its DLA cross section. Figure 4.7 shows the distribution of DLA cross sections as a function of halo mass for our sample of DLAs in the GKj1, GKj25, and BRj25 models at redshifts $z = 1$, $z = 2$, $z = 3$, and $z = 4$. We only show these models as each of the $f_j = 1$ models has a similar distribution of DLA cross sections at a given halo mass as the GKj1 model. The GKj25 and GKfj25 models are also similar.

We can see that in all models and at all redshifts, DLAs are predicted to occupy haloes with a fairly broad range of masses, $10^{10} M_{\odot} \lesssim M_h \lesssim 10^{12} M_{\odot}$. Moreover, the DLA cross-section versus halo mass relation evolves mildly with time in any of the models. This has implications for DLA kinematics which we explore in a later section.

The DLA cross-section at a given halo mass grows with cosmic time in all of our models. By $z = 1$, DLAs in the $f_j = 2.5$ models have halo masses and DLA cross sections that are both typically ~ 1.5 decades larger than at higher redshift while they both span a similar dynamic range. Conversely in the $f_j = 1$ models, there is a significant fraction of small, compact DLAs at all redshifts and evolution is seen as an increase in the number of higher mass DLAs. Additionally, our merger tree mass resolution limit of $M_{\text{res}} = 10^{9.5} M_{\odot}$ and the completeness limit of the host halo catalog ($V_{\text{vir}} = 50 \text{ km s}^{-1}$) also significantly reduces the number of low mass DLAs. These effects are relatively small at low redshift, especially in the $f_j = 2.5$ models. However the average halo mass decreases with increasing redshift causing the mass resolution of our models to become increasingly important, especially in the $f_j = 1$ models.

Recently using observations of DLAs at $2 < z < 3.5$ from the BOSS survey, Font-Ribera et al. (2012, hereafter FR12) found that DLAs with a mean redshift of $\langle z \rangle = 2.3$, have a large range of halo masses with an average halo mass of $M_h = 6 \times 10^{11} M_{\odot}$. For DLAs residing in haloes of mass $M_h \sim 10^{12} M_{\odot}$, they also find a mean DLA cross-section of

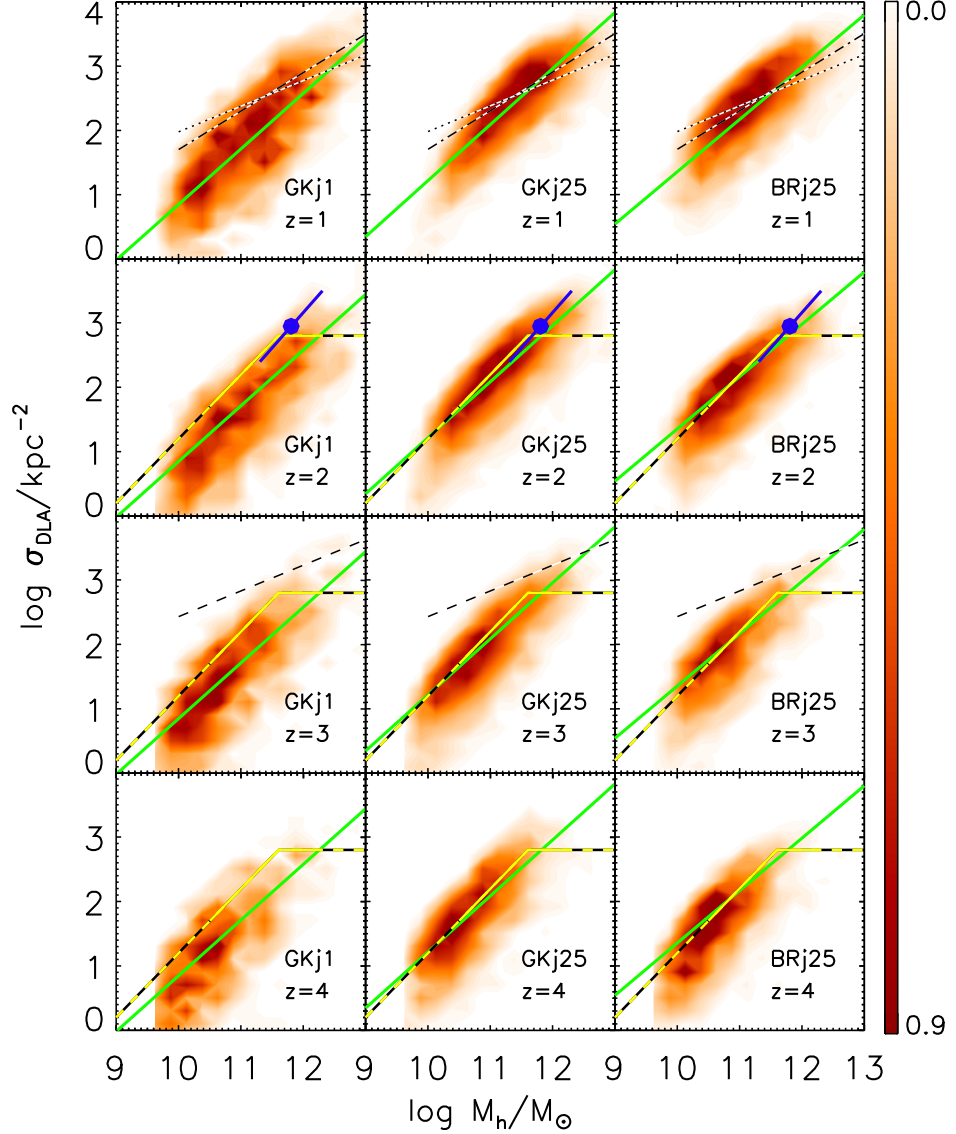


Figure 4.7 Number density distribution of DLA cross section versus halo mass for our sample of DLAs in the GKj1 (left column), GKj25 (middle column), and BRj25 (right column) models at $0.5 < z < 1.5$ (top row), $1.5 < z < 2.5$ (second row), $2.5 < z < 3.5$ (third row), $3.5 < z < 4.5$ (bottom row) with the best-fit slope of the $\sigma_{\text{DLA}} - M_h$ relation for each model at $z = 2$ (green line). At high halo masses, the $\sigma_{\text{DLA}} - M_h$ relation flattens. The data point (blue circle and line) from Font-Ribera et al. (2012) shows their estimate for σ_{DLA} at $\langle z \rangle = 2.3$ with the best-fit $\sigma_{\text{DLA}} - M_h$ slope. We also show the range of σ_{DLA} values and halo masses at $z \sim 3$ for several sets of numerical simulations: the best-fit power law at $1.4 < z < 4$ of Fumagalli et al. (2011, measured, yellow; extrapolated, yellow-black); and the best-fit power laws at $z = 1$ (dotted), $z = 1.6$ (dot-dashed), and $z = 3$ (dashed) from Cen (2012). Compared to Font-Ribera et al. (2012), σ_{DLA} , M_h , and α in the GKj25 model are in the best agreement. Conversely, the $f_j = 1$ models produce σ_{DLA} and α values that are significantly lower than Font-Ribera et al. (2012).

Table 4.1 Halo mass vs. DLA cross-section ($M_h - \sigma_{DLA}$) Relation

	GKfj1	GKfj25	GKj1	GKj25	BRj1	BRj25	FR12
$\langle \log M_h/M_\odot \rangle$	4.9×10^{10}	5.3×10^{10}	8.3×10^{10}	1.1×10^{11}	8.5×10^{10}	8.6×10^{10}	6×10^{11}
$\langle \sigma_{DLA}/\text{kpc}^{-2} \rangle^*$	490 ± 450	1030 ± 740	570 ± 660	1120 ± 850	570 ± 660	900 ± 710	1400
α	0.86	0.86	0.90	0.91	0.78	0.88	1.1 ± 0.1

Our results for DLAs at $\langle z \rangle = 2.3$ correspond to the same mean redshift as Font-Ribera et al. (2012). Note, α changes with halo mass where higher mass halos have flatter $M_h - \sigma_{DLA}$ relations.

* for DLAs with $11.8 < \log M_h/M_\odot < 12.2$ where the errors show the scatter about the mean.

$\sigma_{DLA} = 1400 \text{ kpc}^2$, and a $\sigma_{DLA} - M_h$ relation that scales as $\sigma_{DLA} \propto M_h^\alpha$ where $\alpha = 1.1 \pm 0.1$ with a minimum halo mass of $M_h = 10^9 M_\odot$. In order to make an accurate comparison to Font-Ribera et al. (2012), we select all DLAs in each of our models with redshifts $2 < z < 2.6$, which corresponds to a mean redshift of $\langle z \rangle = 2.3$. Table 4.1 shows our M_h , σ_{DLA} , and α values for DLAs in each of our models. Our $f_j = 2.5$ models produce DLAs with halo masses and DLA cross sections that are the most similar to Font-Ribera et al. (2012). The BRj25 and GKj25 models produce slopes of $\alpha \sim 0.9$, significantly flatter than that calculated in FR12. The second row of Figure 4.7 shows model DLAs that are at a comparable redshift to these observations. This also shows that the $f_j = 2.5$ models produce the most comparable DLA cross sections in massive haloes $M_h \simeq 10^{12} M_\odot$ as FR12. The $f_j = 1$ models produce significantly lower values of σ_{DLA} .

Font-Ribera et al. (2012) also find that DLA halo mass does not correlate with column density. This result indicates that the column density distribution function has a similar shape at low and high halo mass. When we divide our sample in half based on halo mass ($\log M_h/M_\odot > 10^{11}$, $\log M_h/M_\odot < 10^{11}$), we also find no correlation between DLA halo mass and column density. The results of Font-Ribera et al. (2012) strongly support the picture of a significant population of DLAs at $z \sim 2.3$ arising from extended gas associated with more massive galaxies.

We also compare our results to predictions from several different numerical hydrodynamic simulations. We overplot the results from Fumagalli et al. (2011) at $z = 1.4 - 4$, and at $z = 1.0, 1.6, 3.1$ from Cen (2012) in Figure 4.7. DLAs in the GKj1 model are more compact than DLAs observed in any numerical simulation at any redshift. In contrast, the BRj25 and GKj25 models are in very good agreement with the results of Fumagalli et al. (2011). Our $f_j = 2.5$ models are in fair agreement with the predictions of Cen (2012) at

$z = 1$ while DLAs in our models have a much steeper $\sigma_{\text{DLA}} - M_h$ relation. At $z \sim 3$, Cen (2012) finds much larger σ_{DLA} values at a given halo mass than our models or the other simulations predict. This appears to be due to outflows boosting the DLA cross-section. Our models do not directly model outflows, although they may indirectly contribute to our extended disk models. Note that an increasing contribution to the DLA cross-section from outflows or filaments with increasing redshift could manifest in just this way, as larger values of σ_{DLA} at a given halo mass.

At $z \sim 4$, more DLAs may arise in haloes below our resolution limit since our models show a decrease in halo mass and σ_{DLA} with redshift, especially in the GKj1 model. However, the gas fraction in haloes with $\log M_h/M_\odot \lesssim 9.5$ also drops rapidly due to the “squelching” of gas infall by the photoionizing background after re-ionization implemented in our models. At $z < 3$, the steep slope and low fraction of low-halo mass DLAs ($M_h \sim 10^{10} M_\odot$) in the $f_j = 2.5$ models suggests that there are likely not many DLAs arising in haloes below our resolution limit. If σ_{DLA} at a given halo mass also increased with redshift, then we would expect even more DLAs to arise in these low mass haloes. Both Fumagalli et al. (2011) and Cen (2012) discuss the contribution of DLAs arising from streams and clumps to the DLA population at higher redshifts, although the simulations from Cen (2012) only probe haloes more massive than $M_h > 10^{10.5} M_\odot$. At $z \sim 3 - 4$, both find that a large fraction of DLAs originate in filamentary structures and gas clumps extending as far as the virial radius. Conversely at $z < 3$, these intergalactic DLAs make a much smaller contribution to the total DLA population, in keeping with the picture suggested by our results.

4.2.5 Metallicities

Figure 4.8 shows the distribution of cold gas-phase metallicities for all galaxies identified as DLAs at $2 < z < 3.5$ in all of our models compared with SDSS-DR3 and SDSS-DR5 results from observed DLAs in the same redshift range from Rafelski et al. (2012). In this initial set of plots, we show the mass-weighted mean metallicity of the cold gas in our model galaxies. Later, we consider the effects of metallicity gradients.

Our $f_j = 1$ and GKj25 models show a roughly lognormal distribution of DLA metallicities with a peak around $\log Z \sim -0.8$. Both the fixed-UV models show flatter distributions

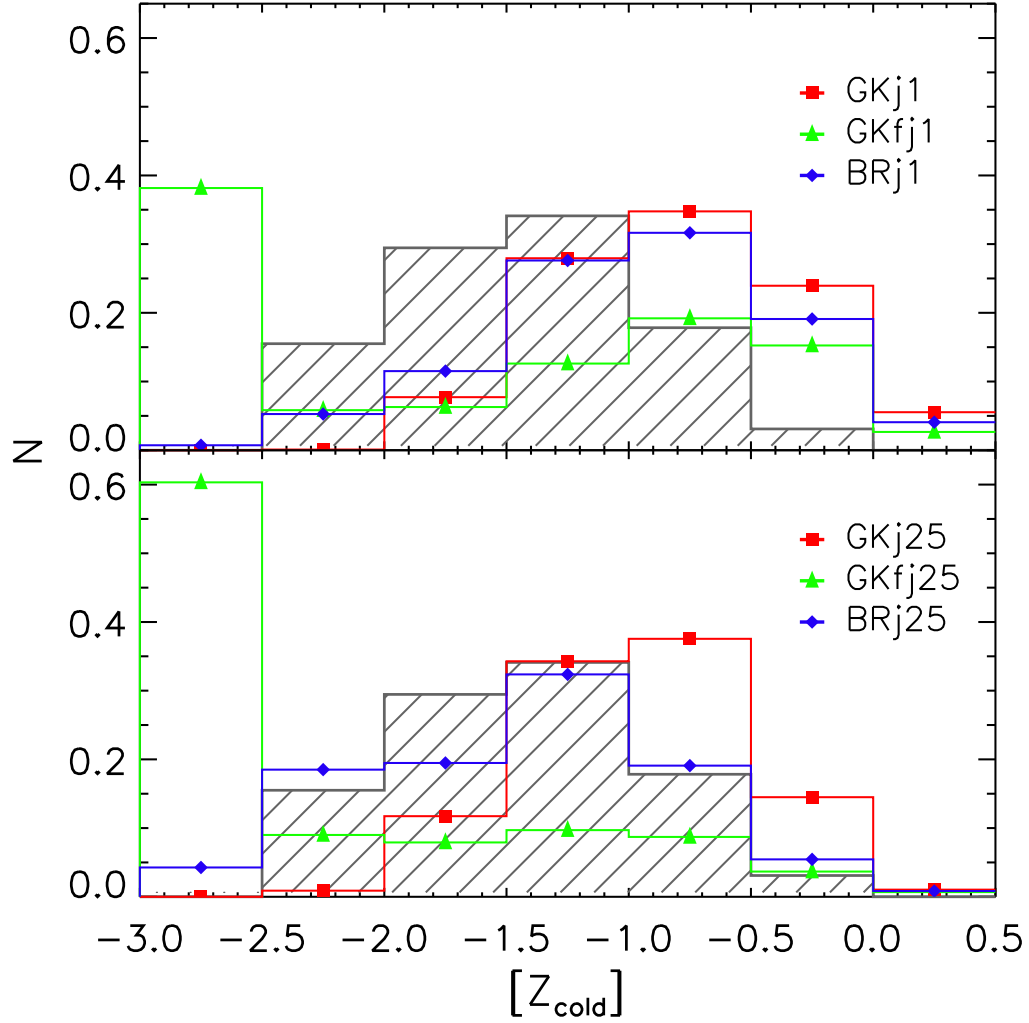


Figure 4.8 Upper panel - distribution of metallicities for all DLAs in the redshift range $2 < z < 3.5$ for the GKfj1 (red), GKj1 (green), and BRj1 (blue) models in the upper panel. Lower panel - same as top except for the GKfj25 (red), GKj25 (green), and BRj25 (blue) models. The observed distribution of DLA metallicities in the same redshift range are overplotted in gray (Rafelski et al. 2012). All the models except GKfj25 produce a distribution with a width similar to that of the observed one, with the BRj25 model producing the best agreement with the observed DLA metallicity distribution. The GKfj1 and GKfj25 models produce a significant number of DLAs with metallicities near the “pre-enriched” metallicity ($\log Z = -3$).

with a large fraction of DLAs with metallicities near the pre-enriched metallicity of $\log Z \sim -3$, indicating that a substantial number have never undergone significant star formation. We discuss these interesting systems further in a moment. DLAs in the merger-based models exhibit metallicity distributions very similar to the $f_j = 1$ models, and so are not shown. Both the GKj25 and the BRj25 models are a good fit to the observed metallicity distribution in both the average metallicity and width. We note that at $z > 3$, our models begin to miss a substantial fraction of DLAs, which likely have lower metallicities on average. This would have the effect of skewing the observed distribution to lower metallicities.

The population of very low metallicity, H_I-rich, nearly “pristine” galaxies predicted by the metallicity-based, fixed-UV GK models is interesting. Scaling the UV radiation field by the galaxy’s star formation rate increases the H₂ fraction in low mass galaxies relative to the model with a UV field fixed to the MW value, allowing these galaxies to form significant stellar components. In the fixed-UV models, the “pristine” galaxies are hosted by low-mass haloes ($\log (M_h/M_\odot) \lesssim 10$) and have stellar masses below $\log M_*/M_\odot < 6.5$. A feature of the metallicity-based picture for H₂ formation is that if gas is low metallicity and low density, H₂ formation is extremely inefficient, the galaxy forms few stars and the gas never becomes enriched, so star formation stalls out. Star formation can be “kick-started” — if the galaxy manages to form even a small amount of stars, e.g., through a merger-triggered burst, this enriches the gas leading to more star formation and enrichment, and the galaxies rather quickly become enriched to significant levels — hence the double peaked distribution. The population of “pristine” haloes is more prevalent in the GKfj25 model because the extended gas configuration leads to more low surface density gas. A similar population has recently been reported in numerical hydrodynamic simulations using a similar metallicity-based prescription for H₂ formation (Kuhlen et al. 2013). It is interesting that DLAs are observed down to $\log Z = -2.5$, but no DLAs have been conclusively shown to have metallicities as low as the “pristine” haloes in the fixed-UV GK models, although they could have been detected if they existed. The presence of a DLA metallicity floor of $\log Z \gtrsim -2.6$ has been discussed by Wolfe et al. (2005) and Rafelski et al. (2012) while systems with lower metallicities have been observed in the Ly α forest (Schaye et al. 2003; Simcoe et al. 2004). Qian & Wasserburg (2003) model star formation in DLAs with a chemical

evolution code and find that star formation in pristine gas enriches it quickly, making the probability of detecting a DLA with $\log Z \lesssim -2.6$ very small. Additionally, we consider whether these pockets of “pristine” gas could really be common at intermediate redshifts, or whether this prediction perhaps reflects limitations in our understanding of how H_2 formation and star formation take place in these environments. We also note that Gnedin & Kravtsov (2010) report that their fitting formulae, used in our GK models, may become unreliable below $\log Z \lesssim -2.5$.

Figure 4.9 shows the probability of selecting a DLA with a given metallicity as a function of redshift for DLAs in the GKfj25 (top), GKj25 (middle), and BRj25 (top) models compared with observational estimates from Rafelski et al. (2012). We also show the best linear fits to DLA metallicity as a function of redshift for each model ($[Z] = \alpha z - [Z0]$). In order to examine the trends with redshift, we exclude DLAs with metallicities below $\log Z < -2.5$ from the fits. Although all of our models predict a shallower evolution in Z with redshift than seen by Rafelski et al. (2012), the agreement with observations is considerably better than in many previous studies. Moreover, our results are also in agreement with Jorgenson et al. (2013) who found evidence for a lack of metallicity evolution over the redshift range $2.2 < z < 4.4$. We present our best-fit parameters and those from Rafelski et al. (2012) and Jorgenson et al. (2013) in Table 4.2. We can see that the population of “pristine” DLAs predicted by the GKfj25 model is present at all redshifts, and the distribution of metallicities in the ‘enriched’ population is as broad as that in the BR models. From this plot, it is apparent that the metallicities of DLAs in our models are in better agreement with the observational estimates in the lower part of the redshift range, $z \lesssim 2$.

Results from integral field unit spectroscopy (e.g. Förster Schreiber et al. 2006) indicate that star-forming galaxies at $z \sim 2$ exhibit typical metallicity gradients of $dZ/dr = 0$ to $-0.3 \text{ dex kpc}^{-1}$ (Jones et al. 2010; Pilkington et al. 2012; Swinbank et al. 2012) and up to $dZ/dr \sim -0.4 \text{ dex kpc}^{-1}$ in quasars (Jones et al. 2013). If DLAs sample the outskirts of galaxies, e.g., with impact parameters of $b \sim 10 \text{ kpc}$ at $2 < z < 3.5$ (typical in our extended disc models), a metallicity gradient could have a significant effect on typical DLA metallicities. Moreover, metallicity gradients in star-forming galaxies are typically measured along the disc while DLA column density gas likely also samples a significant amount of cold

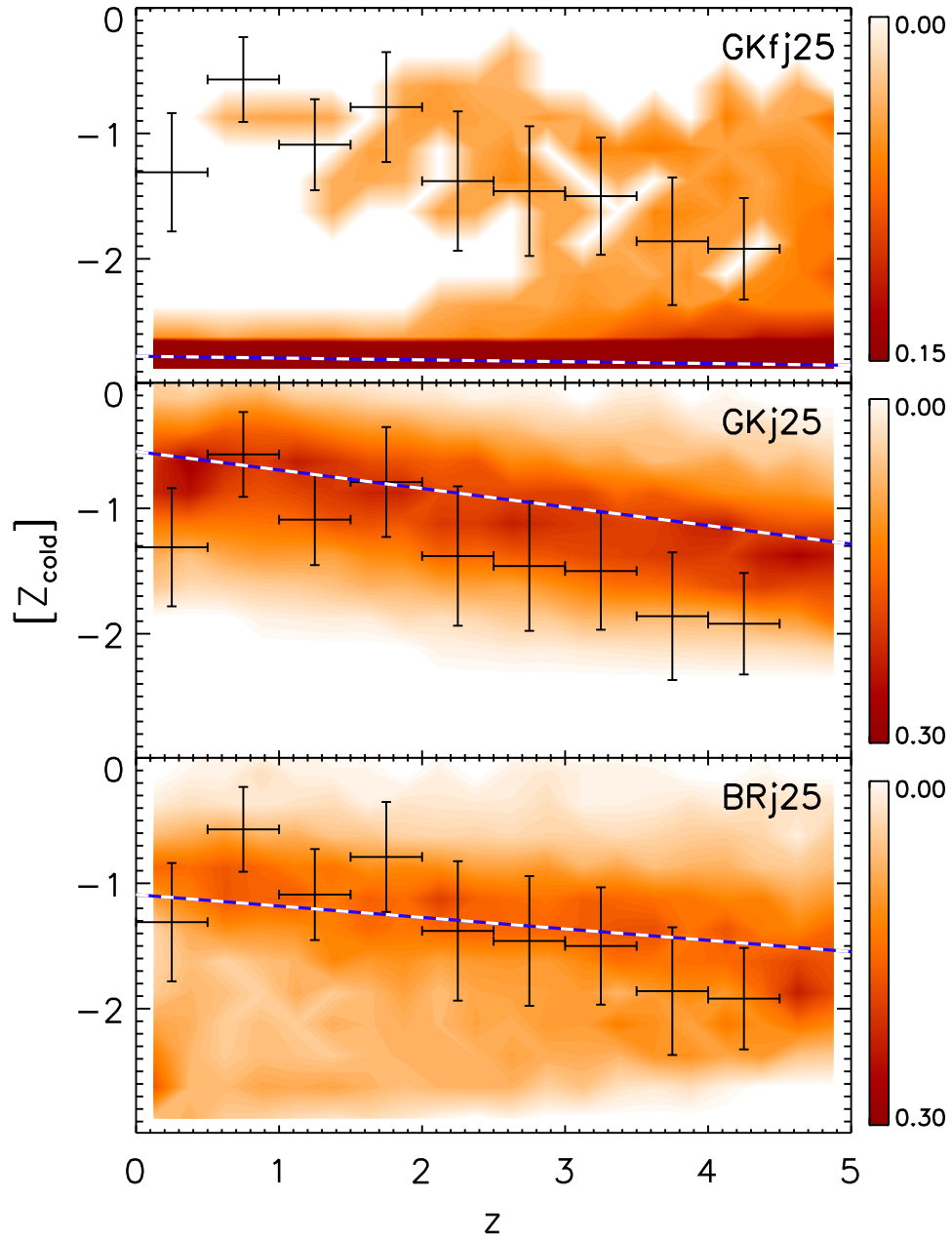


Figure 4.9 Conditional probability of DLA metallicity as a function of redshift in the GKfj25 (top), GKj25 (middle), and BRj25 models (bottom). The best linear fits to the average metallicities for DLAs with $\log Z > -2.5$ (to exclude the very low metallicity population) are overplotted (blue and white). Observation of DLAs from Rafelski et al. (2012) with the 1σ scatter in DLA metallicity are also overplotted. The GKj25 and BRj25 models show a shallow decrease in metallicity with increasing redshift, similar to observations, although the normalization is higher by ~ 0.5 dex in the GKj25 model. A significant number of DLAs in the GKfj25 model have metallicities near the “pre-enriched” metallicity, indicating that essentially no star formation has occurred in these objects.

Table 4.2 DLA Metallicity vs. redshift Best-Fit Parameters

	$\alpha \frac{dZ}{dr}=0$	$[Z0] \frac{dZ}{dr}=0$	$\alpha \frac{dZ}{dr}=-0.1$	$[Z0] \frac{dZ}{dr}=-0.1$
GKfj1	-0.10	-0.61	-0.07	-0.93
GKfj25	-0.11	-1.03	-0.01	-1.55
GKj1	-0.11	-0.64	-0.09	-0.91
GKj25	-0.15	-0.55	-0.19	-0.60
BRj1	-0.14	-0.43	-0.12	-0.71
BRj25	-0.09	-1.10	-0.08	-1.32
R12*	-0.22	-0.65	-	-
J13*	-0.04	-1.06	-	-

Linear fits ($[Z] = \alpha z + [Z0]$) for DLAs at $z < 5$

* observations of DLAs at $z < 5$ from Rafelski et al. (2012) and $2.2 < z < 4.4$ from Jorgenson et al. (2013)

gas *above* the disc where metallicities are almost certainly lower. Recently, Fu et al. (2013) studied the effects of metallicity gradients in semi-analytic models and found they depend on the fraction of metals directly injected into the halo as well as recent mergers, which can re-establish a metallicity gradient. Following the observational studies mentioned above, we implement a metallicity gradient of $dZ/dr = -0.1 \text{ dex kpc}^{-1}$ where the average galaxy metallicity is set to the radius of the average cold gas mass ($r_{ave} = 1.678r_g$). Thus, galaxies with larger cold gas masses will have more extended cold gas distributions. In general, DLAs arising in these galaxies will have larger impact parameters and subsequently be more affected by a metallicity gradient. As H_2 formation in the GK models is metallicity-dependent, if included self consistently, metallicity gradients could also affect other galaxy properties, and might produce results that are different in detail from those shown here. We show the results of the post-processed gradients only to qualitatively illustrate how they can potentially affect the distribution of DLA metallicities. However in the BR models, H_2 forms based on the midplane pressure, so introducing metallicity gradients would not impact other galaxy properties.

The top panel of Figure 4.10 shows the distribution of DLA metallicities in the redshift range $2 < z < 3.5$ before and after implementing a metallicity gradient. For $dZ/dr = -0.1 \text{ dex kpc}^{-1}$, the average shift in DLA metallicity is $\Delta Z = [Z_{DLA}] - [Z_{gal}] \sim -0.3 \pm 0.4$ with a tail extending to $\Delta Z < -1$. DLAs in each of our models have a similar average shift in metallicity. The broadened distribution reflects the large scatter in impact parameter,

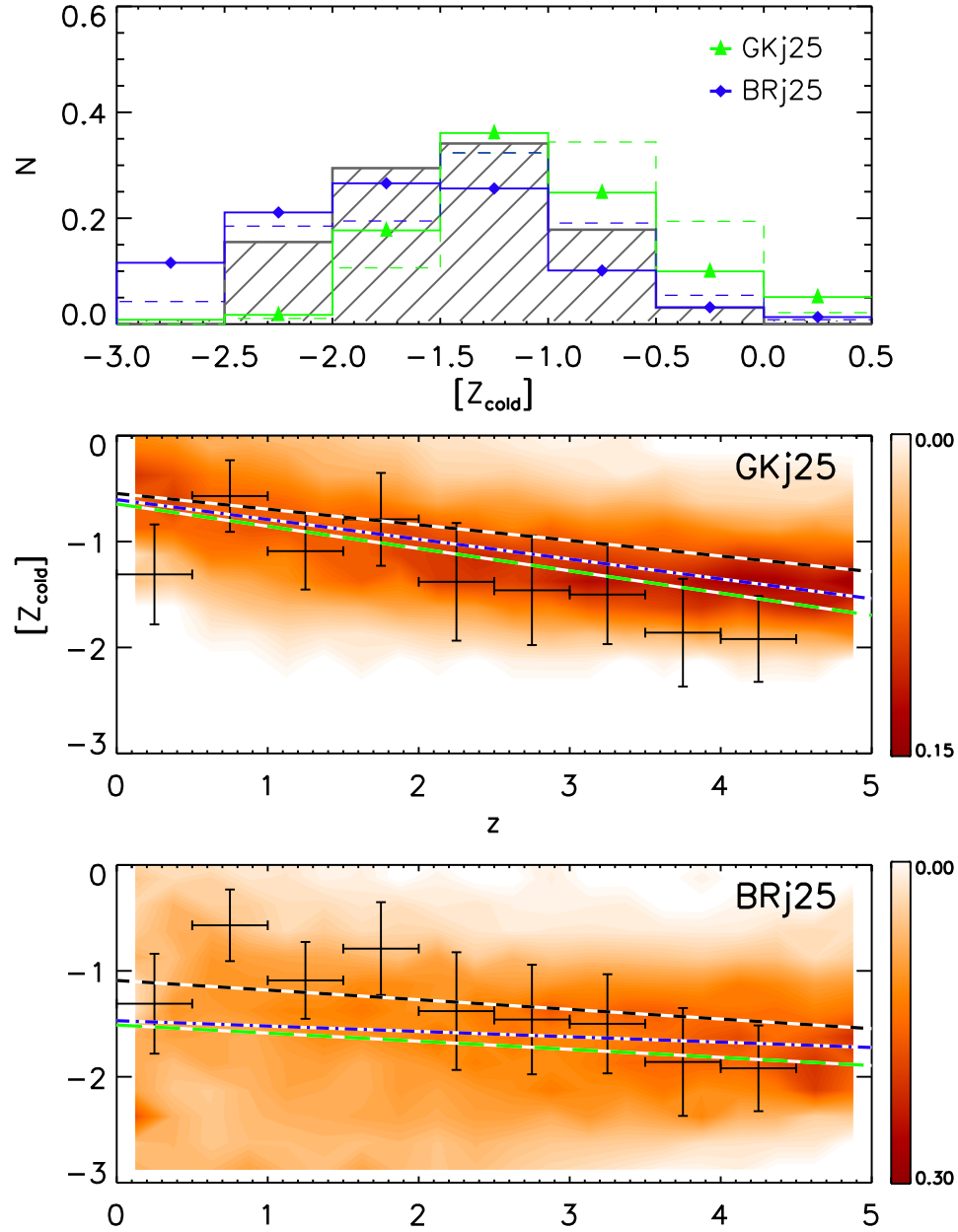


Figure 4.10 Top panel - predicted distribution of metallicities for DLAs at $2 < z < 3.5$ with a metallicity gradient ($dZ/dr = -0.1$ dex kpc^{-1} , solid) and without one (dashed). We exclude the fixed-UV and $f_j = 1$ models for clarity as they exhibit similar shifts in metallicity. Observations of DLAs from Rafelski et al. (2012) are also shown in gray. Middle and bottom panels - conditional probability of DLA metallicity versus redshift including a metallicity gradient as above, for the GKj25 and BRj25 models respectively. Best linear fits ($\log Z > -2.5$) for three metallicity gradients are overplotted: $dZ/dr = 0$ dex kpc^{-1} (black and white dashed line), $dZ/dr = -0.1$ dex kpc^{-1} (blue and white dot-dashed line), and $dZ/dr = -0.2$ dex kpc^{-1} (green and white long-dashed line). Metallicity gradients can have a significant impact on the DLA metallicity and its evolution.

which can be as high as tens of kpc, explaining the tail to low metallicities. Although it is possible for the outskirts of galaxies to have metallicities below $\log Z = -3$, we set this as the floor to the DLA metallicity as it corresponds to the metallicity of pre-enriched gas. The predicted mean metallicity of DLAs in this redshift range in our models is now in quite good agreement with the observations, and the shape of the distribution in the BRj25 models is in good agreement with the observations, though it does produce more systems with very low metallicities. The addition of a metallicity gradient causes the GKj25 model to move into better agreement with observations.

The middle and bottom panels of Figure 4.10 show the conditional probability distribution of DLA metallicities with a metallicity gradient $dZ/dr = -0.1 \text{ dex kpc}^{-1}$ as a function of redshift for the GKj25 and BRj25 models. The linear fits to models with imposed metallicity gradients of $dZ/dr = 0 \text{ dex kpc}^{-1}$, $dZ/drZ = -0.1 \text{ dex kpc}^{-1}$, and $dZ/dr = -0.2 \text{ dex kpc}^{-1}$ are shown for reference. Metallicity gradients cause a systematic shift in the redshift-metallicity relation for the BRj25 model while they make the slope steeper in the GKj25 model.

These trends indicate that sightlines through DLAs in the BRj25 model are sampling similar impact parameters relative to the distribution of cold gas at all redshifts, while those in the GKj25 model are preferentially selecting larger impact parameters at higher redshift. On the other hand, Fumagalli et al. (2011) and Cen (2012) found cold gas to be more extended at higher redshifts, coming from nearby streams flowing into the galaxy.

Overall, the addition of a metallicity gradient yields DLA metallicities in the GKj25 model in better agreement with observations, where stronger metallicity gradients make the above effects more pronounced. We find that a metallicity gradient of $dZ/dr \sim -0.3 \text{ dex kpc}^{-1}$ would be needed to bring the GKj25 metallicities into agreement with observations while no fixed metallicity gradient produces satisfactory results with the BRj25 model. In reality, the slope of the metallicity gradient probably varies from galaxy to galaxy and may be correlated with other galaxy properties. However, this simple exercise highlights the importance of understanding and accounting for metallicity gradients in modeling absorption systems.

Pontzen et al. (2008) found DLA metallicity to be correlated with halo mass, where

the majority of low metallicity DLAs ($\log Z \lesssim -1.5$) were found in haloes with masses $M_h < 10^{9.5} M_\odot$. By comparison, our simulations do not probe this mass range and we find the typical DLA to reside in much higher mass haloes. We also look for a similar trend between halo mass and metallicity by dividing our sample roughly in half based on halo mass ($M_h < 10^{11} M_\odot$, $M_h > 10^{11} M_\odot$), and comparing their metallicity distributions. For each model, DLAs with halo masses $M_h < 10^{11} M_\odot$ make up the vast majority of low metallicity systems where the difference in metallicity for each subset ranges from -0.5 to -1.0 dex. Finally, Neeleman et al. (2013) find a correlation between N_{HI} and metallicity where DLAs with higher column densities have higher metallicities. We also see a similar, but weak trend in our model DLAs. Interestingly, the addition of a metallicity gradient causes this correlation to be *stronger* as it causes sightlines that sample the interior regions of galaxies to preferentially have higher metallicities than those sampling the outskirts of galaxies. Therefore, a strong correlation between metallicity and N_{HI} may also be suggestive of the presence of metallicity gradients in DLAs. A more detailed comparison between metallicities measured through absorption studies and via emission lines in star-forming galaxies, will be presented in the next chapter.

4.2.6 Kinematics

Observationally, low ionization line profiles in DLAs exhibit multiple components with small individual velocity dispersions, yet the relative velocities between each component can be quite large. Therefore, Prochaska & Wolfe (1997) defined a number of statistical measures to probe the characteristics of line profiles. The velocity interval, Δv_{90} , is defined as the difference in velocity between the pixel containing 5% and 95% of the total optical depth. We calculate this statistic for each of our DLAs based on their low ionization absorption line profiles as detailed in Section 4.1.1. This quantity has proven to be the most difficult to reproduce in theoretical models, so we focus on Δv_{90} for our analysis.

Figure 4.11 shows the distribution of velocity widths, Δv_{90} , for DLAs in the $f_j = 1$ and $f_j = 2.5$ models with the Δv_{90} values measured from observed DLAs overplotted (Neeleman et al. 2013). Historically, hierarchical models have had difficulty reproducing this distribution, tending to overproduce low- Δv_{90} objects and underproduce the number

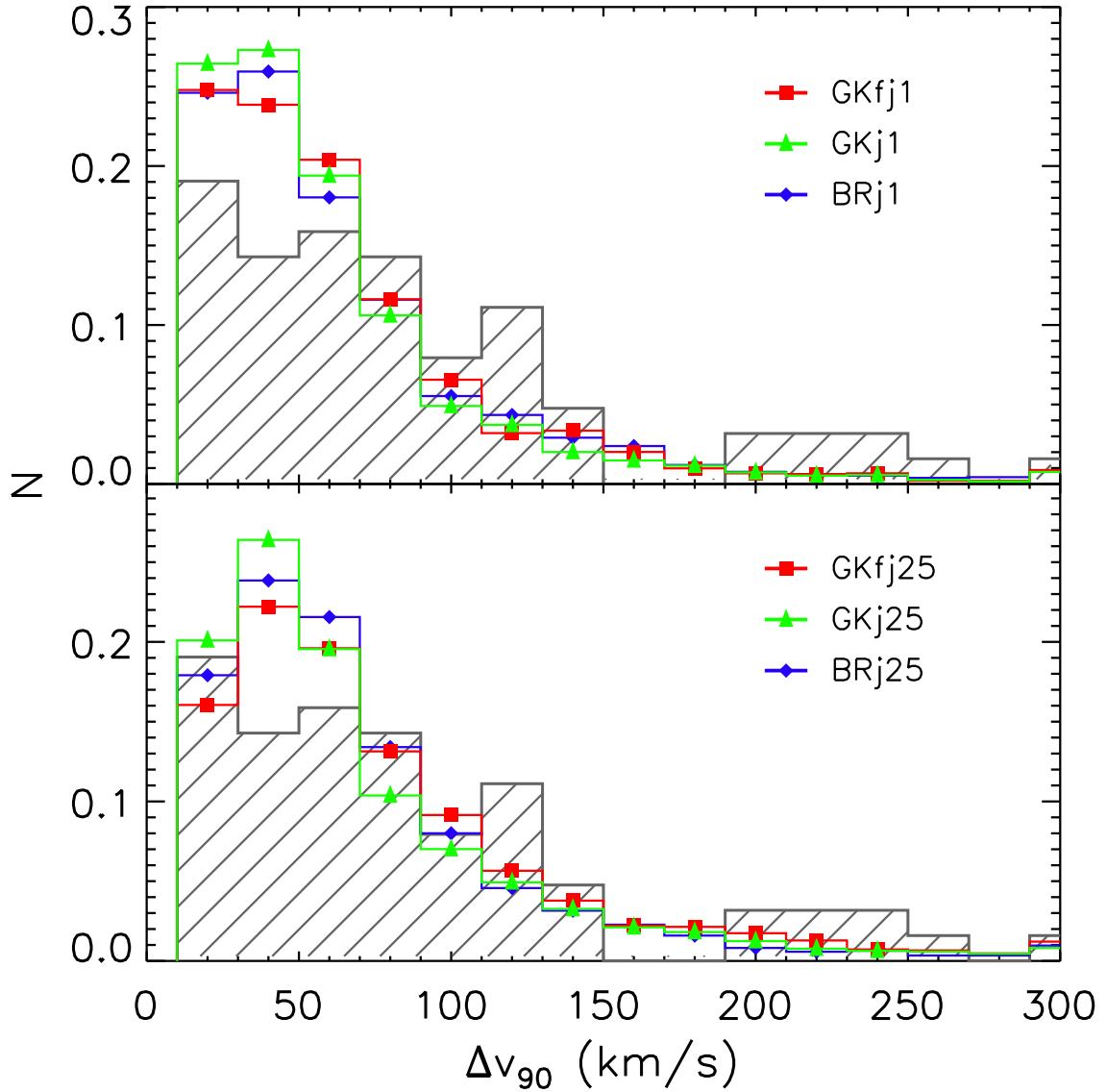


Figure 4.11 Upper panel – distribution of Δv_{90} values for DLAs in the redshift range $2 < z < 3.5$ for the GKfj1 (red), GKj1 (green), and BRj1 (blue) models. Lower panel – same as top except for the GKfj25 (red), GKj25 (green), and BRj25 (blue) models. The observed Δv_{90} distribution from Neeleman et al. (2013) is overplotted for reference. The GKj25 model has a Δv_{90} distribution most consistent to observations of high-redshift DLAs. DLAs with $\Delta v_{90} > 300 \text{ km s}^{-1}$ are shown at $\Delta v_{90} = 300 \text{ km s}^{-1}$. The $f_j = 1$ models produce too many low- Δv_{90} DLAs as has been shown in previous analyses of DLAs in semi-analytic models (e.g. Maller et al. 2001).

Table 4.3 DLA Δv_{90} K-S Test

	D	P _{K-S}
GKfj1	0.18	2.5e-4
GKfj25	0.14	0.017
GKj1	0.23	2.5e-3
GKj25	0.12	0.27
BRj1	0.23	2.6e-3
BRj25	0.18	0.035

For DLAs at $2 < z < 3.5$, compared to observations from Neeleman et al. (2013).

of high- Δv_{90} systems (e.g. Maller et al. 2001; Pontzen et al. 2008). The $f_j = 1$ models have Δv_{90} distributions that peak at low Δv_{90} , which is due to the large number of DLAs hosted by low-mass dark matter haloes. On the other hand, the $f_j = 2.5$ models are noticeably better at reproducing the observed distribution of Δv_{90} . Table 4.3 shows the probability that the distribution of DLA Δv_{90} values in each model are taken from the same distribution as the observed Δv_{90} values as well as the D-statistic from the Kolmogorov-Smirnov test. All $f_j = 1$ models have a $\lesssim 1\%$ chance of being from the same distribution as the observed Δv_{90} values. However, the $f_j = 2.5$ models are more successful, with the GKj25 model producing the most realistic Δv_{90} distribution with a probability of 27%. This kinematic distribution is a significant improvement over those from previous semi-analytic models (e.g. Maller et al. 2001, 2003) and many numerical simulations. Our models do not include other effects such as galactic winds or cold accretion, which will likely increase the Δv_{90} value of a given DLA (e.g., Cen 2012). Note that the $f_j = 1$ models are in slightly better agreement with the data than the $f_j = 1$ discs from previous semi-analytic models (e.g., see Figure 1 in Maller et al. 2001).

The improvement in the Δv_{90} distribution in the $f_j = 2.5$ models is primarily due to two effects. Most importantly, more extended cold gas discs cause DLAs to originate in more massive haloes with larger rotational velocities, as we saw in Figure 4.7. As a secondary effect, more extended gas distributions make it more likely for DLAs to arise from ‘multiple hits’ or lines of sight passing through more than one galaxy within a parent halo. The large number of low mass galaxies in the GKfj25 model causes an excess of DLAs with low Δv_{90} values. The improved success of the $f_j = 1$ models is due to the increased cold gas masses of DLAs in all models causing more higher mass DLAs to be selected. We note that when

cold gas discs are made very thin (e.g. very small values of χ_z), the Δv_{90} distributions also become peaked at low values.

The upper row of Figure 4.12 shows the distribution of halo masses for DLAs in our models over the redshift interval $2 < z < 3.5$. The lower row shows the probability of finding a DLA with a given Δv_{90} value at a given halo mass at the same redshift. The average disc circular velocity and 1σ scatter for galaxies at a given halo mass are also overplotted. We find a similar trend between Δv_{90} and disc velocity as Haehnelt et al. (1998) who found that Δv_{90} tracked disc velocity following $\Delta v_{90} \sim 0.6v_{\text{disc}}$ with a large scatter. As can be seen in the top and bottom panels of Figure 4.12, the extended gas distributions cause DLAs in the $f_j = 2.5$ models relative to the $f_j = 1$ models, specifically the GKj25 and BRj25 models, to originate from more massive haloes, which in turn have higher disc velocities. Conversely, the large number of pristine systems in very low mass haloes in the fixed-UV GK models lowers the average halo mass and Δv_{90} value relative to the other models. DLAs with large Δv_{90} values and low halo masses typically arise from ‘multiple hits’, which are more common in the $f_j = 2.5$ models as can be seen in the bottom row of Figure 4.12.

Figure 4.13 shows the conditional probability distribution of DLA metallicity as a function of Δv_{90} for the GKfj25, GKj25, and BRj25 models. The best-fit power law to the metallicity- Δv_{90} relation for our models and observations is also shown for reference, and the best-fit parameters are given in Table 4.4. In the $f_j = 2.5$ models, systems with high Δv_{90} values have metallicities comparable to observations, while they are slightly higher in the $f_j = 1$ models. At low Δv_{90} , DLAs in the BRj25 model are in reasonable agreement with observations while those in the GKj25 model typically have slightly larger metallicities than is observed. Alternatively, the GKfj25 model produces a significant number of low metallicity, low Δv_{90} systems, but again the metallicity distribution of these objects is peaked towards lower values in the models than the observations indicate. DLAs in the $f_j = 1$ models are not shown as they predict metallicities and Δv_{90} values that are significantly higher and lower, respectively, than observations.

Numerous authors have proposed that the Δv_{90} -metallicity relation may be the DLA version of the well-known mass-metallicity relation (e.g., Prochaska et al. 2008; Møller et al. 2013; Neeleman et al. 2013, and references therein). If the motions of neutral clouds giving

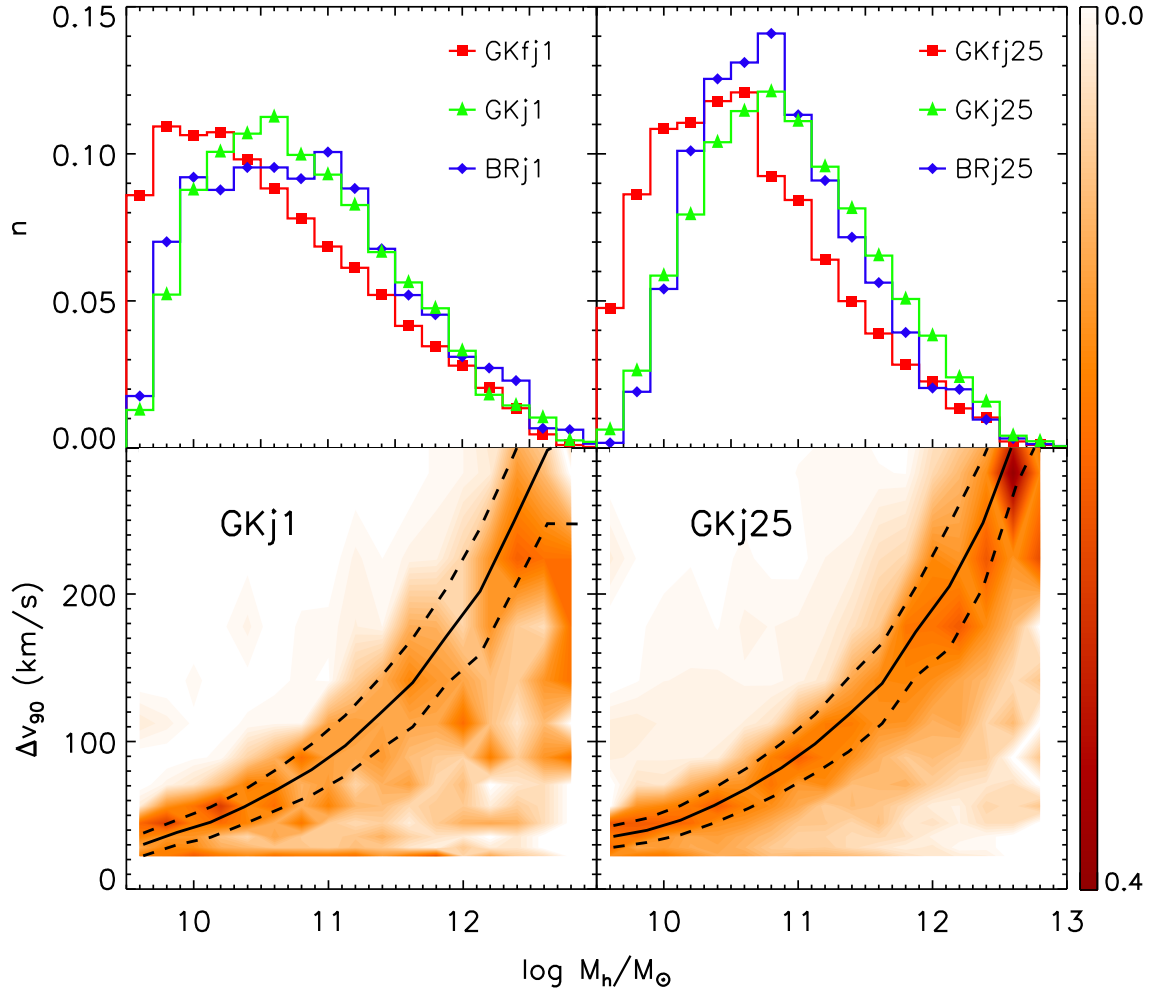


Figure 4.12 Upper left - histogram of the fraction of DLAs with a given halo mass for the GKfj1 (red), GKj1 (green), and BRj1 (blue) models at $2 < z < 3.5$. Upper right - same as upper left except for the GKfj25 (red), GKj25 (green), and BRj25 (blue) models. Lower left - conditional probability of Δv_{90} versus DLA halo mass for the GKj1 model. Lower right - same as lower left except for the GKj25 model. The BRj1 and BRj25 models produce similar Δv_{90} -halo mass relations as the GKj1 and GKj25 models respectively. The average disc velocity (solid line) and 1σ scatter (dashed lines) are overplotted for reference. The higher halo masses of DLAs in the $f_j = 2.5$ models cause them to produce more high- Δv_{90} systems. DLAs with low halo mass and high Δv_{90} values seen in the bottom row arise from ‘multiple hits’ or lines of sight passing through more than one galaxy in the same halo.

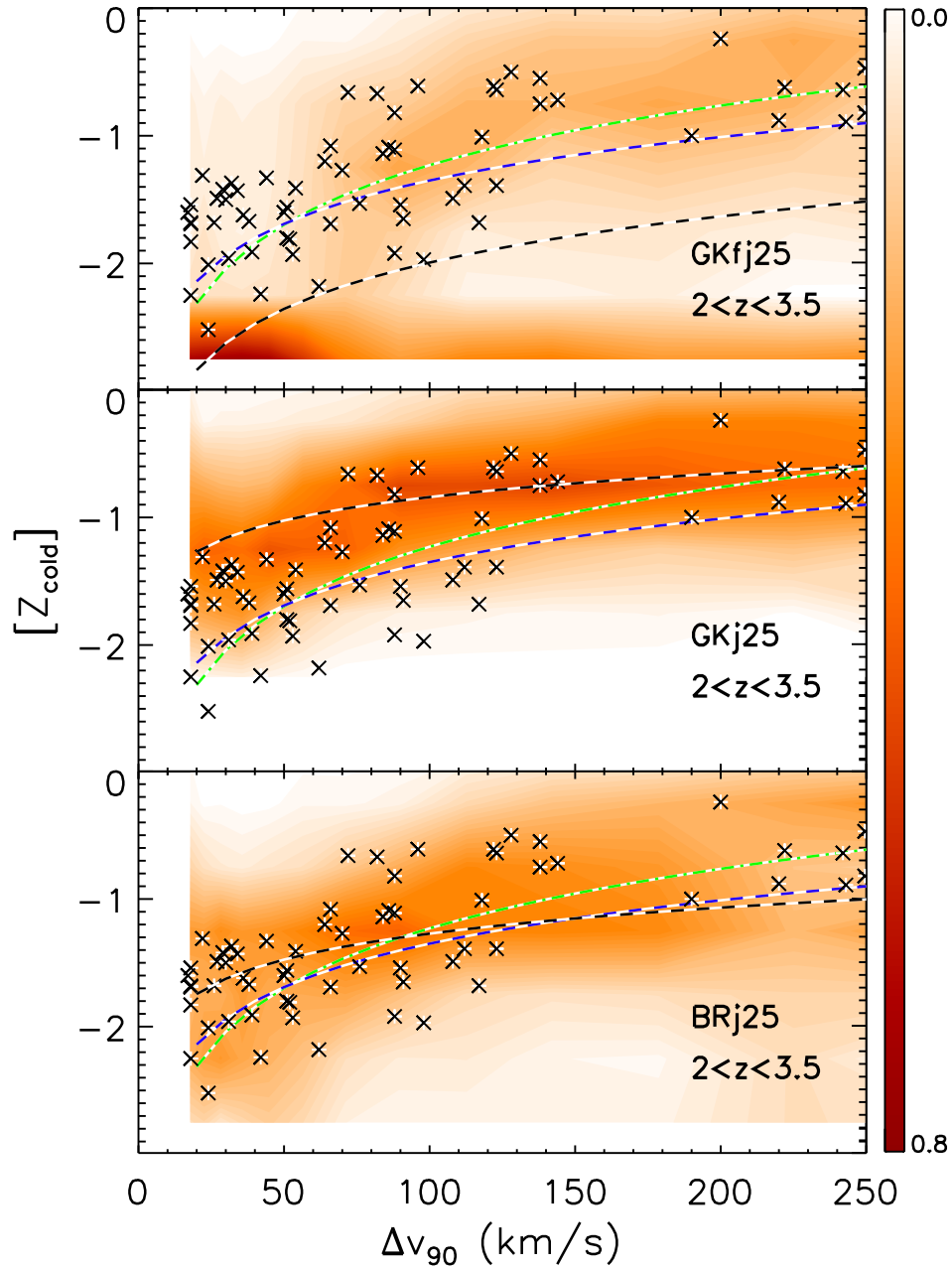


Figure 4.13 Conditional probability of metallicity versus Δv_{90} for DLAs in the redshift range $2 < z < 3.5$. Top panel - GKfj25 model. Middle panel - GKj25 model. Bottom panel - BRj25 model. The best-fit power law for each model is shown by the red and white dashed line. We overplot the observed DLA Δv_{90} versus metallicity relation from Wolfe et al. (2005, crosses), Ledoux et al. (2006, green dot-dashed line), and Jorgenson et al. (2013, blue dashed line). All models show evidence for an increase in metallicity with Δv_{90} , where the BRj25 model is in the best agreement with observations while the GKj25 model does not produce any very low-Z DLAs. At high Δv_{90} , the BRj25 model produces DLAs with metallicities in good agreement with observations.

Table 4.4 DLA Metallicity vs. Δv_{90} Best-Fit Parameters

	$\alpha_{dZ/dr=0}$	$[Z0]_{dZ/dr=0}$
GKfj1	0.66	-2.1
GKfj25	0.77	-2.9
GKj1	0.66	-2.1
GKj25	0.61	-2.1
BRj1	0.69	-2.0
BRj25	0.68	-2.6
L06*	1.55	-4.33
J13*	1.13	-3.61

Linear fits ($[Z] = \alpha \log \Delta v_{90} + [Z0]$) for DLAs at $2 < z < 3.5$.

* observations of 70 absorbers with $\log N_{HI} > 20$ at $1.7 < z < 4.3$ from Ledoux et al. (2006) and 106 DLAs at $2.2 < z < 4.4$ and Jorgenson et al. (2013).

rise to the Δv_{90} values are governed by gravity whether it is rotation, infall, or outflow, then Δv_{90} could be correlated with mass. Indeed, as shown in Figure 4.12, our models do predict a relationship between Δv_{90} and halo mass, although with significant scatter. Similarly, we find galaxies with large Δv_{90} values to be more likely to have higher metallicities. At all values of Δv_{90} , there is significant scatter in DLA metallicity, which is likely affected by galaxy inclination, the stochasticity of neutral clump properties, and infalling or outflowing gas. Moreover, we do find that the presence of a metallicity gradient in all DLAs has the effect of increasing the scatter of the $[Z] - \Delta v_{90}$ distribution as the high- Δv_{90} DLAs are selected from higher mass haloes with a larger range of impact parameters. For this reason, we note that a metallicity gradient can weaken the connection between metallicity and Δv_{90} . Observations of star-forming galaxies show a large range in metallicity gradients, suggesting that this may also be the case in DLAs. Overall, metallicity gradients may contribute to the low observed metallicities and large scatter seen in DLAs.

4.3 Discussion

Studies of HI in absorption are currently the *only* means of probing atomic gas at significant redshift, and this will remain true for quite some time at redshifts much greater than unity, although new radio telescopes such as the Square Kilometer Array (SKA) and its precursors will push studies of HI in emission up to $z \sim 1-1.5$. DLAs are thought to contain the bulk of the HI in the Universe and extensive observations of their properties exist in the literature.

In spite of this, theoretical models of galaxy formation based on the predominant Λ CDM paradigm have not been terribly successful at reproducing several of these observations, and therefore the connection between DLAs and the galaxy population detected through their emission properties remains unclear.

Although our models rely on a number of simplifying assumptions, our study is the first to attempt to predict the properties of DLAs in a model that includes both the cosmological formation of galaxies and the partitioning of the cold ISM in galaxies into different phases (ionized, atomic, and molecular), based on physically motivated recipes. In addition, unlike the numerical hydrodynamic simulations that have been predominantly used for previous studies of DLA properties, our semi-analytic models broadly reproduce a large suite of observations that probe the stellar and dust content of galaxies over a broad redshift range (S08, S12).

4.3.1 On the Distribution of Cold Gas giving rise to DLAs

An interesting general insight is that *in spite* of the freedom we allowed ourself in adjusting, for example, the distribution of cold gas in galactic discs, *none* of the models we considered is really fully satisfactory at reproducing the properties of DLAs over all redshifts *and* the set of ‘calibration’ quantities of $z = 0$ galaxies (e.g., stellar mass functions, HI mass functions, H₂ mass functions). We found that models with “standard” distributions of gas ($f_j = 1$) could not reproduce the column density distribution of DLAs at any redshift, in agreement with the results of previous studies (Maller et al. 2001). This led us to consider models with ‘extended’ gas distributions, which reproduced the HI column density distribution, the cosmic evolution of the line density, and Ω_{DLA} quite well at $z \lesssim 3$. However, the models with extended gas distributions and a metallicity-dependent recipe for H₂ formation were too inefficient at forming stars and predicted stellar fractions that were too low, and fractions that were too high, at $z = 0$. This is because the extended gas models place a large amount of gas at low surface density where it is inefficient at forming stars. The metallicity-based extended-gas model with a varying-UV background (GKj25) performs better than the model with a fixed UV background, as the reduced UV background in low-mass systems results in weaker suppression of the star formation efficiency. The pressure-based extended-gas BRj25

recipe fared better with the $z = 0$ stellar mass function, but still overproduces the number of HI-rich galaxies at $z = 0$.

This may reflect the overly simple assumption of a fixed value of f_j in all galaxies and at all redshifts that we made in this work. We motivated our assumption based on numerical hydrodynamic simulations. These simulations have shown that the average specific angular momentum j of the baryonic disc can be larger than that of the DM halo if low- j material is preferentially ejected by winds (e.g., Brooks et al. 2011; Guedes et al. 2011), if the disc is formed by cold flows (Brooks et al. 2011; Pichon et al. 2011; Stewart et al. 2013), or if the gas is spun up in a gas-rich major merger (Robertson et al. 2006a; Sharma et al. 2012). It is likely that the effective value of f_j in reality varies between galaxies and may depend on cosmic epoch and the star formation and merger history. Our simple “merger” models did not fare well in reproducing the column density distribution or the Ω_{DLA} evolution, indicating that a more physical approach to modeling the extent of the cold gas giving rise to DLAs is needed.

In addition, some authors have suggested that some of the absorbing gas giving rise to DLAs may not be in a rotationally supported disc at all, but may instead be in an outflow (Cen 2012). Although we stated earlier that our ‘extended’ disc models could be interpreted as representing any of these scenarios, this is not entirely consistent. Our models implicitly assume that DLAs arise from the cold gas reservoir that has accumulated within the “box” that we call a galaxy – i.e., gas that has cooled and accreted but not turned into stars or been ejected in an outflow. Assuming that this gas is in an extended configuration leads to large amounts of gas at low surface density where it is inefficient at forming stars. If the cross-section and kinematics of DLAs are significantly affected by gas in an outflow, this would have different implications for the star formation efficiency of galaxies which in turn feeds back into the cold gas content as well as metallicities, etc. We are engaged in a program to study the distribution of gas and metals in high resolution zoom simulations that include a treatment of a multi-phase ISM (Christensen et al. 2012b) in order to study these issues and build more sophisticated semi-analytic models for absorption systems.

4.3.2 Is the flatness of Ω_{DLA} a Cosmic Coincidence?

Regardless of these limitations, we believe that we can make some robust and interesting predictions based on our simple models. Our preferred models, the BR/varying-UV GK models with extended discs, are somewhat successful at reproducing the line density of DLAs and Ω_{DLA} at $z \lesssim 3$, indicating that the majority of HI in DLAs could plausibly be associated with galactic discs. Subsequently, one interesting suggestion we make is that the observed near constancy of Ω_{DLA} from $z \sim 4.5$ to 0.5 is not a reflection of a truly constant global HI density, but rather a cosmic coincidence resulting from the DLA population being increasingly ‘contaminated’ by intergalactic gas in filaments or cold streams at $z \gtrsim 3$, and systematically under-representing the true HI density at $z \lesssim 2$ due to an increasing contribution to the global HI budget from low- N_{HI} systems. Numerical hydrodynamic simulations do indicate that the number of “intergalactic” DLAs increases with increasing redshift (Fumagalli et al. 2011; Cen 2012).

At the same time, it is a concern that in several of our models (in particular the overall more successful BR/varying-UV GK models) the *total* cold gas density in all forms (atomic, and molecular) barely equals (BRj25/GKj25/GKfj1) or is even less than (BRj1/GKj1) the HI density implied by observations of DLAs at $z \gtrsim 3$. On the other hand in the fixed-UV, extended gas model (GKfj25), the total amount of stars at $z = 0$ is much less than observations. We note that a similar problem is seen in many other semi-analytic models and numerical hydrodynamic simulations (e.g. Duffy et al. 2012; Narayanan et al. 2012a; Davé et al. 2013). This may be a reflection of another well-known problem, that low-mass galaxies in these models form too early (Fontanot et al. 2009; Weinmann et al. 2012). Thus overly efficient star formation at high redshift may be consuming or expelling too much gas, leaving behind too little cold gas in galaxies. We note that the models with metallicity-based H_2 formation recipes do appear to fare better in this regard. Moreover, this effect may also be impacted by the decreasing average halo mass of DLAs with redshift and the mass resolution of our models. In this case, a contribution from low mass DLAs below our resolution limit may explain part of this discrepancy.

4.3.3 DLA Host Masses and Kinematics

Correlation studies of DLAs are an interesting and powerful method to directly constrain the DLA cross section as a function of halo mass. Through a cross correlation analysis of DLAs with the Ly α forest at $\langle z \rangle = 2.3$, Font-Ribera et al. (2012) recently found typical DLA halo masses of $M_h \sim 6 \times 10^{11} M_\odot$ and DLA cross sections $\sigma_{\text{DLA}} \sim 1400 \text{ kpc}^2$. Our ‘extended disc’ ($f_j = 2.5$) models, specifically the BRj25 and GKj25 models, produce DLAs with comparable cross sections and halo masses at the same redshift, and the predicted slope of the DLAs cross-section vs halo mass ($\sigma_{\text{DLA}}\text{-}M_h$) is in reasonable agreement with these observations.

We find that the distribution of Δv_{90} for our model DLAs depends on both the gas partitioning recipe and the specific angular momentum of the gas (f_j). The Δv_{90} distributions for our ‘extended disc’ models are significantly better than results from previous SAMs (e.g., Maller et al. 2001) and most numerical hydrodynamic simulations, with our metallicity-based extended-gas, varying-UV (GKj25) model providing the closest match. Similarly to Haehnelt et al. (1998), we find Δv_{90} and disc rotation velocity to be positively correlated, although with a large scatter. The disc rotation velocity corrected for inclination is the primary factor determining the value of Δv_{90} . We show that adopting the extended gas discs shifts DLAs into more massive haloes, which leads to better agreement with the observed Δv_{90} distribution. We still predict fewer very large Δv_{90} systems ($\Delta v_{90} \gtrsim 200 \text{ km/s}$) than are observed. This may be because Δv_{90} is boosted by outflows in some systems, as suggested by the simulations of Cen (2012). Additionally, outflows are known to be common among high-redshift star-forming galaxies (e.g., Steidel et al. 2010, and references therein).

4.3.4 DLA Metallicities

Another insight from our study is a first indication of how observations of gas at high redshift may help constrain our understanding of how H₂ forms in galactic discs and how cold gas is converted into stars on galactic scales. Some workers have emphasized the importance of metallicity in regulating H₂ formation and hence star formation (e.g. Krumholz et al. 2009b;

Gnedin & Kravtsov 2010). However, other authors have suggested that the ISM is self-regulated on the scales of star-forming regions, so that the star formation rate adjusts itself until the turbulent pressure balances the gravitational restoring pressure, thus suggesting that the disc midplane pressure may be the more fundamental quantity (Ostriker et al. 2010; Shetty & Ostriker 2012). Although the metallicity-based, varying-UV background GK model produces slightly better results for DLAs, perhaps the more striking result is how similar are these results overall to those of the pressure-based BR model. In addition, we find that including the effects of a varying UV background in the metallicity-based model produces significantly improved results relative to a model in which the galaxy-to-galaxy variation in the UV field is neglected (e.g. Krumholz et al. 2009b). The fixed-UV GK models make the dramatic prediction that a large fraction of DLAs at all redshifts are composed of nearly “pristine” gas with metallicity $\log Z \lesssim -2.5$, that has never experienced significant star formation. These arise because the metallicity-based models predict that low surface density, low-metallicity gas is extremely inefficient at forming H_2 . In our models, stars can only form out of H_2 so in these systems, stars never form efficiently and never enrich the gas, so remain “barren” unless kick-started by a merger-driven starburst. We were initially concerned that these systems were an artifact of inaccuracies in our models, but a similar population has recently been pointed out in numerical hydrodynamic simulations (Kuhlen et al. 2013), which incorporate a similar metallicity-based recipe for H_2 formation and H_2 -based star formation. Therefore it is interesting to determine how robust these predictions are, and whether such a population is definitively ruled out by observations.

Wolfe et al. (2005) and Rafelski et al. (2012) discuss the presence of a DLA metallicity floor of $\log Z \gtrsim -2.6$, and no lower metallicity DLAs have been discovered, although they could have been detected. Schaye et al. (2003) and Simcoe et al. (2004) find systems in the $\text{Ly}\alpha$ forest with lower metallicities, down to $\log Z \sim -4$. It is worth noting in this context, however, that we assume that the fitting functions based on numerical simulations with chemistry and simplified radiative transfer hold down to gas metallicities of $\log Z \sim -3$, while Gnedin & Kravtsov (2010) note that these approximations are uncertain below metallicities of $\log Z \sim -2.5$. In addition, recent high resolution numerical simulations suggest that in low metallicity gas, HI gas can form directly into stars without going through

a molecular phase (Shetty & Ostriker 2012; Glover & Clark 2012; Shetty et al. 2013).

Another success of our models is improved agreement with the low metallicities and weak metallicity evolution of DLAs, which has been a challenge for previous generations of SAMs and numerical simulations. The reduced efficiency of star formation in systems with low mass and/or low metallicity causes DLAs to typically have lower metallicities than in previous SAMs, thereby increasing the slope of the mass-metallicity relation. Our extended-gas BRj25 and GKj25 models, with the possibility of observationally motivated metallicity gradients, reproduce the mean metallicities of DLAs at $z \lesssim 3$, including the slope of the redshift evolution. At $z \gtrsim 3$, the varying-UV GK model predicts metallicities higher than the observations by up to 0.5 dex while the pressure-based BR model is in better agreement. It is worth noting that as we discussed above, the observed population of DLAs in this regime may be significantly contaminated by intergalactic gas which would be expected to have lower metallicity. However, more recently, Jorgenson et al. (2013) find a much weaker evolution in DLA metallicity than Rafelski et al. (2012). Their sample has a more limited redshift range of $2.2 < z < 4.4$, and they note that they find much flatter metallicity evolution when they take the data set from Rafelski et al. (2012) and only include DLAs in the same redshift range. These results suggest that a significant amount of evolution in the DLA metallicity occurs at $0 < z < 1$ and $z > 4$ (see figure 11 in Jorgenson et al. 2013).

Metallicity gradients as steep as $dZ/dr = -0.3 \text{ dex kpc}^{-1}$ have been observed in $z \sim 2 - 2.5$ star-forming galaxies (Jones et al. 2010). We showed that introducing metallicity gradients of this order significantly changed the predicted metallicity distribution of DLAs and its redshift evolution. Thus our work shows that metallicity gradients may play a significant role in reconciling DLAs metallicities and their evolution with those measured via emission line diagnostics, underlining the importance of understanding and constraining these gradients in simulations and observations.

Another possibility that has been discussed in the literature is that the metallicities of DLAs could be biased low due to a selection effect, as metal-rich DLAs would also be dusty, perhaps causing their background quasars to drop out of colour or magnitude selected QSO samples. However, using radio-selected quasars, Ellison et al. (2001) and Khare et al. (2012)

found no significant population of heavily reddened quasars with foreground DLAs, suggesting that DLAs do not strongly redden quasars. Furthermore through stacking quasars with and without DLAs along the line of sight, Ellison et al. (2005) found that DLAs are associated with very small amounts of dust reddening. These analyses suggest that observations of DLAs are not missing dusty, evolved DLAs and that they are well-characterized by small amounts of dust and low metallicities.

4.4 Conclusions

We have presented predictions for the properties of quasar absorption line systems associated with cold gas in galactic discs, based on a new suite of semi-analytic models that include updated recipes for partitioning gas into an ionized, atomic, and molecular phase, and a molecular hydrogen based star formation recipe. We present results for three different prescriptions for partitioning gas into an atomic and molecular component: one (BR) based on the empirical relationship between molecular fraction and gas midplane pressure from Blitz & Rosolowsky (2006), and two (GK) based on numerical hydrodynamic simulations in which the metallicity and the local UV radiation field play a major role in determining the molecular fraction (Gnedin & Kravtsov 2010, 2011). In one, the local UV radiation field is held fixed to the Milky Way value, while it is allowed to vary in proportion to the galaxy star formation rate in the other. In addition, we considered different approaches for how the cold gas is distributed within galaxies, using the parameter f_j to represent the fraction of the specific angular momentum of the dark matter halo material that is “captured” by the cold gas within galaxies. First, we compared our predicted $z \sim 0$ galaxy stellar mass functions and cold gas mass functions to local observations. We find that models with different physical ingredients produce different amounts of cold gas within galaxies, demonstrating that it is a key diagnostic for constraining theoretical models. We then selected DLAs by passing sightlines through mock catalogs extracted along lightcones from the Bolshoi simulation. The majority of our analysis focused on comparing the properties of these mock DLAs with observations of real DLAs.

We summarize our main results below.

- Models with “standard” gas radial profiles where the cold gas specific angular momentum is equal to that of the dark matter, $f_j = 1$, fail to reproduce the observed column density distribution function and the number density of DLAs. They also fail to reproduce the observed distribution of velocity widths, Δv , of low-ionization metal lines, producing too many low- Δv systems and not enough high- Δv systems.
- Our models with “extended” gas discs ($f_j = 2.5$) are able to reproduce the observed column density distribution function over the range $19 < \log N_{\text{HI}} < 22.5$ at $2 < z < 3.5$ and also the number density of DLAs at $z < 2.5$. The favored extended disc models produce comparable DLA cross sections (σ_{DLA}), halo masses, and predict a $\sigma_{\text{DLA}} - M_{\text{h}}$ relation with slope and normalization that is in agreement with observations at $\langle z \rangle = 2.3$. Moreover at $2 < z < 3.5$, these same models also reproduce the Δv distribution fairly well, primarily because they select DLAs in higher mass haloes with larger rotational velocities. However, they produce too many high- M_{HI} mass galaxies and too few galaxies around the characteristic stellar mass at $z = 0$.
- Our “extended” gas disc models reproduce the observed estimates of the comoving density of HI in DLAs (Ω_{DLA}) at $z \lesssim 3$, with the model with pressure-based gas partitioning and the one with metallicity-based gas partitioning accounting for a varying UV radiation field producing the best agreement. All of our models fail to reproduce the number density of DLAs and amount of HI in DLAs at $z \gtrsim 3$. We suggest that a significant fraction of DLAs at $z \gtrsim 3$ may reside in filaments, cold streams, or clumps of gas not associated with the rotationally supported gas in galactic discs.
- The predictions of our favored “extended” gas disc models for DLA metallicities are in much better agreement with observations than previous studies. Additionally, accounting for metallicity gradients motivated by observations of star-forming galaxies at a comparable redshift to the DLA sample, we obtain very good agreement with the mean metallicity and metallicity-redshift relation in our models. Furthermore, our models predict a correlation between metallicity and kinematics (Δv_{90}) which is in reasonable agreement with observations.

Chapter 5

Relations among Damped $\text{Ly}\alpha$ Absorption Systems and Star-Forming Galaxies in Semi-Analytic Models at $z = 2$

5.1 Introduction

Since star formation occurs in cold gas and at $z \sim 3 - 4.5$, DLAs contained sufficient neutral gas mass to account for a substantial fraction of the local stellar mass density, they are likely repositories for star formation and a key to understanding galaxy formation (Storrie-Lombardi & Wolfe 2000b). At $1 < z < 3$, coinciding with the peak epoch of star formation, star-forming galaxies (SFGs) boast star formation rates of $\text{SFR} \sim 10$ to $> 100 \text{ M}_\odot \text{ yr}^{-1}$ due to high gas fractions, suggesting that there may be substantial overlap between DLAs and SFGs (Shapley et al. 2001; Reddy et al. 2006; Shapley et al. 2005; Tacconi et al. 2010, 2013). In spite of this implicit connection, a clear link between DLAs and star-forming galaxies has not been found. Moreover, as DLAs are detected in absorption, they provide us with one of the best ways in which to study the properties of galaxies' interstellar medium at high redshift. Compared to traditional galaxy surveys, where galaxies are identified based on radiation being emitted by stars, selecting galaxies in absorption represents an orthogonal means of studying galaxy formation that identifies galaxies with large amounts of cold gas that is not directly dependent on either the star formation rate or the stellar mass of the host galaxy. Therefore, understanding the connection between DLAs, SFGs, and the underlying galaxy population will yield insight into galaxies with large cold gas reservoirs and the connection among the properties of these gas-dominated galaxies, those that are rapidly forming stars, and the galaxies in general.

Wide deep surveys have generated large catalogs of star-forming galaxies across the redshift range $1.5 < z < 3.5$ through a variety of color selection techniques (e.g., Steidel

et al. 1996b, 2003, 2004; Daddi et al. 2004; Hathi et al. 2010). Extensive follow-up observations and detailed analyses have generated a wealth of information regarding the physical properties of star-forming galaxies at high redshift. The most common selection method (Steidel et al. 1996b) identifies star-forming galaxies based on the location of the Lyman break. This technique has also been applied using space-based photometry to select UV-bright star-forming galaxies at $1.4 < z < 3$ and at fainter magnitudes (e.g., $B_{435} < 26.5$ for U275-band dropouts at $z \sim 2$) (Hathi et al. 2010; Oesch et al. 2010). Additionally, Daddi et al. (2004) and Reddy et al. (2005) use the “BzK” selection technique to identify galaxies at different near-infrared magnitudes at $1.4 < z < 2.5$, selecting galaxies based on their stellar mass, independent of dust reddening. In spite of these different methods for identifying star-forming galaxies, there is a large overlap fraction among these galaxies (e.g., $\sim 70\%$ of BzKs are also BM/BX galaxies Grazian et al. 2007). The advent of medium-band surveys and accurate photometric redshifts has allowed the identification of a large number of galaxies across a wide range of redshifts (e.g., Whitaker et al. 2011, at $1 < z < 3$), generating samples of galaxies above a given luminosity. These mass-selected galaxies are relatively unaffected by selection effects due to color-selection criteria and better characterize the general galaxy population (Whitaker et al. 2011). While these different selection techniques identify high-redshift galaxies in different ways, galaxies at high redshift are becoming well defined as well as the relations among them.

Large numbers of optically-detected quasars (QSOs) at $z > 2$ in the Sloan Digital Sky Survey (SDSS) have produced a substantial catalog of absorbers at high redshift. In spite of numerous efforts, finding galaxy counterparts to DLAs has been challenging, yielding only a handful of host galaxies (Warren et al. 2001; Krogager et al. 2012). As a result, establishing a connection between DLAs and emission-selected galaxies has remained an open challenge. Nonetheless, observations of [CII] $158\mu\text{m}$ cooling rates in DLAs indicate that they exhibit a bimodality in galaxy properties where some DLAs are consistent with trace amounts of in situ star formation and others are likely associated with a nearby SFG (Wolfe et al. 2008, hereafter W08). In fact, W08 find that the low cooling rate subset is also consistent with DLAs being heated by the extragalactic background light. These DLAs with low cooling rates may arise in low mass halos or intergalactic gas such as clumps or

filaments. On the other hand, the DLAs with high cooling rates are typically found in more massive dark matter halos as tracked by their velocity widths, Δv_{90} which are assumed to correlate with virial velocity. These DLAs also exhibit higher metallicities, higher dust-to-gas ratios (κ), and higher star formation rate surface densities (Σ_{SFR}). Curiously, their H I column density distributions are similar to the low cooling rate subset. Due to the high cooling rates and infrequent occurrence of extended low-surface brightness galaxies (e.g., Wolfe & Chen 2006), W08 comment that the high cooling rate DLAs are likely heated by far-ultraviolet (FUV) radiation from a nearby bulge source, even though few DLA host galaxies have been observed. A natural explanation for these DLAs is that they arise from cold neutral gas surrounding a central star-forming region, such as a nearby star-forming galaxy that is beyond our current detection limits. Furthermore, Cooke et al. (2006) found an overdensity of LBGs and QSOs around DLAs at $z \sim 3$, indicating a possible connection between the size and density of systems with high H I column densities and sources of significant ionizing radiation. Using numerical simulations, Bouché et al. (2005) measured the clustering of DLAs and found them to occupy moderate mass halos with an upper limit of $\log M_h/M_\odot \sim 11.1$. These results indicate that some fraction of DLAs are likely associated with star-forming galaxies, yet an absence of DLA galaxy counterparts may suggest that a substantial fraction stem from a separate populations of objects. Therefore, the connection between the cold gas in which stars will form and the galaxies in which stars are forming is not clear.

In spite of the implicit connection between cold gas and star formation, there has been little theoretical work aimed at studying the relation between DLAs and star-forming galaxies (Pontzen et al. 2008; Cen 2012). This lack of a comparison is likely in part due to the challenge of observationally identifying DLA host galaxies as well as characterizing their properties. In their numerical simulations, Pontzen et al. (2008) found that DLAs at $z = 3$ typically reside in lower mass halos ($10^9 < M_h/M_\odot < 10^{11}$) with very low star formation rates ($SFR < 0.1 M_\odot \text{ yr}^{-1}$) and stellar masses ($10^{6.5} < M_*/M_\odot < 10^{9.5}$). In contrast using a cosmological hydrodynamic simulation, Cen (2012) found DLAs to reside in more massive galaxies ($10^{10} < M_h/M_\odot < 10^{12}$ at $1.6 < z < 4$) where galactic winds play an indispensable role in DLA kinematics. They find DLAs hosts at $3 < z < 4$ to have $SFRs \sim 0.3 - 30 M_\odot$

yr^{-1} and a 20%-30% overlap fraction with LBGs where the majority are further than 100 kpc away from L^* galaxies, suggesting a substantial number arise in intergalactic gas.

As DLAs contain very low metallicities and are observed in the spectra of background quasars, numerous studies have sought to characterize the amount of dust obscuration and its potential bias on the selection of DLAs (Pei et al. 1991; Ellison et al. 2001; Vladilo et al. 2008; Khare et al. 2012). One common technique is to compare the stacked colors of quasars with DLAs along the sight-line to a control sample. Historically, this technique has yielded very small amounts of dust reddening, $E(B - V) \lesssim 0.05$ (e.g., Murphy & Liske 2004; Ellison et al. 2005). Recently, Khare et al. (2012) investigated a sample of 1084 absorption systems with $\log(N_{\text{HI}}) > 20$ at $2.15 < z < 5.2$ and found that $\lesssim 10\%$ have relatively high chemical abundances and cause significant reddening, leading them to conclude that about 10% of DLAs could be missed in color-selected QSO surveys. Furthermore, Ellison et al. (2001) compiled a sample of radio-selected QSOs irrespective of optical magnitude and found the number density per unit redshift of DLAs to be higher toward fainter targets. They found this dust-induced bias indicates that the cosmological HI mass density is likely underestimated along with the number density of DLAs, but by no more than a factor of two at $z \sim 2.3$. Finally, Jorgenson et al. (2006) report the existence of fields with radio-selected QSOs with no optical counterparts, possibly indicating the presence of highly-obscured QSOs possibly due to dusty DLAs. These studies suggest that the majority of DLAs have negligible amounts of dust extinction while some unknown fraction may be heavily obscured, leading to the underestimation of the amount of HI in the Universe.

In this chapter, we use the SAMs developed in SPT14 and PST14 to study the properties of the galaxies that host DLAs; the differences between properties of DLAs as measured along the line of sight and the average for their host galaxies; and the relations among DLA host galaxies, star-forming galaxies, and the underlying galaxy population at a given stellar mass. First, we identify star-forming galaxies using common optical selection techniques, then we “observe” DLAs by passing lines of sight through our lightcones. We restrict our analysis to galaxies at $1.7 < z < 2.3$ where our models are the most successful at reproducing the properties of DLAs and star-forming galaxies. We characterize the properties of DLA host galaxies in terms of their luminosities, colors, masses (stellar, cold gas, and total),

star formation rates, DLA cross-sections, sizes, metallicities, and amount of dust. Through comparing the properties along the DLA line of sight to the average DLA host galaxy properties, we seek to understand how DLAs can be used to understand the distribution and composition of the interstellar medium in high-redshift galaxies. Finally, we use our catalogs of DLAs and star-forming galaxies to study the relations between stellar mass and DLA cross section, cold gas fraction, star formation rate, metallicity, and dust reddening as traced by galaxy scaling relations. This chapter is organized as follows. Sections 5.2 and 5.3 describe how we select DLAs and star-forming galaxy, as well as the relations between model and observed SFGs. We present the properties of DLA host galaxies; compare DLAs to their host galaxies; and compare DLA host galaxies to SFGs in Section 5.4. In Section 5.5, we discuss the implications of our results and their connections to current literature. Finally, we summarize our conclusions in Section 5.6.

5.2 Galaxy Selection

In order to compare the properties of DLAs to star-forming galaxies, we begin by selecting catalogs of each using the same criteria as observational surveys. First, we present our underlying population of galaxies and the relations among stellar mass, H band magnitude, rest-frame B band magnitude, and halo mass in Section 5.2.3. In identifying DLAs, we adopt the same approach as was presented in Berry et al. (2013), which we summarize in Section 5.2.2. In Section 5.2.1, we discuss how we generate catalogs of star-forming galaxies using each galaxy’s photometric colors, then saving those that would be selected in various observational surveys.

5.2.1 Emission-Selected Galaxies

Increasing precision in photometric redshifts allows one to identify galaxies at a specific redshift down to a given magnitude limit, typically in the observed optical (V or R band) or near-infrared (H or K band). At $z \sim 2$, these bands track the rest-frame UV and optical, and select galaxies based on their unobscured star formation rate and stellar mass. We generate catalogs of galaxies down to a specific R and H band magnitude for comparison,

with an R band limit of $R = 25.5$, and H band limits of $H = 26$ and 28 .

The top row of Figure 5.1 shows the conditional probability of selecting a galaxy at $1.7 < z < 2.3$ with a specific stellar mass as a function of observed H band magnitude and rest-frame B magnitude. In contrast to the star formation rate-rest-UV relation, stellar mass is tightly correlated with both observed H band and rest-frame B magnitude over the entire range in stellar mass. Similar to the upper left panel, the bottom left panel shows the conditional probability distribution for selecting a galaxy with a given star formation rate with respect to R band magnitude. For moderate to high star formation rates, the R band magnitude can vary over two magnitudes, and the star formation rate of a galaxy with $R = 25.5$ can easily differ by a factor of five or more. Star formation rate does become more tightly correlated with R band magnitude for fainter galaxies (e.g., $R > 28$), as these galaxies have not produced enough metals to form a substantial amount of dust. The bottom right panel shows the relation between stellar mass and halo mass. Panels 1, 3, and 4 allow for a rough comparison of galaxies with a given observed H-band or rest-frame B-band magnitude to stellar mass, and subsequently to halo mass. They also indicate that at an H band magnitude limit of $H = 28$, galaxies will have a minimum stellar mass of $\sim 2 - 3 \times 10^7 M_\odot$ and correspondingly a minimum halo mass of $\sim 2 - 3 \times 10^{10} M_\odot$. As R band limited catalogs miss galaxies with significant dust extinction, we focus the majority of our analysis with respect to the H band limit, and only utilize the $R < 25.5$ limit as a subset when comparing DLA host galaxies to observational samples of star-forming galaxies within this magnitude limit. This method parallels photometric surveys and selects all galaxies down to a given stellar mass threshold, the underlying galaxy population.

5.2.2 Damped $\text{Ly}\alpha$ Absorption Systems

We obtain a catalog of host haloes by extracting haloes along lightcones from the Bolshoi simulations (Klypin et al. 2011; Behroozi et al. 2010). These lightcones cover a 1 by 1 deg^2 area on the sky over a redshift range $0 < z < 5$ and contain galaxies with dark matter halo masses from $10^{9.5}$ to $10^{14.5} M_\odot$. The Bolshoi simulation starts to become incomplete at $V_{\text{vir}} \simeq 50 \text{ km s}^{-1}$, $M_h \simeq 10^{10} M_\odot$; see Klypin et al. (2011) for more details. Haloes are then populated with galaxies as described above.

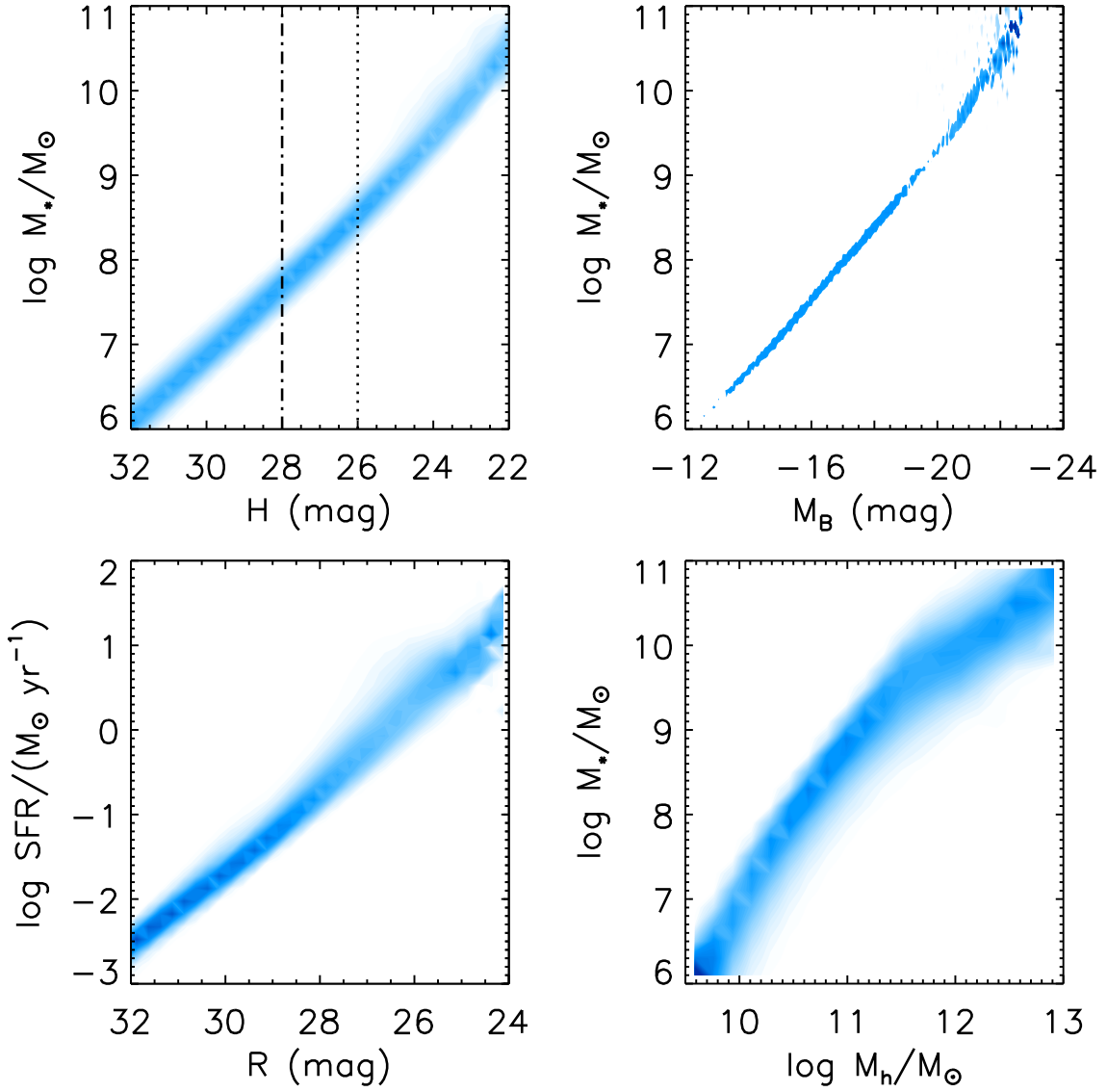


Figure 5.1 Top left - conditional probability distribution of stellar mass as a function of H band magnitude for all galaxies at $1.7 < z < 2.3$ in the GKj25 model. Top right - same as top left except for stellar mass versus rest-frame B band magnitude. Bottom left - star formation rate versus observed R band magnitude. Bottom right - stellar mass versus halo mass. The first two panels illustrate the how stellar mass tracks H band magnitude and rest-frame B band magnitude. The third panel shows the connection between star formation rate and R band magnitude, illustrating the impact of dust in identifying UV-bright galaxies.

For each galaxy, the molecular and atomic hydrogen gas is distributed in a disc with an exponential radial and vertical profile. The vertical scale height is proportional to the radial scale length, $z_g = \chi_z r_g$, where $\chi_z = 0.4$ is a constant, in rough agreement with observations of moderate redshift galaxies. Reasonable values of χ_z (e.g., not razor-thin discs) have a minimal effect on our results.

The central gas density is then defined as $n_0 = M_{\text{cold}} / (4\pi\mu m_H r_g^2 z_g)$, where M_{cold} is the atomic and molecular gas, m_H is the mass of the hydrogen atom, and μ is the mean molecular weight of the gas. The atomic gas density as a function of radius along and height above the plane is given by

$$n_{\text{HI}}(r, z) = n_0 \left(1 - f_{\text{H}_2}(r)\right) \exp\left(-\frac{r}{r_g}\right) \exp\left(-\frac{|z|}{z_g}\right) \quad (5.1)$$

See Figure 1 in Berry et al. (2013) for gas radial profiles for galaxies with different cold gas masses and metallicities in both of our models. The differences in the two gas partitioning recipes impacts the gas distribution, amount of star formation, and gas angular momentum.

The models output the radial distance from the central galaxy for each satellite galaxy, and we assign a random azimuth and polar angle ϕ and θ for each satellite's position with respect to the central. With the positions determined for every galaxy in each lightcone, we generate 20,000 random sightlines and integrate the three-dimensional gas density distribution along the sightline. Each galaxy is given a random orientation angle with respect to the sightline. All sightlines as well as the properties of all haloes with observed column densities above a threshold of $N_{\text{HI}} > 10^{19}$ atoms cm^{-2} are then saved as our catalog of absorption systems. In this chapter, we focus our analysis on systems with $N_{\text{HI}} > 2 \times 10^{20}$ atoms cm^{-2} , i.e., DLAs.

5.2.3 Star-Forming Galaxies

Using the selection criteria of Steidel et al. (2004), we identify a sample of BM/BX galaxies, allowing us to generate a catalog of UV-bright, star-forming galaxies at $z \sim 2$. These galaxies are selected using a color-color diagram of the $U - V$ and $V - R$ colors with an R -band magnitude limit of $R \leq 25.5$. These criteria take advantage of the $\text{Ly}\alpha$ decrement,

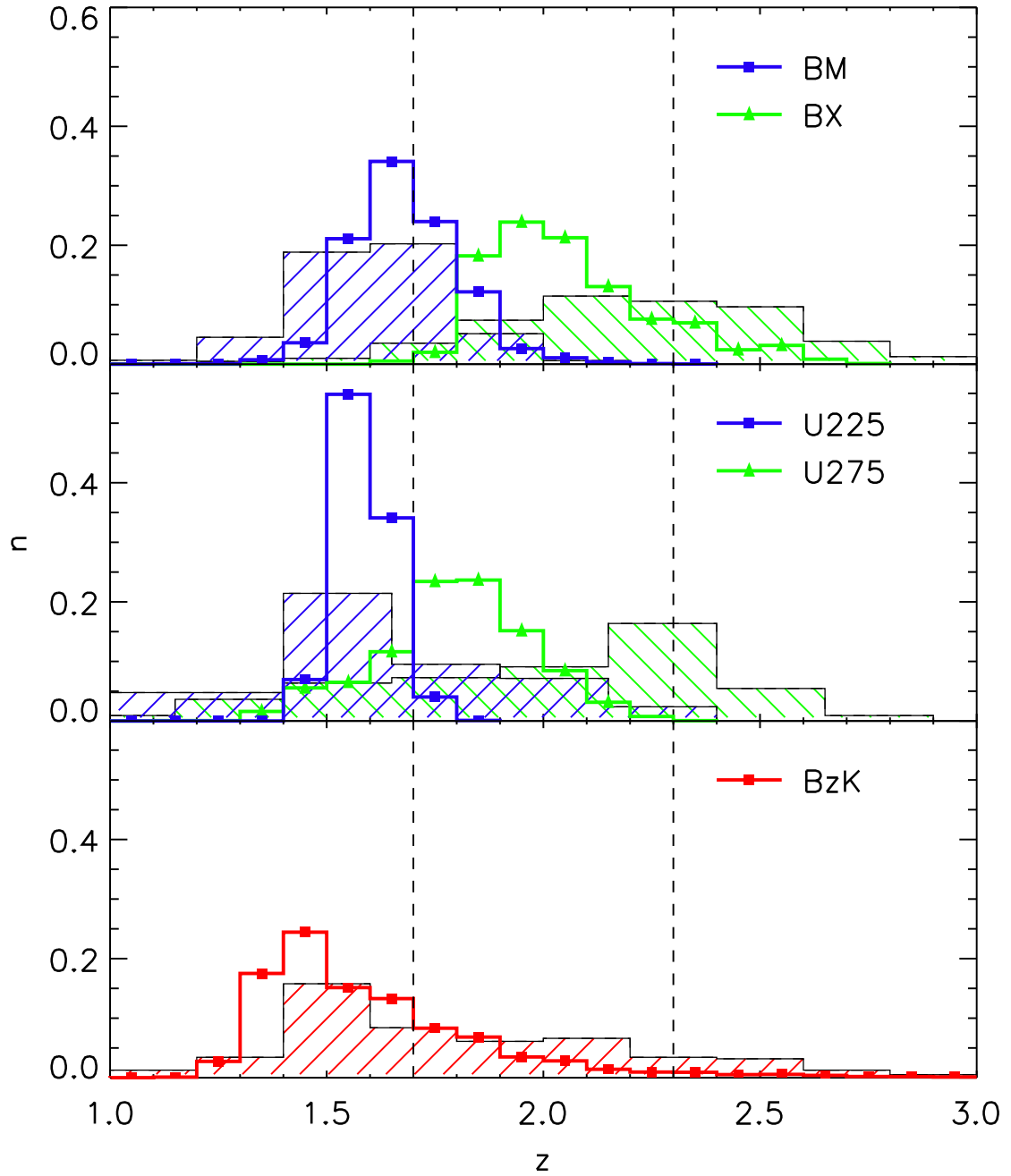


Figure 5.2 Redshift distribution of model and observed SFGs. Top panel - BM (blue squares) and BX (green triangles) galaxies in the GKj25 model with observations of BM and BX galaxies (blue and green hatched regions) from Shapley et al. (2005). Middle panel - same as top except for HST U225- (blue squares) and U275- (green triangles) band dropouts with observations from Hathi et al. (2010). Bottom panel - BzKs (red squares) with observations from Reddy et al. (2005).

similar to galaxies selected via the Lyman break, by selecting galaxies with blue rest-frame UV colors and absorption from intervening neutral hydrogen along the line of sight.

We also generate mock catalogs of HST/WFC3 U_{225} , U_{275} , and U_{336} band dropouts using the F225W, F275W, F336W, B_{435} , and V_{606} filters and the selection criteria of Hathi et al. (2010). Similar to the BXs and LBGs selected from ground-based telescopes, these HST-UV dropouts take advantage of the decrement in galaxy spectra blueward of $\text{Ly}\alpha$. Hathi et al. (2010) find these galaxies to have typical redshifts of $z = 1.6 \pm 0.2$, $z = 2.1 \pm 0.4$, and $z = 2.3 \pm 0.4$ respectively.

Massive galaxies at $1.4 < z < 2.5$ are identified in K -selected samples based on their B -, z -, and K -band photometry (Daddi et al. 2004; Reddy et al. 2005). In this technique, requiring $BzK = (z - K)_{AB} - (B - z)_{AB} > -0.2$ selects star-forming galaxies (BzKs) at these redshifts, independently of their dust reddening. As star-forming BzKs exhibit a broad range of galaxy properties over a large redshift range, we focus our BzK analysis on only the brightest BzKs with K band magnitudes $K < 23$ AB mag. Additionally, there is significant overlap between BXs, HST UV-dropouts, and BzKs, so this magnitude limit allows us to identify only the most massive galaxies. The relative insensitivity to dust reddening of this selection technique also permits us to probe star-forming galaxies with larger amounts of dust that would be missed from rest-UV color selection methods.

We also “observed” passively evolving galaxies and ultra-luminous infrared galaxies, but found little overlap between them and DLAs, in the former due to lack of a significant amount of cold gas and in the latter a small number density. Passively evolving galaxies were selected using $BzK < -0.2$ and $(z - K)_{AB} > 2.5$. Ultra-luminous infrared galaxies were selected based on their bolometric luminosities ($L_{bol} > 10^{11} L_{\odot}$). Due to their small overlap fraction, we did not include them in our analysis.

The faint luminosities and small amounts of dust reddening in $\text{Ly}\alpha$ -emitting galaxies suggests that they may have similar physical properties to DLAs. Our SAMs do not track $\text{Ly}\alpha$ emission, so we are unable to identify galaxies that would be selected as LAEs. Nonetheless, Shapley et al. (2003b) show that LAEs have similar rest-frame colors to LBGs and a large fraction would be selected as LBGs (and BM/BXs), if it were not for the $R \leq 25.5$ magnitude cut. Therefore, we do not compare the population of LAEs to DLAs, although

Table 5.1 Galaxy Properties

Galaxy type	Selection limit	ρ_{obs} arcmin^{-2}	ρ_{BR} arcmin^{-2}	ρ_{GK} arcmin^{-2}
BM/BX	$R < 25.5$	3.8/5.2	0.65/0.73	0.84/1.50
BzK	$K_s < 21$	3.1 ± 0.2	0.79	1.93
U225/U275	$B_{435} < 26.5$	-/-	0.49/0.47	2.54/3.67

we do investigate the relations among faint star-forming galaxies (e.g., BM/BXs) that are not subject to the same magnitude cut. The connection between DLAs and faint BM/BXs may yield insight into the relation between DLAs and LAEs.

5.3 Properties of Model and Observed Star-Forming Galaxies

In this section, we assess the accuracy of our models in reproducing the properties of star-forming galaxies by comparing those in our models to sets of observations. Figure 5.2 shows the redshift distribution of both star-forming galaxies identified in the GKj25 model and those observed in galaxy surveys. We find a comparable redshift distribution in the BRj25 model (not shown). As can be seen in each panel, the distribution of model galaxy redshifts are comparable to observations. In all cases, we find a slightly narrower distribution of galaxy redshifts in the models than is observed. These differences are likely attributable to photometric errors in the observations. Additionally, Table 5.1 shows the number densities of BM/BXs, U225-/U275-band dropouts, and BzKs for our models and observations. Both models underproduce the number of star-forming galaxies where the GKj25 model is more comparable to observations.

As each galaxy type has a different redshift distribution and their properties vary slightly with redshift, we identify a subset with redshifts $1.7 < z < 2.3$ in order to make a more robust comparison to DLAs at the same redshift. At this redshift, BM and BX galaxies exhibit similar galaxy properties, therefore we combine them to form a catalog of UV-bright star-forming galaxies. Similarly, we combine the HST U225- and U275-band dropouts into a catalog of HST UV-bright, star-forming galaxies. In both cases, the majority of galaxies are the higher redshift BX galaxies and HST U275-band dropouts.

Figure 5.3 shows the distribution of stellar masses, star formation rates, and $E(B-V)$

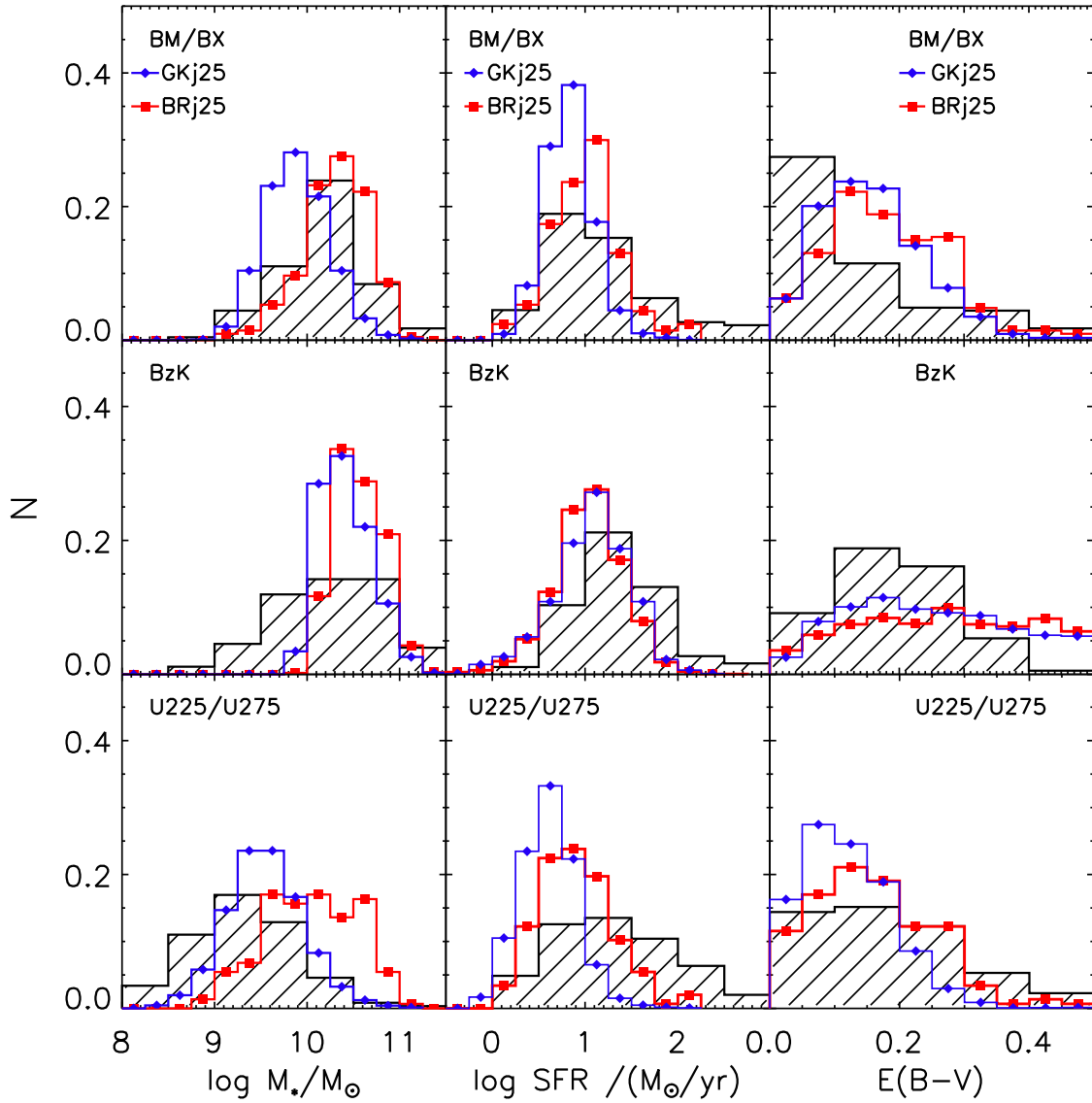


Figure 5.3 Normalized distribution of stellar masses (left column), star formation rates (middle column), and $E(B-V)$ values (right column) are shown for the BRj25 model (red squares), GKj25 model (blue triangles), and observed galaxies (black) at $1.7 < z < 2.3$. Top row - BM/BXs. Middle row - BzKs. Bottom row - HST U225/U275 dropouts. In general, both models produce similar model galaxy properties, which typically have lower star formation rates and comparable $E(B-V)$ values to observed SFGs. Stellar masses for model and observed BM/BXs and BzKs are comparable, yet the models produce higher stellar masses and lower star formation rates than observed HST U225/U275 dropouts.

values for observed and model galaxies in our BRj25 and GKj25 models at $z = 2$. Overall, both models produce similar galaxy properties, which are comparable to observations. Similar to the distribution of observed galaxy redshifts, photometric errors likely contribute to the uncertainty in spectral energy distribution fitting. In comparison to observations, our models produce galaxies with a narrower range in star formation rates and lower star formation rates overall, mainly lacking the tail to high star formation rates. Reproducing the very high star formation rates observed in high redshift galaxies is a current challenge in semi-analytic models (Niemi et al. 2012). Our models also produce larger $E(B-V)$ values and a broader distribution of them. For each type of star-forming galaxy, the BRj25 model produces higher stellar masses than the GKj25 model, varying from ~ 0.2 to ~ 1 dex. The BRj25 model also produces higher star formation rates in BM/BX galaxies and U225-/U275-band dropouts than the GKj25 model. In the remainder of the paper, due to the similarities in galaxy properties and redshifts for our two models, we show the properties of star-forming galaxies in the GKj25 model when the differences are not significant. Overall in spite of producing too few star-forming galaxies, the models produce galaxies with similar properties to observations.

5.4 Results

In this section, we compare the properties of star-forming galaxies and the general galaxy population in our models to model DLAs. We begin by presenting the $z = 2$ distribution functions for our models in Section 5.4.1. In Sections 5.4.2, 5.4.3, and 5.4.4 we present the properties and photometry of DLA host galaxies and compare them to galaxies at similar masses and luminosities. The differences between galaxy properties measured along the line of sight and the average for the host galaxy are presented in Section 5.4.5 and Section 5.4.6. Finally, we discuss DLA host galaxies and star-forming galaxies in the context of galaxy scaling relations in Section 5.4.7.

5.4.1 General Galaxy Population

Our BRj25 and GKj25 models are very similar to those presented in B13 (see also SPT13 and PST13), to which we refer the reader for a more in depth discussion. In order to assess the accuracy of our models at $z = 2$, we first present the $z = 2$ galaxy stellar mass functions (GSMFs), star formation rate functions (SFRFs), H I mass functions (HIMFs), H₂ mass functions (H2MFs), H band magnitude functions, and metallicity functions in Figure 5.4. The upper left panel of Figure 5.4 shows the GSMFs at $z = 2$ for our models and observations. Both of the GSMFs for our models are a good match to the observed GSMFs, although they produce too many galaxies at low stellar masses. The overproduction of low mass galaxies is a known problem for semi-analytic models in the high-redshift universe and has been seen in numerical simulations, although this region is not well constrained at $z = 2$. For both the GSMFs and SFRFs, we introduce uncertainty in measuring the star formation rates and stellar masses by randomly taking a stellar mass and star formation rate from a distribution centered on the true values and with a conservative width of $\Delta M_s = 0.2$ and $\Delta \text{SFR} = 0.2$. This process has a negligible effect on the lower end of the distributions while it flattens the upper end. Similar to the upper left panel, the upper right panel of Figure 5.4 shows the SFRFs for the models along with observations. Again, our models are a reasonable fit to observations, although they underproduce the number of galaxies with high star formation rates. While the BRj25 model is more successful at reproducing the GSMF, the GKj25 model does a better job with the SFRF. This result implies that the stellar mass to star formation rate ratio is not in agreement with observations.

The middle left and right panels show the HIMFs and H2MFs, respectively, for both our models. The HIMFs in each of our models are comparable at high masses although the GKj25 model produces fewer galaxies with intermediate H I masses and more galaxies with low H I masses. Both models predict substantially more H I in galaxies at $z = 2$ than is observed in local galaxies, although the shapes of the HIMFs are comparable. As can be seen in their H2MFs, the GKj25 model predicts that more cold gas is in the molecular phase in galaxies of all masses, especially in more massive galaxies. This result is also reflected in the higher SFRs in the GKj25 model as the metallicity-based H₂ formation recipe is more

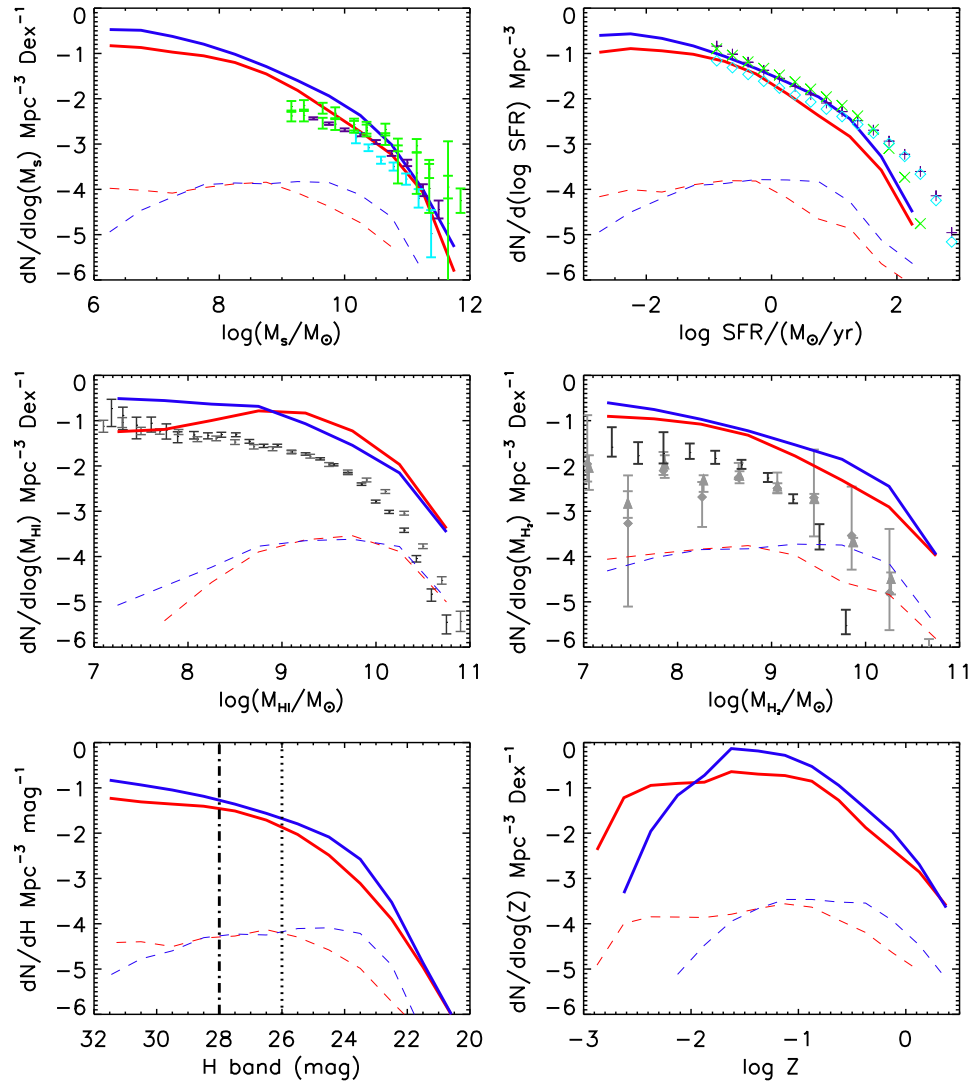


Figure 5.4 Top left - galaxy stellar mass functions (GSMFs, thick lines) and DLA stellar mass functions for 10,000 sightlines (thin lines) in the BRj25 (red) and GKj25 (blue) models at $z = 2$. Top right - same as top left except for star formation rate functions (SFRFs). Middle left - HI mass functions (HIMFs). Middle right - H_2 mass functions (H2MFs). Bottom left - H band magnitude functions. Bottom right - metallicity functions. Observations of GSMFs from Kajisawa et al. (2009, purple, $1.5 < z < 2.5$), Fontana et al. (2006, cyan, $1.6 < z < 2.0$), Marchesini et al. (2009, green, $1.5 < z < 2.0$ and $2.0 < z < 2.5$) are overplotted in the first panel. Observations of the SFRF from Reddy et al. (2008, purple, $z = 2.3$), Magnelli et al. (2011, cyan, $z = 2.0$), Sobral et al. (2012, green, $z = 2.2$) are also shown in the second. Similarly, the local HIMF from Martin et al. (2010) and H2MFs from Keres et al. (2003, gray) and Obreschkow et al. (2009, black) are shown in the third and fourth. The CANDELS wide (dotted line) and deep (dot-dashed line) field H band depths are also overplotted. Both models produce similar distribution functions where the GKj25 model has slightly more efficient H_2 formation.

efficient than the pressure-based model. Both models predict significantly flatter slopes than the local H2MF, which is mainly caused by a larger number of high- H_2 mass galaxies.

The bottom left panel shows the H band magnitude function for each model with the CANDELS wide and deep H-band limits overplotted. The H band traces rest-frame optical light ($\lambda \sim 5500\text{\AA}$ at $z = 2$), which is mainly determined by the galaxy stellar mass. The GKj25 model produces more galaxies at all H band magnitudes than the BRj25 model similar to the GSMFs. See Somerville et al. (2012) and SPT14, for a more in depth comparison of the luminosity functions.

The last panel shows the metallicity distribution functions where metallicities are the average for each galaxy. The metallicity functions differ substantially for each model where the galaxies in the GKj25 model exhibit a roughly log normal distribution peaked at $\log Z \sim -1.5$. On the other hand, metallicities are somewhat lower in the BRj25 model with a much flatter distribution. We find it interesting that DLAs exhibit a metallicity floor of $[Z] \sim -2.6$ to -2.8 , in line with the minimum metallicities observed in our models (Qian & Wasserburg 2003; Wolfe et al. 2005; Rafelski et al. 2012).

In general, the $f_j = 1$ models (e.g., GKj1, BRj1; not shown) produce distribution functions quite similar to each other and $f_j = 2.5$ models except they are more efficient at converting neutral gas into molecular gas, yielding higher stellar masses, star formation rates, and metallicities. This difference is most pronounced at the upper end of the distribution functions. See SPT14 for a more in depth discussion of these models. From our two $f_j = 2.5$ models, both models are quite successful, where the GKj25 model is our preferred model. B13 found both models to be fairly accurate in reproducing the local GSMF, HIMF, and H2MF and the properties of high-redshift DLAs. Again, the GKj25 model was more successful overall. In section 5.3, we showed that the properties of high-redshift star-forming galaxies do not vary significantly among our two models. Therefore, we focus our analysis on the GKj25 model when both models produce similar results.

5.4.2 DLA Host Galaxy Properties

The DLA number densities for 10,000 sightlines at $1.7 < z < 2.3$ are overplotted at the bottom of each panel in Figure 5.4. We are unable to determine the true number density

of DLAs as the DLA cross section and number of sightlines are degenerate. While the normalization is arbitrary, overplotting the distribution of DLA properties at the bottom of each panel of figure 5.4 provides a useful comparison for understanding what types of galaxies typically host DLAs at this redshift.

In terms of their stellar mass functions, DLAs in both models exhibit a relatively flat distribution, indicating that DLAs are equally likely to be selected across a large range in stellar mass, $6 \lesssim \log M_s/M_\odot \lesssim 10.5$. Similar to the GSMFs, there are fewer DLA host galaxies with large stellar masses and more with low stellar masses in the BRj25 model than in the GKj25 model. The number of DLAs in both models drops with decreasing stellar mass below $\log M_*/M_\odot \sim 6$ (not shown). At the high mass end, the shape of the DLA stellar mass distribution in both models tracks their respective GSMFs. The distribution of DLA host galaxy H band magnitudes closely tracks that of the stellar mass distribution (bottom left panel), indicates that H band magnitude is a good tracer of stellar mass in DLAs at $z = 2$. Moreover, the model H band magnitude functions predict that a significant number of DLA host galaxies should be detectable in the CANDELS deep field and a substantial number in the wide field. We further discuss the detectability and photometric properties of DLAs in section 5.4.3.

Similar to the distribution of DLA stellar masses, DLAs in both models show a broad range in star formation rates, $-3 \gtrsim \log \text{SFR}/M_\odot\text{yr}^{-1} \lesssim 1.5$, where those in the BRj25 model typically have lower star formation rates than in the GKj25 model. The number of DLAs with low star formation rates decreases with star formation rate in both models below $\log \text{SFR}/M_\odot\text{yr}^{-1} \lesssim -3$. Due to the dependence of star formation on the density of molecular gas, we find a similar distribution in H_2 mass as star formation rate in both models. This results in DLA host galaxies exhibiting a broad range in H_2 mass which spans ~ 4 decades.

Interestingly, due to the relatively flat distribution of stellar masses and star formation rates over several decades, there is neither a “typical” stellar mass and star formation rate nor a bimodality for DLAs. Due to the turnover at the high end of the GSMF and SFRF and the flat distribution of DLAs up to this turnover, our models predict that a large fraction of galaxies with high stellar masses and star formation rates will host DLAs, specifically

Table 5.2 Average DLA Host Galaxy Properties

		GKj25	BRj25
$\log M_*$	M_\odot	8.7 ± 1.0	8.0 ± 1.1
$\log \text{SFR}$	$M_\odot \text{ yr}^{-1}$	-0.3 ± 1.0	-1.1 ± 1.0
$\log M_{\text{HI}}$	M_\odot	9.4 ± 0.7	9.5 ± 0.5
$\log M_{\text{H}_2}$	M_\odot	8.9 ± 0.9	8.1 ± 1.0
H (mag)	mag	26.2 ± 2.1	28.0 ± 2.5
$\log Z$	Z_\odot	-0.9 ± 0.4	-1.4 ± 0.7
Errors show the 1σ confidence intervals.			

those at and above the knee in the stellar mass and star formation rate function. In both models, galaxies with stellar masses $\log M_*/M_\odot \gtrsim 10$ and SFRs $\log \text{SFR} / (M_\odot \text{ yr}^{-1}) \gtrsim 1$ have the highest probability of hosting DLAs. Moreover, the number density of low mass galaxies increases with decreasing stellar mass and star formation rate while the number of DLAs decreases slightly, which is stronger in the GKj25 model than the BRj25 model. These trends imply that the fraction of low mass galaxies hosting DLAs decreases constantly below $\log M_*/M_\odot \sim 10$ and $\log \text{SFR} / (M_\odot \text{ yr}^{-1}) \sim 1$ in the GKj25 model. The BRj25 model shows similar trends. Nonetheless in both models, although massive, star-forming galaxies are the most likely to host DLAs, they only make up a small fraction ($\lesssim 5 - 10\%$) of the total number of DLAs. The average DLA host galaxy properties for the GKj25 and BRj25 models at $z = 2$ are shown in Table 5.2. Since DLAs contain the majority of the neutral gas content in the Universe, our models indicate that high-HI mass galaxies arise from a wide range in stellar masses.

As can be seen in the middle left panel of Figure 5.4, the most common HI mass for DLAs in both models are at $\log M_{\text{HI}}/M_\odot \sim 9.5$ where the GKj25 model shows a tail to lower HI masses. The HI masses seen in model DLAs is the most consistent of any galaxy property among our models. Similar to the stellar mass functions, galaxies with the largest HI masses are the most likely to host DLAs as is expected given that they will have the largest DLA cross sections. The large distribution of HI masses is consistent with the large range in DLA cross sections found in DLAs in simulations (Fumagalli et al. 2011; Cen 2012; Berry et al. 2013).

The DLA metallicity function for the BRj25 model closely tracks the galaxy metallicity function where DLA host galaxies are found at all metallicities. In contrast, DLAs in the

GKj25 model exhibit a different metallicity distribution where the majority are found in relatively metal-rich galaxies, as high mass galaxies are more likely to host DLAs. This result is interesting given that observations of DLAs indicate that they typically exhibit lower metallicities than star-forming galaxies at the same redshift. Additionally, there appears to be a population of DLAs with low metallicities in the BRj25 model that are not seen in the GKj25 model. We explore the relation between DLA and star-forming galaxy metallicities further in Sec. 5.4.7.

5.4.3 DLA Photometry and Overlap Fraction

Figure 5.5 shows the colors of all galaxies with $H < 28$ (left column), the colors of DLAs with $H < 28$ (middle column), and the apparent magnitudes of DLAs at $1.7 < z < 2.3$ in the GKj25 model. DLAs and galaxies in the BRj25 model (not shown) have similar color-color diagrams. Note that DLA colors are the same as the typical galaxy colors at the same apparent magnitude. This indicates that DLAs do not select galaxies with any specific set of colors. As the contours are dominated by the large number of faint galaxies, we overplot a brighter H band limit of $H < 26$. Brighter DLAs are slightly redder in all color-color diagrams than fainter DLAs, similar to the galaxy population in general.

Due to a large number of DLAs having relatively low $E(B-V)$ values, they also exhibit blue enough colors to be selected by UV color-selected surveys, as can be seen by them falling within the selection regions. As can be seen in the right column, both of our models predict that only a small fraction of DLAs are bright enough to be selected by any of these surveys. This is due to the large number of DLAs with low stellar masses and star formation rates. Therefore, galaxy surveys will be much more successful at detecting DLA hosts by probing fainter magnitudes. Both our models predict that probing down to $R = 28$ will result in a significant improvement in the number of DLA counterparts over surveys limited to $R = 25.5$ at $z = 2$. The NIR is also a good wavelength to look for DLA counterparts as a large number would be detected from deep H band imaging. In spite of the advances in current technology, our models predict that a substantial fraction of DLAs are beyond the detection limit of any current galaxy survey.

The left panel of Figure 5.6 shows the cumulative distribution for all DLAs as a function

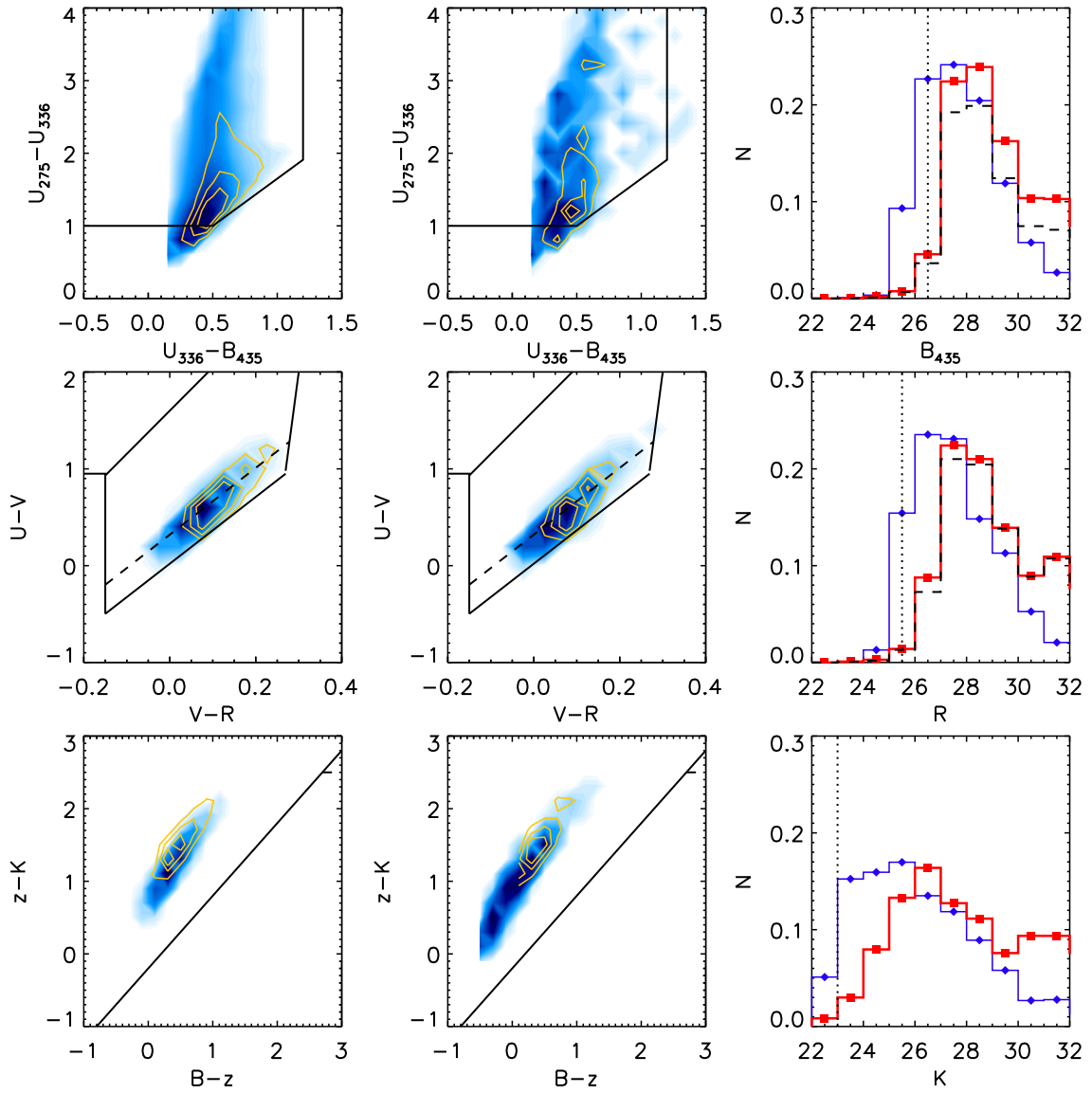


Figure 5.5 Left column - color-color diagrams for all galaxies with $H < 28$ (blue) and $H < 26$ (orange contours) at $1.7 < z < 2.3$ where the color selection regions used to identify high-redshift SFGs overlaid. Middle column - same as left column except for DLAs in the GKj25 model. Right column - distribution of DLA B_{435} , R , and K band magnitudes for DLAs in the BRj25 (red) and GKj25 (blue) models (top to bottom). From top to bottom, each row shows the color-color diagrams used to select HST U275-band dropouts, BM/BX galaxies, and BzK galaxies. The dashed line in the BM/BX color-color diagram shows the different selection region for BM (lower) and BX (upper) galaxies. The dashed lines in the right column show the distribution of DLAs within the associated color selection region for the BRj25 model. Vertical dotted lines indicate the typical magnitude limits for each of these surveys.

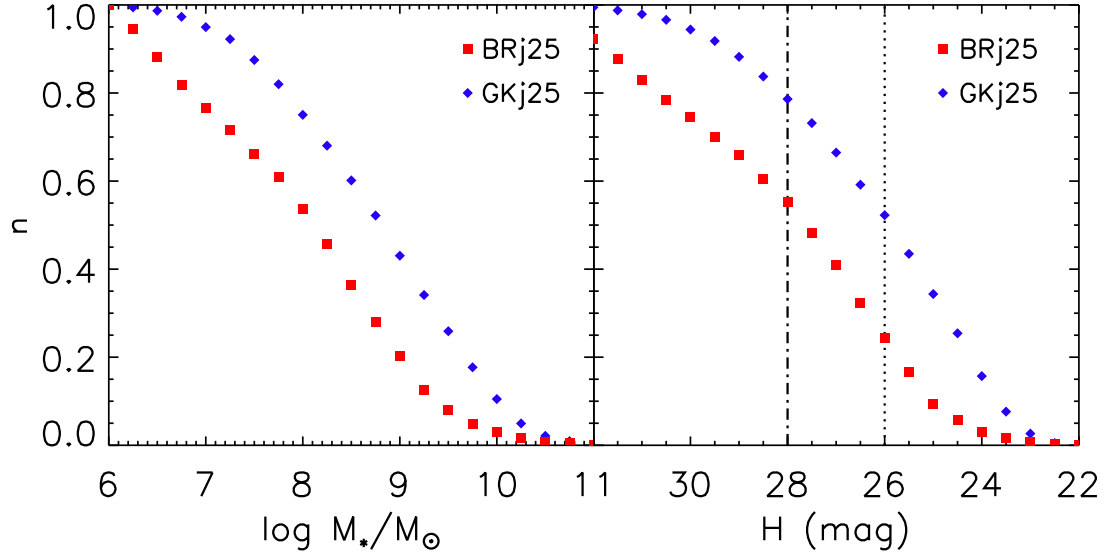


Figure 5.6 Left panel - cumulative distribution of DLA host galaxy stellar masses in the BRj25 (red squares) and GKj25 (blue diamonds) at $z = 2$. Right panel - same as left except for H band magnitude. The vertical dotted and dashed lines at $H=26$ and 28 are the depths of the CANDELS wide and deep fields respectively. Our models predict that deep H band imaging as in the CANDELS fields will allow for a significant number of DLA host galaxies to be identified where the GKj25 model predicts that significantly more DLA host galaxies should be recovered than the BRj25 model.

of decreasing stellar mass at $z = 2$. Both models predict the majority of DLAs to have stellar masses greater than $\log M_s/M_\odot > 8$. The cumulative distributions show how there are significantly more DLAs with higher stellar masses in the GKj25 models. In both models, identifying DLAs with high metallicities ($\log Z > -1$) also selects ones with significantly larger stellar masses (not shown). This result is due to DLAs generally increasing in metallicity with stellar mass, similar to the mass-metallicity relation, which is discussed in more detail in Section 5.4.7.

The right panel of Figure 5.6 shows the cumulative distribution of DLAs as a function of H band magnitude. The GKj25 model predicts that 52% and 79% of DLAs have H band magnitudes $H < 26$ and $H < 28$, leading us to predict that a substantial fraction of DLA host galaxies should be detectable in the CANDELS wide and deep fields respectively. In contrast, the BRj25 model predicts these detection rates to drop to 24% and 55% respectively. Therefore, given a field with a sufficient number of bright quasars, the detection rate of DLA host galaxies going to a depth similar to that in the CANDELS fields should allow

us to differentiate between our two models and determine whether the majority of DLAs at $z = 2$ originate in lower or more moderate mass galaxies. Both of our models predict that there is a significant faint population of DLA host galaxies that will require larger telescopes such as the James Webb Space Telescope. DLAs with high metallicities are significantly brighter in the H band where our models predict that 81% and 70% of DLA host galaxies in our GKj25 and BRj25 models respectively will be observable in the CANDELS wide field. Therefore, searching for galaxy counterparts to high-metallicity DLAs should yield more detections according to our BRj25 model. Krogager et al. (2012) searched for DLA counterparts in high metallicity DLAs which allowed them to more than double the number of detections at $z \gtrsim 2$ (also see Fynbo et al. 2010, 2011). The significant increase in detection rate is qualitatively more consistent with our BRj25 model, although we do note that the majority of our bright DLAs in the GKj25 model have metallicities $[Z] > -1$.

5.4.4 Dust Reddening

The top panel of Figure 5.7 shows the distribution of $E(B-V)$ values for all DLA host galaxies and those with $H < 26$ in the GKj25 model. The bottom panel is similar to the top except for BzKs, BM/BXs, U225-/U275-band dropouts, and all galaxies with $H < 26$. The distribution of $E(B-V)$ values is similar for the BRj25 model. These values reflect the average $E(B-V)$ value for each galaxy assuming a mixed dust geometry. In contrast, the results inferred from stacking quasars with and without DLAs along the line of sight as well as studies of DLAs toward radio-selected quasars reflect the average $E(B-V)$ value in DLA gas along the line of sight assuming a sheet geometry (e.g., Ellison et al. 2005; Khare et al. 2012). As the relation between these two quantities is nontrivial, we do not attempt to calculate the $E(B-V)$ value along the line of sight toward the DLA. Nonetheless, we find that the vast majority of DLA host galaxies have very small $E(B-V)$ values, generally consistent with observations that suggest only trace amounts of reddening in DLAs. For moderate to large impact parameters, the amount of dust reddening along the line of sight is likely lower than that of the host galaxy, while the effect of dust reddening will be stronger due to the difference in dust geometry. The majority of DLA host galaxies with low amounts of dust reddening are associated with low mass, gas rich halos, while all DLA

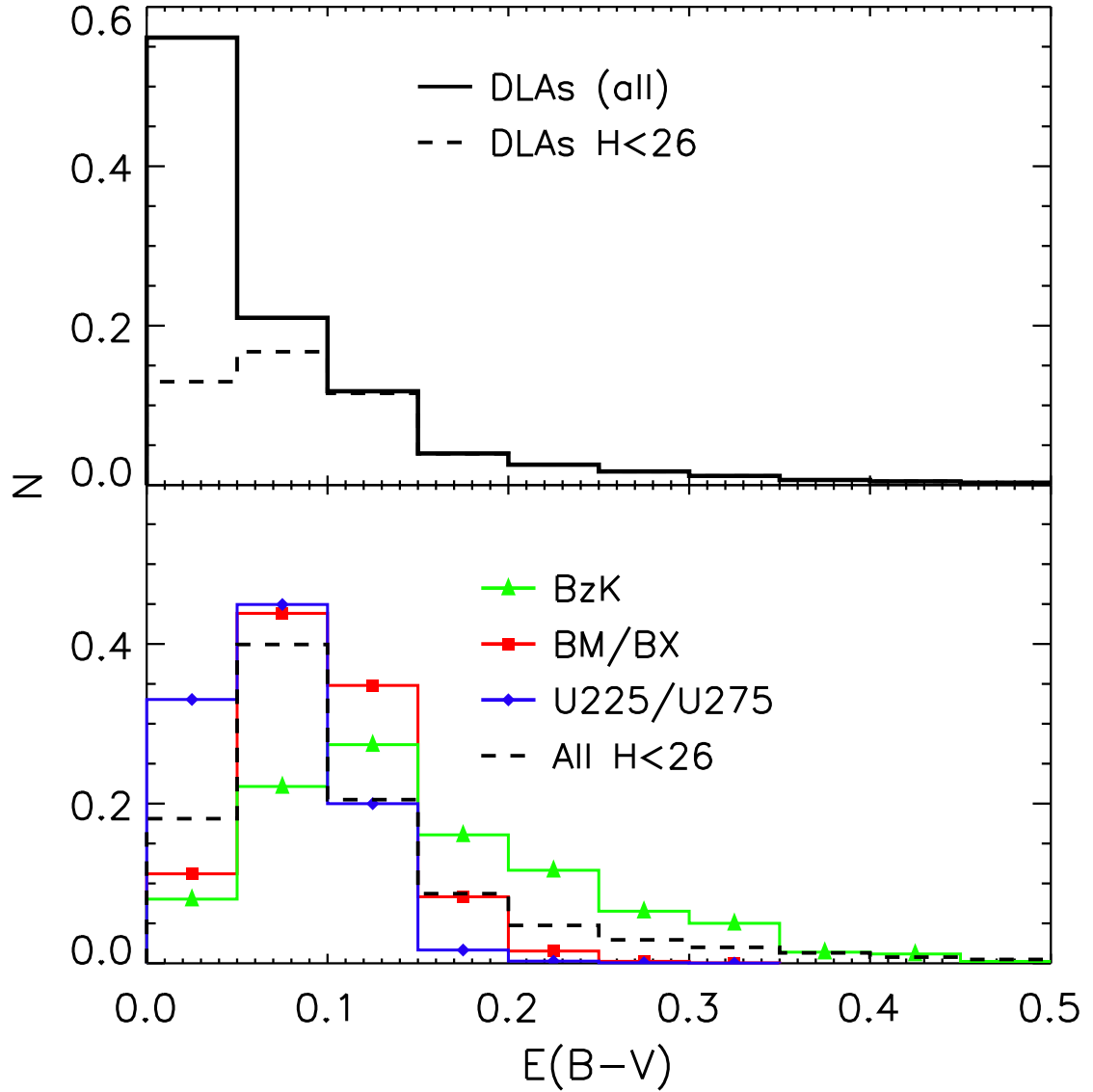


Figure 5.7 Upper panel - distribution of $E(B-V)$ values for all DLA host galaxies (black line) and those with H band magnitudes $H < 26$. Lower panel - same as top except for BzKs (green triangles), BM/BXs (red squares), and HST U225-/U275-band dropouts (blue diamonds) with their associated magnitude limits as well as all galaxies with $H < 26$ (black dashed line). DLA host galaxies have very low $E(B-V)$ values, consistent with observations of DLAs. Model $E(B-V)$ values represent the average for each galaxy and assume a mixed dust geometry while DLA $E(B-V)$ values likely act as more of a screen in front of the background quasar and only sample $E(B-V)$ along the line of sight. DLAs exhibit significantly smaller amounts of dust reddening than any type of star-forming galaxy, owing to the contribution of a significant number of very low mass systems.

host galaxies with significant dust reddening, $E(B-V) > 0.1$, arise in galaxies with $H < 26$. Galaxies with $H < 26$ exhibit a tail to high $E(B-V)$, suggesting that these highly reddened DLAs may be missed from traditional color-selected quasar surveys. They arise in the most massive galaxies with highest metallicities, but represent only a small fraction of the DLA population. We predict the fraction of DLAs with $E(B-V) > 0.2$ to be 17% in the GKj25 model and 7% in the BRj25 model.

Galaxies identified based on their rest-frame ultraviolet colors (BM/BX galaxies and U225-/U275-band dropouts) have smaller amounts of dust reddening than the more massive BzKs, which are selected based on their rest-frame optical colors. Moreover, U225-/U275-band dropouts have less dust reddening than BM/BX galaxies due to those surveys having fainter magnitude limits, causing them to have lower stellar masses. When decreasing the luminosity threshold to $H < 26$ for BM/BXs, BzKs, and U225-/U275-band dropouts(not shown), we find the color selection criteria to have no significant effect on the distribution of $E(B-V)$ values as all galaxies have similar $E(B-V)$ distributions. This result stems from low mass, low luminosity galaxies dominating the number density and being mostly star-forming with very low metallicities, resulting in the majority having low amounts of dust extinction.

5.4.5 DLA Impact Parameter

As DLAs probe gas at different galactocentric radii, they contain information on the size of DLA host galaxies as well as how DLA and galaxy properties may vary as a function of radius. Figure 5.8 shows the distribution of impact parameters for DLAs in the BRj25 and GKj25 models at $1.7 < z < 2.3$ as well as observations of DLAs at $1.92 < z < 3.40$ (Krogager et al. 2012). The distribution of impact parameters in our models does not vary significantly from $z = 3$ to $z = 2$ (not shown). In both models, DLAs have impact parameters that are remarkably similar to observations. Our distribution of impact parameters measure the distance from the DLA line of sight to the center of the host galaxy. Observationally in the case where more than one potential counterpart is found, the natural preference is to measure the distance from the DLA to the nearest galaxy, which could bias the observed distribution to smaller values. With only 10 galaxy counterparts found, it is difficult to

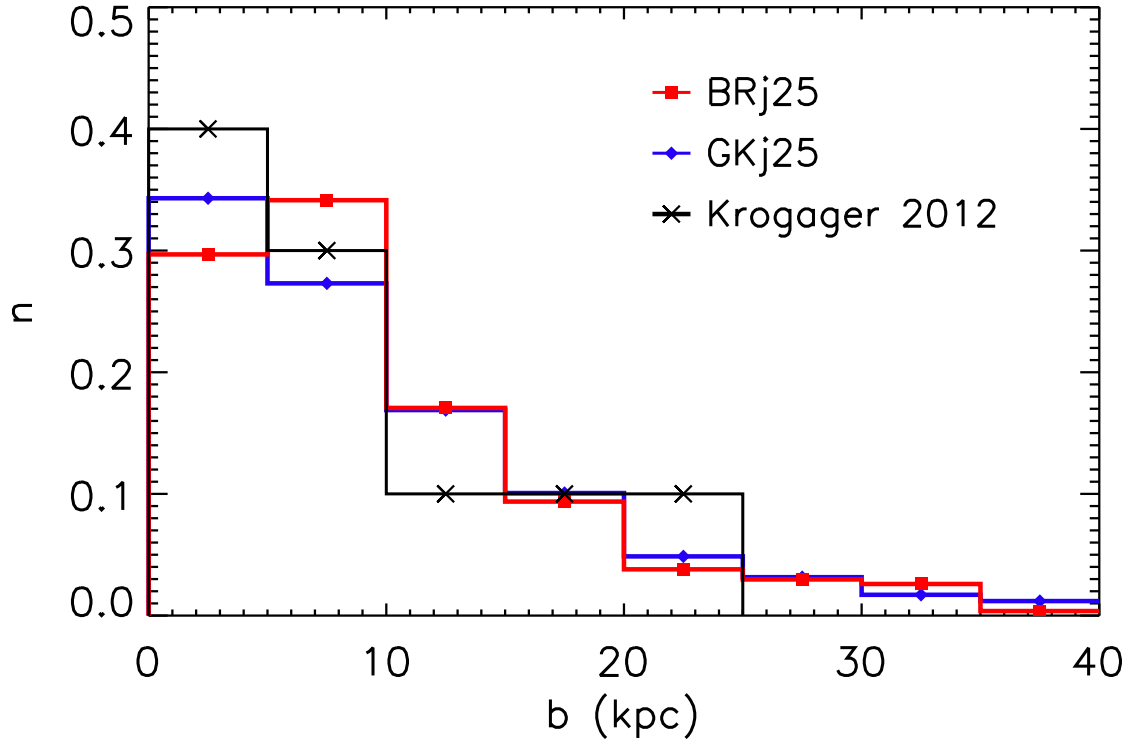


Figure 5.8 Distribution of impact parameters for DLAs at $1.7 < z < 2.3$ in the BRj25 (red squares) and GKj25 (blue diamonds) models with the observations of DLAs at $1.92 < z < 3.40$ overplotted (Krogager et al. 2012, black crosses). DLAs in both models are a close match to observations where the majority of DLAs have impact parameters $b < 10$ kpc, or ~ 1.2 arcsec.

tell how significant this result is. Rahmati & Schaye (2014) examine the relation between different SFR thresholds and which galaxy one would associate the DLA with, and found that a significant number of DLAs originate in galaxies too faint to be detected which could result in them being associated with a different more luminous galaxy at a larger separation. Additionally, observations of DLAs may miss DLA host galaxies at very small impact parameters as the host galaxy may be obscured by the luminosity of the bright background quasar. Krogager et al. (2012) targeted DLAs with metallicities $\log Z > -1$, which may have biased their distribution of DLAs to more massive galaxies. When applying a similar metallicity cut (not shown), we find significantly more massive and more luminous DLA host galaxies. More massive galaxies have larger cold gas masses extending to larger radii, which would likely increase the average impact parameter.

Traditional emission-selected surveys sample the average galaxy properties, while DLAs originate in cold gas at different galactocentric radii, which may cause them to vary substantially. We model the change in galaxy properties that would be measured for a DLA at its given impact parameter relative to the average properties of its host galaxy. Figure 5.9 shows the distribution of H_2 fractions, star formation rates, and metallicities for DLAs at $z = 2$ calculated along the DLA line of sight and averaged over the entire galaxy in the GKj25 model. We do not show the BRj25 model as the difference between DLA and galaxy properties is not very different from the GKj25 model. The H_2 fraction along the line of sight is calculated using the metallicity-based, varying-UV H_2 formation formulae and the cold gas density at that radius. We use the average metallicity and star formation rate for the galaxy for simplicity. Due to the large impact parameters decreasing the cold gas density, the H_2 fractions along the line of sight are significantly lower than the average H_2 fractions for each galaxy. Our models predict 85% of DLAs to have H_2 fractions $f_{H_2} < 0.1$ compared with 79% of host galaxies. The star formation rate and metallicity both likely decrease with radius, which would have the effect of decreasing and increasing the threshold for H_2 formation respectively. The lower H_2 fraction and cold gas density cause the star formation rate along the line of sight to be substantially lower than the average for the host galaxy. Our models predict that DLAs have typical star formation rates of $\sim 2 - 3$ dex lower than their associated host galaxy star formation rates. This effect may explain why DLAs

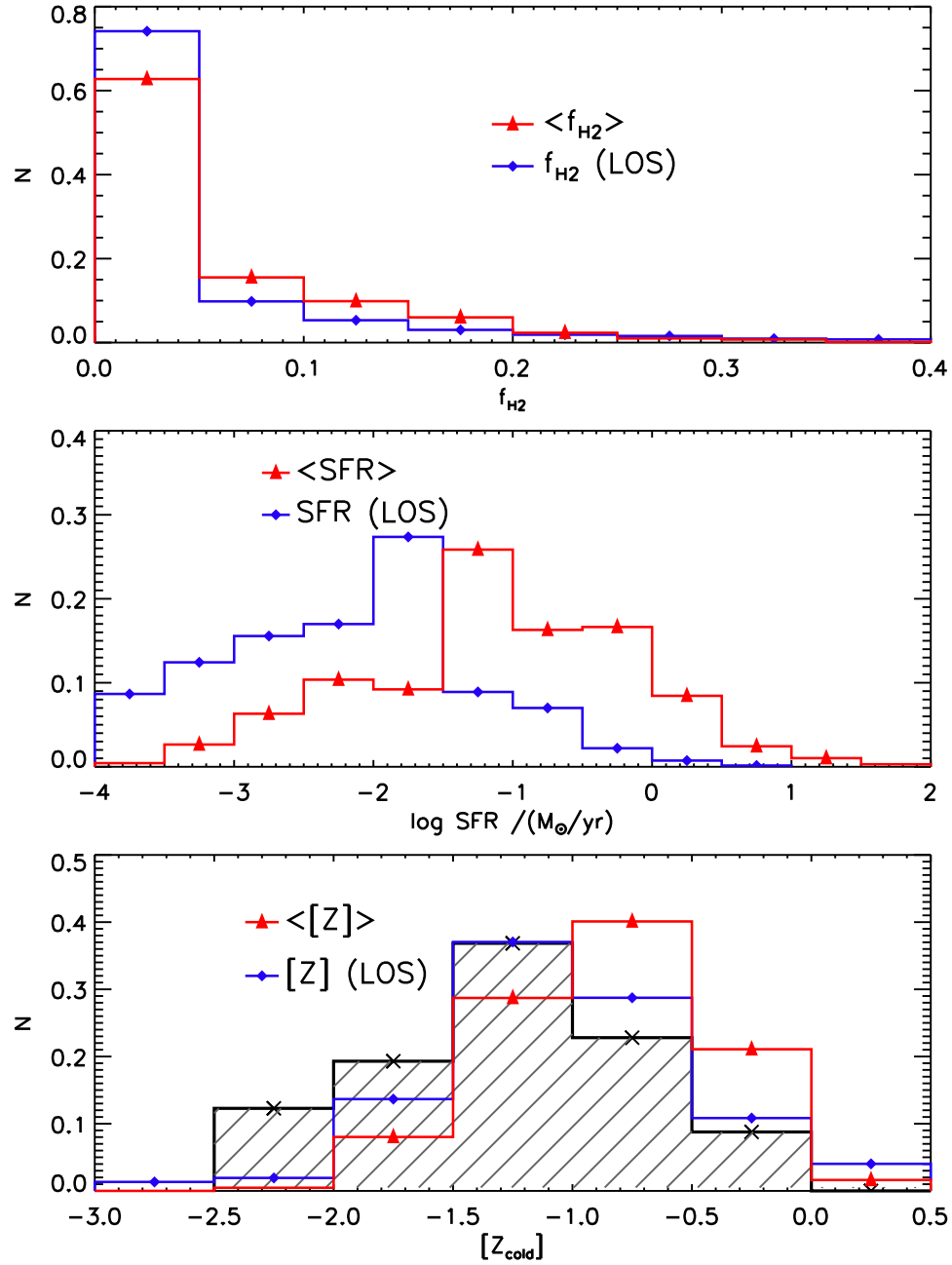


Figure 5.9 Top panel - distribution of average galaxy H_2 fraction (red triangles) and H_2 fraction along the line of sight of the DLA (blue diamonds) at $1.7 < z < 2.3$. Middle panel - same as top except for star formation rates. Bottom panel - same as top except for metallicity with a metallicity gradient of $\nabla Z = -0.1 \text{ dex kpc}^{-1}$. Observations of DLAs at the same redshift (Rafelski et al. 2012) are overplotted in black. All three quantities along the line of sight are substantially lower than the galaxy average, implying there may be a significant offset between quantities measured from along the DLA line of sight and the host galaxy.

have such low star formation rates yet can still be associated with more massive galaxies. In a small number of cases, the DLA line of sight passes through the center of the galaxy where the cold gas density is *higher* than the average of the galaxy. Our models predict that these DLAs will exhibit larger H_2 fractions and higher star formation rates.

5.4.6 Metallicity Gradients

Berry et al. (2013) (Chapter 4) found that modest metallicity gradients ($\nabla Z = -0.1$ dex kpc^{-1}) observed in $z = 2$ star-forming galaxies may contribute to the low metallicities observed in DLAs. Following this work, we further study the effect of metallicity gradients on the properties of $z = 2$ DLAs. Metallicities along the line of sight are calculated assuming a metallicity gradient of $\nabla Z = -0.1$ dex kpc^{-1} where the average metallicity is set at the radius of the average cold gas mass (see Berry et al. 2013, for details). The addition of a modest metallicity gradient causes the model DLA metallicities to be consistent with those of observations. DLA host galaxies with large stellar masses ($\log M_s/M_\odot > 10$) have a similar metallicity distribution as star-forming galaxies of the same mass as in Kulas et al. (2013). These results suggest that DLAs and star-forming galaxies could originate in the same type of galaxy where the difference in metallicity may just be a selection effect. In studies of individual DLAs and their host galaxies, Krogager et al. (2013) and Bouché et al. (2013) found that the DLA metallicity measured from interstellar absorption lines was $\sim 0.2 - 0.5$ dex less than that inferred from nebular emission lines within the host galaxy.

The left column of Figure 5.10 shows the distribution of impact parameters as a function of N_{HI} for DLAs in both models at $z = 2$. Similar to observations, both models produce DLAs which have lower column densities at larger impact parameters, and high- N_{HI} DLAs that typically have smaller impact parameters. The majority of model DLAs have low impact parameters and low column densities, which is not apparent from the observations. As lower column density DLAs are more likely to come from lower mass galaxies, detecting them in the proximity of a nearby quasar may be difficult. The relation between N_{HI} and impact parameter is explained by our modeling of cold gas in galaxies. As cold gas is distributed in exponential disks, high- N_{HI} DLAs will preferentially be selected at low impact parameters where cold gas densities are highest. The majority of low- N_{HI} DLAs

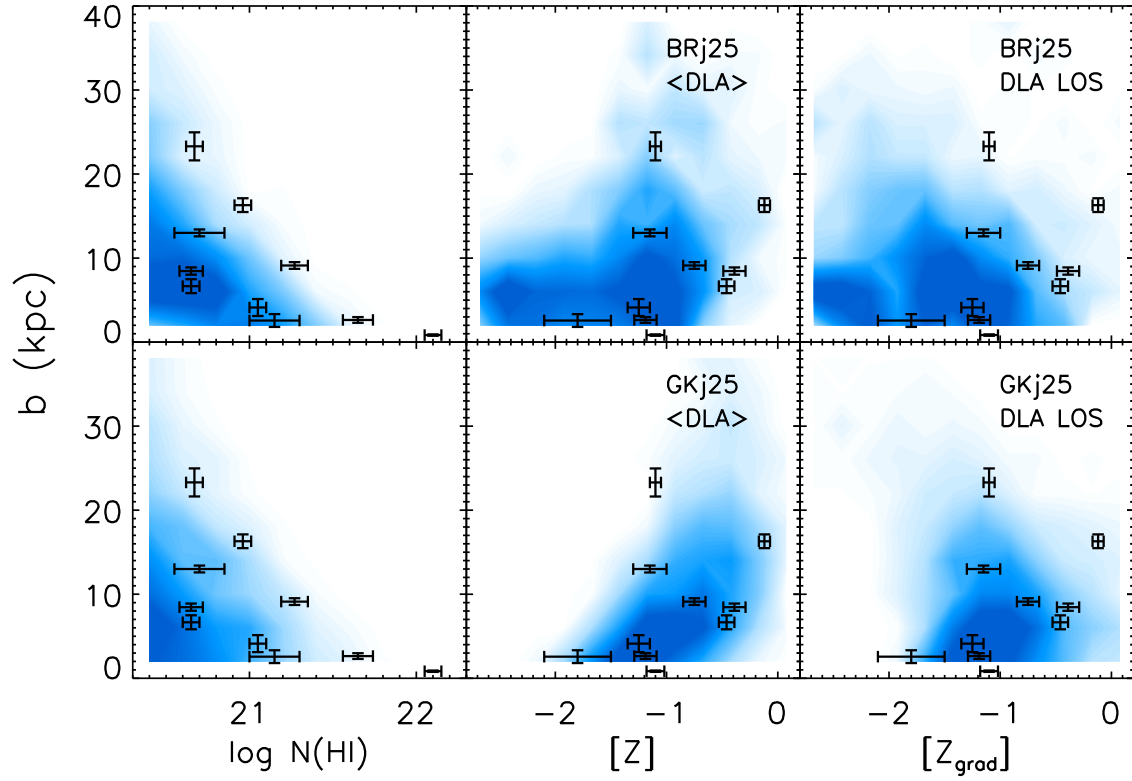


Figure 5.10 Probability of selecting a DLA in the BRj25 (top) and GKj25 (bottom) models at $1.7 < z < 2.3$ with a given impact parameter as a function of N_{HI} (left), average galaxy metallicity (middle), and metallicity along the line of sight with a metallicity gradient (right). Observations of DLAs at $1.92 < z < 3.40$ from Krogager et al. (2012) are overplotted. The distribution of model DLAs closely matches observations where a clear trend is seen between larger impact parameter and both lower N_{HI} and lower metallicity. With a metallicity gradient, DLA metallicities along the live of sight do worse in recovering the shape of the distribution.

are found in low mass galaxies with small impact parameters, while DLAs at large impact parameters preferentially sample the outskirts of galaxies where N_{HI} values are lower.

The middle and right columns of Figure 5.10 show impact parameter as a function of DLA metallicity with and without a metallicity gradient ($\nabla Z = -0.1 \text{ dex kpc}^{-1}$) respectively. The general trend of more massive DLAs having higher metallicities causes the observed relation between impact parameter and metallicity. Observations indicate that galaxies with higher metallicities have larger cold gas masses extending to larger radii, making it more likely for them to be selected as DLAs at larger impact parameters. For the same reason, more massive metal-rich galaxies will be less likely to host DLAs at small impact parameters, explaining the lack of DLAs observed with low impact parameter and high metallicity. Although not included in our models, higher metallicities will also make it more likely for the central regions of these galaxies to contain more dust obscuration, which may redden or extinguish quasars out of optically-selected quasar surveys. Conversely, galaxies with low metallicities are less massive and only have high- N_{HI} gas at small radii. As the low metallicity, low impact parameter DLAs arise in low mass galaxies, we expect observations of DLA host galaxies to miss this faint population.

Given these trends, the BRj25 model produces a large number of DLAs with a large range of average metallicities and low impact parameters. Conversely, the GKj25 model is more successful at reproducing the observed trend between larger impact parameter and higher metallicity. Since metallicity gradients preferentially change DLA metallicity based on impact parameters, DLAs observed at high impact parameter have their metallicities change the most. In our models, we see this as a shift of DLAs horizontally to lower metallicities. For both our models, inputting a metallicity gradient makes them a worse fit to the observations where the difference is so extreme in the BRj25 model that it is clearly inconsistent with observations. These results suggest that a constant metallicity gradient in all galaxies cannot fully explain the low metallicities of DLAs.

While DLAs with low metallicities and large impact parameters are not observed, their presence may indicate the presence of a metallicity gradient. Alternatively, they would also likely be good candidates for DLAs arising in gas not associated with galactic disks, such as intergalactic filaments or clumps. We note that at $z = 2$, our models suggest that DLAs

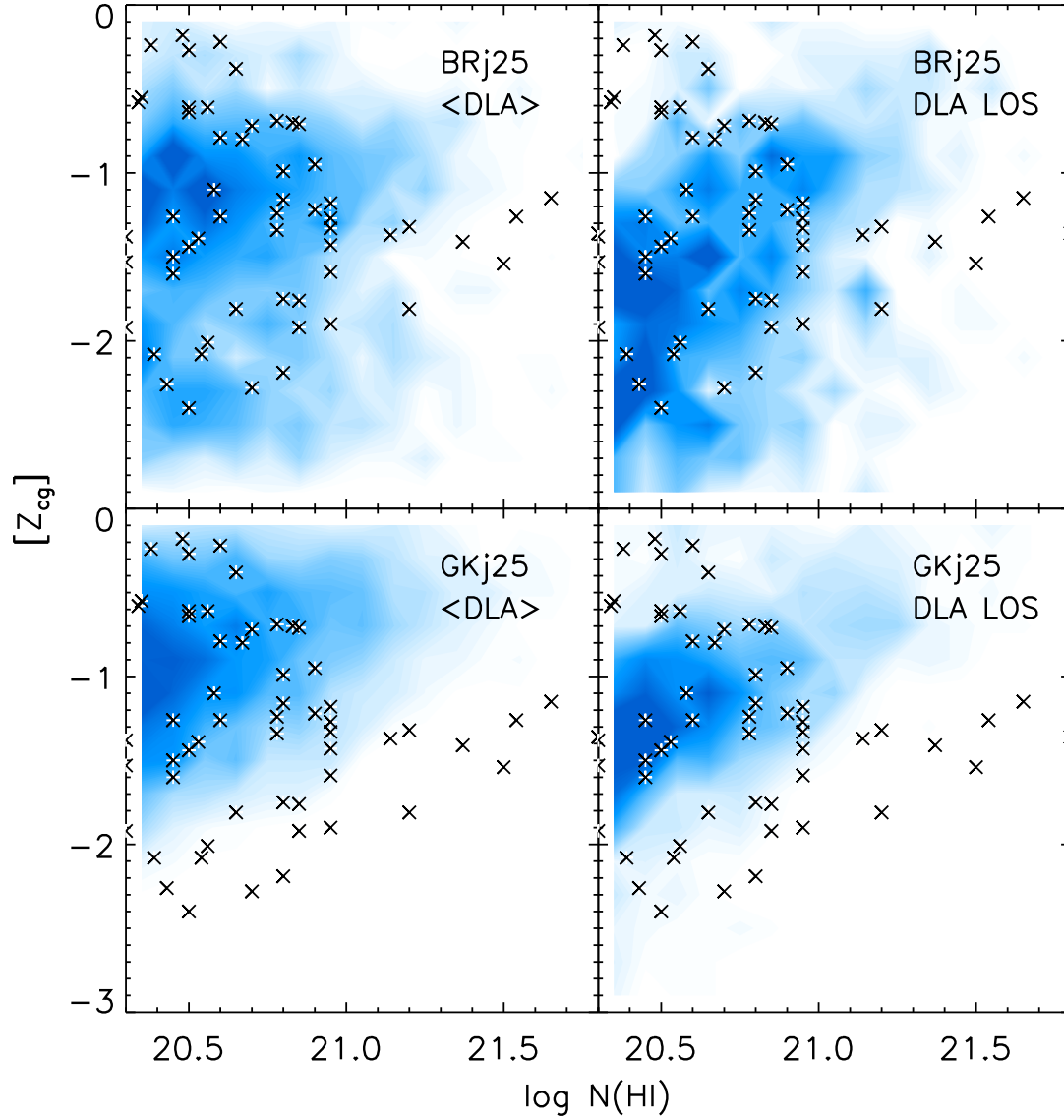


Figure 5.11 Probability of selecting a DLA with a given metallicity as a function of column density for the BRj25 model (upper row) and GKj25 (lower row) at $1.7 < z < 2.3$. DLA host galaxies (left) and DLA metallicity along the line of sight with a metallicity gradient (right). Observations of DLAs at $1.5 < z < 2.5$ from Rafelski et al. (2012) are overplotted. A metallicity gradient lowers the metallicity of low N_{HI} systems while having a small impact on higher metallicity ones. None of our models match the observations well in detail.

arising in intergalactic gas are likely less common than at higher redshifts (e.g., Berry et al. 2013).

Figure 5.11 shows the distribution of DLA metallicity versus column density for both of our models with and without a metallicity gradient. Neither of our models reproduce the distribution well in detail as they fail to reproduce the number of high- N_{HI} systems with low metallicities. The presence of these galaxies is hard to explain as the highest column density gas typically resides in the centers of galaxies where metallicities are higher. Since metallicity gradients have the largest effect on DLAs at larger impact parameters where column densities are lower, they are unable to explain these systems. An alternative explanation is that these systems may be "contaminated" by pristine gas such as in intergalactic streams or clumps, which may be increasing the HI column density and decreasing the metallicity. The BRj25 model predicts a larger range in DLA metallicities than the GKj25 model. The GKj25 model also shows more of a trend between DLA metallicity and column density. Both of our models predict the existence of high column density systems with higher metallicities, which are not seen in observations. The lack of these systems may be a selection effect as they likely also have more dust reddening due to their high column density and metallicity.

5.4.7 Galaxy Scaling Relations

In this section, we identify star-forming galaxies using the BM/BX selection criteria in order to minimize confusion as we find that BzK galaxies and HST U225/U275 band dropouts show similar trends with stellar mass. Additionally, we only show the GKj25 model as the BRj25 model exhibits similar trends. The upper row of Figure 5.12 shows the conditional probability of selecting a DLA host galaxy (left panel) or a star-forming galaxy (right panel) with a given DLA cross section as a function of stellar mass in the GKj25 model. A galaxy's DLA cross-section, σ_{DLA} , is the cross sectional area in kpc^2 corrected for inclination for which its HI column density is $N_{\text{HI}} > 2 \times 10^{20} \text{ atoms cm}^{-2}$.

DLAs preferentially select galaxies with higher σ_{DLA} values by ~ 0.5 dex than a typical galaxy at a given stellar mass where this difference is larger at lower stellar masses than higher ones. This trend results in a flatter slope of the $\sigma_{\text{DLA}}\text{-}M_*$ relation. As DLAs are

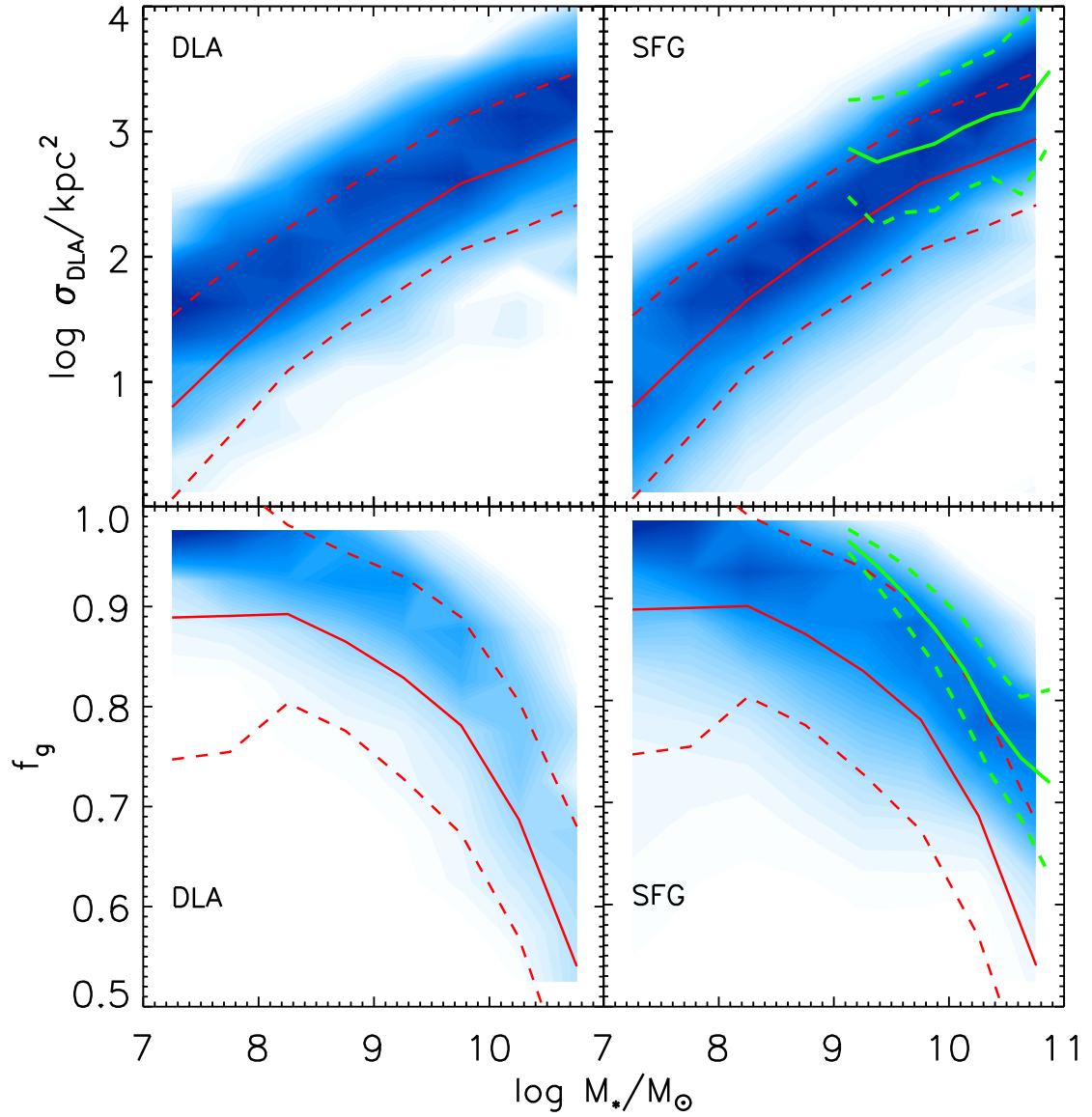


Figure 5.12 Upper row - conditional probability of selecting a DLA with a given DLA cross section (σ_{DLA}) as a function of stellar mass for DLAs (left) and star-forming galaxies identified using the BM/BX selection criteria (right) in the GKj25 model. The average galaxy (red solid lines) and SFG ($R < 25.5$, green solid line) relations and 1σ variation (dashed lines) are overplotted for reference. Lower row - same as top except for the cold gas fractions ($f_g = \frac{M_{\text{HI}} + M_{\text{H}_2}}{M_{\text{HI}} + M_{\text{H}_2} + M_s}$) are shown. Both star-forming galaxies and DLAs preferentially select galaxies with higher σ_{DLA} and f_g values at a given stellar mass. The magnitude limit of $R < 25.5$ identifies star-forming galaxies with a minimum star formation rate and therefore a minimum cold gas mass, where this selection effect is most apparent at low stellar mass.

selected based on their DLA cross section, a smaller fraction of low mass galaxies will have sufficiently large σ_{DLA} values to be identified as DLAs. For the most part, star-forming galaxies follow the $\sigma_{\text{DLA}}\text{-}M_*$ relation seen in normal galaxies with a slightly higher DLA cross section at a given stellar mass. Star-forming galaxies with $R < 25.5$ selects galaxies with a much flatter $\sigma_{\text{DLA}}\text{-}M_*$ slope. The magnitude limit of $R < 25.5$ identifies star-forming galaxies with a star formation rate threshold, which translates into a minimum cold gas mass. As our models generate gas disks for galaxies in a similar way for every galaxy (based on the cold gas mass, halo mass, and halo spin parameter), this minimum cold gas mass is seen as a minimum DLA cross section.

The lower row of Figure 5.12 is similar to the upper row except for the cold gas fractions ($f_g = \frac{M_{\text{HI}}+M_{\text{H}_2}}{M_{\text{HI}}+M_{\text{H}_2}+M_s}$) are shown as a function of stellar mass. DLAs and star-forming galaxies follow the general trend of decreasing cold gas fraction with stellar mass as is seen in the general galaxy population while both preferentially select galaxies with larger amounts of cold gas. At low stellar masses, DLAs are almost entirely composed of cold gas while the cold gas fractions in low mass star-forming galaxies are not as high. Star-forming galaxies show a similar, while not as extreme, trend. Low mass star-forming galaxies with $R < 25.5$ have significantly higher cold gas fractions, again due to the star formation rate threshold. As they decrease in stellar mass, the star formation rate threshold causes the cold gas mass to stay relatively constant, resulting in a higher cold gas fraction.

Similar to Figure 5.12, the upper row of Figure 5.13 shows the relation between star formation rate and stellar mass for DLA host galaxies and star-forming galaxies. The models produce galaxies with star formation rates that are lower than observations by ~ 0.5 dex at a given stellar mass. For the most part, both DLAs and star-forming galaxies follow the $\text{SFR-}M_s$ relation of the underlying galaxy population. DLA host galaxies produce slightly higher star formation rates at low stellar masses, indicating that they are building up stellar mass faster than similar mass galaxies. This is due to their larger DLA cross sections and higher stellar masses boosting their star formation rates. For low mass star-forming galaxies, the $R < 25.5$ magnitude limit again selects galaxies with higher star formation rates due to their higher cold gas masses. The DLA selection criteria has a similar effect to the $R < 25.5$ magnitude limit as both select galaxies with higher cold gas masses and star formation rates

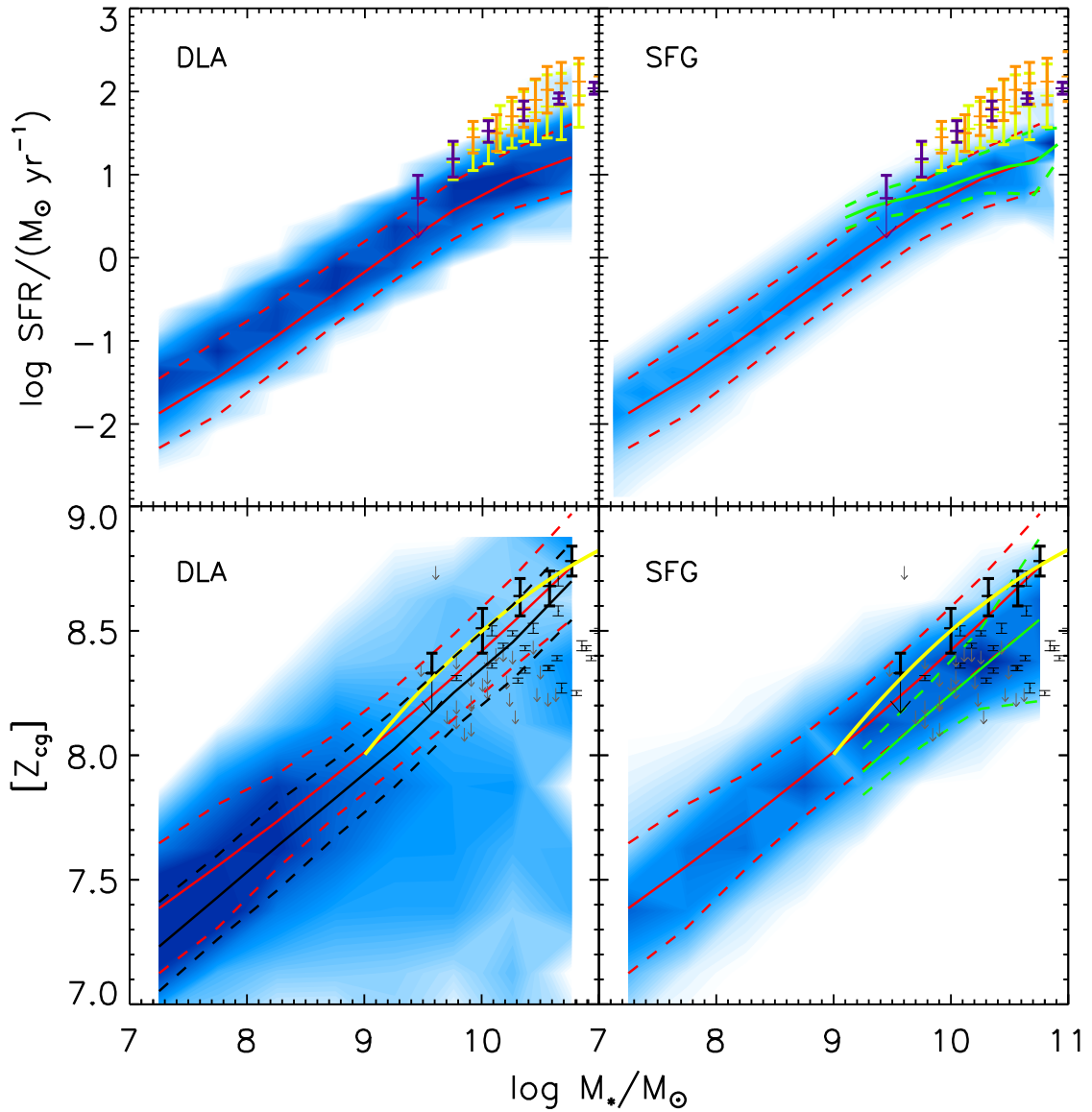


Figure 5.13 Same as Figure 5.12 except for star formation rate (upper row) and DLA metallicity with a metallicity gradient (lower row) are shown versus stellar mass. Radio stacking results from Karim et al. (2011, purple) at $1.6 < z < 2.5$ and observations from Whitaker et al. (2011, yellow, $1.5 < z < 2.0$; orange, $2.0 < z < 2.5$) are overplotted in the upper row. Average metallicities from Erb et al. (2006b), individual BX galaxy metallicities from Kulas et al. (2013), and the best-fit line to Erb et al. (2006b) from Maiolino et al. (2008, yellow) are shown in the lower row. The average DLA host galaxy metallicity without a metallicity gradient is overplotted in black. For the most part, star-forming galaxies and high-mass DLAs lie on the SFR- M_* relation while model galaxies have lower star formation rates than observations. Model galaxies reproduce the mass-metallicity relation quite well while applying a metallicity gradient in DLAs effectively washes it out at higher stellar masses.

at a given stellar mass.

The mass-metallicity relation for DLAs with and without a metallicity gradient ($\nabla Z = -0.1 \text{ dex kpc}^{-1}$) and star-forming galaxies is shown in the lower row of Figure 5.13. Model galaxies reproduce the observed mass-metallicity relation quite well for which DLA host and star-forming galaxies also match fairly closely. DLAs without a metallicity gradient and star-forming galaxies show a trend with stellar mass similar to typical galaxies while they have slightly steeper mass-metallicity relations. This trend is caused by the relatively higher star formation rates at lower stellar mass. DLAs with a metallicity gradient (blue contours) generally show an increase in metallicity with stellar mass although with considerably more scatter. This is in part due to how we model the metallicity gradient as larger galaxies will have a larger range in impact parameter, yielding a larger range in metallicity shifts. In the case of a metallicity gradient in high mass galaxies, this large range in metallicity shifts would have the effect of washing out the mass-metallicity relation for DLAs at $\log M_s/M_\odot \gtrsim 9$. More extreme metallicity gradients or a range of metallicity gradients would further contribute to the scatter. Therefore, the absence of a mass-metallicity relation in high-mass DLAs may indicate that metallicities vary substantially with galactocentric radii. Our results for star-forming galaxies are in better agreement with the observations of individual star-forming galaxies by Kulas et al. (2013) than the stacked results from Erb et al. (2006b). Those with $R < 25.5$ have a lower metallicity at a given stellar mass again related to their higher star formation rates and cold gas masses. Dust extinction causes most SFGs with $R < 25.5$ to either be sufficiently faint to not meet the magnitude limit or not satisfy the UV color selection criteria.

Figure 5.14 is similar to 5.12 except for $E(B-V)$ values are shown. The higher metallicities present in more massive galaxies causes the amount of dust reddening to also increase substantially with stellar mass. This trend is also seen in DLA host and star-forming galaxies, although both select galaxies with lower amounts of dust reddening. For DLA host galaxies, this is due to their large cold gas masses selecting galaxies with higher specific star formation rates and therefore lower average metallicities. The selection effect has a similar effect on star-forming galaxies as they are identified as those with high star formation rates and blue colors. Our model star-forming galaxies with the same magnitude limit of

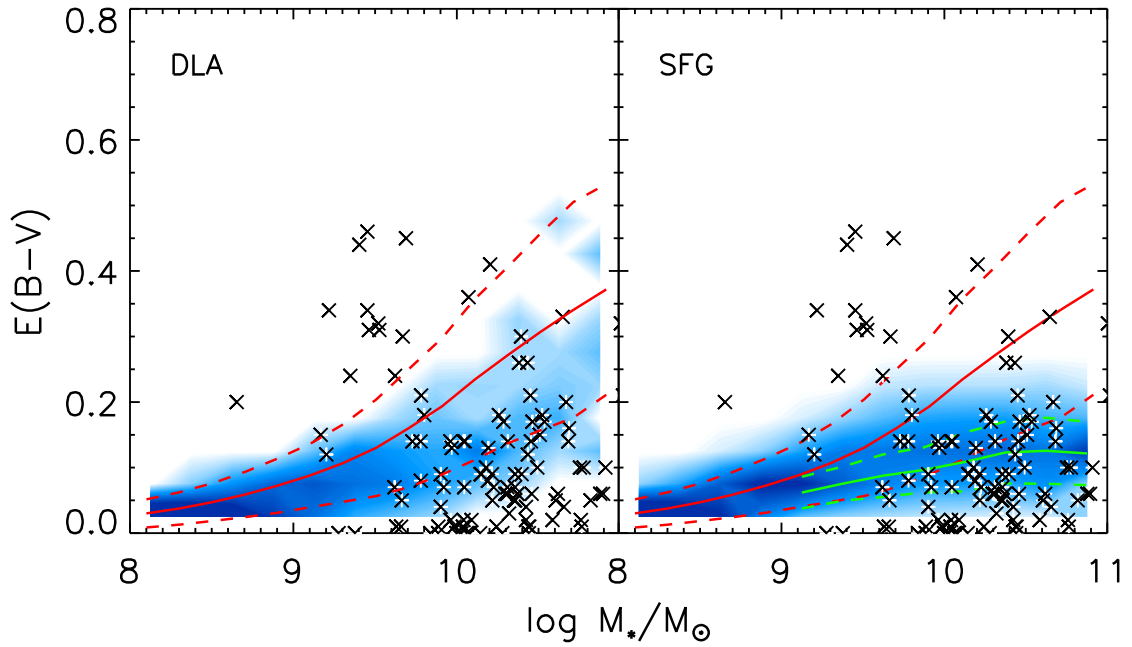


Figure 5.14 Same as Figure 5.12 except for $E(B-V)$ value versus stellar mass. Observations of star-forming galaxies at $1.7 < z < 2.3$ from Reddy et al. (2006) are overplotted (crosses). At high stellar mass, DLA host galaxies and star-forming galaxies have lower $E(B-V)$ values at a given stellar mass than a typical galaxy. Additionally, our sample of star-forming galaxies with $R < 25.5$ preferentially selects those with even lower $E(B-V)$ values than ones at the same stellar mass.

$R < 25.5$ as observations at the same redshift are generally consistent, although observations do contain considerable scatter in the distribution of $E(B-V)$ values. This result may be due to photometric errors or a broader range in galaxy properties. In the models, galaxies with stellar masses below $\log M_s/M_\odot < 8$ have very small amounts of dust reddening due to having insufficient evolution to have built up a substantial amount of dust. These results suggest that the highest mass DLAs may have substantial amount of reddening and would be the most likely to be missed in color-selected quasar surveys. Moreover, they form only a small fraction of the total number of DLAs.

5.5 Discussion

Studies of the interstellar medium at high redshift have largely been limited to observations of DLAs. As DLAs contain the majority of neutral hydrogen in the Universe, they are important reservoirs for future star formation. Given their requisite connection to star formation, we seek to characterize the properties of DLA host galaxies as well as the relations between them and star-forming galaxies. Our models allow us to examine which types of galaxies are selected as DLAs, how DLAs properties differ from their host galaxies, and how they relate to star-forming galaxies identified through common selection techniques.

5.5.1 Properties of DLA Host Galaxies

One interesting insight is that both of our models predict that the number density of $z = 2$ DLA host galaxies at a given stellar mass or star formation rate is constant over several decades. This suggests that massive galaxies are more likely to host DLAs, but DLAs have a relatively equal probability of originating from a large range of galaxies. Therefore, DLA host galaxies do not have a specific set of properties, but rather are characterized by a broad distribution of properties. Since a large number of DLA host galaxies arise in relatively low mass halos, our models predict that many are too faint to be probed by current emission-selected surveys. In spite of this broad distribution of properties, we do see a lower limit on the stellar mass, star formation rate, and metallicity of DLA host galaxies of $\log M_s/M_\odot \gtrsim 6$, $\log SFR/M_\odot \text{yr}^{-1} \gtrsim -3$, and $\log Z \sim -2.5$ on the properties of DLA

host galaxies. In our models, DLAs are selected to have a log normal distribution in HI mass centered on $\log M_s/M_\odot \sim 9.5$. At lower masses, galaxies have an insufficient amount of cold gas to have a substantial DLA cross-section, and are increasingly unlikely to be selected as DLAs. It is important to note that cold gas is distributed as an exponential disk in all galaxies. It is possible that low mass galaxies have alternative cold gas distributions that might increase their DLA cross sections, making it possible that a higher fraction would be selected as DLAs.

Additionally, the majority of model DLAs exhibit similar colors to typical galaxies at the same magnitudes, implying they are not photometrically distinct. As most DLAs are quite faint, they generally exhibit blue colors. This indicates that the majority would be selected using common color-color selection techniques (U-band dropouts, BM/BXs, and/or BzKs) except they are too faint owing to their low stellar masses and star formation rates. Only a small fraction are bright enough to be selected via traditional magnitude limited surveys (e.g., $B_{435} < 26.5$, $R \leq 25.5$ or $K \leq 23$), where they are found across a large range of B-, R-, and H-band magnitudes. Our model predicts that both the near-infrared and optical are well suited to detecting DLA host galaxies at $z = 2$ due to their tracking the stellar mass and star formation rate.

Our pressure-based BRj25 model predicts that DLA host galaxies are $\gtrsim 1$ magnitudes fainter in the R band and $\gtrsim 2$ magnitudes fainter in the H band than the metallicity-based GKj25 model. Due to these differences, our GKj25 (BRj25) model predicts that $\sim 52\%$ ($\sim 24\%$) of DLA host galaxies should be observable in the CANDELS wide field ($H \leq 26$, e.g. see Figure 5.6). These estimates do not take into account the proximity of the DLA host galaxy to the background quasar which will undoubtedly lower this fraction as both models predict that $\sim 60\%$ are within 1 arcsec of the line of sight. However, more massive, more luminous DLAs are more likely to have larger impact parameters. The faintest have H band magnitudes of $H \gtrsim 30$ and will require the next generation of optical/NIR telescopes such as JWST. By restricting our DLA sample to those with $\log Z > -1$, our model predicts that the rate of finding DLA counterparts should increase by $\sim 50\%$, although this will preferentially identify DLAs with large stellar masses. This result is caused by DLA host galaxies generally following the mass-metallicity relation and the relation between H

band magnitude and stellar mass. It is also in agreement with the DLA velocity width distribution being correlated with stellar mass as has been proposed by numerous authors (e.g., Rafelski et al. 2012; Neeleman et al. 2013) and was shown in Berry et al. (2013).

As our models predict that a large fraction of DLAs originate in low mass galaxies, the majority exhibit small amounts of dust reddening ($E(B-V) < 0.1$). With a magnitude limit of $H < 26$, a significant number of DLAs have higher $E(B-V)$ values, $\sim 43\%$ have $E(B-V) > 0.1$, owing to a substantial number originating in higher mass, more luminous galaxies. At these magnitudes, the distribution of DLA $E(B-V)$ values closely matches that of galaxies identified in a similar magnitude-limited survey of $H < 26$, indicating that bright DLA host galaxies at a given magnitude do not exhibit unusually low amounts of dust. The $E(B-V)$ values predicted by our models represent the average across the entire galaxy and assume a mixed dust geometry. Our predictions are not directly comparable to results from stacking quasar lines of sight or radio-selected quasars, as both measure the amount of extinction along the DLA line of sight which is also better represented by a screen geometry. Nonetheless, the amount of dust reddening in DLA host galaxies is generally consistent with low $E(B-V)$ values observed in DLAs.

5.5.2 Properties of DLAs versus Their Host Galaxies

In addition to the broad range of properties exhibited by DLA host galaxies, our models suggest that there is a significant difference between the properties probed along the DLA line of sight as compared to the host galaxy. Recently, observations of a few DLA host galaxies (Krogager et al. 2012, 2013) have allowed us to probe this connection. One insight of this work is the success of our simple cold gas disks in reproducing the observed sizes of DLAs as well as the relation between impact parameter, column density, and metallicity. Our models successfully predicted that the majority of DLA host galaxies should be found within $\sim 1 - 2$ arcsec of the quasar, indicating that the majority of DLAs at $z = 2$ are associated with galactic discs. Moreover, the metallicity-based GKj25 model reproduced the observed distribution of impact parameters as a function of column density and metallicity quite well. Observations and both of our models find a decreasing number of high column density DLAs at larger impact parameters, and a decreasing number of DLAs at a given

impact parameters with increasing column density. These two effects are consistent with DLAs arising in discs where high column density systems must originate in the central regions of a galaxy where cold gas densities are largest. Additionally, as the cold gas density decreases with radius, DLAs at large impact parameters must have low column densities. Note that galaxies with clumpy interstellar media or large infalling clumps could potentially produce high- N_{HI} DLAs at large impact parameters. In spite of these relations, our model predicts the majority of DLAs will be found at low column density and low impact parameter due to the large contribution of low mass DLA host galaxies with small DLA cross sections.

Additionally, our models find that only the highest metallicity systems are found at large impact parameters, indicating that only the most massive galaxies have sufficient cold gas reservoirs to have large enough DLA cross sections to host DLAs with $b > 20$ kpc. However, when we implement a modest metallicity gradient of $\nabla Z = -0.1 \text{ dex kpc}^{-1}$, both our models predict that DLAs at high impact parameter will be more metal poor. These high impact parameter, low metallicity galaxies are not seen in observations and may indicate that metallicity gradients do not significantly contribute to the low metallicities observed in DLAs. Alternatively, if these DLAs did exist, they may instead arise in massive infalling clumps or along cold streams, which would be more common at higher redshifts.

Our models find the presence of high column density, low metallicity DLAs to be difficult to explain. Our cold gas exponential discs have a decreasing gas density with radius, indicating that our models would predict these systems to arise in the central regions of galaxies. However, the highest column density systems tend to arise in more massive galaxies where there is more cold gas and more metals. These systems may be impacted by cold "pristine" gas, such as in clumps or streams, increasing the column density while also diluting the metallicity. Our models do predict the presence of high metallicity, high column density systems, which have not been observed. The absence of these systems may be a selection effect as the high metallicities and column densities may result in more dust reddening, causing them to not be selected in color-selected quasar surveys. The presence of a metallicity gradient would increase the number of these systems as metallicities are typically higher in the central regions of galaxies where column densities are also higher.

Krogager et al. (2012) found an increased number of host galaxy counterparts to high metallicity DLAs, supporting the idea that DLAs follow the mass-metallicity relation. Our models predict that selecting high metallicity DLAs will also bias the impact parameter distribution to larger values for this same reason. Yet, the presence of a metallicity gradient would decrease the average impact parameter of high metallicity DLAs as they would sample the central regions of the galaxy. These effects are clearly nontrivial, speculative, and likely vary greatly from galaxy to galaxy, therefore a detailed examination of DLAs at large impact parameters including the distribution and composition of cold gas at those radii would be necessary to decompose these effects. While only a small number of DLA host galaxies have been identified, DLAs arising in exponential disks are generally consistent with the trends observed between DLA column density, metallicity, and size.

As DLAs preferentially select gas in discs on the outskirts of galaxies, the properties of DLAs as measured along the line of sight likely differ substantially from the central regions of the host galaxy. Using the cold gas density at the location of the DLA, we calculate the H_2 fraction and therefore the star formation rate as would be measured for the DLA. Our models predict that in most cases the H_2 fraction and star formation rate along the DLA line of sight are substantially lower than in the central regions. The small scale radii of the H_2 discs causes the majority of the mass of H_2 to be in the central regions, leading to low H_2 fractions in DLAs. The lower H_2 fractions along the DLA line of sight yield substantially lower star formation rates of ~ 2 decades in the central regions than would be measured for the DLA (e.g., see Figure 5.9).

Due to the large range of DLA host galaxy masses and impact parameters, the star formation rate distribution spans several decades. The width of this distribution is comparable for the DLA, illustrating how some DLAs can show no C II^* absorption indicating star formation rates of $\log \text{SFR} \lesssim -3$ while others exhibit significant star formation. In rare cases, where the DLA line of sight passes through the central regions of the galaxy, H_2 fraction and star formation rate measured in the DLA may be larger than the average for the galaxy. These rare circumstances would provide an opportunity to study the relations between cold gas density, H_2 fraction, and star formation in high-redshift galaxies.

Finally, the average galaxy metallicity has been observed to be a few tenths of a dex

higher than that measured in the DLA (Bouché et al. 2013). Our implementation of a modest metallicity gradient of $\nabla Z = 0.1 \text{ dex kpc}^{-1}$ yields an average shift in metallicity of $\Delta Z = -0.26$, consistent with observations. Our model predicts average metallicities in star-forming galaxies that are consistent with observations of them at $z = 2$. Moreover, implementing a modest metallicity gradient reproduces the metallicities observed in DLAs at the same redshift. As observations of star-forming galaxies at $z \sim 2$ display a large range of metallicity gradients, it is unlikely that all galaxies follow this simplified prescription. However on average, the presence of a metallicity gradient may contribute to the low metallicities observed in DLAs.

5.5.3 DLAs, SFGs, and Galaxy Scaling Relations

At $z = 2$, we find both DLAs and star-forming galaxies to generally follow the trends observed between DLA cross section, cold gas fraction, star formation rate, metallicity, and stellar mass. At a given stellar mass, DLA host galaxies have DLA cross sections compared to the general galaxy population at the same stellar mass where this difference is largest at lower stellar masses. As DLAs are selected based on the DLA cross section and number density of galaxies, the decreasing DLA cross sections with stellar mass and increasing number of low mass systems roughly balance out. While DLAs are comparable in mass and star formation rate to that of the general galaxy population and star-forming galaxies, they do exhibit a flatter $\sigma_{\text{DLA}} - M_s$ relation.

Selecting star-forming galaxies with bright rest-frame ultraviolet continua ($R < 25.5$) identifies galaxies with larger DLA cross sections where this difference is most extreme at the low stellar mass end. This magnitude limit has the selection effect of identifying star-forming galaxies with a minimum star formation rate and therefore a minimum cold gas mass. At lower stellar masses, these galaxies have the same amount of cold gas making their DLA cross sections larger than the typical star-forming galaxy that is not subject to this magnitude limit. Therefore, these galaxies are also more likely to be associated with DLAs. When studying the relation between cold gas fraction and stellar mass, we find similar trends for both DLAs and star-forming galaxies. Due to the large cold gas masses associated with DLA host galaxies, at low stellar masses they are almost entirely composed

of cold gas. The star formation threshold imposed by a rest-UV magnitude limit causes low mass star-forming galaxies with $R < 25.5$ to have extremely high cold gas fractions.

DLA host and star-forming galaxies generally follow the star formation rate-stellar mass relation of the entire galaxy population, where both are fairly accurate tracers of the star formation rate at a given stellar mass. DLA host galaxies do tend to have higher star formation rates at low stellar mass relative to normal galaxies. The magnitude limit of $R < 25.5$ identifies galaxies with a minimum star formation rate that causes lower mass galaxies to have higher star formation rates relative to their stellar mass, although at higher stellar masses this approaches what our models predict as a typical star formation rate. Observations of star-forming galaxies at the same redshift indicate that model galaxies have star formation rates that are too low at a given stellar mass. This suggests that either our prescription for star formation is too inefficient, model galaxies have insufficient cold gas, or the cold gas may be in some other configuration leading to higher cold gas densities in the central regions while still having a significant extended component. In Berry et al. (2013), extended disks are required to produce a host of observed DLA properties at $z \lesssim 2.5$.

Another insight of our study is that both DLA host and star-forming galaxies follow the mass-metallicity relation, which is consistent with observations. However, if DLA metallicity is correlated with the distance from the host galaxy as in the case of a metallicity gradient, then our models predict that high mass DLAs will exhibit a broad range in metallicities. A modest metallicity gradient of $\nabla Z = -0.1 \text{ dex kpc}^{-1}$ will effectively wipe out any trend between stellar mass and metallicity above $\log M_s/M_\odot \gtrsim 9$ due to the large range in impact parameters for massive galaxies. Below this mass, DLAs generally follow the mass-metallicity relation, albeit with a larger scatter. Therefore depending on how prevalent metallicity gradients are, inferring the mass of a DLA based on its metallicity should be treated with caution. Low mass DLAs select galaxies with large cold gas fractions, which causes them to have lower star formation rates, indicating they may be beginning an episode of more intense star formation. The BM/BX color selection criteria and R band magnitude cut preferentially select galaxies with small amounts of dust reddening and a minimum star formation rate which in turn bias them to have lower metallicities. These model galaxies have metallicities that are in agreement with the results of Kulas et al. (2013).

We find that similar to typical galaxies, at low stellar masses DLA host galaxies have not undergone enough star formation to have created a substantial amount of metals, resulting in small amounts of dust extinction. At higher stellar masses, the amount of dust extinction increases with stellar mass, causing high mass DLA host galaxies to be more reddened and therefore likely to be missed from color-selected quasar surveys. The lack of high column density, high metallicity DLAs further supports this hypothesis. Nonetheless, DLA host galaxies exhibit less dust reddening than typical galaxies at the same stellar mass. This difference is caused by their lower metallicities and larger cold gas masses lowering the average amount of dust extinction. Although these measurements of dust reddening are the average for the entire galaxy, our models predict that at a given stellar mass DLAs select galaxies with inherently lower amounts of dust extinction. If DLAs probe the outer regions of galaxies where the metallicities are lower, they should have even lower amounts of dust extinction. Unsurprisingly, we find that model star-forming galaxies selected on their rest-frame ultraviolet colors do not contain significant amounts of dust reddening at any stellar mass.

5.6 Conclusions

Using semi-analytic models of galaxy formation, we study the properties of DLA host galaxies and their relations to star-forming galaxies at $z = 2$. Our preferred model, GKj25, uses a metallicity-based prescription for H_2 formation and an “extended” gas distribution as parameterized by f_j , the ratio of cold gas specific angular momentum to dark matter specific angular momentum. This work builds upon the results of Berry et al. (2013) who showed that this model was the most successful at reproducing the column density distribution, comoving number density of DLAs, cosmological neutral gas density, metallicity distribution, and velocity width distribution of DLAs at $z \lesssim 2.5$. We began by comparing a sample of model star-forming galaxies to observed ones by “observing” model galaxies that were identified using the same selection criteria. After verifying that model star-forming galaxies were similar to observed ones, we characterized the properties of DLA host galaxies; studied the relation between DLAs and their hosts; and compared the properties of DLA host galaxies to star-forming galaxies.

Our main results are as follows

- DLA host galaxies exhibit a broad range of galaxy properties extending over several decades in stellar mass, star formation rate, cold gas mass, and luminosity. As a result, they are equally likely to reside in low and high mass galaxies. This also implies that high mass galaxies are much more likely to host DLAs due the smaller number of high mass galaxies relative to low mass ones. Luminous, high-mass DLA host galaxies also have the largest amounts of dust extinction, which may bias color-selected QSO surveys.
- The photometric colors of DLA host galaxies accurately trace the colors of typical galaxies at a given H band magnitude of which most would be selected in common color-selected surveys if they were sufficiently bright. However, the majority of DLAs are much fainter than common magnitude cuts where a significant number will require the next generation of telescopes such as JWST. Nonetheless, searching for DLAs in the near-infrared, such as the CANDELS survey, or deep R band imaging are promising ways of increasing the number of DLA galaxy counterparts and better understanding the connection between cold gas and star formation in distant galaxies.
- The sizes of DLAs are consistent with observations of DLAs with host galaxy counterparts identified. The relation between impact parameter and column density and metallicity is consistent with DLAs arising in cold gas disks; however, metallicity gradients predict more high impact parameter, low metallicity systems than are observed. The H_2 fraction, star formation rate, and metallicity as measured along the DLA line of sight likely differ substantially from the host galaxy, which may help explain the low star formation rates and metallicities observed in DLAs.
- In general, DLA host galaxies and star-forming galaxies follow the same relations between stellar mass and DLA cross section, cold gas fraction, star formation rate, metallicity, and dust extinction as observed in the overall galaxy population. DLAs preferentially select galaxies with more cold gas, which causes them to have higher cold gas fractions, higher star formation rates, lower metallicities, and less dust extinction at a given stellar mass.

Chapter 6

Galaxy Structure in Numerical Simulations and Semi-Analytic Models

6.1 Introduction

Deep radio surveys sensitive to HI and CO have traced the cold gas components of nearby spiral galaxies out to large galactocentric radii (Walter et al. 2008; Leroy et al. 2009). With these data, Bigiel & Blitz (2012) analyzed the azimuthally averaged radial profiles of HI and CO in spiral galaxies and found remarkably similar galaxy cold gas profiles. They found that in the disk, the total cold gas profile followed an exponential surface density profile, similar to the stellar density profile. The HI density profiles alone are not well-fit by an exponential as the HI surface density is often depressed or flat in the center, where it can even increase as radius increases, then slowly declines in the outer regions. In contrast, the molecular component exhibits much higher surface densities in the central regions; however, it falls off much more rapidly and is well described by an exponential (Young & Scoville 1982; Regan et al. 2001; Leroy et al. 2008; Bigiel et al. 2008a). When Bigiel & Blitz (2012) focus on isolated systems, the scatter becomes even smaller, indicating that these profiles may be a natural phenomenon and emphasizing the importance of understanding this relation in galaxy formation.

In spite of this clear connection between the cold gas disks and their relation to optical disks, observations of CO and HI in individual galaxies still show significant variation in the smaller structures observed in their cold gas density profiles. These density enhancements have also been observed in the radial profiles and morphologies of galaxies in numerical hydrodynamic simulations (Christensen et al. 2012a; Mandelker et al. 2013). At higher redshifts, the size, mass, and amount of internal star formation in these clumps are even larger (Anglés-Alcázar et al. 2014; Inoue & Saitoh 2014), making it vital to better understand

their impact on galaxy formation. Much of this variation is impacted by the merger history of the individual galaxy as well as patterns in its spiral structure. Due to the propensity of molecular gas to form into giant complexes, large clumps and significant density enhancements can arise in the interstellar medium. This results in complex radial profiles that are strongly dependent on the conditions of the interstellar medium as well as some degree of stochasticity. The dominant processes include the rate at which gas cools, how cold gas forms into stars, and the regulation of star formation from stellar winds and SN feedback.

Numerical hydrodynamic simulations offer the advantage of modeling the physical properties that govern galaxy formation over time, including the formation of galactic disks. Cosmic torques create high angular momentum gas, which when accreted smoothly, falls to the center of the halo and forms a disk (White 1984; Barnes & Efstathiou 1987; Quinn & Binney 1992; Maller et al. 2002; Vitvitska et al. 2002). More recent simulations have progressed to the point where their resolution is high enough such that angular momentum is conserved and appropriately sized disks form so that they end up along the Tully-Fisher relation (Governato et al. 2004; Robertson et al. 2006a; Scannapieco et al. 2008; Hopkins et al. 2009a; Agertz 2010; Brooks et al. 2011; Brook et al. 2011; Guedes et al. 2011; Christensen et al. 2012a). In spite of these successes, there were significant challenges in matching the observed galaxy morphologies as bulges predicted in Λ CDM were much larger than observed bulges (Bullock et al. 2001; van den Bosch & Swaters 2001; Binney & Evans 2001; Maller et al. 2002; van den Bosch et al. 2002; D’Onghia et al. 2006; D’Onghia & Navarro 2007). Several authors showed that matching the central mass distribution of galaxies requires the preferential removal of low angular momentum gas, which in turn requires a detailed understanding of the 3-D structure of the interstellar medium at the scale of star formation (Oh et al. 2011; Guedes et al. 2011; Governato et al. 2012; Pontzen & Governato 2012). Christensen et al. (2012a) and Christensen et al. (2014) showed that through a more detailed modeling of the interstellar medium with H_2 -based star formation and self shielding, more realistic bulges can form.

When H_2 -based star formation and self shielding are included, cold gas forms into large clumps similar to molecular clouds, which allows gas to undergo molecular cooling and reach lower temperatures more characteristic of molecular clouds. When massive stars in these

clouds form their feedback is highly concentrated, causing expanding bubbles of hot gas to puncture through the disk. This process generates more cold dense gas and more efficient supernova feedback which remove low angular momentum material and create smaller, more realistic bulges. It also causes the disassociation of H_2 and makes the detailed nature of the ISM even more sensitive to the cooling and heating rates, which can affect the cold gas mass, distribution, clumpiness, and amount available for star formation. These processes create a complex relationship between the ISM, star formation, and feedback, which can be constrained through covering a range of different galaxy masses with a distribution of observational quantities.

In spite of the successes of semi-analytic models in matching observations of high-redshift galaxies in emission and DLAs (Somerville et al. 2012; Berry et al. 2013; Popping et al. 2013b, SPT14, Berry et al. 2014), this model fails to accurately account for or does not model the range of cold gas enhancements, morphologies, chemical distributions, and vertical velocity distributions observed in individual galaxies. Although numerical hydrodynamic simulations still rely heavily on "sub-grid" recipes for important processes such as star formation and feedback, they provide a much more detailed spatial, kinematic, and chemical description of the cold gas and stellar component.

In this chapter, we characterize the nature of the cold gas, stellar mass, metallicity, star formation rate, and vertical velocity dispersion radial profiles in galaxies in the H_2 -based numerical simulations most recently presented in Christensen et al. (2012a) with the goal of improving the radial profiles in galaxies in the SAMs presented in SPT14 and testing their assumptions. In Section 6.2 we present an overview of the numerical hydrodynamic simulations, the ISM model, and star formation recipe. We analyze the radial profiles and evolution of average galaxy properties in Section 6.3, then analyze the dependence of these properties on stellar mass in comparison to the semi-analytic models and observations at $z = 2$ and $z = 0$. In Section 6.4, we discuss the implications of our findings in the context of galaxy evolution and SAMs in general, then parameterize our results for the latter. Finally in Section 6.5, we summarize our key results.

6.2 Numerical Simulations

The simulations described here are high resolution simulations of 15 galaxies with virial masses ranging from $10^{10}M_{\odot}$ to several times $10^{11}M_{\odot}$ and are presented in Table 6.1. They were computed using a WMAP3 cosmology (Spergel et al. 2007): $\Omega_0 = 0.24$, $\Lambda = 0.76$, $h = 0.73$, and $\sigma_8 = 0.77$. Our halo sample was originally selected from lower resolution cosmological volumes where it was then re-simulated at much higher resolution using the “zoom-in” technique (Katz 1992). This approach allows us to follow large-scale structure with a significant number of high-resolution particles. For the dwarf (spiral) galaxies at the time of formation, the DM, gas, and star particle masses were respectively: $1.6 (13) \times 10^4$, $3.3 (27.0) \times 10^3$, and $1.0 (8.0) \times 10^3 M_{\odot}$. The force spline softening was 87 pc (170 pc) for the dwarf (spiral) galaxies where the minimum smoothing length for gas particles is 0.1 times the force softening length. This resolution is sufficient to follow star forming regions as small as $10^4 M_{\odot}$.

Table 6.1 Average Galaxy Properties at $z = 0$

Name	$\log M_s$ M_{\odot}	$\log M_{HI+H_2}$ M_{\odot}	SFR $M_{\odot} \text{ yr}^{-1}$	$[Z]$ Z_{\odot}	r_{s50} kpc	r_{g50} kpc	z_{g50} kpc
h239_1	10.66	9.79	0.35	0.25	4.79	3.34	0.43
h258_1	10.65	9.65	0.32	-0.18	4.83	3.40	0.59
h258_4	10.65	9.62	0.32	0.27	5.13	3.46	0.40
h277_1	10.62	9.62	0.16	0.27	4.33	3.25	0.40
h277_2	9.90	9.48	-0.31	-0.50	3.96	3.38	0.40
h285_1	9.66	9.39	-0.34	-0.75	4.70	3.30	0.34
h285_4	9.58	8.75	-0.44	-0.30	1.79	2.95	0.34
h285_9	9.07	8.72	-0.84	-0.79	2.07	3.25	0.21
h603_1	8.87	9.02	-1.40	-0.98	3.37	3.19	0.36
h603_2	8.66	8.59	-1.37	-1.00	2.79	3.02	0.22
h603_3	8.61	8.03	-1.56	-0.95	1.04	0.84	0.71
h986_1	8.59	8.10	-2.21	-1.10	1.70	1.57	0.57
h986_2	7.77	7.65	-2.80	-1.05	0.76	0.58	0.47
h986_3	7.73	7.96	-2.37	-1.10	0.65	0.67	0.72
h986_8	7.60	6.96	-3.40	-0.95	0.87	0.48	0.23

These simulations were performed with the N-body smooth particle hydrodynamic (SPH) code Gasoline (Wadsley et al. 2004) with a force accuracy criterion of $\Theta = 0.725$, a time step accuracy of $\eta = 0.195$ and a Courant condition of $\eta_C = 0.4$. They contain a cosmic UV radiation field which partially suppresses the collapse of baryons in the smallest

halos (Haardt & Madau 1996; Hoeft et al. 2006; Governato et al. 2007). The star formation and SN feedback schemes used in these models are described in detail in Stinson et al. (2006) and Governato et al. (2007). In these models, thermal energy is released from SN into gas surrounding young star particles, where the gas particles have their cooling shut off for a duration equal to the momentum-conserving phase of the SN blastwave. This period is typically a few million years and is a function of the local density and temperature of the gas, the amount of energy injected, and the cooling rate. Star formation is limited to dense regions of cold gas which depend on the ISM model. Only the star formation efficiency and the fraction of SN energy coupled to the ISM were tuned to reproduce the properties of present-day galaxies over a range of masses (Governato et al. 2007). Brooks et al. (2007) showed this model reproduces the mass-metallicity relation, while Pontzen et al. (2008) used it to analyze the properties of DLAs.

6.2.1 Modeling Cold Gas

In these simulations, we use the most sophisticated ISM model (H_2 + metal line cooling) from Christensen et al. (2012a). In this model, the redshift-dependent UV background radiation is responsible for both gas heating and photoionization. Gas cooling is calculated based on collisional ionization, radiative recombination, photoionization, bremsstrahlung, and line cooling (H, He, and metals). Metal line cooling allows gas to cool more efficiently and to temperatures below 10^4 K, and is calculated for a range of gas temperatures, densities, metallicities, and amounts of UV background assuming ionization equilibrium and optically thin gas using CLOUDY (version 7.02; Ferland et al. 1998). In the IGM, this assumption holds while in the ISM, it can lead to an underestimate of the cooling rate. For instance, the lack of an interstellar radiation field beyond the UV background results in substantially less CII (Christensen et al. 2012b), the principle coolant in more metal-rich gas. To augment this model, (Christensen et al. 2012b) add in the non-equilibrium formation of H_2 , which primarily occurs on dust grains and is dissociated by Lyman-Werner radiation from young, massive stars. Therefore, H_2 only forms in dense regions of the ISM where it is shielded from Lyman-Werner radiation. This model follows the hydrogen chemical network for each gas particle, and assumes the dust fraction is proportional to the metallicity and

the incident Lyman-Werner radiation is based on the light from nearby young star particles. Self-shielding and shielding by dust protect H_2 from photo-dissociation. These effects are also included when calculating the rates of HI photoionization and photoheating. The inclusion of self-shielding reduces heating and results in the formation of cold (100 K) ISM. The more accurate calculation of CII and other low-temperature metal coolants would increase the cooling rates, although shielding is the predominant factor in the formation of cold gas.

6.2.2 Star Formation

The star formation procedure used in these simulations is described in detail in Stinson et al. (2006). If a gas particle has a temperature less than T_{max} and a density greater than ρ_{min} , then a star particle can form with a probability, p , as a function of the dynamical time, t_{form} ,

$$p = \frac{m_{gas}}{m_{star}}(1 - e^{-c*\Delta t/t_{form}}) \quad (6.1)$$

where m_{gas} is the mass of the gas particle, m_{star} is the initial mass of the potential star particle, and $c*$ is the star forming efficiency factor. In this model, we set $c* = 0.1X_{H_2}$ where X_{H_2} is the fraction of hydrogen in the form of H_2 , which eliminates the need for a high density threshold to restrict star formation to molecular clouds. Therefore, we set the density threshold to an arbitrarily low value of $\rho_{min} = 0.1 \text{ amu cm}^{-3}$. We also require that star formation only occurs in gas that has undergone molecular cooling by setting $T_{max} = 1000 \text{ K}$. Through testing the sensitivity of star formation to both ρ_{min} and T_{max} , Christensen et al. (2012a) found that changes of a factor of five to either do not significantly alter the amount of star formation. This recipe naturally limits star formation to dense molecular clouds.

The inclusion of shielding and metal line cooling increases the frequency with which gas particles become Jeans unstable and collapse into stars. Bate & Burkert (1997) showed that when the Jeans length or mass is unresolved, artificial fragmentation can occur, whereby star formation becomes dependent on the details of how it is implemented. Some simulators require that the Jeans instability never occur while others make it the criteria for star

formation. In this model, the Jeans instability can occur, which leads to star formation with the understanding that the newly formed stars will prevent further collapse due to the highly efficient SN feedback heating the surrounding gas.

6.3 Results

In this section, we present the radial profiles and general properties of individual galaxies in the numerical simulations. We also describe the dependence of the galaxy profiles on redshift and stellar mass and compare this to both predictions and assumptions of semi-analytic models. First in Section 6.3.1, we present the radial cold gas, stellar, metallicity, and star formation rate profiles for 15 individual galaxies that span ~ 3 orders of magnitude in stellar mass at both $z = 2$ and 0. Next in Sections 6.3.2 and 6.3.3, we describe the change in average galaxy properties with redshift and stellar mass, then how numerical simulations and semi-analytic models compare to observations.

6.3.1 Individual Galaxy Profiles

Figure 6.1 shows the H I , H_2 , and stellar surface density profiles for 15 galaxies in the numerical simulations at $z = 2$ as a function of their $z = 0$ half-cold gas mass radius (r_{g50}). Galaxies are ordered from most massive to least massive at $z = 0$. The stellar mass profiles are fit with a double exponential to account for the contributions of the disk and bulge components where most galaxies have stellar mass profiles that are well-fit by a double exponential. The interior regions of the massive galaxies ($\log M_s/M_\odot \gtrsim 9.5$) benefit greatly from modeling the bulge component as they have a significantly increased density of stars in the bulge. In spite of these successes, substantial variation in the smaller features of the stellar profiles are not well modeled by these simple profiles. These smaller features mainly originate from small clumps of stars, infalling material, or extended low surface density disks (e.g., panels 1, 2, 4, 5, 6, 7, 11, 12). Qualitatively, observations of local spiral galaxies reveal similar fluctuations in their cold gas surface density profiles (e.g., Bigiel et al. 2008a; Bigiel & Blitz 2012).

We fit the cold gas surface density profiles with an exponential profile, then partition

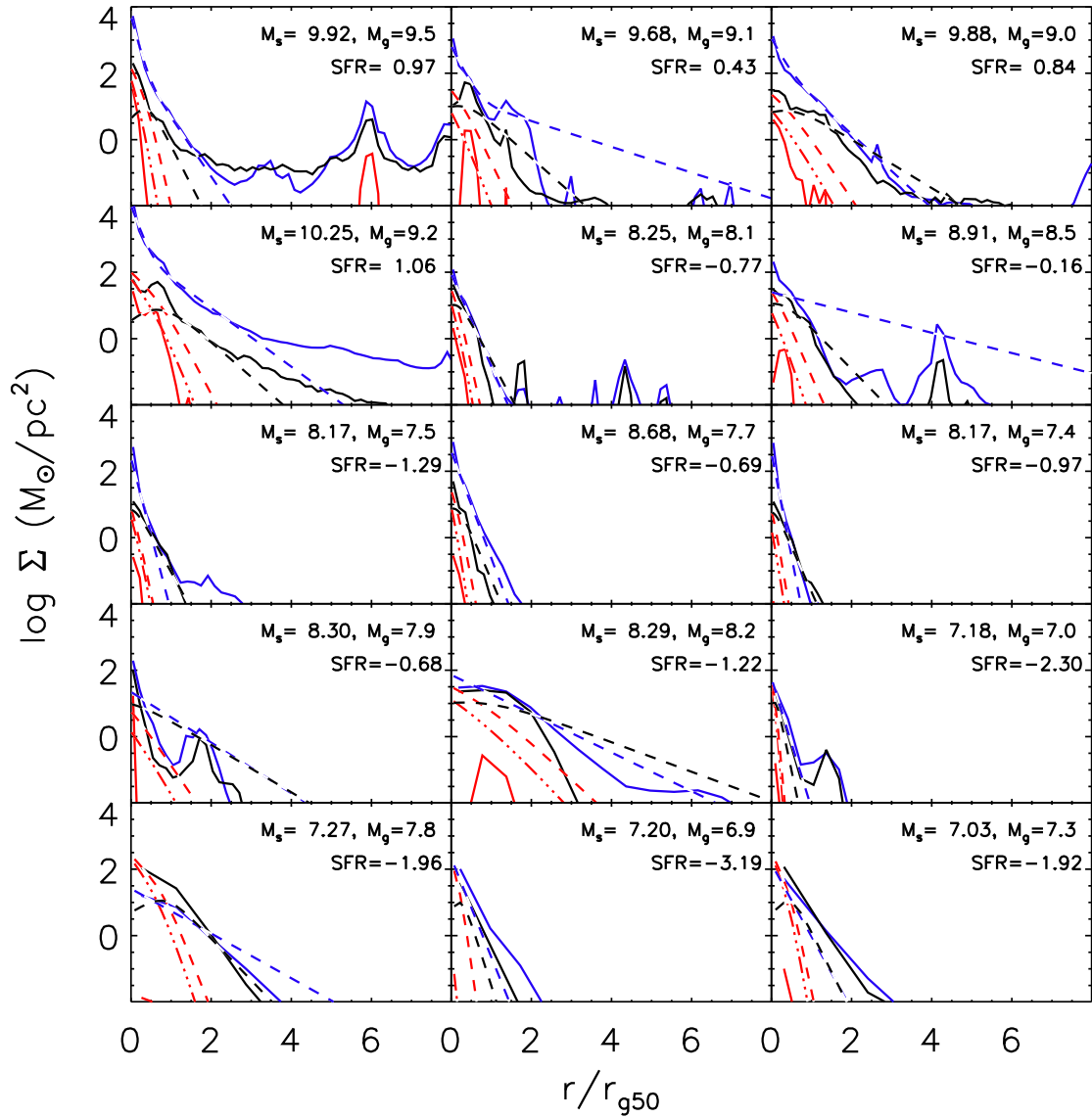


Figure 6.1 HI (black), H₂ (red), and stellar (blue) radial profiles for 15 galaxies in the numerical simulations (solid) at $z = 2$. We fit the total cold gas density profile ($\Sigma_{\text{HI}+\text{H}_2} > 1 M_{\odot} \text{pc}^{-2}$) with an exponential, then use the pressure-based H₂ partitioning recipe (pressure-based) to calculate the HI and H₂ profiles (dashed) as would be calculate in the SAMs. The triple-dot dashed line is metallicity-dependent H₂ recipe. The best-fit exponential stellar profiles (blue dashed line) are also overlaid. Many features in the galaxy profiles are missed by the simple exponential profile, including large clumps of gas and stars, extended cold gas and stellar disks, and off-center clumps of H₂.

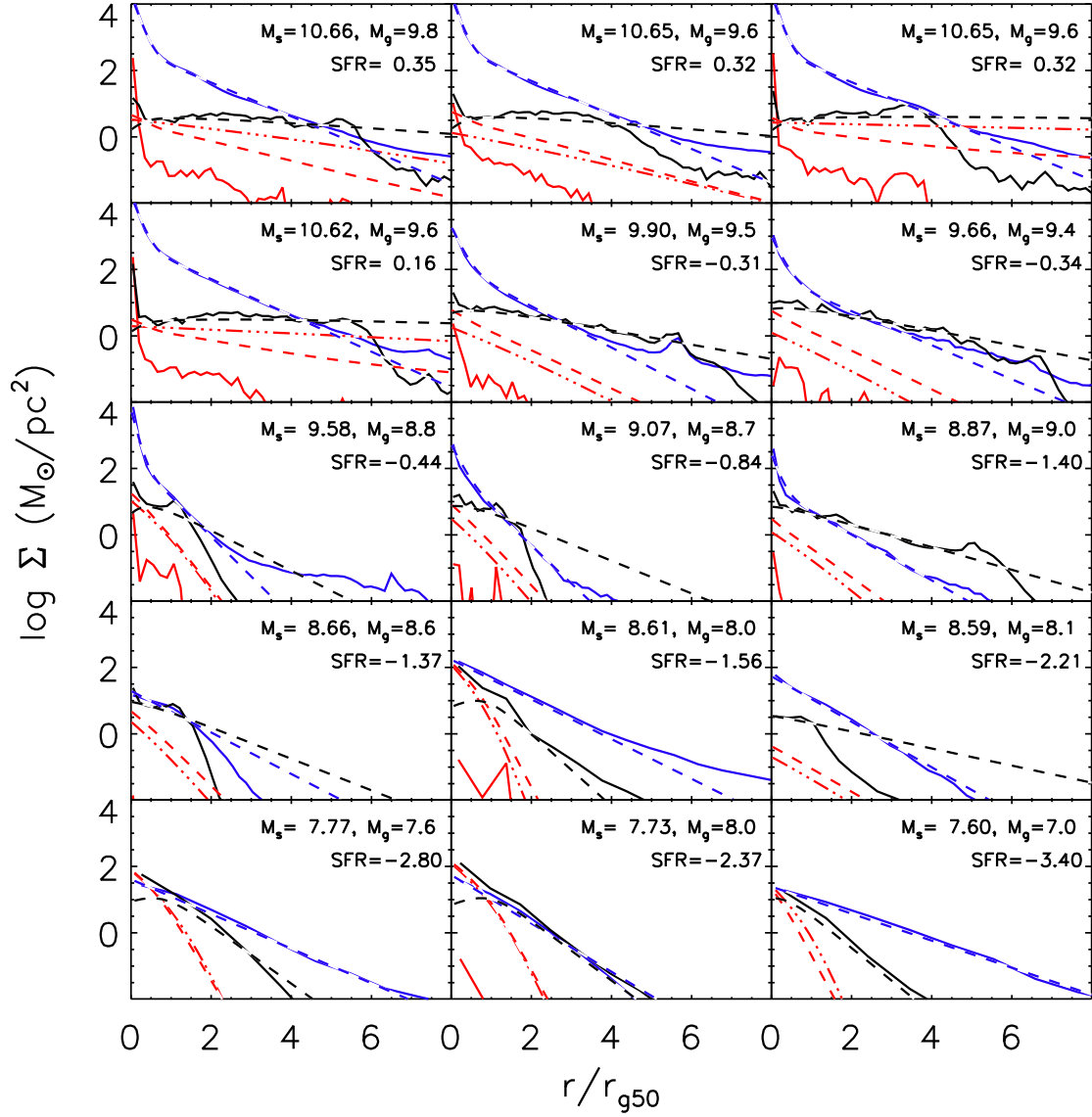


Figure 6.2 Similar to Figure 6.1, except for at $z = 0$. The most massive galaxies have extended cold gas and stellar disks while H_2 is mainly confined to the center of each galaxy. In many of the galaxies, the HI disks cut off at a given surface density, which is modeled in the pressure-based and metallicity-dependent models as HI transitioning into HII at $\log \Sigma_{HI}/(M_\odot \text{ pc}^{-2}) = -0.4$ (Gnedin 2012). Lower mass galaxies' stellar and cold gas disks are better fit by an exponential profile.

the cold gas into HI and H₂ based on the metallicity-dependent and pressure-based recipes as would be calculated in the SAMs. Similar to the stellar radial profiles, the HI radial profiles of a number of galaxies are well-fit by an exponential as the majority of the cold gas is atomic gas. Nonetheless, many of the cold gas disks are poorly fit by exponential profiles as they either have more compact disks, significant extended components, or large clumps of gas. In all galaxies, the mass of H₂ as predicted from the numerical simulations is very small and located in the central regions of the galaxy. The low H₂ fractions would imply low star formation rates; however, due to a strong supernovae feedback recipe that deposits significant energy into the surrounding gas, much of the H₂ becomes dissociated. The stellar and cold gas radial profiles exhibit a broad range in profile shapes and slopes even across a similar range in stellar masses. This suggests substantial variation in properties of individual galaxies.

Compared to numerical simulations, the H₂ profiles calculated using the metallicity-dependent and pressure-based cold gas partitioning models have more H₂ in all cases where the metallicity-dependent model is closer to the numerical simulations. We expect a closer fit between the metallicity-dependent models and numerical simulations as H₂ forms based on the amount of dust and local UV radiation field in the metallicity-dependent models, which is similar to that of the numerical simulations. On the other hand, H₂ formation in the pressure-based model is dependent on the mid-plane pressure as inferred from the local gas and stellar surface density. The similarity between these two models is striking, given that they form H₂ using very different physics.

Figure 6.2 shows the radial profiles for the same galaxies at $z = 0$. Several noticeable differences are observed across these two figures. First, massive galaxies in the numerical simulations all exhibit significant bulge components, which are well described by an exponential profile. In contrast, no low mass galaxies have bulges. Overall, the double exponential fits all the galaxies' stellar profiles remarkably well with the exception of underestimating the amount of stars in a few extended disks. This is largely due to stellar profiles becoming much smoother with cosmic time.

In the more massive galaxies, the HI radial profiles are all very flat and truncate at a given radius. This truncation does not occur at a specific radius or HI surface density, but rather

changes for each galaxy. The exponential profiles well describe the HI disk, although they do not capture the truncation. In the semi-analytic models, the HI disk is assumed to become ionized (HII) at $\log \Sigma_{HI}/(M_{\odot} \text{pc}^2) = 0.4$ (Gnedin 2012), also corresponding to typical surface densities of sub-DLAs. The range in HI surface densities and radii where this truncation occurs may indicate that the threshold for neutral gas changes with galaxy properties. Similar features in HI surface density profiles have been observed in local galaxies in the THINGS survey (e.g., Bigiel et al. 2008a). A more detailed discussion of the underlying cause of this feature will be presented in Berry et al. (2014b, in prep.).

The H₂ gas surface densities predicted by the metallicity-dependent and pressure-based models do not fit any of the galaxies in the numerical simulations. All exponential profiles predict significantly more H₂ in the outer regions of the disk. Additionally in most of the less massive galaxies, these two recipes predict substantial H₂ components while the numerical simulations have no H₂ gas. Similar to $z = 2$, since both recipes predict similar H₂ profiles, we posit that this may be due to them being calibrated on the same data set. In the central regions of the most massive galaxies ($\log M_s/M_{\odot} \gtrsim 10.5$), there is a large concentration of H₂ and in one galaxy HI in the bulge. At these stellar masses, feedback from the central supermassive blackhole, which is not modeled in these simulations may help reduce the amount of H₂ gas in these regions. While the average gas and stellar profiles of a large number of galaxies may be in the form of an exponential (e.g., Bigiel & Blitz 2012), individual galaxies in the numerical simulations and nearby Universe (e.g., Bigiel et al. 2008a) display a broad range in shapes and slopes.

Figure 6.3 shows the metallicity profiles for the same 15 galaxies at $z = 2$ and $z = 0$. In the majority of galaxies at $z = 2$, metallicities do not change much with radius, indicating little evidence for metallicity gradients. Nonetheless, there is substantial variation in the metallicities due to smaller features in individual galaxy profiles. At $z = 0$, more significant metallicity gradients have developed in half of the galaxies, which tend to be the more massive ones, while the lower mass galaxies still show flat profiles. Most galaxies' metallicity gradients also flatten at larger radii. Galaxy metallicity profiles have also become smoother by $z = 0$. There is more variation in metallicity due to smaller features in individual galaxy profiles at $z = 2$ than $z = 0$, indicating that metallicities are smoother at $z = 0$. A

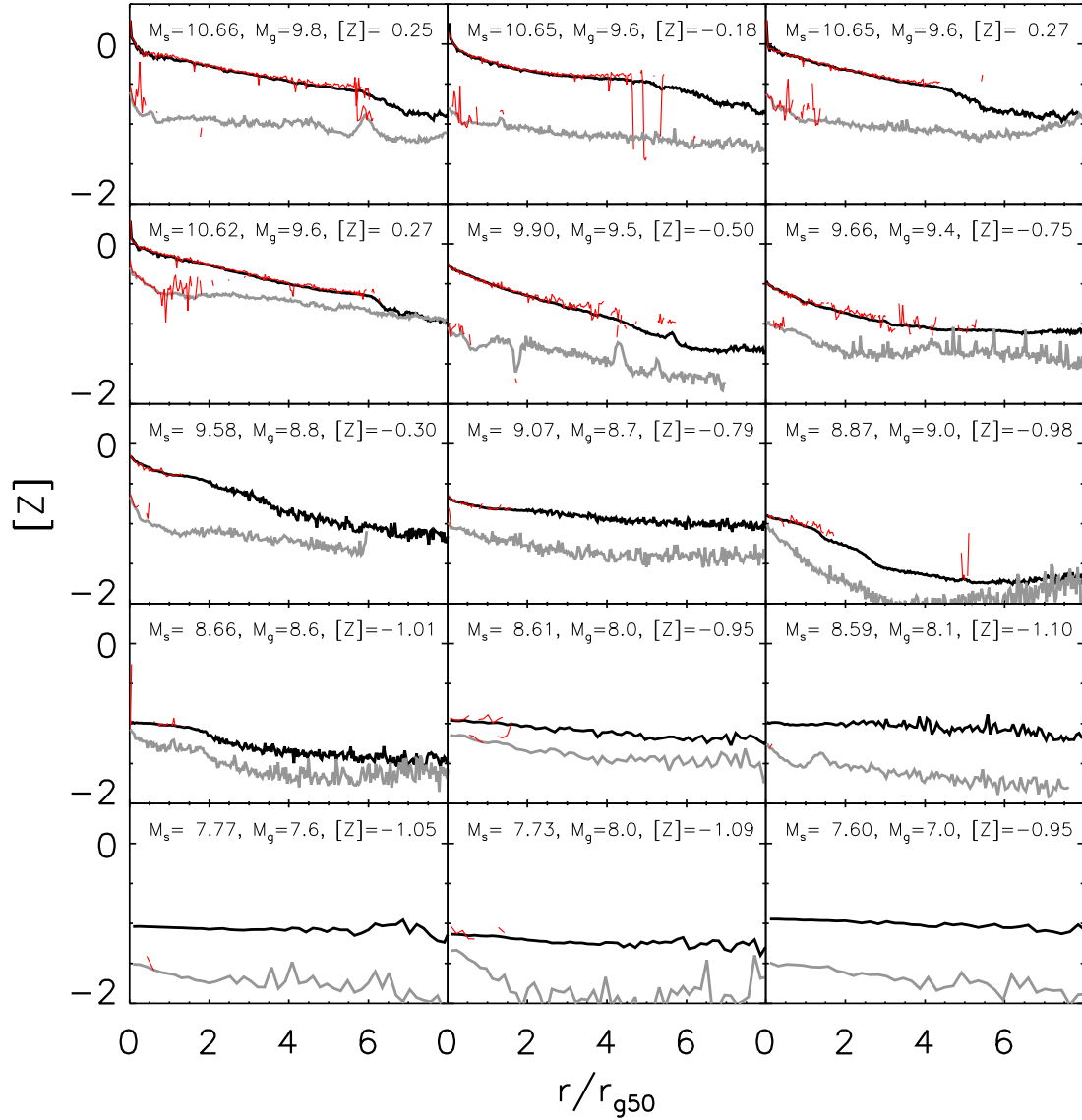


Figure 6.3 Similar to Figure 6.1 except for metallicity profiles are shown at $z = 2$ (gray) and $z = 0$ (black). The star formation weighted metallicities are overlaid at each redshift (red lines). At $z = 2$, galaxies exhibit flat metallicity profiles with little evidence for metallicity gradients except for in the center of a few galaxies. By $z = 0$, a significant amount of metals have amassed in the central regions of the disk in many of the more massive galaxies. In addition, small features in the metallicity profiles at $z = 2$ have smoothed out by $z = 0$.

significant metallicity enhancement is seen in the centers (e.g., the bulges) of the massive galaxies. Weighting the metallicities by star formation rate also has a significant effect on the average metallicities as star formation occurs at smaller radii where metallicities are higher. As a result, this result predicts that metallicities measured from emission lines in HII regions should be significantly higher than those measured in cold gas, especially if those measurements are more likely to sample the outskirts of galaxies as is the case for DLAs.

Through using the H_2 surface density profiles as inferred from the pressure-based and metallicity-dependent H_2 formation recipe, we can create star formation rate profiles for each galaxy. We calculate the H_2 density profile for galaxies in the numerical simulations by taking each galaxy's cold gas density profile (from Figures 6.1 and 6.2), metallicity profile, and average star formation rate and calculating the H_2 gas density using the metallicity-dependent recipe. The pressure-based models predict similar H_2 density profiles, which result in similar star formation rate profiles predicted by the SAMs. The star formation profiles predicted by the SAMs and those from the numerical simulations at $z = 2$ and $z = 0$ are shown in Figure 6.4. We focus on the central regions of each galaxy where the H_2 cold gas mass and star formation are concentrated. The star formation rate surface density profiles predicted by the SAMs are similar to the H_2 surface density profiles in shape except they predict less star formation at a particular radius, indicating a lower star formation efficiency in the numerical simulations or the destruction of H_2 . At $z = 2$, almost all galaxies have large clumps of star formation across a range of radii. These profiles become much smoother with cosmic time. Star formation is also more concentrated in the central regions of the galaxies at $z = 2$ and more extended at $z = 0$, although there is a significant bulge component in some of the more massive galaxies at $z = 0$. In all galaxies except the lowest mass ones, the star formation rates calculated from the pressure-based and metallicity-dependent models are lower than observed in the numerical simulations, which can range from a few tenths of a dex to $\sim 1 - 1.5$ dex. Additionally, assuming the cold gas follows a simple exponential profile misses much of the more detailed structure also seen in the star formation rate profiles, especially at $z = 2$. The pressure-based and metallicity-dependent models do better on the shape of the profile at $z = 0$, but none match the profiles well in detail. In the numerical simulations, since star formation occurs

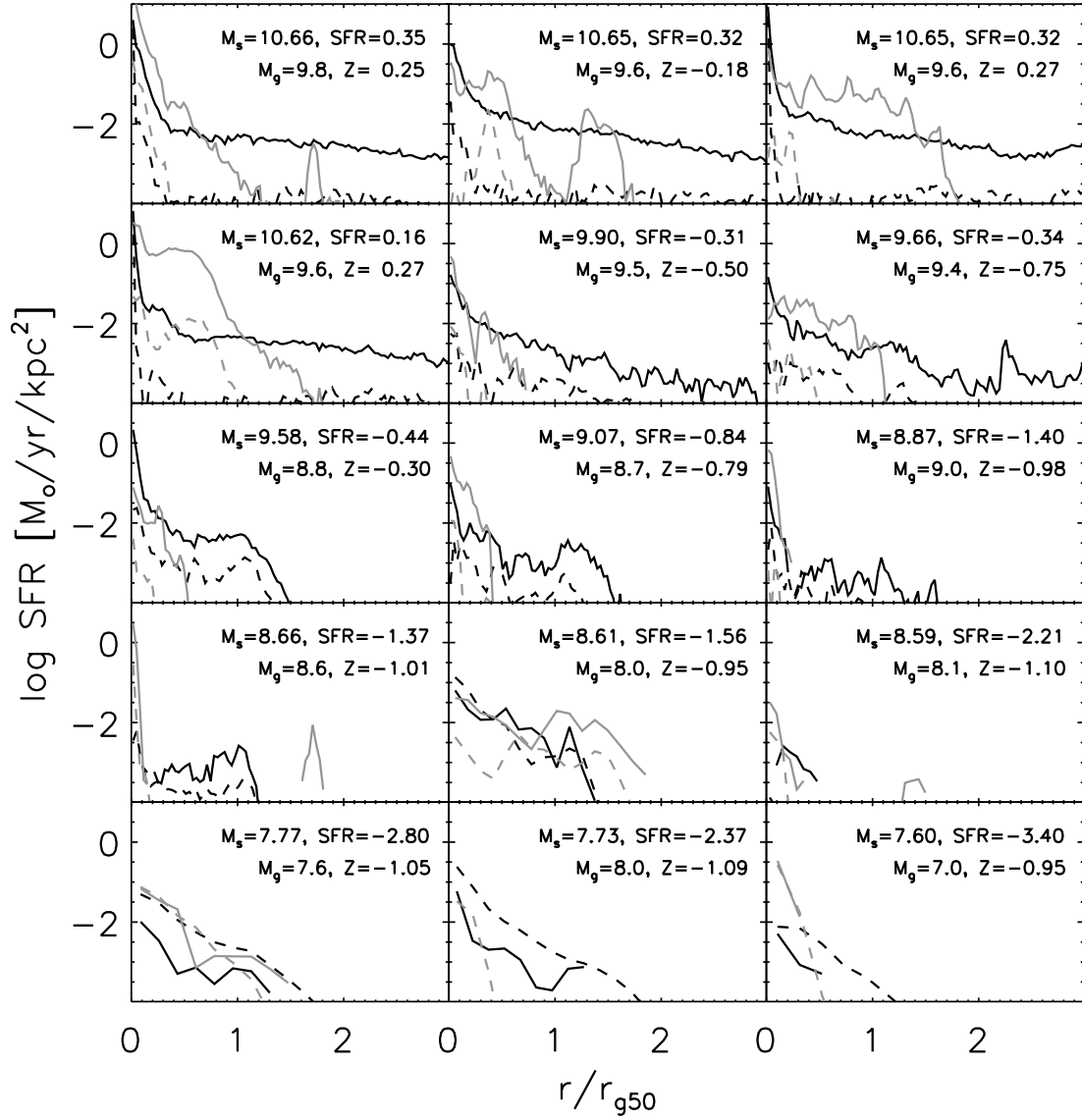


Figure 6.4 Similar to Figure 6.1 except for star formation rate profiles are shown for the numerical simulations (solid) and the metallicity-dependent model (dashed) at $z = 2$ (gray) and $z = 0$ (black). Here, we focus on only the center of each galaxy ($r_{50} < 3$) as this is where the majority of star formation occurs. In most galaxies at $z = 2$, star formation is burstier and confined to the center of each galaxy while at $z = 0$, the star formation profiles are much smoother with a significant portion coming from larger galactocentric radii.

in clumpy molecular gas, the feedback from supernova is highly concentrated, which drives more efficient superwinds and dissociates much of the H_2 and ionizing the surrounding cold gas. This process causes star formation and clouds of cold gas to be more clumpy, and it reduces the total amount of cold gas, especially H_2 .

6.3.2 Average Galaxy Properties

Figure 6.5 shows how a number of galaxy properties evolve with redshift in the numerical simulations at different stellar masses. We also divide the galaxy sample in two based on stellar mass, then overplot the best linear fits to the median galaxy property and the higher/lower stellar mass halves as a function of redshift. Some galaxies grow mildly with redshift while others can increase in mass by $\gtrsim 1.5$ dex from $z = 3$ to $z = 0$, which appears to be independent of stellar mass. The less massive galaxies decrease in star formation rate with redshift while the more massive ones do not change significantly. There is a large amount of variability in the star formation rates of a significant fraction of the galaxies, which is also seen in the specific star formation rates. Although almost all galaxies regardless of mass have a similar range in sSFR and exhibit a ~ 1.5 dex decrease with redshift. Cold gas fractions also vary dramatically within individual galaxies and across different epochs; however the change in cold gas fraction is not highly correlated with the star formation rate. Lower mass galaxies have higher cold gas fractions than more massive galaxies while the average cold gas fractions show a similar decline in galaxies of all masses with cosmic time. Additionally, the average metallicities exhibit substantial variation in the amount of evolution that is observed from $z = 3$ to 0 where more massive galaxies typically increase in metallicity much faster than lower mass galaxies. This is partly due to lower mass galaxies ejecting a higher fraction of their metals and higher star formation rates in massive galaxies.

The size of the stellar disks of all galaxies increases with time where the average galaxy stellar disk can increase in size by a factor of ~ 2 to 5 from $z = 3$ to 0. In dividing the galaxies in half based on stellar mass, we find that less massive galaxies tend to increase in size faster than more massive ones, but this difference is not a large effect. There is also substantial scatter in the size of stellar disks at a given stellar mass or redshift as mergers and dynamic interactions can significantly affect the size of the disk.

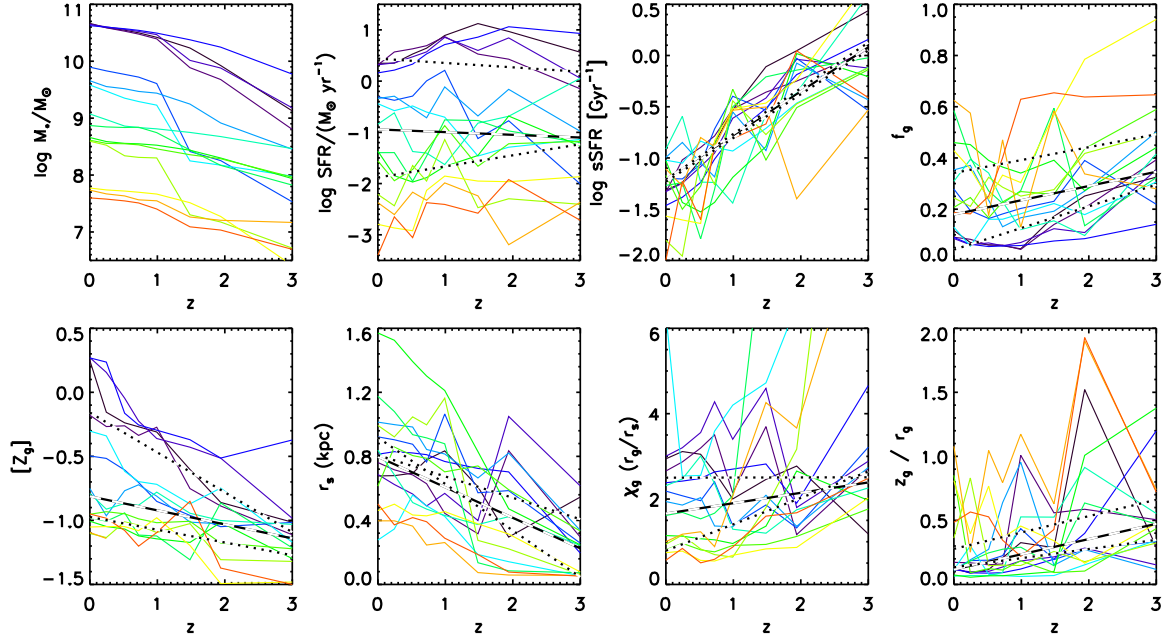


Figure 6.5 Properties of galaxies in the numerical simulations are plotted as a function of redshift and colored via decreasing stellar mass at $z = 0$ (purple to red). Upper row from left to right - stellar mass, star formation rate, specific star formation rate, and cold gas fraction. Lower row - metallicity, stellar scale length, ratio of cold gas to stellar radial scale length (χ_g), and ratio of cold gas scale length to scale height. The best linear fit to the median galaxy properties (dashed line) and the higher/lower stellar mass halves (dotted lines) are overplotted. Over cosmic time, galaxies' stellar components become more extended; their cold gas disks become less extended relative to the stellar disks, and their cold gas disks become flatter.

The size of the cold gas disks relative to the stellar disk sizes decreases mildly with redshift where cold gas disks were relatively $\sim 30\%$ larger at $z = 3$. This decrease is dominated by low mass galaxies which decline in size by a factor of $\gtrsim 2$ while the relative size of cold gas disks in more massive galaxies does not change significantly. Sizes are measured as the radius containing half the cold gas (r_{g50}) or stellar mass (r_{s50}), both of which are strongly affected by infalling clumps which have a larger effect in smaller galaxies. Two effects may cause the decrease in relative cold gas disk size. Star formation in the outer regions of galaxies may consume cold gas. Alternatively, cold gas may continue to collapse and condense causing the cold gas disk to become more compact. Our results also indicate that thickness of cold gas disks (z_{g50}/r_{g50}) typically decreases with cosmic time by $\gtrsim 2$ where more massive galaxies tend to have thinner disks than less massive ones. While cold gas disks are collapsing vertically, there is no clear trend between the scale radius of the disk and time (not shown). In spite of disks becoming thinner, there is significant variation in the thickness of a galaxy's cold gas disk across time and at different stellar masses.

Similar to Figure 6.5, Figure 6.6 shows the relation between each galaxy property and stellar mass from $z = 2$ to $z = 0$. In the majority of our galaxies, star formation rates increase from $z = 2$ to $z = 1$, then decrease to $z = 0$. As expected, higher star formation rates are seen at higher stellar masses at all redshifts. Cold gas fractions decrease with increasing stellar mass at both redshifts where the cold gas fraction is more sensitive to changes in stellar mass at $z = 2$ than $z = 0$. This effect is caused by the most massive galaxies increasing in stellar mass while having comparable cold gas fractions. Since the decrease in cold gas fractions from $z = 2$ to 0 is less than the increase in stellar masses, the f_g - M_s relation shifts to the right. Moreover, lower mass galaxies exhibit a broader distribution of cold gas fractions at a given stellar mass or redshift than higher mass ones. This effect is in part due to the efficient supernovae feedback having a stronger effect on the cold gas components of lower mass galaxies by causing the amount of gas in a cold phase to vary more on shorter timescales.

Galaxy metallicity is more sensitive to changes in stellar mass in higher mass galaxies, leading to a steeper mass-metallicity relation at $z = 0$ than at $z = 2$ as galaxies are more massive at lower redshifts. As galaxies gain more stellar mass and metals, supernovae

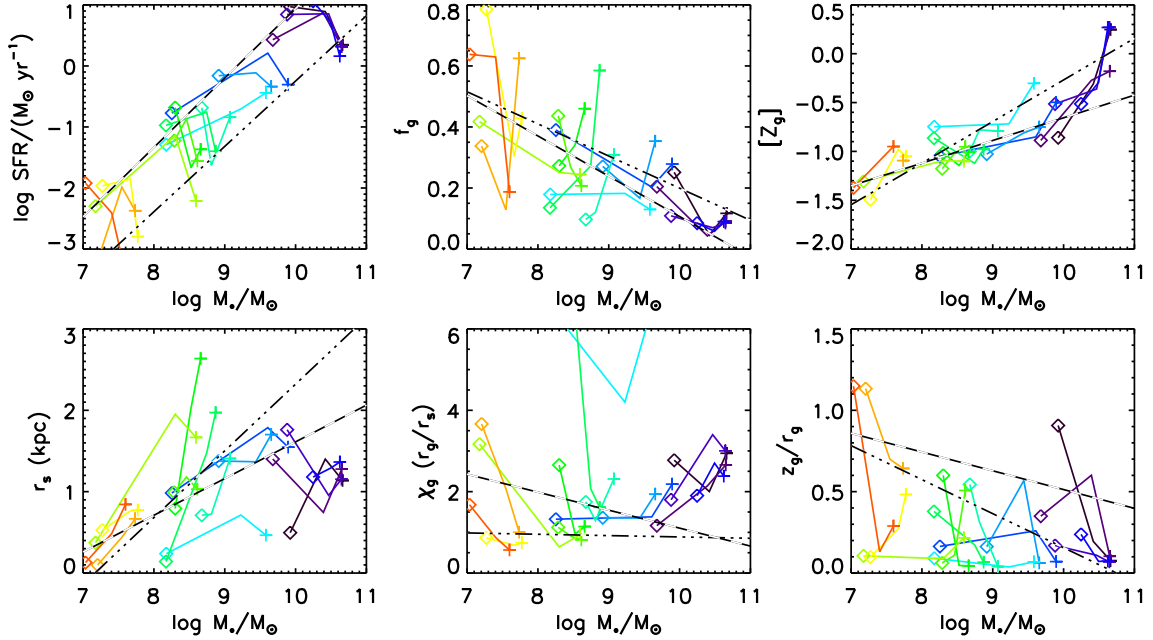


Figure 6.6 Similar to Figure 6.5, except for galaxy properties as a function of stellar mass at redshifts $z = 2$, 1 , and 0 (diamond to cross). Upper row (from left to right) - star formation rate, cold gas fraction, and metallicity. Lower row - stellar scale length, ratio of cold gas to stellar scale length, and ratio of cold gas scale height to scale length. The best linear fit to the median galaxy properties at $z = 2$ (dashed line) and $z = 0$ (triple dot-dashed line) are overplotted. With increasing stellar mass, stellar disks generally increase in size and cold gas disks become flatter at both $z = 0$ and $z = 2$. Here, we also see that low mass galaxies' cold gas components become much more compact with redshift while those of more massive galaxies do not change much.

feedback has a more limited effect in its ability to eject gas from the galaxy and therefore on the amount of cold gas available to form stars. The increase in metals also makes metal line cooling become more efficient, allowing more stars to form and the production of more metals. Additionally, feedback from AGN and supermassive black hole growth is not included in these simulations, which will decrease the star formation rate in the more massive galaxies. Including this effect may lower the metallicities of some of the more massive galaxies.

In general, the large scatter in the properties and evolution of these galaxies indicates that they are poorly fit by simple linear fits, nonetheless we use these simple relations to better understand how galaxies are changing with time. The size of galaxy stellar disks increase with stellar mass as was also seen in Figure 6.5. Furthermore, galaxy disks grow more with redshift than their stellar masses do, which is mostly due to an increase in stellar disk size in lower mass galaxies. Low mass galaxies' cold gas disk sizes relative to their stellar disk sizes decrease with redshift, making their cold gas more compact, while this ratio does not change significantly in massive galaxies. This relation causes galaxies' relative cold gas disk sizes to go from decreasing with stellar mass at $z = 2$ to increasing with stellar mass at $z = 0$. Finally, as galaxy stellar mass increases, the thickness of their cold gas disks (z_{g50}/r_{g50}) becomes flatter. This effect is stronger in more massive galaxies, causing the relation between cold gas disk thickness and stellar mass to become steeper with cosmic time. Finally, the most massive half of our galaxies all have very thin gas disks with $z_{g50}/r_{g50} \lesssim 0.1$.

6.3.3 Galaxy Scaling Relations

The upper row of Figure 6.7 shows the relation between stellar disk size and stellar mass at $z = 0$ and $z = 2$ in the pressure-based $f_j = 1$ model, pressure-based $f_j = 2.5$ model, and the numerical simulations. In the pressure-based models at a given stellar mass, stellar disks increase in size with stellar mass where the pressure-based $f_j = 2.5$ model produces disks that are ~ 0.2 dex larger than in the pressure-based $f_j = 1$ model. Both models have larger stellar disks at $z = 2$ than $z = 0$ by $\sim 0.1 - 0.2$ dex, indicating mild evolution. The stellar disks in the 15 galaxies in the numerical simulations also show a mild evolution with

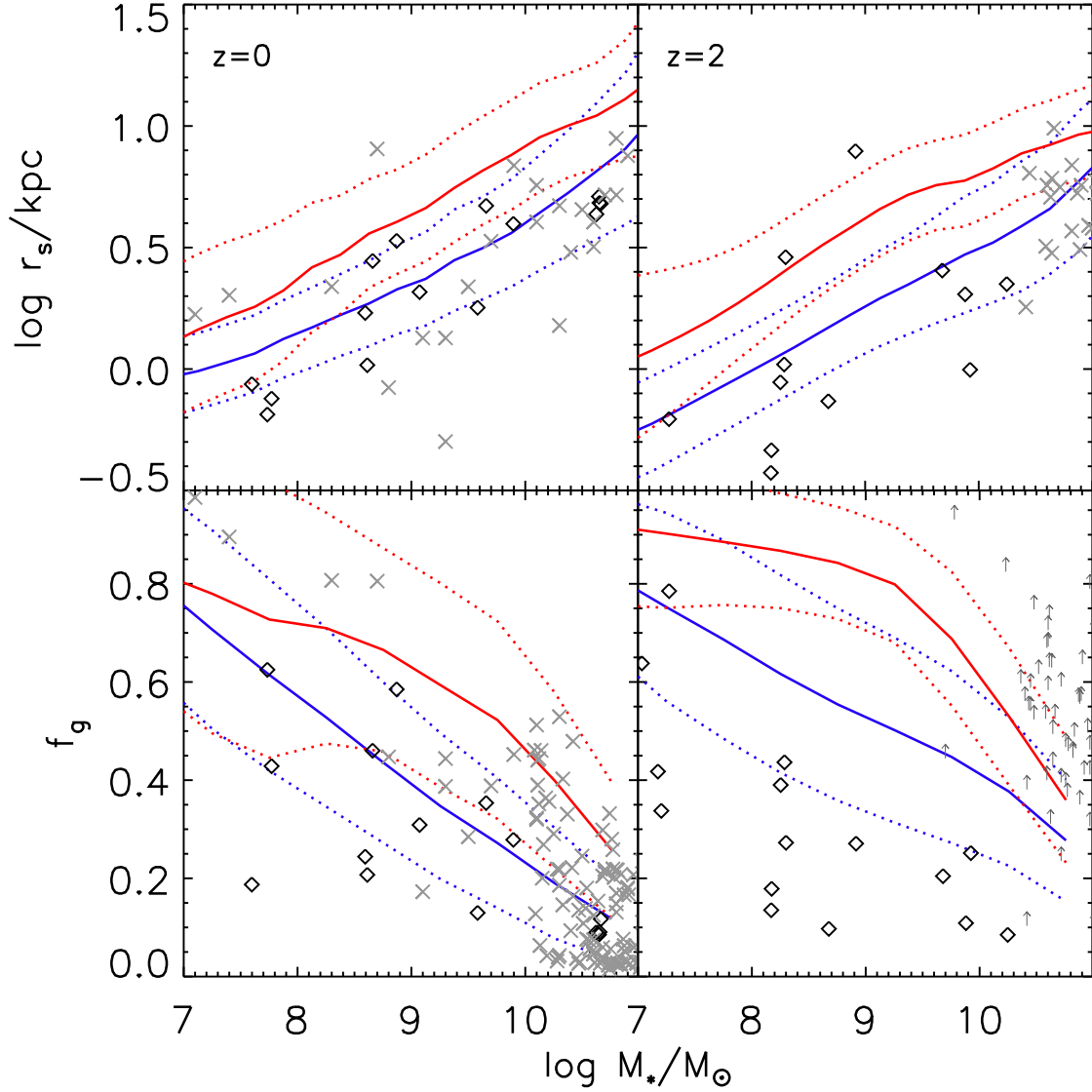


Figure 6.7 Upper row - conditional probability of selecting a galaxy with a given stellar disk size as a function of stellar mass for the median pressure-based $f_j = 1$ (blue solid) and pressure-based $f_j = 2.5$ (red solid) models with the 1σ variance (dotted lines). The r_s values for the 15 galaxies in the numerical simulations are overplotted (black diamonds). Observations from Leroy et al. (2008) at $z = 0$ Tacconi et al. (2013) at $z = 2$ and are overplotted as gray crosses. Lower row - same as top except for cold gas fraction ($f_g = (M_{HI} + M_{H_2})/(M_s + M_{HI} + M_{H_2})$). Left column - $z = 0$. Right column - $z = 2$.

redshift, and a similar trend with stellar mass. The most massive galaxies in the numerical simulations have very massive bulge components that have been removed in order to extract the disk size. The inclusion of AGN feedback may reduce the amount of stellar mass in the central region, thereby increasing the half-stellar mass length in massive galaxies. Galaxies in the numerical simulations at a given stellar mass exhibit a similar range in stellar disk size as the pressure-based models. The numerical simulations predict a much broader range in stellar disk sizes at $z = 2$ than are seen in the SAMs.

The lower row of Figure 6.7 shows the relation between cold gas fraction and stellar mass at $z = 0$ and $z = 2$. Both pressure-based models have larger cold gas fractions ($\sim 0.1 - 0.2$ dex) at $z = 2$ than at $z = 0$. The pressure-based $f_j = 2.5$ model predicts significantly larger cold gas fractions than the pressure-based $f_j = 1$ model at both redshifts. At $z = 2$, the numerical simulations produce galaxies with much less cold gas than the pressure-based models, but at $z = 0$ most of the galaxies are consistent with the pressure-based $f_j = 1$ model. However, this picture is further complicated by the highly uncertain amount of ionized gas in galaxies. In all 15 galaxies in the numerical simulations, the majority of the gas mass is ionized, while the mass of ionized gas is comparable to the amount of neutral gas in the pressure-based models which model the ionized gas as a sheet with a surface density of $\Sigma_{HII} = 0.4 \text{ M}_\odot \text{ pc}^{-2}$. Therefore, galaxies in the SAMs at a given stellar mass typically have more cold gas than those in the numerical simulations. In the numerical simulations, the low cold gas fractions are strongly dependent on the supernovae feedback efficiency in photoionizing the surrounding cold gas. In the SAMs, this photoionizing effect is not included in the supernovae feedback recipe.

Figure 6.8 is similar to Figure 6.7 except it shows the relation between the star formation rate and metallicity with respect to stellar mass. The pressure-based $f_j = 1$ and pressure-based $f_j = 2.5$ models produce similar relations between star formation rate and stellar mass at $z = 0$, where the latter produces galaxies with slightly higher star formation rates at a given stellar mass. The more extended gas distributions in the pressure-based $f_j = 2.5$ model slow the rate of cosmic star formation and allow for more gas to be available to form stars at later cosmic epochs. The galaxies in the numerical simulations lie on the pressure-based $f_j = 2.5$ SFR- M_s relation, although they are consistent with both models.

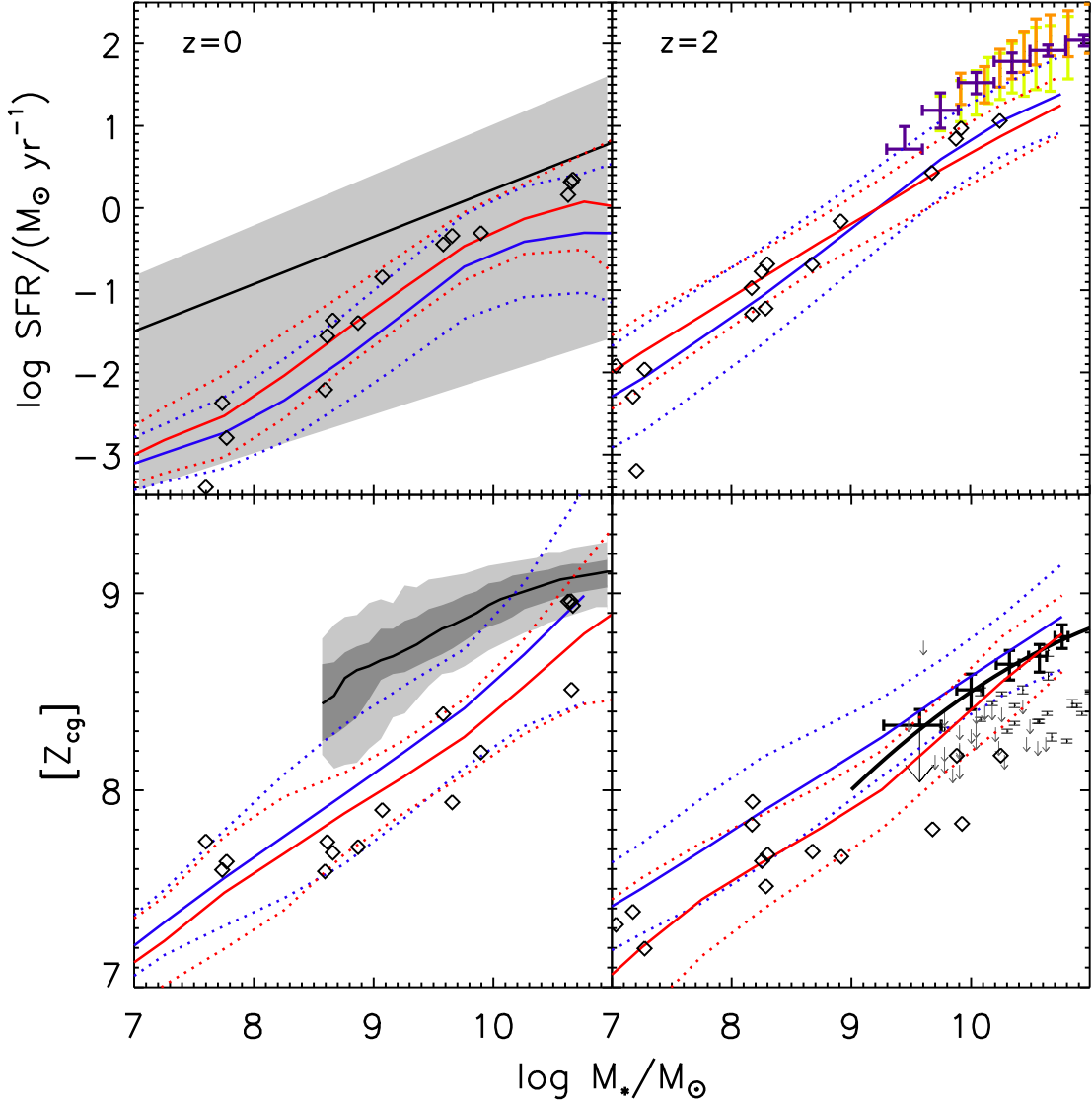


Figure 6.8 Similar to figure 6.7, except for the star formation rates (upper row) and metallicities (lower row) as a function of stellar mass. Left column - $z = 0$. Right column - $z = 2$. Observations of local galaxies and star-forming galaxies at $z = 2$ are overplotted for reference (Brinchmann et al. 2004; Tremonti et al. 2004; Whitaker et al. 2011; Erb et al. 2006d; Kulas et al. 2013; Maiolino et al. 2008).

In general, all of our models produce galaxies with lower star formation rates at a given stellar mass than local observations, but they are also not inconsistent with them. At $z = 2$, the pressure-based models and numerical simulations produce similar SFR- M_s relations, which all underpredict the star formation rates of massive galaxies by ~ 0.5 dex. They also predict a flattening and a shift downward of the SFR- M_s relation with redshift, which are consistent with observations.

All three models produce remarkably similar mass-metallicity relations at $z = 0$, yet they are all steeper than the observed mass-metallicity relation and produce lower metallicities at every stellar mass. This panel is particularly illuminating as the metallicities measured in local galaxies are weighted by the star formation rate while the metallicities in both models are the average cold gas metallicity. Weighting the metallicities by the star formation rate (not shown) causes them to shift upward and be in better agreement with local observations. For a more detailed discussion of this effect, see Berry et al. (2014b, in prep.). Both types of simulations also exhibit substantially more scatter around the relation than is observed in local galaxies. Since the numerical simulations do not include feedback from AGN or black hole growth, the metallicities of the higher mass galaxies ($\log M_s \sim 10.5$) are probably higher than if this process was included. At $z = 2$, the pressure-based models produce galaxy metallicities that are in good agreement with observations of star-forming galaxies at a given stellar mass, especially the pressure-based $f_j = 2.5$ model. The galaxies from the numerical simulations have a shallower slope than the pressure-based models, causing them to predict similar metallicities at low stellar masses and lower metallicities at high stellar masses. The high stellar mass galaxies have metallicities that are lower than but not inconsistent with observations. Both numerical simulations and the pressure-based models predict a smaller shift upward in the mass-metallicity relation from $z = 2$ to 0 than is seen in observations.

6.4 Discussion

Numerical simulations and semi-analytic models provide different but complementary means of studying galaxy formation. As they are based on more fundamental physical processes and make fewer underlying assumptions, numerical simulations allow for a more detailed

understanding of the effect of various processes on the evolution of galaxy properties. Additionally, they allow us to track the evolution of individual galaxies across cosmic time and directly observe how they change. In spite of this powerful technique, they are sufficiently computationally expensive that we are only able to do this for a handful of galaxies. On the other hand, semi-analytic models use simplified assumptions on the physical processes that govern the evolution of galaxy properties. The large increase in computational efficiency allows for a much larger number of galaxies to be modeled and the tracking of populations of galaxies across cosmic time. Moreover, changing the details of these processes is simple and computationally inexpensive. In the previous section, we presented the properties of galaxies in the GASOLINE numerical simulations as well as the results of semi-analytic models, focusing on the radial profiles. In this section, we compare these results

6.4.1 Galaxy Profiles

At $z = 0$, one insight is that bulges develop in all of the massive galaxies where both the stellar bulge and disk components are remarkably well-fit by exponential profiles. In less massive galaxies, the single exponential describing the disk component also fits well. However at large radii in many galaxies, stellar disks either flatten or cut off. Cold gas disks are moderately well-fit by an exponential profile: where they fail to fit central regions and miss significant amounts of H_2 . They also fail to fit the cut off in the HI profiles at radii that vary for each galaxy.

The predicted H_2 surface density profiles from the pressure-based and metallicity-dependent H_2 formation recipes are a poor match to the numerical simulations, especially in the more massive galaxies. This result is interesting as the metallicity-dependent H_2 formation recipe was derived from numerical simulations (Gnedin & Kravtsov 2011) which model H_2 formation in a similar manner to this one. Moreover, the two H_2 formation recipes utilized in the SAMs predict similar H_2 surface density profiles in spite of following different physics for the formation of H_2 . As feedback from supernova in the numerical simulations is more concentrated and therefore more efficient, it is more effective at dissociating H_2 . In lower density regions as in the galactic disk, this feedback mechanism may inhibit further H_2 formation.

Some galaxies exhibit a distinct end in their HI profiles while others have HI disks that slowly decrease in density. The semi-analytic models are a good fit to the interior regions of the HI profiles, but have the HI disks end at $\Sigma = 0.4M_{\odot} \text{ pc}^{-2}$. In most of the galaxies, the HI disks predicted by fitting an exponential to the cold gas surface density profile are larger than those in the numerical simulations. This result is in large part due to disks in the numerical simulations dropping off rapidly at a surface density higher than $\Sigma = 0.4M_{\odot} \text{ pc}^{-2}$.

At $z = 2$, both stellar and cold gas radial profiles are more irregular and have significantly more substructure, which is either due to clumps of gas and stars within the galaxy or infalling material. This substructure is missed by the simple radial profiles employed by the semi-analytic models, which can result in very unsatisfactory fits. The cold gas disks fit with an exponential profile range from being decent to very poor fits to the observed HI profiles. Again, the H_2 formation recipes of both models overpredict the H_2 surface density profiles, although they are a mediocre fit to a few of the more massive galaxies. Unlike at $z = 0$, HI disks are not flat at $z = 2$, but rather decrease constantly, suggesting that perhaps the threshold for ionized gas changes as a function of redshift. Clearly, stellar and cold gas disks are better described by a double exponential or an exponential profile at $z = 0$, than $z = 2$.

Another striking insight is the flatness of galaxies metallicity profiles. Numerous galaxies, especially massive ones, exhibit a modest metallicity gradient at $z = 0$ while only a few show substantial changes in metallicity with radius at $z = 2$. The least massive third of galaxies show almost no change in metallicity with radius. Additionally, metallicity profiles are much smoother at $z = 0$, where higher redshift galaxies show substantial variation in their metallicity at any given radius.

From the larger H_2 surface densities calculated following the recipe in the semi-analytic models, we would naively expect them to predict a higher star formation rate surface density profile than are observed for galaxies in the numerical simulations. Yet in almost all cases, star formation rates are higher in the numerical simulations. This discrepancy is likely due to star formation occurring relatively quickly in the numerical simulations, then feedback from supernovae destroying their molecular birth clouds on short timescales. From $z = 2$ to

0, the star formation rate profiles become much smoother as a function of radius and much flatter. At higher redshifts star formation is clumpy and mostly confined to the central regions. On the other hand at $z = 0$, the star formation rate profiles have become much smoother and flatter. In the more massive galaxies, star formation splits into a relatively quiescent star-forming disk and a starbursting bulge. This evolution from a star-forming bulge to a disk is also seen in the change in slope of the star formation rate profiles predicted by the exponential fits to the cold gas profiles.

6.4.2 Evolution of Galaxy Properties

An insight from the numerical simulations is that over the past 11 Gyr, the star formation rate, cold gas fraction, and size and thickness of the disk vary substantially. Although one would expect the change in cold gas fraction to be correlated with changes in the star formation rate, this does not appear to be the case in our models. One possible reason for this is that stars predominantly form in molecular gas while the majority of the cold gas is in atomic form in these simulations, allowing galaxies' cold gas fractions to change substantially while having a relatively small effect on their star formation rates. We also observed low cold gas fractions at $z = 2$ relative to what the semi-analytic models predict and observations of high-mass star-forming galaxies (Tacconi et al. 2013). This may suggest that galaxies in the numerical simulations have too little cold gas due to the high efficiency with which supernovae inject energy into and photoionize the surrounding gas.

We also observe higher mass galaxies to increase in metallicity faster than low mass ones, leading to a steepening of the mass-metallicity relation with redshift. At $z = 2$, both numerical simulations and the semi-analytic models are in agreement with each other and observations (Erb et al. 2006b; Maiolino et al. 2010; Kulas et al. 2013) while at $z = 0$ they predict lower metallicities at almost all stellar masses where the lowest mass galaxies are furthest from observations. Efficient supernovae feedback would have a stronger effect on low mass galaxies as they have shallower potential wells and star formation occurs on longer timescales. Moreover, both the semi-analytic models and numerical simulations produce lower star formation rates in low mass galaxies than is observed locally. This suggests that the cause of the reduced star formation efficiency in low mass galaxies is present in both

numerical simulations and semi-analytic models. Possible reasons may include the efficiency of supernovae feedback, the ability of cold gas to cool and form molecular gas, and the star formation efficiency. The large variance in cold gas fraction in lower mass galaxies across cosmic time further indicates that efficiency of supernova feedback slows the rate of star formation.

High mass galaxies in the numerical simulations have stellar disks that do not change significantly with stellar mass while they increase in stellar mass from $z = 2$ to 0, causing them to be much more compact than those produced in the semi-analytic models and observed both locally and at $z = 2$. This difference is mainly caused by an increase in stellar surface density in the central regions due to them having massive bulges. Low mass galaxies without bulge components instead move up the r_{s50} - M_s relation from $z = 2$ to 0 in better agreement with the semi-analytic models. As AGN feedback is not modeled in the massive galaxies, accurately including this effect may reduce star formation in the bulge and increase the stellar half-mass radius.

The relative size of the cold gas disks to stellar disks in low mass galaxies becomes smaller with cosmic time while it remains constant in high mass galaxies. This causes the χ_g to go from decreasing with stellar mass at $z = 2$ to increasing with stellar mass at $z = 0$. In contrast, while the cold gas disks of low mass galaxies become more compact with time, high mass galaxies' cold gas disks become much thinner where the most massive 50% have $z_{g50}/r_{g50} \lesssim 0.1$. This is further supported by the decrease in vertical velocity dispersion observed in high mass galaxies from $z = 2$ to 0. In spite of galaxies becoming more compact with time, due to accretion of clumps or streams of infalling material, the size of the cold gas disk can vary substantially at a given stellar mass or redshift for a given galaxy. These variations in cold gas disk size are also observed in terms of the thickness of the disk, indicating the infalling material does not necessarily flow in along the plane of the disk and can subsequently puff it up.

6.5 Conclusions

In this paper, we study the evolution of the radial profiles and average galaxy properties of 15 individual galaxies in numerical simulations from $z = 2$ to 0, which we then compare to predictions from semi-analytic model and observations of galaxies. First focusing on the 15 galaxies, we fit double exponential profiles for a bulge and disk component to the cold gas and stellar profiles of each galaxy. Then using a pressured-based and metallicity-dependent cold gas partitioning, which are also used in the semi-analytic models, we calculate the HI and H₂ profiles for each galaxy. Using the cold gas profiles from the numerical simulations, we partition cold gas into HI and H₂ and use the H₂-based star formation recipe in the SAM to calculate the star formation rate profiles. These steps allow us to compare the distribution of cold gas, the partitioning of cold gas into H₂ and HI, and the formation of stars to assumptions in the semi-analytic models. Additionally, the numerical simulations allow us to track the evolution of individual galaxies and study how their properties evolve. We use this information to study the distribution of galaxy properties at a given redshift or stellar mass and how those relations change with redshift and stellar mass.

Our main results are as follows:

- In most galaxies in the numerical simulations, stellar profiles are well fit by a double exponential for a bulge and disk component, especially at $z = 0$. In some galaxies, cold gas profiles are moderately well-fit by an exponential profile although these simple profiles miss significant substructure seen in the numerical simulations. At $z = 0$, most cold gas disks are very flat which end at a given HI gas density that varies with radius and surface density.
- The metallicity-dependent and pressure-based H₂ formation recipes produce similar H₂ density profiles; however in massive galaxies, both predict substantially more H₂ than is predicted in numerical simulations. Using the H₂-based star formation recipe in the semi-analytic models (K-S relation) and the amount of H₂ in the numerical simulations, we predict much lower star formation rates than are calculated in the numerical simulations. This result may suggest that supernovae feedback is efficient at dissociating H₂ or that the avenue for star formation in the numerical simulations

is more efficient than in the semi-analytic models.

- Metallicity profiles are very flat at $z = 2$ in the numerical simulations where in most galaxies, especially the more massive ones, the interior regions of the disk increase substantially in metallicity with redshift due to the build up of stars. Additionally, the numerical simulations predict much higher metallicities when they are weighted by star formation as is the case in emission-line metallicity measurements.
- As individual galaxies evolve from $z = 3$ to 0, their cold gas fractions decrease and their metallicities increase where more massive galaxies' metallicities increase faster. Their stellar disks grow substantially in size while their cold gas disks become flatter and low mass galaxies' cold gas disks become smaller relative to their stellar disks. This latter effect is due to the build-up of stars in the outer regions of the disk and cold gas condensing and becoming more compact.
- Galaxies in the numerical simulations and semi-analytic models at $z = 0$ generally lie on the same r_s - M_s relation, f_g - M_s relation, $[Z]$ - M_s , and SFR- M_s relation as observations of local galaxies. At $z = 2$, the numerical simulations and semi-analytic models predict similar r_s - M_s , SFR- M_s , and $[Z]$ - M_s relations while the numerical simulations predict lower cold gas fractions. As a result, both types of models predict similar stellar disk sizes and metallicities as observations, but lower star formation rates.

Chapter 7

Conclusions

In this thesis, we studied the relations among the properties of star-forming galaxies, cold neutral gas in and around them, and the process of star formation through an analysis of both observations of star-forming galaxies and “observations” of model galaxies at $z \sim 2-3$. We summarize our main results and present some open questions below.

First in **Chapter 2**, we analyzed spectra of star-forming galaxies at $2 < z < 3.5$, where we studied the relations among Ly α emission, intrinsic UV spectral slope, redshift, outflow kinematics, low- and high-ionization absorption, and nebular emission for a sample of galaxies spanning a similar luminosity range. Our goal was to understand the effect of star formation and supernova feedback on galaxy-scale outflows in galaxies with different sets of properties. By combining individual galaxy spectra based on different physical properties, we created sets of composite spectra which we used to evaluate the dependence of outflow properties on galaxies. We found a strong link between strong Ly α emission and weaker low-ionization absorption lines, stronger nebular emission, and bluer rest-ultraviolet slopes with a lack of correlation with high ionization line strength and total velocity offset. These trends indicate that galaxies with stronger Ly α emission have less dust, smaller covering fractions of neutral gas, and less dust in their outflowing component, but are still ejecting large amounts of ionized gas at high velocities. While many effects contribute to the amount of Ly α a galaxy emits, galaxies with strong Ly α emission have generally been shown to be younger, less massive, less evolved, and relatively highly star forming as compared to those without. If our Ly α -emitting galaxies are representative of typical LAEs, then these results support the physical picture of them being galaxies undergoing one of their first starbursts. Moreover, these starbursts are powerful enough to ionize significant amounts of neutral gas and drive it from the galaxy.

Through further study of star-forming galaxies, outflows of cold and ionized gas, and the surrounding circum-galactic medium, we will be able to better understand the relationship between galaxies and their environments. These relations include the rate and amount of enrichment of the intergalactic medium, the ability of galactic winds to eject metals and cold gas from galaxies, the detailed nature of supernova feedback, the cessation of star formation due to feedback, and the geometry of the interstellar medium and outflowing components in distant galaxies.

Next, we shifted our focus from observations to simulations about how the properties of neutral gas surrounding distant galaxies evolve with cosmic time. In doing this, we use semi-analytic models to observe model DLAs, thereby allowing us to study the relation between cold neutral gas within and around galaxies and the host galaxies themselves. Semi-analytic models are based on a cold dark matter framework for structure formation whereupon physical processes govern the evolution of galaxies. Based on physically-motivated “recipes” to model physical processes and track galaxy properties, semi-analytic models can provide mock catalogs for very large numbers of galaxies, allowing us to study the effects of different processes on a statistical number of galaxies. We presented the framework for these semi-analytic models in **Chapter 3**.

Using these semi-analytic models, we generated sets of lightcones for each combination of cold gas partitioning recipes and different gas distribution recipes. We tested a pressure-based recipe and two metallicity-based recipes with a fixed and varying UV radiation field for partitioning cold gas into atomic and molecular components. Then, we generate three sets of models for the size of cold gas disks in galaxies with cold gas specific angular momentum equal to that of the dark matter (“standard” gas disks), equal to 2.5 times that of the dark matter (“extended” gas disks), and based on whether the central galaxy had undergone no mergers, only a minor merger, or a major merger (“merger” models). In **Chapter 4**, we observed model DLAs and compare them to the properties of observations of DLAs across cosmic time. We found that “standard” gas disks failed to reproduce the observed column density distribution, the line density of DLAs, the distribution of velocity widths (Δv) as measured by low-ionization state metal systems, the cosmological neutral gas density (Ω_{HI}), and the metallicity distribution at $z < 3$, regardless of the gas partitioning. On the

other hand, our models with extended radial gas profiles with either a pressure-based gas partitioning or metallicity-based recipe with a varying UV radiation field reproduced quite well the column density distribution, line density of DLAs, Ω_{HI} , and Δv distribution at $z < 3$. The success of the latter models over previous ones in reproducing the evolution of neutral gas across time in addition to the properties of local galaxies suggests an improved understanding of the physical processes that govern H_2 formation and the size of cold gas disks. However, all of the models underproduce the number of DLAs and HI gas density at $z > 3$, suggesting that DLAs at high redshift arise from a different physical phenomenon, such as outflows, clumps of cold gas, or filaments. If this is the case, the flatness in the number of DLAs and HI gas density over the redshift interval $0 < z < 5$ may be due to a cosmic coincidence where the majority of DLAs at $z > 3$ arise from intergalactic gas in filaments or streams while those at $z < 3$ arise predominantly in galactic discs. As our models do not include contributions from clumps, filaments, or streams, including these features might yield insight into the apparent rise in their relative contribution to the number of DLAs and HI gas density at $z > 3$. Our favored models also reproduce the distribution of DLA metallicities and their dependence on redshift and Δv , particularly when we include the effects of metallicity gradients. However, subsequent work indicates that these are likely not ubiquitous among high-redshift galaxies. The success of these results further suggests an improved understanding of how molecular hydrogen forms in atomic gas, then turns into stars, which enrich the surrounding interstellar medium.

An interesting direction for future work would be to investigate the contribution of outflowing and infalling cold gas to the DLA cross section at high redshifts. The goal of this study would be to determine whether a better description of cold gas around galaxies at high redshift would reproduce the high number density of DLAs and Ω_{HI} in the universe at $z > 3$ as well as the velocity width distribution. Including lower mass halos would also allow us to probe the contribution of less massive galaxies to the number of DLAs and Ω_{HI} . Additionally, better modeling of how stars and metals are distributed in galaxy disks would put constraints on the number and strength of metallicity gradients in distant galaxies. This may also yield insight into the origin of very low metallicities observed in DLAs at $z \gtrsim 4$.

Having studied the nature and evolution of cold gas in and around galaxies through

observing model DLAs, we focus on characterizing the properties of galaxies that host DLAs and how they relate to star-forming galaxies at $z = 2$. We use our catalog of DLAs selected in the previous chapter, then select model star-forming galaxies through “observing” using the same selection techniques as observational surveys. In **Chapter 5**, we showed that galaxies that host DLAs have large cold gas masses, but otherwise exhibit a broad range of galaxy properties. DLA host galaxies generally fall along common galaxy scaling relations and exhibit similar colors and luminosities as similar mass galaxies, suggesting that they are fairly similar to “typical” galaxies at the same redshift. As DLAs have a similar probability of exhibiting a given set of galaxy properties, our models predict that more massive galaxies are the most likely to host DLAs due to them being a relatively small fraction of the overall number of galaxies. For the same reason, DLA host galaxies will have a relatively small probability of being quite massive. As the majority of DLAs are relatively faint with low star formation rates, we also predict that deep near-infrared imaging is the most promising avenue for recovering the highest number of DLA host galaxies. Our extended gas disk models also reproduce the observed sizes of DLAs and the relation between size, column density, and metallicity, indicating that cold gas disks must be more extended at higher redshifts. We also found that since DLAs preferentially arise in the outer regions of galaxies there are substantial differences between the average H_2 fraction, star formation rate, and metallicity measured along the DLA line of sight and the average for the host galaxy. Finally, almost all DLA host galaxies should be detected with JWST.

The large range in galaxy properties associated with DLA host galaxies, their low luminosities, and the difference between line of sight and average galaxy properties imply that correctly identifying DLA host galaxies will continue to be quite challenging, even with deeper near-infrared and/or optical imaging. With more powerful telescopes, detecting DLA host galaxies will become easier which will also yield insight into the nature of their properties and any selection effects imposed by galaxies being detected as DLAs. Through observing both DLAs and their hosts, we will also be able to better understand the variation in galaxy properties as a function of galactocentric radius as well as the distribution and properties of cold gas at different radii.

Finally in **Chapter 6**, we studied 15 galaxies in high-resolution numerical simulations,

which we compared to predictions from semi-analytic models with the objective of gaining a better understanding of the distribution of cold gas in galaxies. We found that the stellar and cold gas profiles are moderately well-fit by exponential profiles as modeled in the SAMs, although much small scale structure is missed. The differences between the pressure-based and metallicity-dependent cold gas partitioning recipes are relatively small, although both predict significantly more molecular gas in the disk than are produced in the numerical simulations. At $z = 0$, most cold gas disks are flat and truncate at a given HI gas density that varies for each galaxy. This result is qualitatively consistent with semi-analytic models which truncate at the same HI gas density for all galaxies, although it is quantitatively different. Using the cold gas radial profiles and the metallicity-dependent cold gas partitioning, we apply the star formation recipe from the semi-analytic models (KS relation) to the numerical simulations. This process predicts much less star formation than is predicted by the numerical simulations, indicating that the latter is either more efficient at forming stars or at disassociating H₂. Most galaxy metallicity profiles are flat at $z = 2$ where the interior regions of the disk enrich substantially with redshift. These profiles also indicate that emission-line metallicities measured from HII regions in the central component can be much higher than those measured in cold gas at large radii, especially in high mass galaxies. As DLAs preferentially select the outskirts of galaxies, this effect may contribute to the low metallicities observed in DLAs. As individual galaxies evolve from $z = 3$ to 0, their stellar disks grow by $\gtrsim 2$ in size, their cold gas disks become flatter, and low mass galaxies' cold gas disks become smaller relative to their stellar disks while massive galaxies' cold gas disks do not change significantly. Galaxies in the numerical simulations and semi-analytic models at $z = 0$ generally lie on the same r_s - M_s relation, f_g - M_s relation, and SFR- M_s relation as observations of local galaxies. At $z = 2$, both types of simulations predict similar r_s - M_s , SFR- M_s , and $[Z]$ - M_s relations, where they predict similar stellar disk sizes and metallicities as observations, but lower star formation rates. These trends suggest that in spite of their simplifying assumptions, semi-analytic models are generally capturing the dominant processes that govern galaxies' average physical properties.

One significant improvement to the semi-analytic models would be to better characterize the distribution of molecular clouds in galaxies. This process would add an element of

stochasticity to the cold gas radial profiles, making them more realistic by providing smaller scale density enhancements seen in the profiles of galaxies in the numerical simulations. Another interesting avenue would be to better understand how the sizes of cold gas disks evolve with redshift as well as what causes the truncation of HI disks. A further investigation into the relation between H_2 , HI and star formation would help reconcile the differences between the star formation recipes in the two simulations. This process will invariably affect the mass-metallicity relation and the amount of cold gas present in galaxy disks, i.e., the cold gas fraction. A better understanding of the location and process through which stars form would also yield insight into the build up of metals and the strength of metallicity gradients. Finally, a more in-depth look at how metallicities are measured from HII regions and cold gas may give insight into the differences between metallicities observed along the DLA line of sight and those measured for the host galaxy.

Bibliography

- Adelberger, K. L., & Steidel, C. C. 2000, *ApJ*, 544, 218
- Agertz, O. 2010, in *From Stars to Galaxies: Connecting our Understanding of Star and Galaxy Formation*
- Agertz, O., Teyssier, R., & Moore, B. 2011, *MNRAS*, 410, 1391
- Altay, G., Theuns, T., Schaye, J., Booth, C. M., & Dalla Vecchia, C. 2013, *ArXiv e-prints*
- Altay, G., Theuns, T., Schaye, J., Crighton, N. H. M., & Dalla Vecchia, C. 2011, *ApJ*, 737, L37
- Anglés-Alcázar, D., Davé, R., Özel, F., & Oppenheimer, B. D. 2014, *ApJ*, 782, 84
- Atek, H., Kunth, D., Hayes, M., Östlin, G., & Mas-Hesse, J. M. 2008, *A&A*, 488, 491
- Avila-Reese, V., Colín, P., Valenzuela, O., D’Onghia, E., & Firmani, C. 2001, *ApJ*, 559, 516
- Baldry, I. K., Driver, S. P., Loveday, J., Taylor, E. N., Kelvin, L. S., Liske, J., Norberg, P., Robotham, A. S. G., Brough, S., Hopkins, A. M., Bamford, S. P., Peacock, J. A., Bland-Hawthorn, J., Conselice, C. J., Croom, S. M., Jones, D. H., Parkinson, H. R., Popescu, C. C., Prescott, M., Sharp, R. G., & Tuffs, R. J. 2012, *MNRAS*, 421, 621
- Baldry, I. K., Glazebrook, K., & Driver, S. P. 2008, *MNRAS*, 388, 945
- Barnes, J., & Efstathiou, G. 1987, *ApJ*, 319, 575
- Bate, M. R., & Burkert, A. 1997, *MNRAS*, 288, 1060
- Battisti, A. J., Meiring, J. D., Tripp, T. M., Prochaska, J. X., Werk, J. K., Jenkins, E. B., Lehner, N., Tumlinson, J., & Thom, C. 2012, *ApJ*, 744, 93
- Behroozi, P. S., Conroy, C., & Wechsler, R. H. 2010, *ApJ*, 717, 379
- Berry, M., Gawiser, E., Guaita, L., Padilla, N., Treister, E., Blanc, G. A., Ciardullo, R., Francke, H., & Gronwall, C. 2012, *ApJ*, 749, 4
- Berry, M., Somerville, R. S., Haas, M. R., Gawiser, E., Maller, A., Popping, G., & Trager, S. C. 2013, *ArXiv e-prints*
- Bigiel, F., & Blitz, L. 2012, *ApJ*, 756, 183
- Bigiel, F., Leroy, A., Walter, F., Brinks, E., de Blok, W. J. G., Madore, B., & Thornley, M. D. 2008a, *AJ*, 136, 2846
- . 2008b, *AJ*, 136, 2846

- Bigiel, F., Leroy, A. K., Walter, F., Brinks, E., de Blok, W. J. G., Kramer, C., Rix, H. W., Schrubba, A., Schuster, K.-F., Usero, A., & Wiese Meyer, H. W. 2011, *ApJ*, 730, L13
- Binney, J. J., & Evans, N. W. 2001, *MNRAS*, 327, L27
- Birnboim, Y., & Dekel, A. 2003, *MNRAS*, 345, 349
- Blanc, G. A., Adams, J. J., Gebhardt, K., Hill, G. J., Drory, N., Hao, L., Bender, R., Ciardullo, R., Finkelstein, S. L., Fry, A. B., Gawiser, E., Gronwall, C., Hopp, U., Jeong, D., Kelzenberg, R., Komatsu, E., MacQueen, P., Murphy, J. D., Roth, M. M., Schneider, D. P., & Tufts, J. 2011, *ApJ*, 736, 31
- Blitz, L., & Rosolowsky, E. 2004, *ApJ*, 612, L29
- . 2006, *ApJ*, 650, 933
- Blumenthal, G. R., Faber, S. M., Flores, R., & Primack, J. R. 1986, *ApJ*, 301, 27
- Blumenthal, G. R., Faber, S. M., Primack, J. R., & Rees, M. J. 1984, *Nature*, 311, 517
- Bondi, H. 1952, *MNRAS*, 112, 195
- Bouché, N., Gardner, J. P., Katz, N., Weinberg, D. H., Davé, R., & Lowenthal, J. D. 2005, *ApJ*, 628, 89
- Bouché, N., Murphy, M. T., Kacprzak, G. G., Péroux, C., Contini, T., Martin, C. L., & Dessauges-Zavadsky, M. 2013, *Science*, 341, 50
- Bower, R. G., Benson, A. J., Malbon, R., Helly, J. C., Frenk, C. S., Baugh, C. M., Cole, S., & Lacey, C. G. 2006, *MNRAS*, 370, 645
- Boylan-Kolchin, M., Ma, C.-P., & Quataert, E. 2008, *MNRAS*, 383, 93
- Braun, R. 2012, *ApJ*, 749, 87
- Brinchmann, J., Charlot, S., White, S. D. M., Tremonti, C., Kauffmann, G., Heckman, T., & Brinkmann, J. 2004, *MNRAS*, 351, 1151
- Bromm, V., & Larson, R. B. 2004, *ARA&A*, 42, 79
- Brook, C. B., Governato, F., Roškar, R., Stinson, G., Brooks, A. M., Wadsley, J., Quinn, T., Gibson, B. K., Snaith, O., Pilkington, K., House, E., & Pontzen, A. 2011, *MNRAS*, 415, 1051
- Brooks, A. M., Governato, F., Booth, C. M., Willman, B., Gardner, J. P., Wadsley, J., Stinson, G., & Quinn, T. 2007, *ApJ*, 655, L17
- Brooks, A. M., Solomon, A. R., Governato, F., McCleary, J., MacArthur, L. A., Brook, C. B. A., Jonsson, P., Quinn, T. R., & Wadsley, J. 2011, *ApJ*, 728, 51
- Bruce, V. A., Dunlop, J. S., Cirasuolo, M., McLure, R. J., Targett, T. A., Bell, E. F., Croton, D. J., Dekel, A., Faber, S. M., Ferguson, H. C., Grogin, N. A., Kocevski, D. D., Koekemoer, A. M., Koo, D. C., Lai, K., Lotz, J. M., McGrath, E. J., Newman, J. A., & van der Wel, A. 2012, *MNRAS*, 427, 1666

- Bullock, J. S., Kolatt, T. S., Sigad, Y., Somerville, R. S., Kravtsov, A. V., Klypin, A. A., Primack, J. R., & Dekel, A. 2001, *MNRAS*, 321, 559
- Cabanac, R. A., Valls-Gabaud, D., & Lidman, C. 2008, *MNRAS*, 386, 2065
- Calzetti, D., Kinney, A. L., & Storchi-Bergmann, T. 1994, *ApJ*, 429, 582
- Cassata, P., Le Fèvre, O., Garilli, B., Maccagni, D., Le Brun, V., Scodeggio, M., Tresse, L., Ilbert, O., Zamorani, G., Cucciati, O., Contini, T., Bielby, R., Mellier, Y., McCracken, H. J., Pollo, A., Zanichelli, A., Bardelli, S., Cappi, A., Pozzetti, L., Vergani, D., & Zucca, E. 2011, *A&A*, 525, A143
- Cen, R. 2012, *ApJ*, 748, 121
- Chabrier, G. 2003, *PASP*, 115, 763
- Christensen, C., Governato, F., Quinn, T., Brooks, A. M., Fisher, D. B., Shen, S., McCleary, J., & Wadsley, J. 2012a, *ArXiv e-prints*
- Christensen, C., Quinn, T., Governato, F., Stilp, A., Shen, S., & Wadsley, J. 2012b, *MNRAS*, 425, 3058
- Christensen, C. R., Brooks, A. M., Fisher, D. B., Governato, F., McCleary, J., Quinn, T. R., Shen, S., & Wadsley, J. 2014, *MNRAS*
- Ciardullo, R., Gronwall, C., Wolf, C., McCathran, E., Bond, N. A., Gawiser, E., Guaita, L., Feldmeier, J. J., Treister, E., Padilla, N., Francke, H., Matković, A., Altmann, M., & Herrera, D. 2012, *ApJ*, 744, 110
- Coles, P., & Lucchin, F. 2002, *Cosmology: The Origin and Evolution of Cosmic Structure*, Second Edition
- Collins, J. A., Shull, J. M., & Giroux, M. L. 2003, *ApJ*, 585, 336
- Cooke, J., Wolfe, A. M., Gawiser, E., & Prochaska, J. X. 2006, *ApJ*, 652, 994
- Cowie, L. L., & Hu, E. M. 1998, *AJ*, 115, 1319
- Croton, D. J., Springel, V., White, S. D. M., De Lucia, G., Frenk, C. S., Gao, L., Jenkins, A., Kauffmann, G., Navarro, J. F., & Yoshida, N. 2006, *MNRAS*, 365, 11
- Daddi, E., Cimatti, A., Renzini, A., Fontana, A., Mignoli, M., Pozzetti, L., Tozzi, P., & Zamorani, G. 2004, *ApJ*, 617, 746
- Davé, R., Katz, N., Oppenheimer, B. D., Kollmeier, J. A., & Weinberg, D. H. 2013, *ArXiv e-prints*
- De Lucia, G., & Blaizot, J. 2007, *MNRAS*, 375, 2
- Dekel, A., & Birnboim, Y. 2006, *MNRAS*, 368, 2
- Dessauges-Zavadsky, M., D’Odorico, S., Schaerer, D., Modigliani, A., Tapken, C., & Vernet, J. 2010, *A&A*, 510, A26+
- Di Matteo, T., Springel, V., & Hernquist, L. 2005, *Nature*, 433, 604

- Dijkstra, M., Lidz, A., & Wyithe, J. S. B. 2007, *MNRAS*, 377, 1175
- D’Onghia, E., Burkert, A., Murante, G., & Khochfar, S. 2006, *MNRAS*, 372, 1525
- D’Onghia, E., & Navarro, J. F. 2007, *MNRAS*, 380, L58
- Draine, B. T. 1978, *ApJS*, 36, 595
- Duffy, A. R., Kay, S. T., Battye, R. A., Booth, C. M., Dalla Vecchia, C., & Schaye, J. 2012, *MNRAS*, 420, 2799
- Dutton, A. A., & van den Bosch, F. C. 2009, *MNRAS*, 396, 141
- Eisenstein, D. J., Weinberg, D. H., Agol, E., Aihara, H., Allende Prieto, C., Anderson, S. F., Arns, J. A., Aubourg, É., Bailey, S., Balbinot, E., & et al. 2011, *AJ*, 142, 72
- Eisenstein, D. J., Zehavi, I., Hogg, D. W., Scoccimarro, R., Blanton, M. R., Nichol, R. C., Scranton, R., Seo, H.-J., Tegmark, M., Zheng, Z., Anderson, S. F., Annis, J., Bahcall, N., Brinkmann, J., Burles, S., Castander, F. J., Connolly, A., Csabai, I., Doi, M., Fukugita, M., Frieman, J. A., Glazebrook, K., Gunn, J. E., Hendry, J. S., Hennessy, G., Ivezić, Z., Kent, S., Knapp, G. R., Lin, H., Loh, Y.-S., Lupton, R. H., Margon, B., McKay, T. A., Meiksin, A., Munn, J. A., Pope, A., Richmond, M. W., Schlegel, D., Schneider, D. P., Shimasaku, K., Stoughton, C., Strauss, M. A., SubbaRao, M., Szalay, A. S., Szapudi, I., Tucker, D. L., Yanny, B., & York, D. G. 2005, *ApJ*, 633, 560
- Ellison, S. L., Hall, P. B., & Lira, P. 2005, *AJ*, 130, 1345
- Ellison, S. L., Yan, L., Hook, I. M., Pettini, M., Wall, J. V., & Shaver, P. 2001, *A&A*, 379, 393
- Elmegreen, B. G. 1989, *ApJ*, 338, 178
- . 1993, *ApJ*, 411, 170
- Erb, D. K., Shapley, A. E., Pettini, M., Steidel, C. C., Reddy, N. A., & Adelberger, K. L. 2006a, *ApJ*, 644, 813
- . 2006b, *ApJ*, 644, 813
- Erb, D. K., Steidel, C. C., Shapley, A. E., Pettini, M., Reddy, N. A., & Adelberger, K. L. 2006c, *ApJ*, 646, 107
- . 2006d, *ApJ*, 646, 107
- Erkal, D., Gnedin, N. Y., & Kravtsov, A. V. 2012, *ArXiv e-prints*
- Ferland, G. J., Korista, K. T., Verner, D. A., Ferguson, J. W., Kingdon, J. B., & Verner, E. M. 1998, *PASP*, 110, 761
- Finkelstein, S. L., Rhoads, J. E., Malhotra, S., & Grogin, N. 2009, *ApJ*, 691, 465
- Finkelstein, S. L., Rhoads, J. E., Malhotra, S., Grogin, N., & Wang, J. 2008, *ApJ*, 678, 655
- Flores, R., Primack, J. R., Blumenthal, G. R., & Faber, S. M. 1993, *ApJ*, 412, 443

- Font-Ribera, A., Miralda-Escudé, J., Arnau, E., Carithers, B., Lee, K.-G., Noterdaeme, P., Pâris, I., Petitjean, P., Rich, J., Rollinde, E., Ross, N. P., Schneider, D. P., White, M., & York, D. G. 2012, *JCAP*, 11, 59
- Fontana, A., Salimbeni, S., Grazian, A., Giallongo, E., Pentericci, L., Nonino, M., Fontanot, F., Menci, N., Monaco, P., Cristiani, S., Vanzella, E., de Santis, C., & Gallozzi, S. 2006, *A&A*, 459, 745
- Fontanot, F., De Lucia, G., Monaco, P., Somerville, R. S., & Santini, P. 2009, *MNRAS*, 397, 1776
- Förster Schreiber, N. M., Genzel, R., Lehnert, M. D., Bouché, N., Verma, A., Erb, D. K., Shapley, A. E., Steidel, C. C., Davies, R., Lutz, D., Nesvadba, N., Tacconi, L. J., Eisenhauer, F., Abuter, R., Gilbert, A., Gillessen, S., & Sternberg, A. 2006, *ApJ*, 645, 1062
- Fu, J., Guo, Q., Kauffmann, G., & Krumholz, M. R. 2010, *MNRAS*, 409, 515
- Fu, J., Kauffmann, G., Huang, M.-l., Yates, R. M., Moran, S., Heckman, T. M., Davé, R., Guo, Q., & Henriques, B. M. B. 2013, *MNRAS*, 434, 1531
- Fumagalli, M., Prochaska, J. X., Kasen, D., Dekel, A., Ceverino, D., & Primack, J. R. 2011, *MNRAS*, 418, 1796
- Fynbo, J. P. U., Laursen, P., Ledoux, C., Møller, P., Durgapal, A. K., Goldoni, P., Gullberg, B., Kaper, L., Maund, J., Noterdaeme, P., Östlin, G., Strandet, M. L., Toft, S., Vreeswijk, P. M., & Zafar, T. 2010, *MNRAS*, 408, 2128
- Fynbo, J. P. U., Ledoux, C., Noterdaeme, P., Christensen, L., Møller, P., Durgapal, A. K., Goldoni, P., Kaper, L., Krogager, J.-K., Laursen, P., Maund, J. R., Milvang-Jensen, B., Okoshi, K., Rasmussen, P. K., Thorsen, T. J., Toft, S., & Zafar, T. 2011, *MNRAS*, 413, 2481
- Gardner, J. P., Katz, N., Hernquist, L., & Weinberg, D. H. 1997, *ApJ*, 484, 31
- Gawiser, E., Francke, H., Lai, K., Schawinski, K., Gronwall, C., Ciardullo, R., Quadri, R., Orsi, A., Barrientos, L. F., Blanc, G. A., Fazio, G., Feldmeier, J. J., Huang, J.-s., Infante, L., Lira, P., Padilla, N., Taylor, E. N., Treister, E., Urry, C. M., van Dokkum, P. G., & Virani, S. N. 2007, *ApJ*, 671, 278
- Gawiser, E., van Dokkum, P. G., Gronwall, C., Ciardullo, R., Blanc, G. A., Castander, F. J., Feldmeier, J., Francke, H., Franx, M., Habertzettl, L., Herrera, D., Hickey, T., Infante, L., Lira, P., Maza, J., Quadri, R., Richardson, A., Schawinski, K., Schirmer, M., Taylor, E. N., Treister, E., Urry, C. M., & Virani, S. N. 2006a, *ApJ*, 642, L13
- . 2006b, *ApJ*, 642, L13
- Gawiser, E., van Dokkum, P. G., Herrera, D., Maza, J., Castander, F. J., Infante, L., Lira, P., Quadri, R., Toner, R., Treister, E., Urry, C. M., Altmann, M., Assef, R., Christlein, D., Coppi, P. S., Durán, M. F., Franx, M., Galaz, G., Huerta, L., Liu, C., López, S., Méndez, R., Moore, D. C., Rubio, M., Ruiz, M. T., Toft, S., & Yi, S. K. 2006c, *ApJS*, 162, 1
- Giavalisco, M. 1998, in *The Hubble Deep Field*, ed. M. Livio, S. M. Fall, & P. Madau, 121

- Glover, S. 2013, in *Astrophysics and Space Science Library*, Vol. 396, *Astrophysics and Space Science Library*, ed. T. Wiklind, B. Mobasher, & V. Bromm, 103
- Glover, S. C. O., & Clark, P. C. 2012, *MNRAS*, 426, 377
- Gnedin, N. Y. 2000, *ApJ*, 542, 535
- . 2012, *ApJ*, 754, 113
- Gnedin, N. Y., & Kravtsov, A. V. 2010, *ApJ*, 714, 287
- . 2011, *ApJ*, 728, 88
- Gnedin, O. Y., Kravtsov, A. V., Klypin, A. A., & Nagai, D. 2004, *ApJ*, 616, 16
- Governato, F., Mayer, L., Wadsley, J., Gardner, J. P., Willman, B., Hayashi, E., Quinn, T., Stadel, J., & Lake, G. 2004, *ApJ*, 607, 688
- Governato, F., Willman, B., Mayer, L., Brooks, A., Stinson, G., Valenzuela, O., Wadsley, J., & Quinn, T. 2007, *MNRAS*, 374, 1479
- Governato, F., Zolotov, A., Pontzen, A., Christensen, C., Oh, S. H., Brooks, A. M., Quinn, T., Shen, S., & Wadsley, J. 2012, *MNRAS*, 422, 1231
- Grazian, A., Salimbeni, S., Pentericci, L., Fontana, A., Nonino, M., Vanzella, E., Cristiani, S., de Santis, C., Gallozzi, S., Giallongo, E., & Santini, P. 2007, *A&A*, 465, 393
- Greif, T. H., Glover, S. C. O., Bromm, V., & Klessen, R. S. 2010, *ApJ*, 716, 510
- Grimes, J. P., Heckman, T., Aloisi, A., Calzetti, D., Leitherer, C., Martin, C. L., Meurer, G., Sembach, K., & Strickland, D. 2009, *ApJS*, 181, 272
- Groenewegen, M. A. T., Lamers, H. J. G. L. M., & Pauldrach, A. W. A. 1989, *A&A*, 221, 78
- Gronwall, C., Ciardullo, R., Hickey, T., Gawiser, E., Feldmeier, J. J., van Dokkum, P. G., Urry, C. M., Herrera, D., Lehmer, B. D., Infante, L., Orsi, A., Marchesini, D., Blanc, G. A., Francke, H., Lira, P., & Treister, E. 2007, *ApJ*, 667, 79
- Guaita, L., Acquaviva, V., Padilla, N., Gawiser, E., Bond, N. A., Ciardullo, R., Treister, E., Kurczynski, P., Gronwall, C., Lira, P., & Schawinski, K. 2011, *ApJ*, 733, 114
- Guaita, L., Gawiser, E., Padilla, N., Francke, H., Bond, N. A., Gronwall, C., Ciardullo, R., Feldmeier, J. J., Sinawa, S., Blanc, G. A., & Virani, S. 2010, *ApJ*, 714, 255
- Guedes, J., Callegari, S., Madau, P., & Mayer, L. 2011, *ApJ*, 742, 76
- Guimarães, R., Petitjean, P., de Carvalho, R. R., Djorgovski, S. G., Noterdaeme, P., Castro, S., Poppe, P. C. D. R., & Aghaee, A. 2009, *A&A*, 508, 133
- Guo, Q., White, S., Li, C., & Boylan-Kolchin, M. 2010, *MNRAS*, 404, 1111
- Haardt, F., & Madau, P. 1996, *ApJ*, 461, 20
- Haehnelt, M. G., Steinmetz, M., & Rauch, M. 1998, *ApJ*, 495, 647

- Haiman, Z., Rees, M. J., & Loeb, A. 1996, *ApJ*, 467, 522
- Hansen, M., & Oh, S. P. 2006, *MNRAS*, 367, 979
- Hathi, N. P., Ryan, Jr., R. E., Cohen, S. H., Yan, H., Windhorst, R. A., McCarthy, P. J., O’Connell, R. W., Koekemoer, A. M., Rutkowski, M. J., Balick, B., Bond, H. E., Calzetti, D., Disney, M. J., Dopita, M. A., Frogel, J. A., Hall, D. N. B., Holtzman, J. A., Kimble, R. A., Paresce, F., Saha, A., Silk, J. I., Trauger, J. T., Walker, A. R., Whitmore, B. C., & Young, E. T. 2010, *ApJ*, 720, 1708
- Heckman, T. M., Armus, L., & Miley, G. K. 1990, *ApJS*, 74, 833
- Heckman, T. M., Robert, C., Leitherer, C., Garnett, D. R., & van der Rydt, F. 1998, *ApJ*, 503, 646
- Helfer, T. T., Thornley, M. D., Regan, M. W., Wong, T., Sheth, K., Vogel, S. N., Blitz, L., & Bock, D. C.-J. 2003, *ApJS*, 145, 259
- Hinshaw, G., Larson, D., Komatsu, E., Spergel, D. N., Bennett, C. L., Dunkley, J., Nolte, M. R., Halpern, M., Hill, R. S., Odegard, N., Page, L., Smith, K. M., Weiland, J. L., Gold, B., Jarosik, N., Kogut, A., Limon, M., Meyer, S. S., Tucker, G. S., Wollack, E., & Wright, E. L. 2013, *ApJS*, 208, 19
- Hoeft, M., Yepes, G., Gottlöber, S., & Springel, V. 2006, *MNRAS*, 371, 401
- Hopkins, P. F., Cox, T. J., Younger, J. D., & Hernquist, L. 2009a, *ApJ*, 691, 1168
- . 2009b, *ApJ*, 691, 1168
- Hopkins, P. F., et al. 2009c, *MNRAS*, 397, 802
- Inoue, S., & Saitoh, T. R. 2014, *ArXiv e-prints*
- Jones, T., Ellis, R., Jullo, E., & Richard, J. 2010, *ApJ*, 725, L176
- Jones, T., Ellis, R. S., Richard, J., & Jullo, E. 2013, *ApJ*, 765, 48
- Jones, T., Stark, D. P., & Ellis, R. S. 2012, *ApJ*, 751, 51
- Jorgenson, R. A., Murphy, M. T., & Thompson, R. 2013, *ArXiv e-prints*
- Jorgenson, R. A., Wolfe, A. M., Prochaska, J. X., Lu, L., Howk, J. C., Cooke, J., Gawiser, E., & Gelino, D. M. 2006, *ApJ*, 646, 730
- Kajisawa, M., Ichikawa, T., Tanaka, I., Konishi, M., Yamada, T., Akiyama, M., Suzuki, R., Tokoku, C., Uchimoto, Y. K., Yoshikawa, T., Ouchi, M., Iwata, I., Hamana, T., & Onodera, M. 2009, *ApJ*, 702, 1393
- Karim, A., Schinnerer, E., Martínez-Sansigre, A., Sargent, M. T., van der Wel, A., Rix, H.-W., Ilbert, O., Smolčić, V., Carilli, C., Pannella, M., Koekemoer, A. M., Bell, E. F., & Salvato, M. 2011, *ApJ*, 730, 61
- Katz, N. 1992, *ApJ*, 391, 502
- Kauffmann, G. 1996, *MNRAS*, 281, 475

- Kauffmann, G., & Charlot, S. 1994, *ApJ*, 430, L97
- Kauffmann, G., Li, C., Fu, J., Saintonge, A., Catinella, B., Tacconi, L. J., Kramer, C., Genzel, R., Moran, S., & Schiminovich, D. 2012, *MNRAS*, 422, 997
- Kennicutt, Jr., R. C. 1989, *ApJ*, 344, 685
- . 1998, *ApJ*, 498, 541
- Keres, D., Yun, M. S., & Young, J. S. 2003, *ApJ*, 582, 659
- Kereš, D., Katz, N., Weinberg, D. H., & Davé, R. 2005, *MNRAS*, 363, 2
- Khare, P., vanden Berk, D., York, D. G., Lundgren, B., & Kulkarni, V. P. 2012, *MNRAS*, 419, 1028
- Kimm, T., Devriendt, J., Slyz, A., Pichon, C., Kassin, S. A., & Dubois, Y. 2011, *ArXiv e-prints*
- Klypin, A. A., Trujillo-Gomez, S., & Primack, J. 2011, *ApJ*, 740, 102
- Komatsu, E., Smith, K. M., Dunkley, J., Bennett, C. L., Gold, B., Hinshaw, G., Jarosik, N., Larson, D., Nolte, M. R., Page, L., Spergel, D. N., Halpern, M., Hill, R. S., Kogut, A., Limon, M., Meyer, S. S., Odegard, N., Tucker, G. S., Weiland, J. L., Wollack, E., & Wright, E. L. 2011, *ApJS*, 192, 18
- Kornei, K. A., Shapley, A. E., Erb, D. K., Steidel, C. C., Reddy, N. A., Pettini, M., & Bogosavljević, M. 2010, *ApJ*, 711, 693
- Kravtsov, A., & et al. 1999, in *Evolution of Large Scale Structure : From Recombination to Garching*, ed. A. J. Banday, R. K. Sheth, & L. N. da Costa, 261
- Krogager, J.-K., Fynbo, J. P. U., Ledoux, C., Christensen, L., Gallazzi, A., Laursen, P., Møller, P., Noterdaeme, P., Péroux, C., Pettini, M., & Vestergaard, M. 2013, *MNRAS*, 433, 3091
- Krogager, J.-K., Fynbo, J. P. U., Møller, P., Ledoux, C., Noterdaeme, P., Christensen, L., Milvang-Jensen, B., & Sparre, M. 2012, *MNRAS*, 424, L1
- Krumholz, M. R., & Dekel, A. 2012, *ApJ*, 753, 16
- Krumholz, M. R., & Gnedin, N. Y. 2011, *ApJ*, 729, 36
- Krumholz, M. R., McKee, C. F., & Tumlinson, J. 2008, *ApJ*, 689, 865
- . 2009a, *ApJ*, 693, 216
- . 2009b, *ApJ*, 699, 850
- . 2009c, *ApJ*, 699, 850
- Kuhlen, M., Madau, P., & Krumholz, M. 2013, *ArXiv e-prints*
- Kulas, K. R., McLean, I. S., Shapley, A. E., Steidel, C. C., Konidakis, N. P., Matthews, K., Mace, G. N., Rudie, G. C., Trainor, R. F., & Reddy, N. A. 2013, *ApJ*, 774, 130

- Kulas, K. R., Shapley, A. E., Kollmeier, J. A., Zheng, Z., Steidel, C. C., & Hainline, K. N. 2011, ArXiv e-prints
- Kulkarni, G., Rollinde, E., Hennawi, J. F., & Vangioni, E. 2013, *ApJ*, 772, 93
- Lagos, C. D. P., Baugh, C. M., Lacey, C. G., Benson, A. J., Kim, H.-S., & Power, C. 2011, *MNRAS*, 418, 1649
- Lai, K., Huang, J.-S., Fazio, G., Gawiser, E., Ciardullo, R., Damen, M., Franx, M., Gronwall, C., Labbe, I., Magdis, G., & van Dokkum, P. 2008, *ApJ*, 674, 70
- Laursen, P., Sommer-Larsen, J., & Razoumov, A. O. 2011, *ApJ*, 728, 52
- Ledoux, C., Petitjean, P., Fynbo, J. P. U., Møller, P., & Srianand, R. 2006, *A&A*, 457, 71
- Lehnert, M. D., & Heckman, T. M. 1996, *ApJ*, 462, 651
- Leitherer, C., Robert, C., & Heckman, T. M. 1995, *ApJS*, 99, 173
- Leitherer, C., Schaerer, D., Goldader, J. D., González Delgado, R. M., Robert, C., Kune, D. F., de Mello, D. F., Devost, D., & Heckman, T. M. 1999, *ApJS*, 123, 3
- Leitherer, C., Tremonti, C. A., Heckman, T. M., & Calzetti, D. 2011, *AJ*, 141, 37
- Leroy, A. K., Walter, F., Bigiel, F., Usero, A., Weiss, A., Brinks, E., de Blok, W. J. G., Kennicutt, R. C., Schuster, K.-F., Kramer, C., Wiesenmeyer, H. W., & Roussel, H. 2009, *AJ*, 137, 4670
- Leroy, A. K., Walter, F., Brinks, E., Bigiel, F., de Blok, W. J. G., Madore, B., & Thornley, M. D. 2008, *AJ*, 136, 2782
- Li, C., & White, S. D. M. 2009, *MNRAS*, 398, 2177
- Lu, Y., Wechsler, R. H., Somerville, R. S., Croton, D., Porter, L., Primack, J., Behroozi, P. S., Ferguson, H. C., Koo, D. C., Guo, Y., Safarzadeh, M., Finlator, K., Castellano, M., White, C. E., Sommariva, V., & Moody, C. 2013, ArXiv e-prints
- Macciò, A. V., Kang, X., Fontanot, F., Somerville, R. S., Koposov, S., & Monaco, P. 2010, *MNRAS*, 402, 1995
- Madau, P. 1995, *ApJ*, 441, 18
- Madau, P., Pozzetti, L., & Dickinson, M. 1998, *ApJ*, 498, 106
- Magnelli, B., Elbaz, D., Chary, R. R., Dickinson, M., Le Borgne, D., Frayer, D. T., & Willmer, C. N. A. 2011, *A&A*, 528, A35
- Maiolino, R., Mannucci, F., Cresci, G., Gnerucci, A., Troncoso, P., Marconi, A., Calura, F., Cimatti, A., Cocchia, F., Fontana, A., Granato, G., Grazian, A., Matteucci, F., Nagao, T., Pentericci, L., Pipino, A., Pozzetti, L., Risaliti, G., & Silva, L. 2010, *The Messenger*, 142, 36
- Maiolino, R., Nagao, T., Grazian, A., Cocchia, F., Marconi, A., Mannucci, F., Cimatti, A., Pipino, A., Ballero, S., Calura, F., Chiappini, C., Fontana, A., Granato, G. L., Matteucci, F., Pastorini, G., Pentericci, L., Risaliti, G., Salvati, M., & Silva, L. 2008, *A&A*, 488, 463

- Malhotra, S., & Rhoads, J. E. 2002, *ApJ*, 565, L71
- Maller, A. H., Dekel, A., & Somerville, R. 2002, *MNRAS*, 329, 423
- Maller, A. H., Prochaska, J. X., Somerville, R. S., & Primack, J. R. 2001, *MNRAS*, 326, 1475
- . 2003, *MNRAS*, 343, 268
- Mandelker, N., Dekel, A., Ceverino, D., Tweed, D., Moody, C. E., & Primack, J. 2013, *ArXiv e-prints*
- Marchesini, D., van Dokkum, P. G., Förster Schreiber, N. M., Franx, M., Labbé, I., & Wuyts, S. 2009, *ApJ*, 701, 1765
- Martin, A. M., Papastergis, E., Giovanelli, R., Haynes, M. P., Springob, C. M., & Stierwalt, S. 2010, *ApJ*, 723, 1359
- Martin, C. L. 1999, *ApJ*, 513, 156
- . 2005, *ApJ*, 621, 227
- Martin, C. L., & Kennicutt, Jr., R. C. 2001, *ApJ*, 555, 301
- Mathis, J. S., Mezger, P. G., & Panagia, N. 1983, *A&A*, 128, 212
- Meiring, J. D., Tripp, T. M., Prochaska, J. X., Tumlinson, J., Werk, J., Jenkins, E. B., Thom, C., O’Meara, J. M., & Sembach, K. R. 2011, *ApJ*, 732, 35
- Mo, H. J., Mao, S., & White, S. D. M. 1998, *MNRAS*, 295, 319
- Møller, P., Fynbo, J. P. U., Ledoux, C., & Nilsson, K. K. 2013, *MNRAS*, 430, 2680
- Monaco, P., Fontanot, F., & Taffoni, G. 2007, *MNRAS*, 375, 1189
- Murphy, E. J., Condon, J. J., Schinnerer, E., Kennicutt, R. C., Calzetti, D., Armus, L., Helou, G., Turner, J. L., Aniano, G., Beirão, P., Bolatto, A. D., Brandl, B. R., Croxall, K. V., Dale, D. A., Donovan Meyer, J. L., Draine, B. T., Engelbracht, C., Hunt, L. K., Hao, C.-N., Koda, J., Roussel, H., Skibba, R., & Smith, J.-D. T. 2011, *ApJ*, 737, 67
- Murphy, M. T., & Liske, J. 2004, *MNRAS*, 354, L31
- Murray, N., & Rahman, M. 2010, *ApJ*, 709, 424
- Nagamine, K., Springel, V., & Hernquist, L. 2004a, *MNRAS*, 348, 421
- . 2004b, *MNRAS*, 348, 435
- Nagamine, K., Springel, V., & Hernquist, L. 2005, in *IAU Symposium*, Vol. 216, *Maps of the Cosmos*, ed. M. Colless, L. Staveley-Smith, & R. A. Stathakis, 266
- Nagamine, K., Wolfe, A. M., Hernquist, L., & Springel, V. 2007, *ApJ*, 660, 945
- Nakamura, F., & Umemura, M. 2001, *ApJ*, 548, 19
- Narayanan, D., Bothwell, M., & Davé, R. 2012a, *MNRAS*, 426, 1178

- Narayanan, D., Krumholz, M. R., Ostriker, E. C., & Hernquist, L. 2012b, *MNRAS*, 421, 3127
- Neeleman, M., Wolfe, A. M., Prochaska, J. X., & Rafelski, M. 2013, *ApJ*, 769, 54
- Neufeld, D. A. 1991, *ApJ*, 370, L85
- Niemi, S.-M., Somerville, R. S., Ferguson, H. C., Huang, K.-H., Lotz, J., & Koekemoer, A. M. 2012, *MNRAS*, 421, 1539
- Nilsson, K. K., Møller, P., Möller, O., Fynbo, J. P. U., Michałowski, M. J., Watson, D., Ledoux, C., Rosati, P., Pedersen, K., & Grove, L. F. 2007, *A&A*, 471, 71
- Nilsson, K. K., Tapken, C., Møller, P., Freudling, W., Fynbo, J. P. U., Meisenheimer, K., Laursen, P., & Östlin, G. 2009, *A&A*, 498, 13
- Noterdaeme, P., Petitjean, P., Carithers, W. C., Pâris, I., Font-Ribera, A., Bailey, S., Aubourg, E., Bizyaev, D., Ebelke, G., Finley, H., Ge, J., Malanushenko, E., Malanushenko, V., Miralda-Escudé, J., Myers, A. D., Oravetz, D., Pan, K., Pieri, M. M., Ross, N. P., Schneider, D. P., Simmons, A., & York, D. G. 2012, *A&A*, 547, L1
- Noterdaeme, P., Petitjean, P., Ledoux, C., & Srianand, R. 2009, *A&A*, 505, 1087
- Obreschkow, D., Croton, D., De Lucia, G., Khochfar, S., & Rawlings, S. 2009, *ApJ*, 698, 1467
- Oesch, P. A., Bouwens, R. J., Carollo, C. M., Illingworth, G. D., Magee, D., Trenti, M., Stiavelli, M., Franx, M., Labbé, I., & van Dokkum, P. G. 2010, *ApJ*, 725, L150
- Oh, S.-H., Brook, C., Governato, F., Brinks, E., Mayer, L., de Blok, W. J. G., Brooks, A., & Walter, F. 2011, *AJ*, 142, 24
- Ono, Y., Ouchi, M., Shimasaku, K., Akiyama, M., Dunlop, J., Farrah, D., Lee, J. C., McLure, R., Okamura, S., & Yoshida, M. 2010, *MNRAS*, 402, 1580
- Osterbrock, D. E., & Mathews, W. G. 1986, *ARA&A*, 24, 171
- Ostriker, E. C., McKee, C. F., & Leroy, A. K. 2010, *ApJ*, 721, 975
- Ostriker, E. C., & Shetty, R. 2011, *ApJ*, 731, 41
- Ouchi, M., Shimasaku, K., Akiyama, M., Simpson, C., Saito, T., Ueda, Y., Furusawa, H., Sekiguchi, K., Yamada, T., Kodama, T., Kashikawa, N., Okamura, S., Iye, M., Takata, T., Yoshida, M., & Yoshida, M. 2008, *ApJS*, 176, 301
- Ouchi, M., Shimasaku, K., Furusawa, H., Miyazaki, M., Doi, M., Hamabe, M., Hayashino, T., Kimura, M., Kodaira, K., Komiyama, Y., Matsuda, Y., Miyazaki, S., Nakata, F., Okamura, S., Sekiguchi, M., Shioya, Y., Tamura, H., Taniguchi, Y., Yagi, M., & Yasuda, N. 2003, *ApJ*, 582, 60
- Ouchi, M., Shimasaku, K., Furusawa, H., Saito, T., Yoshida, M., Akiyama, M., Ono, Y., Yamada, T., Ota, K., Kashikawa, N., Iye, M., Kodama, T., Okamura, S., Simpson, C., & Yoshida, M. 2010, *ApJ*, 723, 869

- Panter, B., Jimenez, R., Heavens, A. F., & Charlot, S. 2007, *MNRAS*, 378, 1550
- Papovich, C., Dickinson, M., & Ferguson, H. C. 2001, *ApJ*, 559, 620
- Partridge, R. B., & Peebles, P. J. E. 1967, *ApJ*, 147, 868
- Peebles, P. J. E. 1969, *ApJ*, 155, 393
- Pei, Y. C., Fall, S. M., & Bechtold, J. 1991, *ApJ*, 378, 6
- Pentericci, L., Grazian, A., Fontana, A., Castellano, M., Giallongo, E., Salimbeni, S., & Santini, P. 2009, *A&A*, 494, 553
- Pentericci, L., Grazian, A., Fontana, A., Salimbeni, S., Santini, P., de Santis, C., Gallozzi, S., & Giallongo, E. 2007, *A&A*, 471, 433
- Percival, W. J., Sutherland, W., Peacock, J. A., Baugh, C. M., Bland-Hawthorn, J., Bridges, T., Cannon, R., Cole, S., Colless, M., Collins, C., Couch, W., Dalton, G., De Propriis, R., Driver, S. P., Efsthathiou, G., Ellis, R. S., Frenk, C. S., Glazebrook, K., Jackson, C., Lahav, O., Lewis, I., Lumsden, S., Maddox, S., Moody, S., Norberg, P., Peterson, B. A., & Taylor, K. 2002, *MNRAS*, 337, 1068
- Péroux, C., Dessauges-Zavadsky, M., D’Odorico, S., Sun Kim, T., & McMahon, R. G. 2005, *MNRAS*, 363, 479
- Péroux, C., McMahon, R. G., Storrie-Lombardi, L. J., & Irwin, M. J. 2003, *MNRAS*, 346, 1103
- Pettini, M., Rix, S. A., Steidel, C. C., Adelberger, K. L., Hunt, M. P., & Shapley, A. E. 2002, *ApJ*, 569, 742
- Pettini, M., Shapley, A. E., Steidel, C. C., Cuby, J.-G., Dickinson, M., Moorwood, A. F. M., Adelberger, K. L., & Giavalisco, M. 2001, *ApJ*, 554, 981
- Pettini, M., Steidel, C. C., Adelberger, K. L., Dickinson, M., & Giavalisco, M. 2000, *ApJ*, 528, 96
- Pichon, C., Pogosyan, D., Kimm, T., Slyz, A., Devriendt, J., & Dubois, Y. 2011, *MNRAS*, 418, 2493
- Pilkington, K., Few, C. G., Gibson, B. K., Calura, F., Michel-Dansac, L., Thacker, R. J., Mollá, M., Matteucci, F., Rahimi, A., Kawata, D., Kobayashi, C., Brook, C. B., Stinson, G. S., Couchman, H. M. P., Bailin, J., & Wadsley, J. 2012, *A&A*, 540, A56
- Pirzkal, N., Malhotra, S., Rhoads, J. E., & Xu, C. 2007, *ApJ*, 667, 49
- Pontzen, A., & Governato, F. 2012, *MNRAS*, 421, 3464
- Pontzen, A., Governato, F., Pettini, M., Booth, C. M., Stinson, G., Wadsley, J., Brooks, A., Quinn, T., & Haehnelt, M. 2008, *MNRAS*, 390, 1349
- Popping, G., Somerville, R. S., & Trager, S. C. 2013a, *ArXiv e-prints*
- . 2013b, *ArXiv e-prints*

- Prochaska, J. X., Chen, H.-W., Wolfe, A. M., Dessauges-Zavadsky, M., & Bloom, J. S. 2008, *ApJ*, 672, 59
- Prochaska, J. X., Gawiser, E., Wolfe, A. M., Cooke, J., & Gelino, D. 2003, *ApJS*, 147, 227
- Prochaska, J. X., Herbert-Fort, S., & Wolfe, A. M. 2005, *ApJ*, 635, 123
- Prochaska, J. X., & Wolfe, A. M. 1997, *ApJ*, 487, 73
- . 2009, *ApJ*, 696, 1543
- Qian, Y.-Z., & Wasserburg, G. J. 2003, *ApJ*, 596, L9
- Quider, A. M., Pettini, M., Shapley, A. E., & Steidel, C. C. 2009, *MNRAS*, 398, 1263
- Quinn, T., & Binney, J. 1992, *MNRAS*, 255, 729
- Rafelski, M., Wolfe, A. M., Prochaska, J. X., Neeleman, M., & Mendez, A. J. 2012, *ApJ*, 755, 89
- Rahmati, A., & Schaye, J. 2014, *MNRAS*, 438, 529
- Ranalli, P., Comastri, A., & Setti, G. 2003, *A&A*, 399, 39
- Rao, S. M., Turnshek, D. A., & Nestor, D. B. 2006, *ApJ*, 636, 610
- Razoumov, A. O., Norman, M. L., Prochaska, J. X., Sommer-Larsen, J., Wolfe, A. M., & Yang, Y.-J. 2008, *ApJ*, 683, 149
- Reddy, N. A., Erb, D. K., Steidel, C. C., Shapley, A. E., Adelberger, K. L., & Pettini, M. 2005, *ApJ*, 633, 748
- Reddy, N. A., Steidel, C. C., Fadda, D., Yan, L., Pettini, M., Shapley, A. E., Erb, D. K., & Adelberger, K. L. 2006, *ApJ*, 644, 792
- Reddy, N. A., Steidel, C. C., Pettini, M., Adelberger, K. L., Shapley, A. E., Erb, D. K., & Dickinson, M. 2008, *ApJS*, 175, 48
- Regan, M. W., Thornley, M. D., Helfer, T. T., Sheth, K., Wong, T., Vogel, S. N., Blitz, L., & Bock, D. C.-J. 2001, *ApJ*, 561, 218
- Rieke, G. H., Alonso-Herrero, A., Weiner, B. J., Pérez-González, P. G., Blaylock, M., Donley, J. L., & Marcillac, D. 2009, *ApJ*, 692, 556
- Robertson, B., Bullock, J. S., Cox, T. J., Di Matteo, T., Hernquist, L., Springel, V., & Yoshida, N. 2006a, *ApJ*, 645, 986
- Robertson, B., Cox, T. J., Hernquist, L., Franx, M., Hopkins, P. F., Martini, P., & Springel, V. 2006b, *ApJ*, 641, 21
- Robertson, B., Yoshida, N., Springel, V., & Hernquist, L. 2004, *ApJ*, 606, 32
- Robertson, B. E., & Kravtsov, A. V. 2008, *ApJ*, 680, 1083
- Robitaille, T. P., & Whitney, B. A. 2010, *ApJ*, 710, L11

- Rupke, D. S., Veilleux, S., & Sanders, D. B. 2005, *ApJS*, 160, 115
- Scannapieco, C., Tissera, P. B., White, S. D. M., & Springel, V. 2008, *MNRAS*, 389, 1137
- Schaye, J. 2004, *ApJ*, 609, 667
- Schaye, J., Aguirre, A., Kim, T.-S., Theuns, T., Rauch, M., & Sargent, W. L. W. 2003, *ApJ*, 596, 768
- Schmidt, M. 1959, *ApJ*, 129, 243
- Schneider, D. P., Richards, G. T., Hall, P. B., Strauss, M. A., Anderson, S. F., Boroson, T. A., Ross, N. P., Shen, Y., Brandt, W. N., Fan, X., Inada, N., Jester, S., Knapp, G. R., Krawczyk, C. M., Thakar, A. R., Vanden Berk, D. E., Voges, W., Yanny, B., York, D. G., Bahcall, N. A., Bizyaev, D., Blanton, M. R., Brewington, H., Brinkmann, J., Eisenstein, D., Frieman, J. A., Fukugita, M., Gray, J., Gunn, J. E., Hibon, P., Ivezić, Ž., Kent, S. M., Kron, R. G., Lee, M. G., Lupton, R. H., Malanushenko, E., Malanushenko, V., Oravetz, D., Pan, K., Pier, J. R., Price, III, T. N., Saxe, D. H., Schlegel, D. J., Simmons, A., Snedden, S. A., SubbaRao, M. U., Szalay, A. S., & Weinberg, D. H. 2010, *AJ*, 139, 2360
- Schneider, R., Ferrara, A., Natarajan, P., & Omukai, K. 2002, *ApJ*, 571, 30
- Schwartz, C. M., Martin, C. L., Chandar, R., Leitherer, C., Heckman, T. M., & Oey, M. S. 2006, *ApJ*, 646, 858
- Shapley, A. E., Steidel, C. C., Adelberger, K. L., Dickinson, M., Giavalisco, M., & Pettini, M. 2001, *ApJ*, 562, 95
- Shapley, A. E., Steidel, C. C., Erb, D. K., Reddy, N. A., Adelberger, K. L., Pettini, M., Barmby, P., & Huang, J. 2005, *ApJ*, 626, 698
- Shapley, A. E., Steidel, C. C., Pettini, M., & Adelberger, K. L. 2003a, *ApJ*, 588, 65
- . 2003b, *ApJ*, 588, 65
- Sharma, S., Steinmetz, M., & Bland-Hawthorn, J. 2012, *ApJ*, 750, 107
- Shetty, R., Kelly, B. C., & Bigiel, F. 2013, *MNRAS*, 430, 288
- Shetty, R., & Ostriker, E. C. 2012, *ApJ*, 754, 2
- Shull, J. M., & van Steenberg, M. 1982, *ApJS*, 48, 95
- Simcoe, R. A., Sargent, W. L. W., & Rauch, M. 2004, *ApJ*, 606, 92
- Sobral, D., Best, P. N., Matsuda, Y., Smail, I., Geach, J. E., & Cirasuolo, M. 2012, *MNRAS*, 420, 1926
- Somerville, R. S., Barden, M., Rix, H.-W., Bell, E. F., Beckwith, S. V. W., Borch, A., Caldwell, J. A. R., Häußler, B., Heymans, C., Jahnke, K., Jogee, S., McIntosh, D. H., Meisenheimer, K., Peng, C. Y., Sánchez, S. F., Wisotzki, L., & Wolf, C. 2008a, *ApJ*, 672, 776
- Somerville, R. S., Gilmore, R. C., Primack, J. R., & Domínguez, A. 2012, *MNRAS*, 423, 1992

- Somerville, R. S., Hopkins, P. F., Cox, T. J., Robertson, B. E., & Hernquist, L. 2008b, *MNRAS*, 391, 481
- . 2008c, *MNRAS*, 391, 481
- Somerville, R. S., & Kolatt, T. S. 1999, *MNRAS*, 305, 1
- Somerville, R. S., & Primack, J. R. 1999, *MNRAS*, 310, 1087
- Somerville, R. S., Primack, J. R., & Faber, S. M. 2001, *MNRAS*, 320, 504
- Spergel, D. N., Bean, R., Doré, O., Nolta, M. R., Bennett, C. L., Dunkley, J., Hinshaw, G., Jarosik, N., Komatsu, E., Page, L., Peiris, H. V., Verde, L., Halpern, M., Hill, R. S., Kogut, A., Limon, M., Meyer, S. S., Odegard, N., Tucker, G. S., Weiland, J. L., Wollack, E., & Wright, E. L. 2007, *ApJS*, 170, 377
- Springel, V., Yoshida, N., & White, S. D. M. 2001, *NA*, 6, 79
- Steidel, C. C., Adelberger, K. L., Shapley, A. E., Pettini, M., Dickinson, M., & Giavalisco, M. 2000, *ApJ*, 532, 170
- . 2003, *ApJ*, 592, 728
- Steidel, C. C., Bogosavljević, M., Shapley, A. E., Kollmeier, J. A., Reddy, N. A., Erb, D. K., & Pettini, M. 2011, *ApJ*, 736, 160
- Steidel, C. C., Erb, D. K., Shapley, A. E., Pettini, M., Reddy, N., Bogosavljević, M., Rudie, G. C., & Rakic, O. 2010, *ApJ*, 717, 289
- Steidel, C. C., Giavalisco, M., Dickinson, M., & Adelberger, K. L. 1996a, *AJ*, 112, 352
- Steidel, C. C., Giavalisco, M., Pettini, M., Dickinson, M., & Adelberger, K. L. 1996b, *ApJ*, 462, L17
- . 1996c, *ApJ*, 462, L17+
- Steidel, C. C., Shapley, A. E., Pettini, M., Adelberger, K. L., Erb, D. K., Reddy, N. A., & Hunt, M. P. 2004, *ApJ*, 604, 534
- Stewart, K. R., Brooks, A. M., Bullock, J. S., Maller, A. H., Diemand, J., Wadsley, J., & Moustakas, L. A. 2013, *ArXiv e-prints*
- Stewart, K. R., Kaufmann, T., Bullock, J. S., Barton, E. J., Maller, A. H., Diemand, J., & Wadsley, J. 2011, *ApJ*, 738, 39
- Stinson, G., Seth, A., Katz, N., Wadsley, J., Governato, F., & Quinn, T. 2006, *MNRAS*, 373, 1074
- Storrie-Lombardi, L. J., McMahon, R. G., & Irwin, M. J. 1996, *MNRAS*, 283, L79
- Storrie-Lombardi, L. J., & Wolfe, A. M. 2000a, *ApJ*, 543, 552
- . 2000b, *ApJ*, 543, 552
- Strickland, D. K., Heckman, T. M., Colbert, E. J. M., Hoopes, C. G., & Weaver, K. A. 2004, *ApJ*, 606, 829

- Sutherland, R. S., & Dopita, M. A. 1993, *ApJS*, 88, 253
- Swinbank, A. M., Sobral, D., Smail, I., Geach, J. E., Best, P. N., McCarthy, I. G., Crain, R. A., & Theuns, T. 2012, *MNRAS*, 426, 935
- Tacconi, L. J., Genzel, R., Neri, R., Cox, P., Cooper, M. C., Shapiro, K., Bolatto, A., Bouché, N., Bournaud, F., Burkert, A., Combes, F., Comerford, J., Davis, M., Schreiber, N. M. F., Garcia-Burillo, S., Gracia-Carpio, J., Lutz, D., Naab, T., Omont, A., Shapley, A., Sternberg, A., & Weiner, B. 2010, *Nature*, 463, 781
- Tacconi, L. J., Neri, R., Genzel, R., Combes, F., Bolatto, A., Cooper, M. C., Wuyts, S., Bournaud, F., Burkert, A., Comerford, J., Cox, P., Davis, M., Förster Schreiber, N. M., García-Burillo, S., Gracia-Carpio, J., Lutz, D., Naab, T., Newman, S., Omont, A., Saintonge, A., Shapiro Griffin, K., Shapley, A., Sternberg, A., & Weiner, B. 2013, *ApJ*, 768, 74
- Talia, M., Mignoli, M., Cimatti, A., Kurk, J., Berta, S., Bolzonella, M., Cassata, P., Daddi, E., Dickinson, M., Franceschini, A., Halliday, C., Pozzetti, L., Renzini, A., Rodighiero, G., Rosati, P., & Zamorani, G. 2012, *A&A*, 539, A61
- Tapken, C., Appenzeller, I., Noll, S., Richling, S., Heidt, J., Meinköhn, E., & Mehlert, D. 2007, *A&A*, 467, 63
- Tegmark, M., Blanton, M. R., Strauss, M. A., Hoyle, F., Schlegel, D., Scoccimarro, R., Vogeley, M. S., Weinberg, D. H., Zehavi, I., Berlind, A., Budavari, T., Connolly, A., Eisenstein, D. J., Finkbeiner, D., Frieman, J. A., Gunn, J. E., Hamilton, A. J. S., Hui, L., Jain, B., Johnston, D., Kent, S., Lin, H., Nakajima, R., Nichol, R. C., Ostriker, J. P., Pope, A., Scranton, R., Seljak, U., Sheth, R. K., Stebbins, A., Szalay, A. S., Szapudi, I., Verde, L., Xu, Y., Annis, J., Bahcall, N. A., Brinkmann, J., Burles, S., Castander, F. J., Csabai, I., Loveday, J., Doi, M., Fukugita, M., Gott, III, J. R., Hennessy, G., Hogg, D. W., Ivezić, Ž., Knapp, G. R., Lamb, D. Q., Lee, B. C., Lupton, R. H., McKay, T. A., Kunszt, P., Munn, J. A., O'Connell, L., Peoples, J., Pier, J. R., Richmond, M., Rockosi, C., Schneider, D. P., Stoughton, C., Tucker, D. L., Vanden Berk, D. E., Yanny, B., York, D. G., & SDSS Collaboration. 2004, *ApJ*, 606, 702
- Treister, E., Virani, S., Gawiser, E., Urry, C. M., Lira, P., Francke, H., Blanc, G. A., Cardamone, C. N., Damen, M., Taylor, E. N., & Schawinski, K. 2009, *ApJ*, 693, 1713
- Tremonti, C. A., Heckman, T. M., Kauffmann, G., Brinchmann, J., Charlot, S., White, S. D. M., Seibert, M., Peng, E. W., Schlegel, D. J., Uomoto, A., Fukugita, M., & Brinkmann, J. 2004, *ApJ*, 613, 898
- Tremonti, C. A., Moustakas, J., & Diamond-Stanic, A. M. 2007, *ApJ*, 663, L77
- Tumlinson, J., Thom, C., Werk, J. K., Prochaska, J. X., Tripp, T. M., Weinberg, D. H., Peebles, M. S., O'Meara, J. M., Oppenheimer, B. D., Meiring, J. D., Katz, N. S., Davé, R., Ford, A. B., & Sembach, K. R. 2011, *Science*, 334, 948
- van de Voort, F., Schaye, J., Altay, G., & Theuns, T. 2012, *MNRAS*, 421, 2809
- van den Bosch, F. C., Abel, T., Croft, R. A. C., Hernquist, L., & White, S. D. M. 2002, *ApJ*, 576, 21

- van den Bosch, F. C., & Swaters, R. A. 2001, *MNRAS*, 325, 1017
- Verhamme, A., Schaerer, D., Atek, H., & Tapken, C. 2008, *A&A*, 491, 89
- Verhamme, A., Schaerer, D., & Maselli, A. 2006, *A&A*, 460, 397
- Vitvitska, M., Klypin, A. A., Kravtsov, A. V., Wechsler, R. H., Primack, J. R., & Bullock, J. S. 2002, *ApJ*, 581, 799
- Vladilo, G., Prochaska, J. X., & Wolfe, A. M. 2008, *A&A*, 478, 701
- Wadsley, J. W., Stadel, J., & Quinn, T. 2004, *NA*, 9, 137
- Walter, F., Brinks, E., de Blok, W. J. G., Bigiel, F., Kennicutt, Jr., R. C., Thornley, M. D., & Leroy, A. 2008, *AJ*, 136, 2563
- Warren, S. J., Møller, P., Fall, S. M., & Jakobsen, P. 2001, *MNRAS*, 326, 759
- Weiner, B. J., Coil, A. L., Prochaska, J. X., Newman, J. A., Cooper, M. C., Bundy, K., Conselice, C. J., Dutton, A. A., Faber, S. M., Koo, D. C., Lotz, J. M., Rieke, G. H., & Rubin, K. H. R. 2009, *ApJ*, 692, 187
- Weinmann, S. M., Pasquali, A., Oppenheimer, B. D., Finlator, K., Mendel, J. T., Crain, R. A., & Macciò, A. V. 2012, *MNRAS*, 426, 2797
- Whitaker, K. E., Labbé, I., van Dokkum, P. G., Brammer, G., Kriek, M., Marchesini, D., Quadri, R. F., Franx, M., Muzzin, A., Williams, R. J., Bezanson, R., Illingworth, G. D., Lee, K.-S., Lundgren, B., Nelson, E. J., Rudnick, G., Tal, T., & Wake, D. A. 2011, *ApJ*, 735, 86
- White, S. D. M. 1984, *ApJ*, 286, 38
- Wise, J. H., Turk, M. J., Norman, M. L., & Abel, T. 2012, *ApJ*, 745, 50
- Wolfe, A. M., & Chen, H.-W. 2006, *ApJ*, 652, 981
- Wolfe, A. M., Fan, X.-M., Tytler, D., Vogt, S. S., Keane, M. J., & Lanzetta, K. M. 1994, *ApJ*, 435, L101
- Wolfe, A. M., Gawiser, E., & Prochaska, J. X. 2005, *ARA&A*, 43, 861
- Wolfe, A. M., Lanzetta, K. M., Foltz, C. B., & Chaffee, F. H. 1995, *ApJ*, 454, 698
- Wolfe, A. M., & Prochaska, J. X. 2000, *ApJ*, 545, 591
- Wolfe, A. M., Prochaska, J. X., Jorgenson, R. A., & Rafelski, M. 2008, *ApJ*, 681, 881
- Wolfe, A. M., Turnshek, D. A., Smith, H. E., & Cohen, R. D. 1986, *ApJS*, 61, 249
- Wong, T., & Blitz, L. 2002, *ApJ*, 569, 157
- Young, J. S., & Scoville, N. 1982, *ApJ*, 258, 467
- Yuma, S., Ohta, K., Yabe, K., Shimasaku, K., Yoshida, M., Ouchi, M., Iwata, I., & Sawicki, M. 2010, *ApJ*, 720, 1016

- Zafar, T., Péroux, C., Popping, A., Milliard, B., Deharveng, J.-M., & Frank, S. 2013, *A&A*, 556, A141
- Zheng, Z., Cen, R., Trac, H., & Miralda-Escudé, J. 2010, *ApJ*, 716, 574
- Zwaan, M. A., Meyer, M. J., Staveley-Smith, L., & Webster, R. L. 2005a, *MNRAS*, 359, L30
- Zwaan, M. A., van der Hulst, J. M., Briggs, F. H., Verheijen, M. A. W., & Ryan-Weber, E. V. 2005b, *MNRAS*, 364, 1467